Dipole-dipole interaction in a degenerate quantum gas

Bose-Einstein condensation of chromium atoms

Von der Fakultät Mathematik und Physik der Universität Stuttgart
zur Erlangung der Würde eines Doktors der
Naturwissenschaften (Dr. rer. nat.) genehmigte Abhandlung

vorgelegt von

Axel Rudolf Griesmaier

aus Böblingen

Hauptberichter:	Prof. Dr. Tilman Pfau
Mitberichter:	Prof. Dr. Jörg Wrachtrup
Tag der mündlichen Prüfung:	14. Juli 2006

Physikalisches Institut der Universität Stuttgart

2007

D 93

Für Annette

Table of Contents

Table of Contents i

Zusammenfassung v

Abstract xi

Introduction 1

1 Bose-Einstein condensation 7
- 1.1 Indistinguishability and statistics . . . 8
- 1.2 The Bose-Einstein distribution . . . 9
- 1.3 Bose-Einstein condensation of a free ideal gas . . . 10
- 1.4 Real gases and external potentials . . . 12
  - 1.4.1 Ideal Bose-gases in harmonic traps . . . 13
  - 1.4.2 Finite systems . . . 15
  - 1.4.3 Weak interactions in a Bose-gas . . . 16
- 1.5 A free falling interacting condensate . . . 22
- 1.6 Conclusion . . . 23

2 The apparatus 25
- 2.1 Chamber . . . 25
- 2.2 Magnetic trap . . . 27
- 2.3 Cooling and repumping lasers . . . 27
- 2.4 Optical dipole trap . . . 29
- 2.5 Laser system for optical pumping . . . 29
- 2.6 Computer Control . . . 30

3 Measurement procedure 33
- 3.1 Absorption imaging . . . 33
- 3.2 Reduction of fringe patterns in absorption images . . . 36
- 3.3 Extracting data from images . . . 41
  - 3.3.1 Determination of temperature and number of atoms . . . 41
- 3.4 Time of flight series . . . 45

4 Chromium atoms in an optical dipole trap **47**
4.1 The physics of optical trapping . . . 48
4.1.1 The Lorentz model . . . 49
4.2 Trap geometry . . . 51
4.2.1 Harmonic approximation . . . 52
4.3 Heating by photon scattering . . . 53
4.4 An optical trap for chromium atoms . . . 54
4.5 Expected properties of the trap . . . 56
4.6 Determination of the trapping parameters . . . 58
4.6.1 Axial frequency in the single beam trap . . . 58
4.6.2 Trap frequencies in the crossed dipole trap . . . 60
4.6.3 Radial frequencies in the single beam trap . . . 62
4.7 Loading the optical trap . . . 62
4.7.1 Preparation of a cold cloud in the magnetic trap . . . 62
4.7.2 Transfer into the optical trap . . . 65
4.8 Transfer to the lowest Zeeman state . . . 68

5 Evaporative cooling in the dipole trap **73**
5.1 Theoretical description . . . 74
5.1.1 Forced evaporation . . . 75
5.1.2 Evaporative cooling in dipole traps . . . 77
5.2 Evaporative cooling of chromium . . . 78
5.2.1 Plain evaporation . . . 78
5.2.2 Forced evaporative cooling in the single beam trap . . . 79
5.2.3 Cooling in the crossed configuration . . . 82
5.2.4 Discussion of the optimised evaporation ramp . . . 85

6 Molecular dynamics simulation of the evaporation process **89**
6.1 Basic idea . . . 90
6.2 Comparison with experimental data . . . 96
6.3 Simulation with different parameters . . . 98
6.3.1 Comparison of phase space densities . . . 98
6.3.2 Comparison of spatial densities . . . 100
6.4 Conclusions . . . 102

7 Bose-Einstein condensation of chromium atoms **103**
7.1 Reaching degeneracy . . . 103
7.2 Analysing the BEC transition . . . 106
7.3 Expansion of the condensate . . . 108
7.4 Lifetime of the condensate . . . 109
7.5 Conclusion . . . 113

8 Magnetic dipole-dipole interaction in a Bose-Einstein condensate **115**
8.1 Theoretical description . . . 115

8.1.1 Interaction potential . . . 115
8.1.2 Trapped dipolar condensates . . . 117
8.1.3 Expansion dynamics of a dipolar condensate . . . 119
8.2 Observation of dipole-dipole interaction in a degenerate quantum gas . . . 122
8.3 Measurement of the dipole-dipole strength parameter . . . 127
8.3.1 Direct determination of the scattering length . . . 129
8.3.2 Determination of the dipole-dipole strength parameter . . . 131
8.3.3 s-wave scattering length of ^{52}Cr . . . 132
8.4 Conclusion . . . 133

9 Summary and outlook **135**

Appendix **138**

A Chromium **139**

B Feshbach resonances in chromium collisions – an overview **143**

C Atoms in light fields **149**

D Matlab program to calculate the number of scattered photons **155**

E List of publications **159**

Bibliography **160**

Zusammenfassung

Gegenstand dieser Arbeit ist die experimentelle Realisierung eines Bose-Einstein-Kondensats (BEK) mit Chrom-Atomen [1]. Darüber hinaus konnte in diesem Kondensat erstmalig ein mechanischer Effekt der magnetischen Dipol-Dipol-Wechselwirkung (MDDW) der Atome in einem Gas experimentell nachgewiesen werden [2]. Damit ist das Chrom BEK das derzeit einzige System für die Untersuchung von Dipol-Dipol-Wechselwirkungen in entarteten Quantengasen.
Die Erzeugung eines BEK, also eines makroskopischen Quantenzustands in einem Vielteilchen-System, in einem ultrakalten verdünnten atomaren Gas gelang erstmals 1995 fast zeitgleich in den Gruppen von Eric Cornell und Carl Wieman sowie Wolfgang Ketterle mit Rubidium- bzw. Natrium-Atomen [3, 4] und Randy Hulet mit Lithium [5]. Dieser experimentelle Fortschritt, der den Beweis eines 70 Jahre zuvor von Bose und Einstein theoretisch vorhergesagten Effektes darstellt, hat eine neue, faszinierende Richtung der modernen Atom- und Quantenphysik geprägt und inzwischen unzählige experimentelle sowie theoretische Arbeiten nach sich gezogen. Nur sechs Jahre später wurden Wieman, Cornell und Ketterle für ihre Arbeit zur Erforschung der Eigenschaften dieses neuen Materiezustandes mit dem Nobel-Preis für Physik 2001 ausgezeichnet. In den vergangenen zehn Jahren gelang, neben den bereits erwähnten Elementen Rubidium, Natrium und Lithium, die Erzeugung von BEK in Gasen der Alkalimetalle, Kalium [6] und Cäsium [7], sowie mit Wasserstoff [8], metastabilem Helium [9] und Ytterbium [10].
Im Gegensatz zu einem klassischen Gas spielen Wechselwirkungen zwischen den Atomen eines Bose-Einstein-Kondensates eine wichtige Rolle. Tatsächlich bestimmen die vorhandenen Wechselwirkungen trotz ihrer geringen Stärke alle grundlegenden physikalischen Eigenschaften der BEK. Ihre Stärke, Symmetrie und Reichweite sowie das Wechselspiel der damit verbundenen Energieskalen mit den äußeren (magnetischen und optischen) Potentialen, in denen die BEKs gehalten werden, sind für die faszinierenden Phänomene verantwortlich, die in Bose-Einstein-Kondensaten beobachtet werden können. Alle Spezies, die bislang kondensiert werden konnten, wechselwirken praktisch ausschließlich über die kurzreichweitige und räumlich isotrope Kontaktwechselwirkung, die durch die s-Wellen-Streuung der Atome zustande kommt. Diese Art der

Wechselwirkung kann durch einen einzigen Parameter, die sog. s-Wellen-Streulänge a, charakterisiert werden und ist vergleichbar mit dem harten, elastischen Stoß zweier Billardkugeln auf dem Tisch. Zu den wohl spektakulärsten Effekten die daraus resultieren, zählen die Erzeugung quantisierter Wirbel und Wirbel-Gitter [11, 12, 13], die Implosion ("Bosenova") eines Kondensates, die durch einen plötzlichen Vorzeichen-Wechsel der Kontakt Wechselwirkung von repulsiver zu attraktiver Wechselwirkung vermittelt wird [14], sowie der Quanten-Phasenübergang von der superfluiden in die Mott-Isolator-Phase in einem drei-dimensionalen optischen Gitter [15, 16]. Optische Gitter wurden auch eingesetzt, um das sogenannte Tonks-Girardeau-Regime zu erreichen, in dem die "Fermionisierung" bosonischer Teilchen aufgrund ihrer repulsiven Wechselwirkung beobachtet werden kann [17]. Die beiden letzteren Effekte sind besonders von Bedeutung, da sie eine Verbindung zwischen der Atomoptik und der Physik stark korrelierter Vielteilchen-Systeme in der Festkörperphysik herstellen. In diesem Sinne können atomoptische Experimente als idealisierte Systeme zum Studium typischer Festkörper-Phänomene eingesetzt werden [18].
Gegenüber den atomaren Spezies, die bisher erfolgreich für die Erzeugung von Bose-Einstein-Kondensaten verwendet werden, besitzen Chrom-Atome zusätzlich zur Kontaktwechselwirkung eine signifikante magnetische Dipol-Dipol-Wechselwirkung. Aufgrund ihrer elektronischen Struktur mit sechs ungepaarten Elektronen mit paralleler Spin-Ausrichtung im Grundzustand (Gesamtspin $S = 6$), besitzen Chrom-Atome ein außergewöhnlich großes magnetisches Dipolmoment von $6\,\mu_B$[1]. Da die Stärke der MDDW mit dem Quadrat des magnetischen Moments skaliert, ist sie in einem Chrom-BEK 36 mal größer als bei Alkali-Atomen, die nur ein ungepaartes Elektron besitzen. Die relative Stärke der MDDW zur Kontaktwechselwirkung wird durch den Parameter $\varepsilon_{dd} = \frac{\mu_0 \mu_m^2 m}{12\pi\hbar^2 a}$ charakterisiert. Dieser Parameter ist für Chrom $\varepsilon_{dd} = 0.15$, wobei $a = 103\ a_0 \approx 5.45\,\text{nm}$ die von uns durch Feshbach-Resonanz-Messungen [19] experimentell bestimmte s-Wellen-Streulänge von Chrom ist[2]. Damit ist die Stärke der MDDW von Chrom-Atomen mit der Kontaktwechselwirkung vergleichbar.
Die MDDW unterscheidet sich dabei wesentlich von der Kontaktwechselwirkung, da sie zum einen langreichweitig ist, also statt der lokalen Dichte die gesamte Dichteverteilung herangezogen werden muss, um das Wechselwirkungpotential eines Teilchens im Kondensat zu berechnen. Zum anderen ist sie anisotrop, d.h. ihr Vorzeichen und ihre Stärke hängen vom Winkel ab, unter dem die in einem äußeren magnetischen Feld ausgerichteten Dipole zueinander stehen. Durch diese grundlegend anderen Eigenschaften der MDDW kommen neue kollektive Phänomene zustande, die in den letzten Jahren wachsendes theoretisches und experimentelles Interesse geweckt haben. Ein Überblick

[1] Das "Bohr-Magneton" $\mu_B = \frac{\hbar e}{2m_e} \approx 9.27{\cdot}10^{-24}\,\text{J/T}$ ist die natürliche Einheit des magnetischen Dipolmoments.

[2] a_0 ist der sog. "Bohrradius" – der Radius der niedrigsten Elektronenbahn im Bohrschen Atommodell.

über einige der erwarteten Eigenschaften dipolarer Kondensate findet sich weiter unten im Text.
Experimente zur Bose-Einstein-Kondensation in verdünnten Gasen werden in magnetischen oder optischen Atomfallen im Ultrahochvakuum durchgeführt. Der Übergang von einem klassischen Gas in ein BEK erfolgt dabei typischerweise bei kritischen Temperaturen unterhalb $1\,\mu$K. Zum Erreichen dieser Temperaturen werden meist mehrere Kühlverfahren eingesetzt. Üblicherweise beginnt die Präparation mit dem Einfang und der Laserkühlung der Atome in einer magneto-optischen Falle (MOT). Die hier erreichbaren Temperaturen und Dichten sind jedoch durch inelastische Wechselwirkungen der Atome in Gegenwart des für solche Fallen nötigen nahresonanten Laserlichts begrenzt. Erreichen Dichte und Atomzahl in der MOT ihre stationären Werte, werden die Atome daher meist in magnetische Fallen überführt. In diesen Fallen wird die atomare Wolke durch Verdampfungskühlung [20, 21, 22, 23] bis zum Erreichen der kritischen Temperatur gekühlt. Durch die starke Dipol-Dipol Wechselwirkung der Chrom-Atome ist die Erzeugung eines Chrom BEK mit diesen Standardverfahren jedoch nicht möglich. Mit starken Dipolmomenten geht neben den interessanten Effekten, die auf dem elastischen Teil der Dipol-Dipol Wechselwirkung beruhen, auch eine erhöhte Wahrscheinlichkeit inelastischer Stoßprozesse durch dipolare Relaxation einher. Diese inelastische Wechselwirkung kommt dadurch zustande, dass die Anisotropie der Dipol-Dipol Wechselwirkung Stoßprozesse erlaubt, bei denen ein oder beide Stoßpartner ihre magnetische Quantenzahl m_J ändern, wobei eine Konversion zwischen innerem Drehimpuls der Spins und äußerem Drehimpuls der beiden Stoßpartner in ihrem Schwerpunktssystem stattfindet. Dabei wird, je nach Anfangs- und Endzustand der Atome, innere (Zeeman-)Energie in äußere, kinetische Energie umgewandelt oder umgekehrt. Da statische magnetische Fallen lediglich durch ein lokales Minimum des magnetischen Feldes realisierbar sind[3], befinden sich Atome in einer magnetischen Falle notwendigerweise in energetisch hohen Zeeman-Zuständen. In der Magnetfalle, die im Rahmen dieser Arbeit zum Fangen ultrakalter Chrom-Atome eingesetzt wird, sind die Atome im energetisch höchsten Zeeman-Niveau (magnetische Quantenzahl $m_J = +3$) des Grundzustands $^7S_3$ Spin-polarisiert. Bei dipolaren Relaxations-Stößen wird daher stets Zeeman-Energie freigesetzt, was zum Aufheizen der Atomwolke und zum Verlust von Atomen aus der Falle führt. In vorangegangen Arbeiten wurde gezeigt, dass die Wahrscheinlichkeit solcher inelastischer Prozesse während des evaporativen Kühlens von Chrom-Atomen in einer Magnetfalle durch die Dichtezunahme so stark anwächst, dass die Erzeugung eines Chrom-BEK in solchen Fallen nicht möglich ist [25].
Zur Vermeidung der inelastischen Verluste war es nötig, die Atome aus der Magnetfalle in eine weit rot-verstimmte optische Dipolfalle zu transferieren. Solche Fallen sind in

[3] Die Erzeugung eines lokalen Magnetfeldmaximums in einem statischen Magnetfeld ist nach den Maxwell-Gleichungen im freien Raum nicht möglich [24].

der Lage, Atome unabhängig von ihrem Zeeman-Zustand zu halten. Nach dem Transfer in die optische Falle konnten die Atome daher durch optisches Pumpen im energetisch niedrigsten Zustand ($m_J = -3$) polarisiert werden, in dem in Gegenwart eines (relativ schwachen) Magnetfeldes eine Änderung des Zeeman-Zustandes durch dipolare Relaxation energetisch verboten ist. Dadurch konnte die Lebensdauer des gefangenen Ensembles von 6.3 s auf 142 s gesteigert werden. Diese Erhöhung der Lebensdauer ist eine entscheidende Voraussetzung für das Erreichen der kritischen Temperatur durch Verdampfungskühlung in der optischen Falle. Um für die Verdampfungskühlung ausreichende elastische Stoßraten der Atome zu erzielen, war die Erhöhung der zentralen Dichte der Wolke nötig. Die optische Falle wurde daher als gekreuzte Falle durch zwei Laserstrahlen realisiert. Durch die experimentelle Optimierung der Verdampfungskühlung, sowie durch systematische Verbesserung der Systemstabilität und Atomzahl, konnte schließlich die kritische Temperatur für den Übergang zum Bose-Einstein-Kondensat von 450 nK erreicht werden. Zu diesem Zeitpunkt befanden sich noch etwa 10^5 Atome in der optischen Falle. Inzwischen sind wir in der Lage, fast reine Kondensate mit bis zu 10^5 Atomen zu erzeugen.
Die Anisotropie der Dipol-Dipol Wechselwirkung führt, wie in [26, 27, 28, 29] theoretisch vorhergesagt und in der vorliegenden Arbeit experimentell gezeigt wurde, zu einer Anisotropie der Dichteverteilung eines dipolaren Bose-Einstein-Kondensates. Durch diese Anisotropie hängen viele der für ein solches Kondensat erwarteten Phänomene von der Symmetrie des Fallenpotentials ab. Es wurden Stabilitäts-Kriterien für dipolare Kondensate in unterschiedlichen Fallengeometrien hergeleitet [27, 26, 30], sowie Modifikationen der Grundzustands-Wellenfunktion und des Anregungsspektrums berechnet [26, 28, 30, 31]. So wird in einem scheibenförmigen Potential bei dominanter Dipol-Dipol Wechselwirkung das Auftreten eines Roton-Maxons [32] im Anregungsspektrum erwartet. In Spinorkondensaten [33, 34] führt die Kombination von großem Dipolmoment und großem Spin der Chrom-Atome zu neuen Effekten wie der Konversion von Spin in äußeres Drehmoment [35]. In 2-dimensionalen optischen Gittern wurden neue Quantenphasen theoretisch gefunden. Hierbei finden abhängig von der Tiefe des optischen Gitters Übergänge zwischen der superfluiden Phase mit homogener makroskopischer Wellenfunktion, der “supersoliden” Phase, bei der eine periodische Modulation der makroskopischen Wellenfunktion vorliegt, und der “Schachbrett” Phase, die eine isolierende Phase mit abwechselnd besetzten und unbesetzten Gitterplätzen darstellt, statt [36]. Auch die Bildung von quantisierten Wirbeln und Wirbel-Gittern in rotierenden dipolaren Kondensaten wird durch die relative Stärke der MDDW stark beeinflusst [37, 38, 39].
Die MDDW kann durch rotierende Magnetfelder in ihrer Stärke und ihrem Vorzeichen abgestimmt werden [40]. Wir erwarten, dass wir durch den Einsatz dieser Technik und mit Hilfe von Feshbach Resonanzen zur Einstellung der Kontaktwechselwirkung in der Lage sein werden, die relative Stärke der MDDW über weite Bereiche zu variieren und

deren Einfluss auf die oben genannten Effekte zu untersuchen.
Der Nachweis der MDDW zwischen Chrom-Atomen im BEK stellt ein weiteres zentrales Kapitel der vorliegenden Arbeit dar. Er konnte durch die Untersuchung der Expansionsdynamik von Kondensaten mit unterschiedlicher Polarisation der atomaren magnetischen Dipolmomente bezüglich der Fallengeometrie erbracht werden. Durch die Anisotropie der MDDW wird eine Anisotropie in der Dichteverteilung eines in einer Atomfalle gefangenen BEK erzeugt. Diese Anisotropie gegenüber einer rein isotropen Wechselwirkung beruht darauf, dass in Gegenwart einer anisotropen Wechselwirkung die Gesamtenergie des Systems durch Umlagerung der Atome verkleinert werden kann. Dabei führt diese Umordnung im Falle der MDDW zu einer Elongation in Richtung eines äußeren homogenen Magnetfeldes und zu einer Kontraktion in transversaler Richtung. Die Feldstärke des homogenen Magnetfelds spielt hierbei keine Rolle, da es lediglich als Quantisierungsachse zur Ausrichtung der vorhandenen Dipolmomente dient. Die Anisotropie der Dichteverteilung bleibt auch nach dem Abschalten der Falle, während der freien Expansion des BEK, bestehen. Sie äußert sich bei der Analyse von Absorptionsbildern der fallenden Atomwolke durch ein gegenüber reiner Kontaktwechselwirkung verändertes Längenverhältnis $R_{\parallel}/R_{\perp}$, wobei $R_{\parallel}$ und $R_{\perp}$ die räumliche Ausdehnung des Kondensats in Richtung des äußeren Magnetfeldes bzw. in einer dazu senkrechten Richtung sind. Der experimentelle Nachweis dieser Anisotropie in der Expansion eines Chrom Bose-Einstein-Kondensates in einem externen Magnetfeld stellt neben der Erzeugung des BEK das zentrale experimentelle Ergebnis dieser Arbeit dar. Die Messungen wurden mit einem BEK durchgeführt, das in einer ebenfalls anisotropen Falle präpariert wurde. Der Vergleich von Messreihen, in denen das Magnetfeld parallel bzw. orthogonal zur elongierten Achse der Atomfalle ausgerichtet war, zeigt eindeutig die erwartete Elongation entlang der Feldrichtung und die dazu orthogonale Kontraktion. Durch die Bestimmung des Längenverhältnisses eines expandierenden Chrom BEK nach unterschiedlich langen Flugzeiten, konnte die Dynamik der Expansion mit theoretischen Berechnungen verglichen werden. Dieser Vergleich zeigt eine nahezu perfekte Übereinstimmung des erwarteten mit dem beobachteten Verhalten und liefert zum einen den Beweis des dipolaren Charakters eines Chrom Bose-Einstein-Kondensates, zum anderen zeigt er die Richtigkeit der theoretischen Beschreibung dieses Systems, die auf den hydrodynamischen Gleichungen eines Superfluids unter Hinzunahme der anisotropen Wechselwirkung basiert.
Die asymptotische Ausdehnungsgeschwindigkeit der Atomwolke für lange Flugzeiten mit unterschiedlichen Magnetfeldrichtungen (Polarisationen) wurde darüber hinaus benutzt, um die relative Stärke ε_{dd} der MDDW im Vergleich zur Stärke der Kontaktwechselwirkung zu bestimmen. Um diese Messgröße von der jeweiligen Atomzahl N in einer Messung unabhängig zu machen, wurde die Eigenschaft ausgenutzt, dass die Ausdehnung des expandierten BEK mit $N^{1/5}$ skaliert. Durch eine Reskalierung der Expansionsdaten mit der mittleren Atomzahl aller Einzelmessungen, wird der statis-

tische Fehler der Expansionsgeschwindigkeit deshalb stark reduziert. Dadurch konnte $\varepsilon_{dd} = 0.159 \pm 0.034$. mit sehr kleinem relativen Fehler bestimmt werden. Da die Stärke der MDDW exakt berechenbar ist, konnte aus dem gemessenen Wert von ε_{dd} die Stärke der Kontaktwechselwirkung berechnet und damit ein sehr genauer experimenteller Wert für die s-Wellen-Streulänge von $a_{Cr} = (96 \pm 20)\ a_0$ angegeben werden. Diese Art der Streulängen-Bestimmung ist ausschließlich durch die starke Dipol-Dipol Wechselwirkung der Chrom-Atome möglich und zeichnet sich gegenüber vielen anderen Methoden durch ihre weitgehende Unabhängigkeit von der in Einzelmessungen vorhandenen Zahl der Atome aus. Die erhaltene Streulänge und relative Dipol-Dipol-Wechselwirkungsstärke sind in sehr guter Übereinstimmung mit der aus Feshbach-Resonanz-Messungen bestimmten Streulänge von $a_{Cr} = (103 \pm 13)\ a_0$, sowie der daraus zu erwartenden relativen Stärke der MDDW von $\varepsilon_{dd} = 0.148$.

Abstract

In this thesis, I present the generation of a Bose-Einstein condensate (BEC) of chromium atoms. This constitutes the first realisation of a Bose-Einstein condensate of atoms with strong dipole-dipole interaction. Due to the special electronic and magnetic properties of chromium atoms, standard methods cannot be applied to generate a chromium BEC. The production of a chromium BEC requires novel experimental strategies involving magneto-optical, magnetic and optical trapping, cooling, and pumping techniques which are discussed in this thesis. The BEC transition occurs at a temperature of T_c =450 nm in our crossed optical dipole trap. We are able to create almost pure BECs consisting of 10^5 atoms. I investigate in detail the transition from a classical gas to the BEC phase. An efficient algorithm for classical molecular dynamics simulation of the evaporative cooling sequence is used to model the evaporative cooling process in the optical dipole trap. The results of this simulation are in very good agreement with the experimental findings and are used to develop more efficient cooling strategies in the optical trap.
Compared to all other BECs that have been created so far, chromium atoms have an extraordinarily large magnetic dipole moment and therefore underlie strong magnetic dipole-dipole interaction. This interaction is, in contrast to the contact interaction that stems from s-wave scattering of the atoms, long-range and anisotropic. In a chromium BEC, the strength of the dipole-dipole interaction is comparable to the contact interaction. A steadily growing number of theoretical publications (triggered also by the successful generation of the chromium BEC) show that many interesting new phenomena are expected to occur in a "dipolar" BEC where atoms interact significantly via dipole-dipole forces. The experimental investigation of the expansion dynamics of the chromium BEC that is presented in this thesis provides the first experimental proof of a mechanical effect of (magnetic) dipole-dipole interaction in a gas. In this regard, the chromium condensate has shown to *be* a dipolar BEC.
As compared with the case of a BEC interacting solely via the common contact interaction, magnetic dipole-dipole interaction leads to an elongation along the direction of an external magnetic field and a contraction orthogonal to it. The condensate is described by a hydrodynamic model of superfluids considering dipole-dipole interaction and the experimental results are in excellent agreement with the theoretical predictions.

By a quantitative analysis of the expansion dynamics, I determine the relative strength parameter of the dipole-dipole interaction $\varepsilon_{dd} = 0.159 \pm 0.034$ and deduce the s-wave scattering length $a = (96 \pm 20)\ a_0$. These two quantities allow us to completely describe the interaction of the atoms in the condensate. The experimental results presented in this thesis – the successful generation of a chromium BEC and the proof of its dipolar character – make the chromium BEC the most promising system for further investigations of dipolar effects in degenerate quantum gases.

Introduction

The first observation of Bose-Einstein condensation in a dilute atomic vapour – the emergence of a macroscopic quantum state in a many body system – marked the start of a new era in quantum and atomic physics. Within only a few months in 1995, three groups reported the successful generation of Bose-Einstein condensates (BEC) in ultracold rubidium [3], sodium [4], and lithium [5] gases. Only six years later, Carl Wieman, Eric Cornell, and Wolfgang Ketterle were honoured with the 2001 Nobel prize in physics for their pioneering work on the physics of this new state of matter. Since then, the field has gained the ever growing interest of experimentalists as well as theoreticians. In the following years BECs succeeded in vapours of hydrogen [8] in 1998, potassium [6] and metastable helium [9] in 2001, and cesium [7] and ytterbium [10] in 2003.
All of these elements have their own characteristics. Rubidium and sodium are the "working horses". They are very well understood systems which permit the routine production of very large condensates [41] with comparably low technical effort. Lithium is outstanding due to its effective attractive interaction, and the existence of bosonic and fermionic isotopes which have been brought to degeneracy at the same time [42]. Hydrogen is the simplest atomic system which allows for exact calculations of interatomic potentials. Potassium is also interesting because it has bosonic and fermionic isotopes, and metastable helium is outstanding due to its high internal energy which offers distinguished diagnostic possibilities [43]. Cesium atoms show a very broad Feshbach resonance [44, 45, 46] which makes them perfectly suited for control of the scattering properties, besides being of technical interest since cesium atomic clocks define our time standard. Ytterbium – so far the only non-alkali, non-rare gas atom in the BEC family – stands out due to its vanishing magnetic moment which makes it a promising candidate for precision measurements.
With chromium, the ninth element joins the family of Bose-Einstein condensates [1, 47]. The peculiarities of chromium point in yet another direction. It is outstanding because it introduces a new kind of interaction into the field of degenerate quantum gases. In contrast to all chemical elements that have been successfully brought to quantum degeneracy, chromium atoms have an extraordinarily large magnetic moment of $6\,\mu_B$ in their $^7S_3$ ground state. Since the long-range and anisotropic magnetic dipole-dipole

interaction (MDDI) scales with the square of the magnetic moment, this comes along with a MDDI between two chromium atoms that is a factor of 36 higher than in alkali BECs. The large magnetic moment stems from the unique electronic structure. While the alkalis, which form the largest group among the Bose-Einstein condensates, all have rather simple electronic configuration with only one valence electron, chromium has six valence electrons with aligned spins (total spin quantum number $S = 3$). In contrast to a classical gas, interactions play an important role in a BEC. In fact, although these interactions are very weak, all essential properties of Bose-Einstein condensates of dilute atomic gases are determined by the strength, range, and symmetry of the interactions present.

In all Bose-Einstein condensates that have been created so far, the short-range and isotropic contact interaction that arises from s-wave scattering between the atoms is by far dominating. Many exciting phenomena based on this type of interaction have been studied (reviews are given in [48, 49]). Early experiments with the newly available state of matter aimed at studies of the influence of interactions on the thermodynamic properties of the gas. Deviations of the specific heat and the transition temperature from ideal gas theory were studied [50] and the mean-field interaction energy was measured [51]. Interactions also manifest in the excitation spectrum of a Bose-Einstein condensate by a modification of the eigenfrequencies of elementary excitations [52, 53, 54]. With the generation of quantised vortices and vortex latices [11, 12, 13] in Bose-Einstein condensates, another spectacular type of collective excitations was observed, a phenomenon characteristic for superfluid systems.

The use of Feshbach resonances to tune the contact interaction has opened new possibilities of control over such systems. The fact that the s-wave scattering length is not fixed but can be tuned by application of an external magnetic field allows one to explore extreme regimes from strongly repulsive to very small and strongly attractive interaction. One prominent example called “Bosenova” is the collapse and explosion of a BEC when the contact interaction is suddenly changed from repulsive to attractive [14]. Feshbach resonances have also been used to create BECs of bosonic molecules formed by fermionic atoms [55, 56, 57] and to study the BEC-BCS crossover in these systems [58, 59, 60, 61, 62, 63].

The quantum-phase transition from a superfluid to a Mott-insulator state [15, 16] observed in three- and one-dimensional lattices, respectively, is also a result of the sophisticated interplay between external potentials, quantum-statistics, and inter-particle interaction. Optical lattices were also used to enter the Tonks-Girardeau regime [17], where the so called “fermionisation” of bosonic atoms due their repulsive interaction is observed when the dimensionality of the confining potential is reduced. With these experiments, Bose-Einstein condensates and dilute gases entered the field of strongly correlated many-body systems – a regime that had previously been a domain of solid-state physics. In this sense, an atomic gas can act as a model system for solid-state

physics [18].

Having this in mind, it is evident that creating a Bose-Einstein condensate of atoms that are subject to an interaction with different symmetry and range than the contact interaction will also introduce new collective phenomena. It has been shown in [26, 27, 28, 29], that the anisotropy of the MDDI introduces an anisotropy in the density distribution of a trapped dipolar condensate. The experimental observation of a modification of the condensate expansion due to the MDDI that was proposed in [64] is a central point of this thesis. The regime of dominant dipole-dipole interaction can be entered by using a Feshbach resonance to lower the contact interaction,. Moreover, a continuous transition between both regimes of dominant dipole-dipole or contact interaction is possible.
Many exciting phenomena are expected in a system with dominating dipole-dipole interaction. Due to the anisotropic character of the MDDI, most of them depend strongly on the symmetry of the trap. Modifications of the ground state wave function were predicted [26, 28] and the stability criteria of dipolar condensates in different trap geometries were studied [27, 26, 30]. In pancake-shaped traps [32], modifications of the eigenmodes of elementary excitations are expected [30, 31], as well as the occurrence of a roton-maxon in the excitation spectrum. The existence of new quantum phases was proposed for the case of a dipolar condensate in a two-dimensional optical lattice. Depending on the angle between the magnetic moments and the lattice plain and on the lattice depth, transitions between the superfluid, the supersolid (a superfluid with a periodic modulation of the macroscopic wave function) and the insulating checkerboard phase (similar to a Mott-insulator but where occupied lattice-sites are neighboured by unoccupied ones), are predicted to occur [36]. Dipolar BECs are also discussed in the context of spinor condensates [33, 34]. The combination of large spin and magnetic moment leads to interesting new effects like the conversion of spin into angular momentum [35]. Very recently, the influence of MDDI on the formation of vortex lattices in rotating dipolar BECs has been studied [37, 38, 39]. In these publications, a dramatic influence of the relative strength of the MDDI with respect to the s-wave interaction on the symmetry of the generated lattice structure was found. If the dipole-dipole interaction is strong enough, the existence of 2D-solitons is expected [65]. Tuning of the MDDI is possible by spinning the quantisation axis of the atomic dipoles [40] together with Feshbach tuning of the contact interaction. This allows for the exploration of all these effects in regimes of almost arbitrary different ratio between the two types of interaction. The huge variety of physical phenomena that are predicted for dipolar BECs and the steadily growing number of theoretical work on these effects make dipolar quantum gases one of the most exciting fields of atom optics. With the generation of a Bose-Einstein condensate of dipolar chromium atoms, it becomes possible to start exploring these fascinating phenomena experimentally, too.

The path, however, that finally led to the generation of a chromium BEC was long and required a lot of important experimental and theoretical work on all aspects of cooling and trapping. Two experimental setups and a yearly growing number of lasers involved in the experiment were needed. In contrast to the alkalis, only little was known about the spectroscopic and scattering properties of atomic chromium when our chromium experiment was started. The complex electronic structure made ab-initio calculations of the molecular potentials difficult and important spectroscopic properties and trapping strategies were unknown. The s-wave scattering length – the most important parameter for evaporative cooling, of which neither sign nor modulus was known – had to be determined experimentally to find out whether the generation of a Cr-BEC would work at all. The successful operation of a chromium magneto-optical trap and repumping on the intercombination lines [66] as well as the development of a continuous loading scheme [67, 68, 69] of chromium atoms into a magnetic trap were important steps towards the production of a chromium BEC.
Further progress was achieved with the first measurement [70] of the s-wave scattering length a_{Cr} =170±39 a_0 and the development of a Doppler cooling technique that allowed us to cool the sample optically within the magnetic trap [71]. Later, the scattering length was determined with much higher accuracy to be a_{Cr} =102±13 a_0 at zero magnetic field from a comparison of experimentally observed Feshbach resonances to theoretical results [19](see also Appendix B).
With respect to magnetic trapping and evaporative cooling in a magnetic trap, an extraordinary large magnetic moment is not always of advantage. Besides the many promising possibilities of studying dipole-dipole interaction in a quantum gas with chromium, the dipole-dipole interaction also induces new loss mechanisms. The probability of inelastic collisions due to dipolar relaxation [25] scales with the third power of the total spin. This leads to very large loss rates of magnetically trapped chromium atoms of β_{dr} =2.5·10^{-12} cm^3/s at B =1 G and T =10 μK. This extreme dipolar relaxation rate causes standard condensation techniques to fail in a magnetic trap and necessitates much more elaborate methods for the creation of a chromium BEC. Also a different approach relying on cryogenic buffer gas loading and evaporative cooling of chromium did not succeed due to large losses [72, 73].
The preparation technique that is finally used to generate a chromium Bose-Einstein condensate combines magneto-optical, magnetic and optical cooling, pumping, and trapping techniques [47]. It requires novel strategies, that are adapted to the special electronic structure of chromium and the need to circumvent relaxation processes that originate from the dipolar character of the atoms.

This thesis

In this thesis, I present the all important experimental aspects of the first realisation of a Bose-Einstein condensate of ^{52}Cr atoms. Bose-Einstein condensation of chromium is achieved by evaporative cooling in a far-off-resonant crossed optical dipole trap. I analyse and document the preparation techniques, starting with a pre-cooled sample of 10^8 atoms in a static magnetic trap at roughly the Doppler temperature of 124 μK and a phase space density of $\sim 10^{-9}$. Quantum degeneracy is finally reached at a temperature of 450 nK. Meanwhile, we are able to produce pure condensates containing up to 10^5 atoms. In this sense, this thesis also documents a trip through phase-space over nine orders of magnitude in phase-space density.

The magnetic dipole-dipole interaction among chromium atoms manifests itself in the direct observation of a polarisation dependence in the expansion dynamics of the chromium BEC. This constitutes the first observation of a mechanical effect of dipole-dipole interaction in a gas, similar to magnetostriction and electrostriction which are well known effects in solids.

Analysing the expansion of the dipolar condensate, I determine the relative strength of the dipole-dipole interaction of ε_{dd} =0.159±0.034 which is in excellent agreement with the theoretical prediction of 0.148 . Based on the measured value of ε_{dd}, I present a novel way to determine the s-wave scattering length. It is noteworthy that this kind of measurement is independent of the determination of the number of atoms. This is a clear advantage over many other techniques that are commonly used to determine the scattering length, e. g. by a measurement of the mean-field potential. The chromium scattering length is determined to be $(96 \pm 20)\ a_0$, also in very good agreement with previous measurements.

The thesis is structured as follows:
In Chapter 1, I give a summary of basic BEC physics, starting with an illustrative introduction to the phenomenon of Bose-Einstein condensation. The theoretical concepts that are used later on for comparison with experimental findings are discussed. Starting from BEC in a free ideal gas, the theory is extended to real, interacting gases in external potentials. Anisotropic and long-range dipole-dipole interaction in a BEC are considered in the first sections of Chapter 8.
Chapters 2 to 5 are devoted to the experimental techniques used to produce and detect a chromium BEC. These Chapters may be skipped by the reader who is not so interested in the technical parts. References to the relevant parts and formulas are found in the experimental chapters.
The experimental apparatus that was used for all measurements presented in this thesis is briefly discussed in Chapter 2. In Chapter 3, I present the methods used for taking, processing and evaluating absorption images.
Chapter 4 discusses the theoretical and experimental aspects of trapping chromium atoms in an optical dipole trap. I give an overview of the cooling and trapping techniques that are used to prepare a cloud of chromium atoms first in a magnetic trap which is later on transferred to an optical trap. Further cooling of the chromium sample by evaporation in the optical dipole trap is treated in the subsequent Chapter 5.
Chapters 6 to 8 contain the important experimental results of this thesis. A fast classical molecular dynamics simulation program that is capable of simulating the evaporation process in arbitrary external potentials is presented in Chapter 6. The program is used to develop new strategies for optical trapping and evaporative cooling of chromium atoms. The generation of a Bose-Einstein condensate of chromium atoms will be presented in Chapter 7. Special attention is given to the dependence of the condensate fraction on the temperature and to the lifetime of the condensate.
In Chapter 8, I present the first experimental observation of a direct, mechanical effect of dipole-dipole interaction in a gas. The expansion of a dipolar condensate with different alignment of the atomic magnetic dipole moments is examined and compared to the theoretical predictions of dipolar superfluid hydrodynamic theory which is also introduced at the beginning of this chapter. The experimental results are used for a precise determination of the relative strength of dipole-dipole interactions and the s-wave scattering length of chromium.
The general and spectroscopic properties of chromium that are relevant for the experiments or experimental techniques described in this thesis, are summarised in Appendix A. In Appendix B, I will a give a brief overview of the Feshbach resonances that we have found in collisions of ultra-cold chromium atoms. I conclude with a summary of the experimental findings and an outlook to future experiments.

1 Bose-Einstein condensation

Abstract

This chapter is devoted to the theoretical description of Bose-Einstein condensation in a dilute atomic vapour. The specific statistical properties of Bosons as well as Bose-Einstein condensation of a free ideal gas in the thermodynamical limit and sometimes even a trapped gas are treated in almost all textbooks on statistical-mechanics (see e.g. [74]). These basic physical concepts of Bose-Einstein condensation are important to distinguish between a classical thermal sample and a Bose-Einstein condensate and thus to be able to discern the appearance of this strange kind of matter in the experiment. I will therefore summarise also these basics in the next sections as an introduction to condensate physics.

The observation of a Bose-Einstein condensate in a dilute gas is an interesting effect in itself due to its quantum-statistical origin. But what is really making a gaseous Bose-Einstein condensate such an exciting system is in fact the non-ideal character of real Bose condensed gases - the small repulsive or attractive forces which act between the particles and the sophisticated interplay of the energy scales related to these internal and the external forces. Section 1.4 will therefore treat the more important and realistic case of a finite number of non-ideal, interacting atoms trapped in an external potential. The influence of the trapping potential will be discussed in 1.4.1 and the consequences of the limited number of atoms in real systems will be analysed in 1.4.2. Section 1.4.3 treats Bose-Einstein condensation under the influence of weak isotropic interaction among the atoms. Finally, the expansion of a condensate released from a trap is discussed in Section 1.5. The experimental observation of long-range dipolar interaction in a Bose-Einstein condensate is a central point of this thesis and the consequences of such interactions are astounding and might seem a little counterintuitive. The theoretical background of dipole-dipole interaction in BECs will therefore be discuss together with the experimental findings in Chapter 8.

	non degenerate	partly degenerate	fully degenerate
distinguishable particles			
realizations	6	3	1
relative probability	0.6	0.3	0.1
indistinguishable particles			
realizations	1	1	1
relative probability	0.33	0.33	0.33

Figure 1.1: Dependence of the statistical weight of degenerate and non-degenerate states on indistinguishability explained with the example of three cubes being arranged in different ways. In the top figure, the cubes are distinguishable. There are $6 = 3!$ ways to arrange the cubes in a non-degenerate way whereas only the rightmost arrangement represents a fully degenerate state. With indistinguishable, grey cubes, all three possible types of arrangements have the same statistical weight. In this case, the degenerate state has $N!$ larger weight statistical weight than before.

1.1 Indistinguishability and statistics

In contrast to other condensation phenomena where particles start to build compounds due to their interaction, Bose-Einstein condensation –the macroscopic occupation of one state– is driven only by the indistinguishability and the symmetry properties of the particles. In this context, indistinguishability not only means particles which have identical properties and "look" the same but a principle impossibility to distinguish them. This is a pure quantum effect since classical particles could – even if they all have the same properties – be distinguished by means of their trajectories if one would only look close enough. Once the position and momentum of a classical particle and the surrounding potential are known, its trajectory can be predicted for all times. For a quantum mechanical particle, the Heisenberg uncertainty principle forbids such a localisation with a resolution better than the volume of a unit phase space cell of h^3. Hence such a particle's position is always smeared out over a volume in phase space instead of being localised at one point. If two quantum mechanical particles come closer than this volume in phase space, it is impossible to tell afterwards which was the one or the other. This intrinsic indistinguishability influences the statistical properties of such particles. Consider three cubes like in Figure 1.1, distinguishable by their colour. Now we ask for the ways how they can be arranged by stacking them on the floor. Let us distinguish 3 different situations: 1) if the cubes all sit on top of each other and only one touches the floor, we call this a non-degenerate state because each cube is found on a

different level; 2) if two of the cubes are lying on the floor, the state is partly degenerate; and 3) if all cubes are lying on the floor, we call the system fully degenerate because all cubes are found on the same level. Now we want to know how likely the system is to be found in a degenerate or non-degenerate state. The non-degenerate state can be produced by six different arrangements of the three cubes, the partly degenerate state by three, and the fully degenerate state by only one arrangement. If all arrangements of the cubes have the same a priory probability, the relative probability of finding the system in a fully degenerate state is one in ten or 10%. With a probability of 30%, it will be found in a partly degenerate state, and 60% of the arrangements are non-degenerate. Now we make the cubes indistinguishable by taking away their colour. We ask again for the probabilities of degenerate and non-degenerate states and find that in contrast to the coloured cubes, there is only one non-degenerate state and also only one which is partly degenerate. Still, there is one arrangement representing the fully degenerate state. Thus, the relative probabilities of partly and fully degenerate states of the system have grown to one third of all possible arrangements whereas the probability of finding a non-degenerate arrangement of cubes is now also only one third. The fact that the cubes are indistinguishable increased the probability of finding the system in a degenerate state in our simple model by more than a factor of three. Compared with the non-degenerate state, the fully degenerate state has gained a factor of six in statistical weight. This gain of statistical weight of degenerate states grows with the faculty of the number of particles. It seems that the consequent way to approach degeneracy is by adding more and more bosonic particles to the system until non-degenerate arrangements become so unlikely that one observes a macroscopic occupation of one state. The way in which Bose-Einstein condensation in an atomic vapour is motivated in the following sections is very similar to this way of thinking.

1.2 The Bose-Einstein distribution

The ground state, i.e. the distribution of particles among the states $|\, i \,\rangle$ with energies E_i of a system $\mathcal{S}$ in thermodynamic equilibrium is easily treated in the grand-canonical ensemble which allows exchange of particles and energy between $\mathcal{S}$ and a much larger reservoir $\mathcal{R}$. Assuming equal a priori probabilities for every micro-realisation of a given total energy E_{tot} and number of particles N_{tot} in the system (the micro-canonical ensemble[1]), it turns out that in the grand-canonical ensemble the probability of finding $\mathcal{S}$ in *any* of the micro-realisations of a *certain* E_{tot} and N_{tot} is proportional to the Boltzmann factor $e^{-\frac{E_{tot}-\mu N_{tot}}{k_B T}}$. This is found by applying the micro-canonical ensemble to the complete system $\mathcal{S}+\mathcal{R}$. The state of a system filled with indistinguishable bosons

[1] In the micro-canonical ensemble, $\mathcal{S}$ contains a fixed total energy and number of particles.

is fully specified by the set of occupation numbers $\{n_i\}$ of the states $|\,i\,\rangle$. The total energy of a certain configuration $\{n_i\}$ is found by summing over all energy levels times their occupation numbers $E_{tot}^{\{n_i\}} = \sum_i n_i E_i$ and the total number is given by the sum of the occupation numbers of all states $N_{tot} = \sum_i n_i$. Knowing that the Pauli-principle restricts occupation numbers for fermions to values $n_i = 0$ or 1, whereas for bosons in principle arbitrary $n_i = 0, 1, 2, 3, ...\infty$ are allowed, one can already anticipate here that there will be a fundamental difference in the statistics of bosons and fermions. In the following, only bosons are being considered. At a certain temperature T the partition function $\Xi(T, \mu)$, where μ is the chemical potential[2], is obtained by summing the Boltzmann factors $e^{-\frac{E_{tot}-\mu N_{tot}}{k_B T}}$ of all possible micro-configurations $\{n_i\}$:

$$\Xi(T,\mu) = \sum_{\{n_i\}} e^{-\beta(E_{tot}^{\{n_i\}} - N_{tot}^{\{n_i\}}\mu)} = \sum_{\{n_i\}} e^{-\beta\sum_i (n_i E_i - n_i \mu)} = \sum_{\{n_i\}} \prod_i e^{-\beta(n_i E_i - n_i\mu)}. \tag{1.1}$$

The chemical potential μ is the energy needed to add a particle to the system and $\beta \equiv \frac{1}{k_B T}$ was introduced for simplicity. If we define the fugacity $z = e^{\beta\mu}$, the partition function reads

$$\Xi(T,\mu) = \sum_{\{n_i\}} \prod_i z^{n_i} e^{-\beta n_i E_i} = \sum_{n_0=0}^{\infty} z^{n_0} e^{-\beta E_0 n_0} \cdot \sum_{n_1=0}^{\infty} z^{n_1} e^{-\beta E_1 n_1} \cdot ... = \prod_i \Xi_i \tag{1.2}$$

where Ξ_i are the single particle partition functions

$$\Xi_i = \sum_{n_i=0}^{\infty} z^{n_i} e^{-\beta n_i E_i} = \frac{1}{1 - z e^{-\beta E_i}}. \tag{1.3}$$

A certain number n_i of particles in state i is then found with the statistical probability $1/\Xi_i \cdot z^{n_i} e^{-\beta E_i n_i}$, where the normalisation factor $1/\Xi_i$ accomplishes the constraint that the probability of finding any number of particles in state $|\,i\,\rangle$ be one, $\sum_{n_i=0}^{\infty} 1/\Xi_i \cdot \; z^{n_i} e^{-\beta E_i n_i} = 1$. Now we have everything at hand to calculate the average occupation number of state $|\,i\,\rangle$ for bosons, the *Bose-Einstein distribution function*:

$$\langle n_i \rangle = \frac{1}{\Xi_i} \sum_{n_i=0}^{\infty} n_i z^{n_i} e^{-\beta E_i n_i} = z \frac{\partial}{\partial z} ln \Xi_i = \frac{1}{z^{-1} e^{\beta E_i} - 1} = \frac{1}{e^{\beta(E_i - \mu)} - 1} \tag{1.4}$$

1.3 Bose-Einstein condensation of a free ideal gas

From Eqn. (1.4) follows that μ be smaller than the smallest single-particle energy E_0 to provide that a) $\langle n_i \rangle$ stays positive for all states and b) the occupation number $\langle n_0 \rangle$

[2] The chemical potential is a measure of how much the free energy of a system changes by adding or removing a number of particles while all other variables of the system (such as temperature and pressure etc.) are kept constant.

does not diverge which would happen if $E_0 = \mu$. This leads to the dilemma that for $T \to 0$, all occupation numbers n_i and therefore also N_{tot} would be 0. If one demands a fixed non-zero number of particles N_{tot} in the system, the only way to circumvent this problem is that for $T \to 0$, the chemical potential μ tends towards E_0 in such a way that the lowest single-particle state has a macroscopic but not infinite occupation.
The total number of particles in the system can be easily calculated using Eqn. (1.4):

$$\langle N_{tot} \rangle = \sum_i \langle n_i \rangle = \sum_i \frac{1}{z^{-1} e^{\beta E_i} - 1} = \sum_{E_j} \frac{g_j}{z^{-1} e^{\beta E_j} - 1}. \tag{1.5}$$

Here we have replaced the summation over the different states by the sum over all existing energies and account for the possibility of finding the same energy for different states by introducing the *degree of degeneracy* g_j. In the thermodynamic limit for a homogeneous system, the energy difference between the levels tends to 0, leading to a continuous distribution of states with infinitesimally small energy difference. In this case the degree of degeneracy is replaced by the *density of states* $D(E)$ which is

$$D(E) = \frac{V}{(2\pi)^2} \left(\frac{2m}{\hbar^2} \right)^{3/2} \sqrt{E} \tag{1.6}$$

for free particles in a box with volume V. In the thermodynamical limit of an infinite system, the total number of particles diverges as well as the size of the system, thus one calculates the density instead of the number of particles:

$$n = \frac{\langle N \rangle}{V} = \frac{1}{V} \int_0^\infty \frac{D(E)}{z^{-1} e^{\beta E} - 1} dE + \frac{1}{V} \frac{z}{1-z} = \frac{1}{\lambda_{dB}^3} g_{3/2}(z) + \frac{1}{V} \frac{z}{1-z}, \tag{1.7}$$

where the ground-state population is treated separately in the right term because $D(E = 0) = 0$. Here we have introduced the thermal *deBroglie-Wavelength* $\lambda_{dB} = \sqrt{2\pi\hbar^2 / m k_B T}$ and the *polylogarithm* or *Bose-Einstein integral* [75]

$$g_\alpha(z) = \sum_{j=1}^{\infty} \frac{z^j}{j^\alpha}. \tag{1.8}$$

When the density on the left side of Eqn. (1.7) is increased, the chemical potential included in the fugacity z on the right increases continuously ($z \to 1$). As the chemical potential approaches its upper bound given by the ground state energy E_0, the density in the excited states saturates at a maximum value of

$$n_{max}^{ex} = g_{3/2}(1) / \lambda_{dB}^3.$$

For $z = 1$, the Einstein integral $g_\alpha(1)$ is identical to the Riemann-ζ function $\zeta(\alpha)$. If the density is increased further (by adding more and more particles to the system with

constant volume and temperature), the occupation of excited states can not increase anymore and thus all the excess particles have to populate the ground state of the system and form a *Bose-Einstein condensate (BEC)*. The product $\rho = n\lambda_{dB}^3$ is called *phase-space density* (PSD). This dimensionless quantity measures the number of atoms per unit cell in phase space with 6-dimensional volume $\Delta p^3 \Delta x^3 = h^3$. Equation (1.3) formulates a critical phase-space density of

$$\rho_c = n\lambda_{dB}^3 = \zeta(3/2) = 2.612... \tag{1.9}$$

for which the occupation of the excited states saturates and the atoms of a free ideal gas start to populate the ground state macroscopically.
Instead of increasing the number of particles, the temperature can be lowered to saturate the excited state population, too. At the *critical temperature* for the occurrence of Bose-Einstein condensation, the number of particles in the system is equal to the maximum number of atoms in excited states $N = N_{max}(T_c) = 1/\lambda_{dB}(T_c^{free})^3\zeta(3/2)V$. If we use the definition of the deBroglie wavelength and resolve this equation, we get an expression for T_c^{free}:

$$T_c^{free} = \frac{2\pi\hbar^2}{mk_B}\left(\frac{n}{\zeta(3/2)}\right)^{2/3}. \tag{1.10}$$

If the sample is cooled below T_c^{free}, the population of the ground state grows. Using Eqn. (1.7) and the fact that below T_c^{free} the number of ground state particles is $N_0(T) = N - N_{max}(T)$, one gets the expression

$$\frac{N_0(T)}{N} = 1 - \frac{\zeta(3/2)}{\lambda^3}\frac{V}{N} = 1 - T^{3/2}\left(\frac{mk_B}{2\pi\hbar^2}\right)^{3/2}\frac{\zeta(3/2)}{n} = 1 - \left(\frac{T}{T_c^{free}}\right)^{3/2} \tag{1.11}$$

for the fraction of particles in the ground state[3] depending on the temperature. Obviously, the condensate fraction depends on the ratio T/T_c [4].

1.4 Real gases and external potentials

So far neither external forces nor forces between the atoms have been discussed. Instead, we have only treated the case of an ideal gas of an infinite number of non-interacting particles in a homogeneous surrounding. In contrast, experiments on Bose-Einstein condensates are carried out in atomic traps with a limited number of atoms that interact with each other. In the following sections, Bose-Einstein condensation under these realistic conditions will be discussed.

[3] This quantity is often referred to as the *condensate fraction*.
[4] $t = T/T_c$ is often referred to as the *reduced temperature*.

1.4.1 Ideal Bose-gases in harmonic traps

The traps used to generate Bose-Einstein condensates of dilute gases can usually be approximated by a 3-dimensional harmonic oscillator potential $U_{ext} = m/2(\omega_x^2 x^2 + \omega_y^2 y^2 + \omega_z^2 z^2)$. The energy of a quantum mechanical state in this potential, characterised by the quantum numbers $\vec{n} = (n_x, n_y, n_z)$ is $E_{\vec{n}} = \hbar(\omega_x(n_x + 1/2) + \omega_y(n_y + 1/2) + \omega_z(n_z + 1/2))$. In such a trap the phase space distribution of non-interacting thermal Bosons is

$$f(\vec{r}, \vec{p}) = \frac{1}{(2\pi\hbar)^3} \frac{1}{\exp\left(\frac{U_{ext}(\vec{r}) + \vec{p}^2/2m}{k_B T}\right)}$$

and the spatial distribution is given by the integral over momentum space

$$n_T(\vec{r}) = \int f(\vec{r}, \vec{p}) d^3p = \frac{1}{\lambda_{dB}^3} g_{3/2}(e^{-\frac{U_{ext}(\vec{r})}{k_B T}}).$$

In a similar way, one obtains the momentum distribution

$$n_T(\vec{p}) = \int f(\vec{r}, \vec{p}) d^3r = \frac{1}{(\lambda_{dB} m \omega_{ho})^3} g_{3/2}(e^{-\frac{p^2}{2mk_B T}}),$$

where $\omega_{ho} = (\omega_x \omega_y \omega_z)^{1/3}$ is the geometric mean of the trap frequencies.
At a given temperature, the total number of atoms is now determined in analogy to Eqn. (1.5) by

$$N = \sum_{n_x, n_y, n_z} \frac{1}{e^{\beta(E_{n_x, n_y, n_z} - \mu)} - 1}. \tag{1.12}$$

As in the case of a uniform gas, the ground state population becomes macroscopic when the chemical potential approaches the ground state energy

$$\mu \to \mu_C = \frac{3}{2}\hbar\overline{\omega}, \tag{1.13}$$

where $\overline{\omega} = (\omega_x + \omega_y + \omega_z)/3$ is the arithmetic mean of the trapping frequencies. The population of the excited states is

$$N - N_0 = \sum_{n_x, n_y, n_z \neq 0} \frac{1}{e^{\beta(\omega_x n_x + \omega_y n_y + \omega_z n_z)} - 1} = \int_0^\infty \frac{dn_x dn_y dn_z}{e^{\beta(\omega_x n_x + \omega_y n_y + \omega_z n_z)} - 1}, \tag{1.14}$$

where the sum on the left may be replaced by the integral on the right if the level spacing $\hbar\overline{\omega}$ is much smaller than the thermal energy $k_B T$, allowing to treat these states like a continuum. Solving the integral leads to

$$N - N_0 = \zeta(3) \left(\frac{k_B T}{\hbar \omega_{ho}}\right)^3. \tag{1.15}$$

Following the argumentation of the previous section, we make use of the fact that the excited states saturate for $T \to T_c^0$ to calculate the transition temperature [76] which results in

$$T_c^0 = \frac{\hbar\omega_{ho}}{k_B}\left(\frac{N}{\zeta(3)}\right)^{1/3} \approx 0.94\frac{\hbar\omega_{ho}}{k_B}N^{1/3}. \tag{1.16}$$

Below this temperature, the ground state population grows as

$$\frac{N_0}{N} = 1 - \left(\frac{T}{T_c^0}\right)^3. \tag{1.17}$$

In a system of non-inreacting particles, the ground state of N particles is given by a simple product state[5] $\Phi(\vec{r_1}, \vec{r_2}, ..., \vec{r_N}) = \prod_j \phi_0(\vec{r_j})$, where $\phi_0(\vec{r})$ is the lowest single particle state

$$\phi_0(\vec{r}) = \left(\frac{m\omega_{ho}}{\pi\hbar}\right)^{3/4} e^{-\frac{m}{2\hbar}(\omega_x x^2+\omega_y y^2+\omega_z z^2)},$$

and the density distribution

$$n(\vec{r}) = N|\phi_0(\vec{r})|^2$$

has therefore a Gaussian shape with a size that is independent of the number of particles. The size is given by the oscillator lengths $\sigma_{x,y,z} = 1/\sqrt{(2)}a_{ho,x,y,z} = (\frac{\hbar}{2m\omega_{x,y,z}})^{1/2}$. The ratios of the trapping frequencies are reflected by the ratios of the widths in x, y and z direction: $\sigma_x : \sigma_y : \sigma_z = \frac{1}{\omega_x} : \frac{1}{\omega_y} : \frac{1}{\omega_z}$. which can be compared to the size of a thermal cloud at a temperature $k_BT \gg \hbar\omega$ given by the Maxwell-Boltzmann distribution. Such a thermal distribution has a width $\sigma_T = a_{ho}(k_BT/\hbar\omega)^{1/2}$ – always much larger than that of the condensate. The appearance of a sharp peak in the density distribution is therefore one indication of the presence of a Bose-Einstein condensate in a trapped gas. In analogy to Eqn. (1.4.1) for the thermal cloud, the momentum distribution in the condensate can be calculated by integrating the density distribution (1.4.1) over space. The thermal distribuion is always isotropic, whereas the condensed particles are localised with an uncertainty of h^3 in phase space. Hence their momentum distribution in an anisotropic potential is anisotropic, too. The variance $\sigma_{p,i}$ of their momentum distribution in direction i is inverse proportional to the harmonic oscillator length $a_{ho,i} = \sqrt{\hbar/(m\omega_i)}$ in that direction:

$$\sigma_{p,i} = \frac{\hbar}{\sqrt{2}a_{ho}} = \sqrt{\hbar m\omega_i/2}.$$

If a gas is released from a non-spherical trap and allowed to expand freely by a sudden switch-off of the confining potential, the way it expands is a clear indication of whether it is a thermal gas or in a Bose-condensed state. After long expansion times, a thermal

[5] Writing the state of the system as a product of identical single particle states implies the assumption that the state of a particle be independent of the states of all other particles.

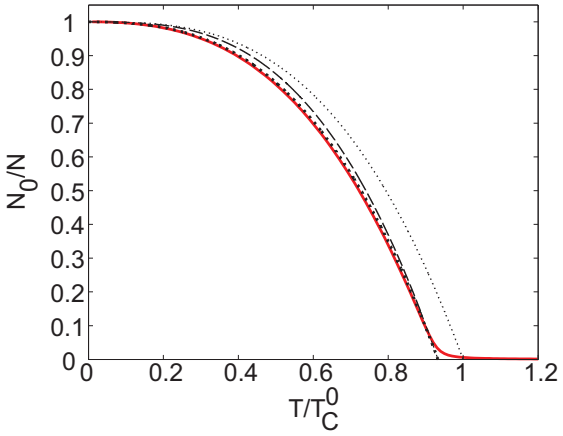

Figure 1.2: Ground state fraction dependance on T/T_c^0 of a non interacting Bose gas. Solid red line: exact solution by solving Eqn. (1.18) numerically, thin dotted line: thermodynamic limit, thick dotted line: using Eqn. (1.19), dashed line: using Eqn. (1.17) and T_c from Eqn. (1.20) instead of T_c^0.

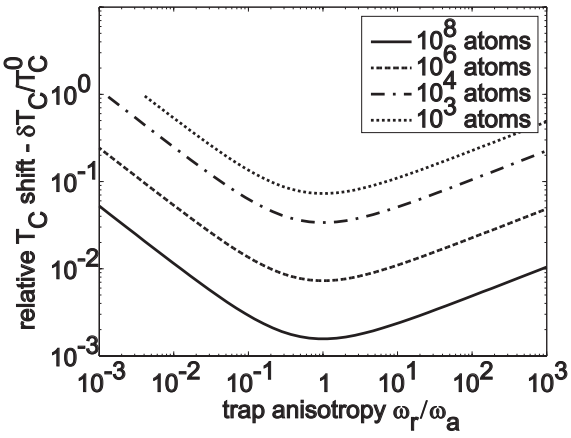

Figure 1.3: Relative transition temperature shift $-\delta T_c/T_c$ due to the trap anisotropy ω_r/ω_a for different numbers of atoms. Note that the T_c shift is always to lower temperatures for anistropic traps. ω_a and ω_r are the trap frequencies along and perpendicular to the symmetry axis of the trap, respectively.

cloud will always obtain a spherical shape due to its isotropic momentum distribution whereas a condensate expands anisotropically with a larger momentum in the direction where it initially obeyed the stronger confinement. The aspect ratio of the condensate is hence inverted during time of flight.

1.4.2 Finite systems

In experiments, the number of trapped atoms is limited. Very large traps contain up to 10^{10} atoms and condensates containing more than 10^7 atoms have been realised [77, 41]. Although these are large samples from an experimentalist's point of view, the thermodynamical limit is never truly reached. Compared to the case of the thermodynamical limit, in systems with finite numbers of particles, the onset of degeneracy in the ground state is smeared out and shifted. To obtain a correction for the transition temperature we consider a cloud of atoms confined in a 3d harmonic potential. For simplicity, we assume equal trap frequencies ω in all directions. Again, the total number of particles is given by the sum over the populations n_j of all states but the ground state ($j > 1$). If the summation

$$N = \sum_{j=1}^{\infty} z^j \left(\sum_{n=0}^{\infty} e^{-jn\beta\hbar\omega} \right)^3 = \sum_{j=1}^{\infty} \frac{z^j}{(1 - e^{-j\beta\hbar\omega})^3} \tag{1.18}$$

is carried out numerically, one can find the value of z corresponding to a certain temperature and number of atoms $\tilde{N}$ by iteratively varying z and comparing the result of Eqn. (1.18) with $\tilde{N}$. To obtain an approximation for the condensate fraction without this numeric approach, the sum can be rewritten as $N = 1/(1-z) + \sum_{j=1}^{\infty} z^j (1/(1 - e^{-j\beta\hbar\omega})^3 - 1)$ and expanded in powers of j. Keeping the two highest powers of $k_B T/\hbar\omega$ results in[6]

$$N - N_0 = g_3(z) \left(\frac{k_B T}{\hbar\omega}\right)^3 + \frac{3}{2} g_2(z) \left(\frac{k_B T}{\hbar\omega}\right)^2. \tag{1.19}$$

Ketterle and van Druten have calculated the transition temperature for finite systems under this approximation in [78] using again saturation of the excited states as the criterion. They get a corrected value for the critical temperature of

$$T_c = T_c^0 + \delta T_c = T_c^0 \left(1 - \frac{\zeta(2)\zeta(3)^{-2/3}}{2} \frac{1}{N^{1/3}}\right) \approx (1 - 0.7275 \frac{1}{N^{1/3}}) T_c^0. \tag{1.20}$$

Figure 1.2 shows that equations (1.19) and (1.20) provide a good approximation of the exact solution except for temperatures very close to the critical temperature (see e.g. [79]).
In the case of non-isotropic trapping potentials, a correction factor of $\frac{1}{3}\sum \omega_i / (\prod \omega_i)^{1/3} = \frac{\overline{\omega}}{\omega_{ho}}$ has to be applied to the shift of the transition temperature $\delta T_c = T_c - T_c^0$ in Eqn. (1.20):

$$T_c = (1 - 0.7275 \frac{\overline{\omega}}{\omega_{ho}} \frac{1}{N^{1/3}}) T_c^0. \tag{1.21}$$

This factor is always larger than 1, thus the transition temperature in a system with a finite number of atoms is lower the more anisotropic the trap is. Figure 1.3 shows the dependence of the shift of the critical temperature for different numbers of atoms. Ketterle and van Druten also derive a finite-size correction to the condensate fraction of Eqn. (1.11):

$$\frac{N_0}{N} = 1 - \left(\frac{T}{T_c^0}\right)^3 - \frac{3\overline{\omega}\zeta(2)}{2\omega_{ho}[\zeta(3)]^{2/3}} \left(\frac{T}{T_c^0}\right)^2 N^{-1/3}.$$

1.4.3 Weak interactions in a Bose-gas

For a real gas with interactions between the atoms, the calculation of the ground state and thermodynamic properties becomes much more difficult because the Hamiltonian now contains interaction terms which depend on the interatomic distances. Usually, this problem is solved by treating it in a mean field approach (described in detail in [79]).

[6] As shown by Ketterle and van Druten [78], the same result can also be obtained by choosing the approximation $D(E) = 1/2((E/\hbar\omega)^2 + 3(E/\hbar\omega))$ for the density of states and proceeding like in Section 1.3.

In second quantisation, the Hamiltonian that describes a system of N interacting bosons trapped in an external potential is given by

$$\hat{H} = \int d\vec{r}\hat{\Psi}^\dagger(\vec{r}) \left[-\frac{\hbar^2}{2m}\nabla^2 + U_{ext}(\vec{r}) \right] \hat{\Psi}(\vec{r}) + \frac{1}{2}\int d\vec{r}d\vec{r}'\hat{\Psi}^\dagger(\vec{r})\hat{\Psi}^\dagger(\vec{r}')V(\vec{r}-\vec{r}')\hat{\Psi}(\vec{r})\hat{\Psi}(\vec{r}'),$$

where $\hat{\Psi}^\dagger(\vec{r})$ and $\hat{\Psi}(\vec{r})$ are the bosonic creation and annihilation operators at position $\vec{r}$, respectively. $V(\vec{r}-\vec{r}')$ is the two-body interaction potential.

The Gross-Pitaevskii equation and Thomas-Fermi approximation

The equation of motion for the condensate wave function is derived by writing down the Heisenberg equation $i\hbar\frac{\partial}{\partial t}\hat{\Psi}(\vec{r},t) = [\hat{\Psi}, \hat{H}]$ with the Hamiltonian from Eqn. (1.4.3). Without going into detail, this is the point where the symmetry properties of the Bosons[7] come into play by the commutator relations of the bosonic field $[\hat{\Psi}(\vec{r}), \hat{\Psi}^\dagger(\vec{r}')] = \delta(\vec{r}-\vec{r}')$, $[\hat{\Psi}(\vec{r}), \hat{\Psi}(\vec{r}')] = 0$, and $[\hat{\Psi}^\dagger(\vec{r}), \hat{\Psi}^\dagger(\vec{r}')] = 0$. This equation can usually not be solved analytically and numerical solutions are also not convenient. The problem can be simplified using a mean field approach by replacing the field operator $\hat{\Psi}$ with its expectation value $\phi(\vec{r}) = \langle\hat{\Psi}(\vec{r},t)\rangle$. In doing so one neglects fluctuations of the ground state wave function, assuming that the physical properties do not change dramatically by annihilating a particle at one position and creating one at another. To justify this, most of the particles have to be in the ground state, which means that this approximation can be good only in systems far below the transition temperature. In such a fully condensed state, all atoms are in the same single particle ground state where $\phi(\vec{r})$ is given by the product of the single particle states (compare Eqn. (1.4.1)) and condensates containing N or $N \pm 1$ particles are almost identical. The classical field $\phi(\vec{r})$ is related to the condensate density by $n_0(\vec{r}) = |\phi(\vec{r})|^2$ and often referred to as the *condensate wave function*.
The relevant interactions in ultra-cold gases are collisions which can be described by a single parameter, the s-wave scattering length [80, 81, 82], independent of the exact details of the interaction potentials. Therefore the interaction term $V(\vec{r}-\vec{r}')$ can be replaced by a δ-like contact potential

$$V(\vec{r}'-\vec{r}) = g\delta(\vec{r}'-\vec{r}) = \frac{4\pi\hbar^2 a}{m}\delta(\vec{r}'-\vec{r})$$

with a coupling constant g that is only related to the s-wave scattering length a and mass m. The scattering length a characterises the range of the interaction. If this range is much smaller than the average inter-particle distance ($n|a|^3 \ll 1$), the total N-particle interaction can be represented by the sum of all pair interactions and the above

[7] The corresponding commutator relation of Fermions would be $[\hat{\Psi}(\vec{r}), \hat{\Psi}^\dagger(\vec{r}')]_+ = \delta(\vec{r}-\vec{r}')$.

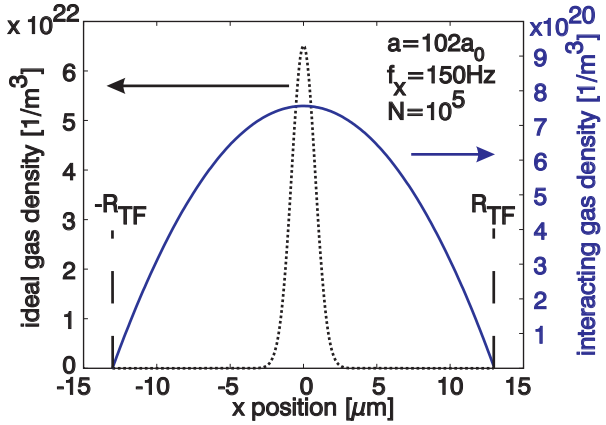

Figure 1.4: Influence of s-wave interaction on the condensate density distribution in the trap, calculated for 10^5 atoms in a trap with frequencies $f_x = 150Hz$, $f_y = 900Hz$ and $f_z = 700Hz$. Dashed line: ideal gas, solid line: interacting gas with the chromium scattering length of $a_{Cr} = 102\ a_0$. Note the different scales for the two distributions.

treatment is justified. If we use this contact potential and replace the field operator $\hat{\Psi}$ by the expectation value, we get the time dependent *Gross-Pitaevskii equation* (GPE)

$$i\hbar\frac{\partial}{\partial t}\phi(\vec{r},t) = \left(-\frac{\hbar^2}{2m}\nabla^2 + U_{ext}(\vec{r}) + g\phi^2(\vec{r},t)\right)\phi(\vec{r},t) \tag{1.22}$$

which describes the atomic motion in the external field and the molecular field generated by all the other atoms in the condensate. In the stationary case where the only time dependence is in the global phase $\phi(\vec{r},t) = \phi(\vec{r})e^{-i\varphi t} = \phi(\vec{r})e^{-\frac{i\mu}{\hbar}t}$ and $\phi(\vec{r})$ is a real function, the time dependence can be separated out and one gets the time independent *stationary Gross-Pitaevskii equation* which is similar to the Schrödinger equation but additionally contains a nonlinear interaction term which depends on the local density $n(\vec{r}) = \phi(\vec{r})^2$:

$$\left(-\frac{\hbar^2\nabla^2}{2m} + U_{ext}(\vec{r}) + g|\phi(\vec{r})|^2\right)\phi(\mathbf{r}) = \mu\phi(\vec{r}). \tag{1.23}$$

Although in the experiments discussed in this thesis, the gases are always dilute and weakly interacting systems ($n|a|^3 \ll 1$), interactions can contribute significantly to the GPE. The average total interaction energy in Eqn. (1.23) is $E_{int} = N g\tilde{n}$, $\tilde{n}$ being the average density which is of the order of N/a_{ho}^3. The interaction energy is thus $E_{int} \approx N^2 g a_{ho}^{-3} \propto N^2 a/a_{ho}^3$. To have an intuitive feeling of the importance of the interactions, this value can be compared to another important energy in the system: the kinetic energy of the atoms. The average kinetic energy is on the order of the ground state energy of the harmonic oscillator $E_{kin} \approx N\hbar\omega$ and thus proportional $E_{kin} \propto N a_{ho}^{-2}$. A measure for the ratio of interaction energy to kinetic energy is then given by

$$\frac{E_{int}}{E_{kin}} \approx N\frac{a}{a_{ho}}$$

In typical experiments, a/a_{ho} is on the order of 1/1000 which means that for atom numbers of 10^3 and more, interactions play an important role. Typical BEC experiments realise condensates containing 100 to 10^7 atoms and the chromium condensates that will be discussed in this work contained up to 10^5 atoms. Hence in most experimental situations and particularly our chromium condensates, interactions are not only important but are the dominating contribution to the GPE.
In this case, the contribution of the *quantum pressure* (kinetic energy) term $\hbar^2\nabla^2/2m \cdot \sqrt{n(\vec{r})}$ in the GPE (1.23) only plays a role in the very outer regions of the condensate and can be neglected to find a direct solution for the condensate wave function and density distribution:

$$\left[U_{ext}(\vec{r}) + g|\phi(\vec{r})^2\right]\phi(\vec{r}) = \mu\phi(\vec{r})$$

with the solution

$$n_{TF}(\vec{r}) = \phi_{TF}(\vec{r})^2 = max(\frac{1}{g}(\mu - U_{ext}(\vec{r}), 0).$$

This is the so called *Thomas-Fermi (TF) approximation*. The relation between chemical potential, number of particles, and trapping frequencies is fixed by the normalisation of the density $n_{TF}(\vec{r})$:

$$\mu = \frac{\hbar\omega_{ho}}{2}\left(\frac{15Na}{a_{ho}}\right)^{2/5}.$$

This implies that the energy that is needed to add a particle to the system is the same everywhere and is equal to the chemical potential, given solely by the sum of the external potential and interaction energy $\mu = U_{ext}(\vec{r}) + E_{int} = U_{ext}(\vec{r}) + gn(\vec{r})$. As a consequence, the condensate has in this approximation a sharp boundary where the condensate density vanishes ($n = 0$). This boundary is given by the condition $U_{ext}(\vec{r}) = \mu$ which defines the *Thomas-Fermi radii* of the cloud in terms of trap frequencies and the chemical potential (Eqn. (1.4.3)):

$$R_i = \sqrt{\frac{2\mu}{m\omega_i^2}}, i = x, y, z.$$

As becomes clear from Eqn. (1.4.3), the density profile in the Thomas-Fermi approximation recovers the inverse shape of the trapping potential with aspect ratios of

$$\frac{R_i}{R_j} = \frac{\omega_j}{\omega_i}$$

The density n_0 in the center of the cloud where $U_{ext} \equiv 0$ is given by the interaction energy

$$n_0 = \frac{\mu}{g}.$$

The solution given by Eqn. (1.4.3) is a good approximation of the condensate density when $\frac{N|a|}{a_{ho}}$ is a large number compared with 1 or in other words if $E_{int} \gg E_{kin}$ in

Eqn. (1.4.3). The total interaction energy stored in the system is $E = \int gn(\vec{r})^2 d^3r = 2/7\mu N_0$. The influence of interaction on the density distribution of a Bose-Einstein condensate is shown in Figure 1.4.3. The figure shows the density distributions of an ideal gas and of an interacting gas with a scattering length of $a = 102\ a_0$ in a trap with a frequency of 150 Hz. The peak density of the interacting gas is more than a factor of 100 lower than that of an ideal gas and the Thomas-Fermi radius of the interacting gas is 16 times larger than the width of the ideal condensate. The distributions were calculated for trap-parameters that are very close to the parameters of the trap where finally a BEC of chromium was created.

Critical temperature of a trapped interacting gas

To calculate the influence of interactions on the ground state occupation and its temperature dependence, the use of the Gross-Pitaevskii equation (1.23) is not sufficient. It seems obvious, that due to the interaction between the condensed particles, in the case of repulsive interaction, the peak density is reduced and one can expect the transition of the critical pase space density $n_{peak}\lambda_{dB}^3 > \zeta(3/2)$ at lower temperatures compared with a non interacting system. Interaction among atoms in the thermal cloud and between thermal atoms and the condensate fraction leads also to a suppression of the thermal density in the center and to occupation of higher energy states than without interaction. Since the classical field Φ describes only the ground state atoms, such interaction effects where thermal atoms are involved are not incorporated in this equation.
To estimate the influence of interaction on the critical temperature, one can use an approach similar to the one for trapped ideal gases in Section 1.4.1. The atoms are now not only trapped in an external potential but additionally feel the interaction with the self-consistent mean field such that they are moving in an effective potential [83]:

$$H = \frac{-\hbar^2\nabla^2}{2m} + U_{eff}(\vec{r}) = \frac{-\hbar^2\nabla^2}{2m} + U_{ext}(\vec{r}) + 2gn(\vec{r}),$$

where $n(\vec{r})$ is the total density $n = n_c + n_T$. The thermal density can be calculated by replacing $U_{ext}(\vec{r})$ in Eqn. (1.4.1) by $U_{eff}(\vec{r}) - \mu$:

$$n_T(\vec{r}) = \frac{1}{\lambda_{dB}^3} g_{3/2} e^{-\frac{U_{eff}(\vec{r})-\mu}{k_B T}}.$$

Right at the critical temperature T_c, the total number of atoms has to fulfill the condition

$$N = \int n_T(\vec{r}, \mu_c, T_c) d^3r$$

where the critical chemical potential μ_c is the lowest energy eigenvalue of the Hamiltonian (1.4.3), similar to the considerations made in Sections 1.3 and 1.4.1. The leading

contribution to the total energy in a large system stems from the interactions, thus it can be approximated by

$$\mu_c^0 = 2gn(0).$$

The central density $n(0)$, which one would gain from a self consistent solution of the Schrödinger equation using the Hamiltonian (1.4.3), can be approximated by the peak density of the non interacting model (1.4.1). In [84, 79] Giorgini et al. have calculated the shift $\delta T_c = T_c - T_c^0$ of the critical temperature in presence of interaction by an expansion of the right-hand side of Eqn. (1.4.3) around $\mu_c = mu_c^0$ and $T_c = T_c^0$:

$$\delta T_c = -1.33 \frac{a}{a_{ho}} N^{1/6} T_c.$$

Including also finite size corrections (Eqn. (1.20)), the relative shift of the critical temperature of an interacting trapped gas [84] is

$$\frac{\delta T_c}{T_c^0} \approx -0.728 \frac{\omega_{ho}}{\overline{\omega}} N^{-1/3} - 1.33 \frac{a}{a_{ho}} N^{1/6}.$$

For a simpler representation of the condensate fraction in presence of interactions, we first define the following two parameters: The first one is the ratio between the chemical potential (Eqn. (1.4.3)) of the interacting system calculated with the Thomas-Fermi approximation at $T = 0$ and the critical temperature T_c^0 of the non-interacting model:

$$\vartheta = \frac{\mu}{k_B T_c^0} = \alpha \left(N^{1/6} \frac{a}{a_{ho}} \right)^{2/5},$$

where additionally the numerical coefficient $\alpha = 15^{2/5} \zeta(3)^{1/3}/2 \simeq 1.57$ has been introduced. The second parameter is the reduced temperature $t = \frac{T}{T_c^0}$, i.e. the ratio between the temperature of the system and the critical temperature of the ideal gas. The temperature dependence of the condensed number of atoms can be calculated by integrating the distribution function (1.4.1) over the whole phase space:

$$N_T = \frac{1}{(2\pi\hbar)^3} \int \frac{1}{\exp[(p^2/2m + U_{eff}(\vec{r}) - \mu)/k_B T] - 1} d^3r d^3p,$$

where one neglects the kinetic term and takes the Thomas-Fermi approximation for the effective mean field potential $U_{eff}(\vec{r}) - \mu \equiv |U_{ext}(\vec{r}) - \mu|$. With the parameters ϑ and t that we have introduced above, the condensate fraction of an interacting gas is given by [79]

$$\frac{N_0}{N} = 1 - t^3 - \frac{\zeta(2)}{\zeta(3)} \vartheta t^2 (1 - t^3)^{2/5}.$$

1.5 A free falling interacting condensate

The treatment of the expansion dynamics of an interacting condensate released from a trap is not as simple as for an ideal gas that was discussed in Section 1.4.1. In that case, we found that a condensate released from an anisotropic trap expands anisotropically. The reason was an inhomogeneous momentum distribution due to the uncertainty principle which revealed an anisotropy opposite to the anisotropy of the spatial distribution in the trap. This argumentation can not be kept in the Thomas-Fermi approximation where the kinetic energy term is neglected. Instead, the expansion dynamics is determined by the interaction energy where the problem in describing the expansion theoretically is that after the trap is switched off, the interaction energy is converted into kinetic energy. The kinetic term can therefore not be neglected anymore and the Thomas-Fermi approximation is not suited to describe the expansion. Castin and Dum have used a classical model to describe the evolution of the density distribution after release from a trap [85] (compare also Section 8.1.3). They show that also in this case, the condensate expansion is anisotropic.
Their approach is to use a classical gas as a model where the force given by the gradient of the total energy

$$\vec{F}(\vec{r},t) = -\nabla \left(U_{ext}(\vec{r},t) + g n_{cl}(\vec{r},t) \right)$$

acts on every particle. In the equilibrium situation, just before switching off the trap at $t = 0$, this force vanishes ($\vec{F}(\vec{r},0) = 0$) and the classical steady state density is equal to the Thomas-Fermi solution of Eqn. (1.4.3): $n_{cl}(\vec{r},0) = n_{TF}(\vec{r},0) = N_0|\Phi_{TF}(\vec{r})|^2$. When the trap potential is switched off suddenly at $t = 0$, the first term in Eqn. (1.5) vanishes and the atoms experience a force $F(\vec{r}) = -\nabla(g\ n_{TF}(\vec{r},0)) = \nabla U_{ext}(\vec{r},0)$, accelerating them outwards[8]. Obviously, the initial acceleration is proportional to the gradient of the confining potential in every direction. Hence, if the cloud was trapped in an anisotropic potential, the expansion of a condensate is anisotropic like in the case of a non-interacting gas. In the classical model used by Castin and Dum and in the case of harmonic external potentials, the cloud experiences only a dilatation without changing the shape of the distribution. Every infinitesimal volume element with initial position $r_i(0)$ (where $i = [x, y, z]$) of the expanding condensate moves along a trajectory given by the simple scaling law

$$r_i(t) = \lambda_i(t) r_i(0), \quad i = [x, y, z]$$

[8] Here $U_{ext}(\vec{r},0)$ is the external potential *just before* the trap is switched off.

with the global scaling parameters $\lambda_i(t)$ which do not depend on the position. The density distribution of the condensate at a time t is therefore given by

$$n_{cl}(\vec{r},0) = max\left(\frac{\mu - \sum_i \frac{m\omega_i^2 r_i^2}{2\lambda_i^2(t)}}{g\lambda_x(t)\lambda_y(t)\lambda_z(t)}, 0\right),$$

which has still the shape of an inverted parabola having widths of $W_i = 2\lambda_i(t)R_i$. Newton's law $m\ddot{\vec{r}}(t) = \vec{F}(\vec{r}(t),t)$ with $\vec{F}$ from Eqn. (1.5) leads to a set of coupled differential equations for the scaling parameters $\lambda_i(t)$:

$$\ddot{\lambda}_i = \frac{\omega_i(0)^2}{\lambda_i\lambda_x\lambda_y\lambda_z} \quad i = [x,y,z].$$

The starting conditions are $\lambda_i(0) = 1$ and $\dot{\lambda}_i(0) = 0$ since the gas is initially at rest. In the case of an axially symmetric trap with $\omega_x = \omega_y = \omega_\perp$ and $\omega_z = \epsilon\omega_\perp$, the scaling parameters can be expanded in powers of ϵ and the set of differential equations (1.5) is solvable. To zeroth order in ϵ one obtains

$$\lambda_\perp(t) = \sqrt{1+\omega_\perp^2(0)t^2},$$

and $\lambda_z(t) = 1$ and to second order in ϵ, the time dependence of the axial scaling parameter λ_z is

$$\lambda_z(t) = 1 + \epsilon^2\left(\omega_\perp(0)t\arctan(\omega_\perp(0)t) - \ln\sqrt{1+\omega_\perp^2(0)t^2}\right) + O(\epsilon^4).$$

Where one sees that after some time ($\omega^2t^2 \gg 1$), both directions tend to expand linearly. After a certain time, the width $W_\perp$ of the expanding condensate in radial direction will overhaul the axial radius W_z, changing the aspect ratio of the condensate

$$\frac{W_\perp(t)}{W_z(t)} = \epsilon\frac{\lambda_\perp(t)}{\lambda_z(t)}$$

from $W_\perp(t)/W_z(t) < 1$ to $W_\perp(t)/W_z(t) > 1$. Monitoring the aspect ratio in dependence of the time of ballistic expansion is thus a powerful technique because unlike the widths $W_\perp$ and W_z, the aspect ratio does not depend on the number of atoms. In the limit of large times ($t \gg 1/\omega_{bot}$), the aspect ratio approaches an asymptotic value of $W_\perp(t)/W_z(t) = 2/\pi\epsilon$.

1.6 Conclusion

In this chapter I have summarised the basic theoretical concepts of Bose-Einstein condensation that are used in the later discussion of the experimental findings in Chapters 7

and 8. Starting from a descriptive approach to BEC, the theoretical description was extended from BEC in a free ideal gas to trapped gases and finite systems. Finally, it was shown that interactions among atoms influence the properties of a Bose-Einstein condensate significantly. Although BECs are dilute systems, the interaction energy has turned out to be much larger than the kinetic energy if the number of atoms in the condensate and the scattering length are large enough. This causes a dramatic change of the density distribution of a trapped BEC compared to an ideal gas. Interactions also manifest themselves in a shift of the critical temperature and modified dynamics of expanding BECs.

2 The apparatus

Abstract

All experiments that are discussed in this thesis have been carried out in an ultra high vacuum steel chamber. An outline drawing of the main parts is depicted in Figure 2.1. Large parts of the whole experimental setup like the cooling and repumping lasers, the chamber, the magnetic trap and computer control facilities have been developed and installed by the team of people working in our lab and have already been discussed in several previous works [86, 87, 88, 89, 68, 90]. They shall only be summarised in this chapter to give the reader the core information needed to understand the experimental procedure. Within the framework of this thesis, a frequency-doubled laser system for optical pumping was assembled (Section 2.5) and a new setup of the optical dipole trap was implemented (Section 2.4).

2.1 Chamber

The setup of the vacuum apparatus [86, 87] consists of two chambers: the lower oven chamber and the upper trapping chamber. A beam of chromium atoms is generated in the lower chamber by a resistively heated high temperature effusion cell operating at 1600 ^{o}C. The pressure in this chamber is held on a 10^{-9} mbar level by a 75 l/s Ion getter pump during operation of the effusion cell. An 80 cm long Zeeman slower connects the oven to the upper science chamber which contains the magneto-optical, magnetic and optical traps and where all experiments are performed. This chamber is also pumped by a 75 l/s Ion getter pump and additionally by a thin layer of titanium as a getter material on the inner walls of the chamber which can be refreshed by a titanium sublimator from time to time. The pressure in the upper chamber stays beyond the range of our ion gauge of $<10^{-11}$ mbar all the time during operation of the apparatus. This low pressure in the region of the trap is a very important prerequisite to keep the probability of collisions between trapped atoms and molecules from the background gas low which allows for long storage time of the trapped atoms.

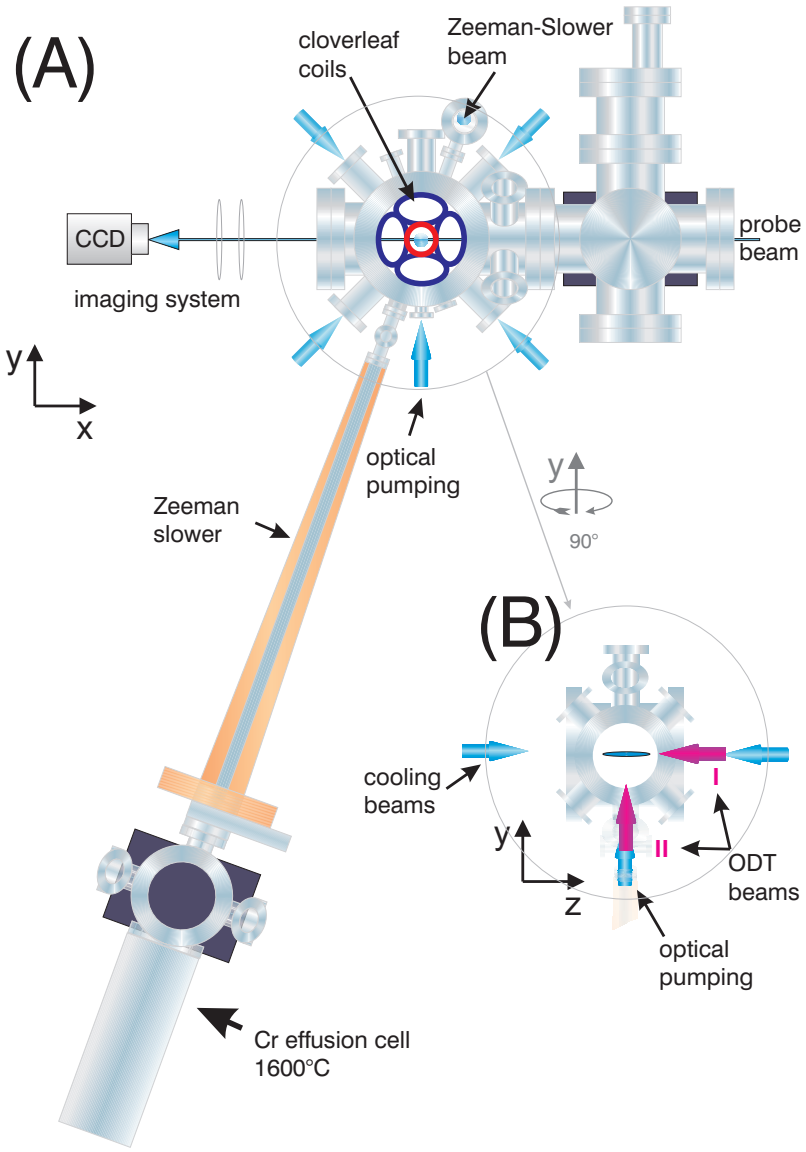

Figure 2.1: Schematic setup of our experiment: a) whole apparatus, b) upper chamber seen in the direction of the probe beam. The horizontal beam I of the dipole trap propagates in z-direction and carries a power of up to 9.8 W. The vertical beam II defines our y-direction and has a maximum power of 4.8 W.

2.2 Magnetic trap

The magnetic trapping potential [87] is generated by a set of water-cooled coils in cloverleaf configuration [51]. The currents through the coils can be ramped up to 300 A to generate a maximum axial curvature of 324 G/cm^2 and a maximum radial gradient of 201 G/cm resulting in typical trap frequencies of 73 Hz in axial and 800 Hz in radial direction at 1 G offset field. All currents can be set and switched by our Labview based computer control system [88, 89]. The symmetry axis of the magnetic trap is in horizontal direction and defines the *z-axis* of the experimental setup. The vertical axis is referred to as the *y-axis* and the third one as the *x-axis*. Three extra sets of coils are wound around the body of the chamber to produce additional homogeneous magnetic fields (∼2 G/A per pair of coils) in all three directions. They are separately controllable to compensate for external fields and the offset field produced by the magnetic trap as well as to apply the quantisation fields necessary for imaging and optical pumping. Fast switching of all magnetic fields is provided by the use of MOSFETs and – particularly for large currents – IGBTs (insulated gate bipolar transistors) [1].

2.3 Cooling and repumping lasers

The main laser system of the apparatus produces the blue light at 425.6 nm that is needed for optical cooling and imaging on the $^7S_3 \leftrightarrow {}^7P_4$ transition [68, 90]. Infrared light with a wavelength of 851.1 nm from a Titanium:Sapphire laser[2] pumped by an argon ion laser[3] is frequency-doubled by a brewster cut Lithium Triborate (LBO) crystal in a monolithic ring cavity. The system is stabilised by Doppler-free polarisation spectroscopy of the $^7S_3 \leftrightarrow {}^7P_4$ transition in a chromium hollow cathode lamp with a lock-in technique to reduce noise. With a pumping laser power of 17 W and an infrared power of 2 W, we are able to produce 800 mW of blue light. In normal experimental operation, we limit the blue power to ∼500 mW because higher intensities lead to thermal lens effects in the crystals of the acousto-optical modulators (AOM) used to adjust frequencies and intensities.
Atoms can decay from the excited state $^7P_4$ of the cooling transition to the metastable $^5D_4$ and $^5D_3$ states in which they are decoupled from the cooling light. To transfer the atoms in $^5D_4$ back to the ground state via the $^7P_3$ state, we use a 5 mW external cavity [4] diode laser system [92] resonant with the $^5D_4 \leftrightarrow {}^7P_3$ transition at 663.2 nm. A second

[1] Semikron
[2] Coherent, MBR110
[3] Coherent, Sabre R 25 TSM
[4] Littrow configuration [91]

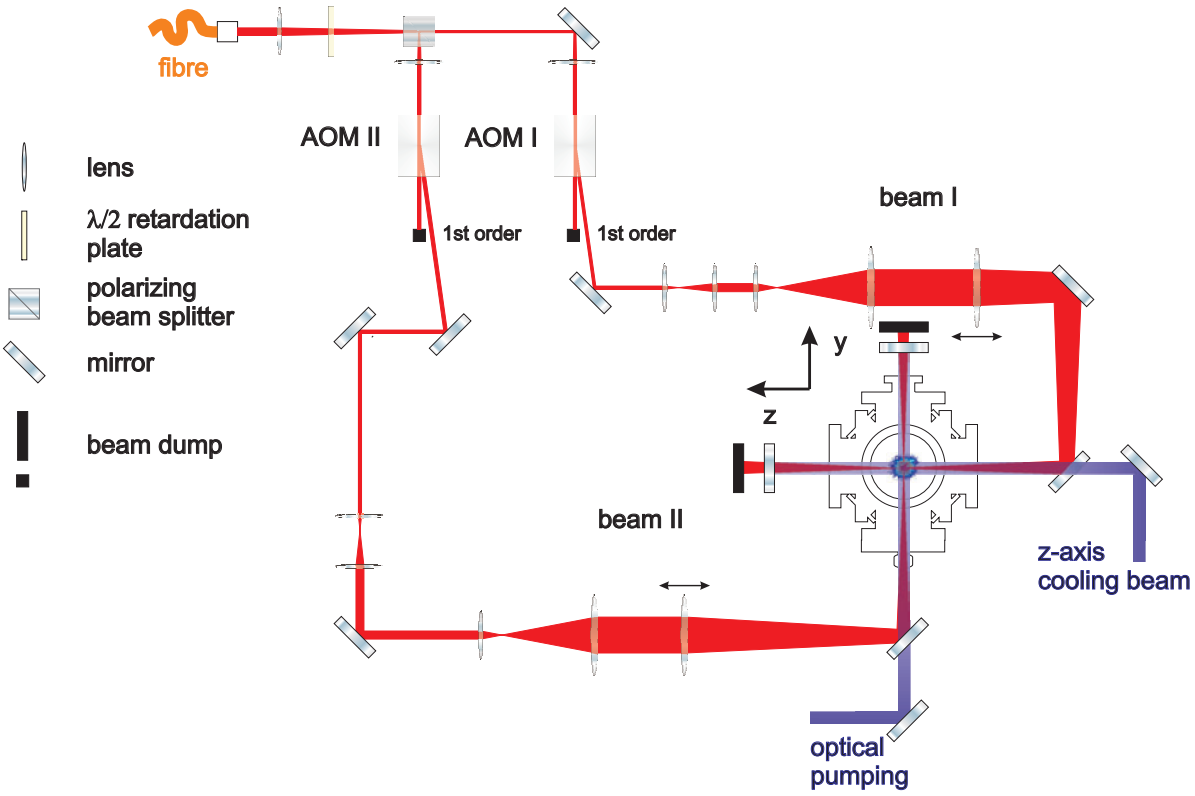

Figure 2.2: Outline of the optical dipole trap setup. Beam I is in horizontal (z-) direction, Beam II is in vertical (y) direction.

laser system with identical setup is available for the $^5D_3 \leftrightarrow {}^7P_3$ transition at 654 nm but is usually not used because the gain in atom number is small compared to the previous one and not worth maintaining this system. These lasers are locked to the modes of a Fabry-Perot resonator close to the transition wavelength using the Pound-Drever-Hall sideband modulation scheme [93]. The cavity is made of Zerodur and Invar – which have very low thermal expansion coefficients – and it has a free spectral range of 75 MHz. A small part of the light is used for locking and can be shifted by double-pass AOMs, such that the output of the laser systems are on resonance with the atomic transitions. The thermal drift of the cavity is about 2 MHz/h.

All lasers can be switched on and off by mechanical shutters and the cooling and imaging light can additionally be dimmed and tuned in a range of $\pm 10\Gamma$ around resonance by AOMs.

2.4 Optical dipole trap

The laser that is used to generate the light for the optical trap is an Yb-fibre laser[5] that operates at a wavelength of 1064 nm and provides a maximum power of 20 W. This laser has a linewidth of $\Delta\lambda$ =1.65 nm, corresponding to a coherence length of $\lambda^2/\Delta\lambda$ =0.7 mm which prevents the formation of a standing wave in the optical trap. The optical setup that is used to prepare two TEM_{00} mode beams and to focus them to the center of the experimental chamber is depicted in Figure 2.2. The light coming from the laser is collimated to a diameter of 4.7 mm by the head of the fibre. The linear polarisation of the light allows one to split it up into two beams with adjustable intensity ratios using a polarising beam splitter and a $\lambda/2$-plate. Acousto-optical modulators in both optical beam paths allow for a precise, independent control of both laser intensities and the possibility of a rapid switch-off for time of flight imaging with a suppression of the laser intensity of ∼45 dB. Two telescopes in each of the beam paths are used to expand the beams before they are focussed by two f =500 nm lenses with 5 cm diameter. The main beam is focussed to a waist of 29.5 μm and shone in in horizontal direction through the center of the cloverleaf coils of the magnetic trap. It usually carries optical powers of 9 W to 12 W. The second beam is shone in in vertical direction through a viewport from below the chamber. It is focussed to 50 μm and used to form a dimple in the potential of the horizontal beam (see Chapter 4). Usual operation of this beam is at 4-5 W. In the center of the chamber, the two beams cross under an angle of 90°. The two final mirrors before the chamber are equipped with coatings that are highly reflective for the 1064 nm trap light and highly transmissive at 425 nm. In this way, the horizontal MOT beam and the vertical pumping beam on the $^7S_3 \rightarrow {}^7P_3$ transition can be shone in from behind these two mirrors. The properties of the trap for chromium atoms are discussed in Sections 4.4 and 4.5.

2.5 Laser system for optical pumping

Optical pumping (see Section 4.8) of the atoms from $m_J = +3$ to $m_J = -3$ on the $^7\mathrm{S}_3 \leftrightarrow {}^7\mathrm{P}_3$ transition requires light with a wavelength of 427.6 nm. To generate this light, an additional laser system was set up in the framework of this thesis. It is based on an injection locked master-slave [94] diode laser system operating at twice the blue wavelength (855.2 nm). This infrared light is frequency doubled by a potassium-niobate ($KNbO_3$) crystal [95, 96] in a home made monolithic ring cavity [97]. A schematic representation of the laser setup is found in Figure 2.3.
Once the laser is on resonance, the grating of the master diode is locked to the nearest

[5] IPG PYL-20M-LP

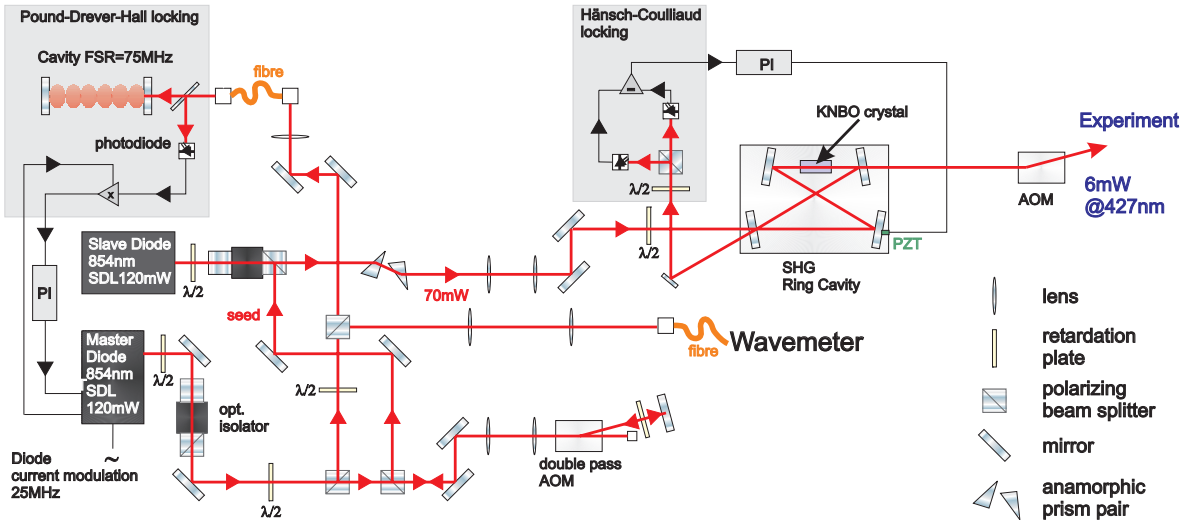

Figure 2.3: Schematic setup of the frequency doubled master-slave diode laser system used to generate the 427.6 nm light for optical pumping.

lock point of the Pound-Drever error signal of the same reference cavity on which also the repumping lasers for the metastable states (see Section 2.3) are locked. Due to the free spectral range of 75 MHz, this lock point is at most 37.5 MHz (in the infrared light) away from resonance. The slave laser is shifted back on resonance by a double-pass acousto-optical modulator (AOM) between master and slave diode. With about 70 mW of infrared power coming from the slave diode, the system produces up to 6 mW of blue light at 427.6 nm. However, for the pumping only a few hundred microwatt are needed.

2.6 Computer Control

Two standard PC computer systems are used to control the apparatus and take and save the camera images. Additionally, a third PC allows on-the-fly evaluation of the images. The current setup uses 32 digital[6] and 16 analog[7] channels to control the most important experimental parameters. The analog cards provide ±10 V output and can additionally be amplified, damped, and biased by a stack of isolated amplifiers to adapt the output to the range required by the device. In this way one can make use of the full 12Bit resolution of the D-A-converter for any kind of required input range. All digital channels are isolated from the computer output by opto-couplers and provide 50 Ω outputs with a maximum load of 50 mA per channel. We are able to trigger arbitrary sequences on all analog and digital channels at a rate of 10 kHz. A command

[6] National Instruments type PCI-6533 PCI card
[7] National Instruments type PCI-6713 PCI card

interpreter [89] is capable of generating sequences of patterns which define the system status for a certain period of time. The input to this interpreter can be generated very comfortably by a graphical user interface[8]. The system allows the use of constants and variables, provides the possibilities to programm loops of sequences, supports the call of external modules, and is able to interpret standard mathematical operations within the sequences. It is therefore possible to write very complex programs that vary a system parameter in a certain way within a loop. It is also possible to program time varying ramps for the analog channels which makes programming evaporation ramps very comfortable. The relevant system parameters of a sequence are saved to a file format that is readable by our Matlab[9]-based evaluation software and can thus be easily incorporated in the data acquisition procedure. The LabView-patterns are saved together with the images of one experimental run, such that it is always possible to reconstruct or repeat the complete experiment.

[8] National Instruments Labview
[9] Mathworks

3 Measurement procedure

Abstract

In all experiments that are described in this thesis, data acquisition is based on only one very powerful measurement technique, namely the optical imaging of a free falling cloud of atoms. With a proper model to describe the behaviour of the cloud during ballistic flight and knowledge of the initial trap parameters, all thermodynamic quantities can be extracted from only these pictures. All experiments follow the same basic cycle: 1) the preparation of a cold atomic cloud within the dipole trap, either purely thermal at a temperature above T_c or below T_c with a condensate fraction present, 2) the sudden release of the atoms from the trap and 3) subsequent mapping of the spatial density distribution after a time of free fall (TOF) and expansion (typically between 1-20 ms).

The methods that have been used to take and process images for this thesis will be presented in this chapter. It starts with a general discussion on how to take and process absorption images. This is followed by a description of the imaging system used in our setup. Subsequently, I will discuss a scheme to improve the quality of absorption images by reducing fringe patterns by mathematical means. Finally, the way of extracting the interesting thermodynamic quantities out of the processed images will be explained. From a single image taken after a time t of free expansion, one obtains the current density distribution $n_{TOF}(t)$. With the knowledge of the trap parameters ω_i, the temperature T of the cloud can be determined from a single image. Even more precise measurements of T that do not require exact knowledge of the trap parameters are obtained when analysing the dependence of $n_{TOF}(t)$ of the density distribution on the expansion time in a series of images.

3.1 Absorption imaging

Throughout the experiments presented in this thesis, the method used to image the atomic cloud is absorption imaging. In this technique, the cloud is illuminated with a probe beam of resonant light in the direction of the imaging system (see Figure 3.1) and

casts a shadow on the photosensitive chip of a CCD (charge coupled device) camera. While passing in x-direction through a cloud of atoms with density distribution $n(\vec{r})$, the intensity $I(\vec{r})$ of the probe beam with frequency ω_p is reduced by

$$dI(\vec{r}) = -\sigma(\omega_p)n(\vec{r})I(\vec{r})dx,$$

where $\sigma(\omega_p)$ is the photon scattering cross section. With the considerations made in Appendix C, this cross section can be calculated from the power of light scattered by an atom:

$$P_{sc} = \sigma(\omega_p)I = \hbar\omega_p\Gamma_{sc}(\omega_p).$$

From the scattering rate Γ_{sc} in the low intensity limit[1] and from Eqn. (3.1), one obtains the light scattering cross section

$$\sigma(\omega_p) = P_{sc}/I = \frac{\hbar\omega_p\Gamma_{sc}(\omega_p)}{I} = \frac{\hbar\omega_p\Gamma}{2I_s}\frac{1}{1+\left(\frac{2\delta}{\Gamma}\right)^2}.$$

Integration of Eqn. (3.1) along x yields:

$$I(\vec{r}) = I(x,y,z) = I_0 e^{-\sigma(\omega_p)\int_{-\infty}^{x} n(x',y,z)dx'}$$

which is equal to Beer's law $I(x) = I_0 e^{-\rho_O x}$ for constant density n where ρ_O is the optical density. As a result, the intensity profile $I(x,y,z)$ of the probe beam after crossing the cloud contains information on the *column density*

$$n(y,z) = \int_{-\infty}^{\infty} n(x',y,z)dx' = \frac{1}{\sigma(\omega_p)} ln\left(\frac{I_0(x,y)}{I(x,y)}\right)$$

In practice, three images are taken with the CCD camera after every experiment: first the absorption image of the cast shadow of the cloud which delivers the intensity profile $I_a(y,z)$, and second a reference image $I_r(y,z)$ of the probe beam intensity profile without atoms present. For technical reasons, the exposure time of the camera chip is much longer than the time for which the atoms are illuminated by the probe beam. Hence, we finally take a background image $I_b(y,z)$ where the probe beam is off to identify stray light and electronic background noise in the camera picture. The first two images are taken in quick succession (a delay of 350 ms) to prevent large fluctuations of the probe beam power and pointing between the images. After the first image is taken, resonant light is shone on the atoms for 100 ms to blow away the cloud making use of the light pressure force (see Eqn. (C.7)). To prevent the cloud from being disturbed too much by the momentum diffusion induced by resonant scattering during probe light exposure, we chose the shortest exposure time that can be triggered with our setup which is 100 μs.

[1] In the low intensity limit $s = I/I_s \ll 1$ and is therefore neglected in the denominator of Eqn. (C). I_s is the saturation intensity defined in Eqn. (C.5).

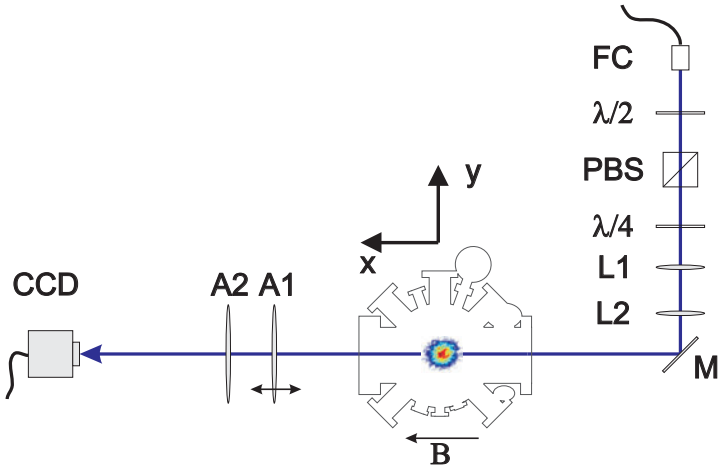

Figure 3.1: Outline of the imaging system. FC: Fiber coupler; PBC: polarising beam splitter; $\lambda/2$, $\lambda/4$: wave plates; M: mirror; L1, L2: lenses used to expand the probe beam; A1, A2 achromats f =300 mm; CCD: camera.

The density profile $n(y,z)$ (Eqn. (3.1)) is then calculated from the three intensity distributions:

$$n(y,z) = -\frac{1}{\sigma(\omega_p)} ln \frac{I_a(y,z) - I_b(y,z)}{I_r(y,z) - I_b(y,z)}.$$

Imaging system

The experimental setup allows photographs of the cloud from two directions: from above the chamber (y-direction) and from the side (x-direction, compare Fig. 3.1). Both imaging systems use two lenses to map the cloud onto the chip of a progressive scan CCD-camera[2]. Because of the limited optical access and the resulting small numerical aperture in the vertical axis, images taken in this direction are of rather poor quality. Therefore we use pictures taken in the vertical direction only to control the proper alignment of the dipole trap and for similar qualitative purposes. The setup of the imaging system in horizontal direction is outlined in Fig. 3.1. It mainly consists of two identical 2 inch achromats with a focal length of 300 mm and a measured magnification of 1.0. The probe light is guided to the chamber via a polarisation maintaining optical fibre. Fast switching is provided by a double-pass AOM in front of the fibre coupler. After the fibre, the light passes a $\lambda/2$-wave plate and a polarising beam splitter cube to adjust the intensity of the probe beam. A $\lambda/4$-wave plate provides the possibility to generate $\sigma+$ or $\sigma-$ light, depending on which Zeeman state has to be detected. Sharp focussing of the imaging system is achieved by moving the first achromat which is mounted on a translation stage as such that the object plane of the

[2] PCO Pixelfly QE

system runs through the cloud.
A standard USAF-1951 test target[3] was used to determine the spatial resolution of the imaging system. The measured resolution of $\sim 8\,\mu$m is just above the diffraction limit of $\Delta x = 2.44\lambda f/d = 6.2\,\mu$m. Here $f = 300\,$mm is the focal length of the lenses, $d = 5\,$cm is the lens diameter and $\lambda = 425\,$nm is the wavelength of the light used for imaging. The resolution coincides with the pixel size of the CCD of $6.45\,\mu$m in both, horizontal and vertical direction on the image. Before an image is taken, a small homogeneous magnetic field is applied along the direction of the probe beam to align the atomic dipole moments. The direction of this field is the same for the detection of both, $m_J = +3$ or $m_J = -3$ atoms in the ground state. Its magnitude corresponds to a detuning of $\pm 2.5\Gamma$ from the $m_J = \pm 3 \rightarrow m_J = \pm 4$ transition, respectively. In both cases, the σ-polarised light pumps the atoms to the extreme Zeeman-state $m_J = \pm 3$ from where they can only be excited to $m_J = \pm 4$, permitting to treat them as two-level atoms.
Sharp focussing of the cloud is provided by minimising refraction effects, a method that has been discussed by A. Marte in [98].

3.2 Reduction of fringe patterns in absorption images

Due to the many optical elements in the path of the probe beam, the presence of fringe patterns in the images originating from smallest dust particles on some of these elements is almost unavoidable. In principle, if all the setup was absolutely stable in a mechanical sense, these fringes would be identical in both the absorption and reference image and would thus vanish after application of Eqn. (3.1). Small fluctuations of the position of the scattering dust particles however, even on the order of a fraction of a micron with respect to the camera chip, lead to a phase shift between the patterns in absorption and reference images. A position change of half the wavelength of the imaging light already leads to the maximum shift of π of the pattern phase and a full visibility in the processed image. As a result, the final processed image is distorted by numerous ring patterns which reduce the quality of fits to the density distribution as depicted schematically in Fig. 3.2. This particularly matters for small numbers of atoms or long times of flight, where the optical density has already severely dropped and comes close to the typical order of depth of these fringes of about $5 - 10\%$ of the probe light intensity. The origin of these fluctuations could be mechanical vibrations transmitted to the chamber or the optical setup when switching on the quantisation field for imaging. A running cooling fan of the camera would also be one possible source for vibrations. In

[3] Newport RES-1

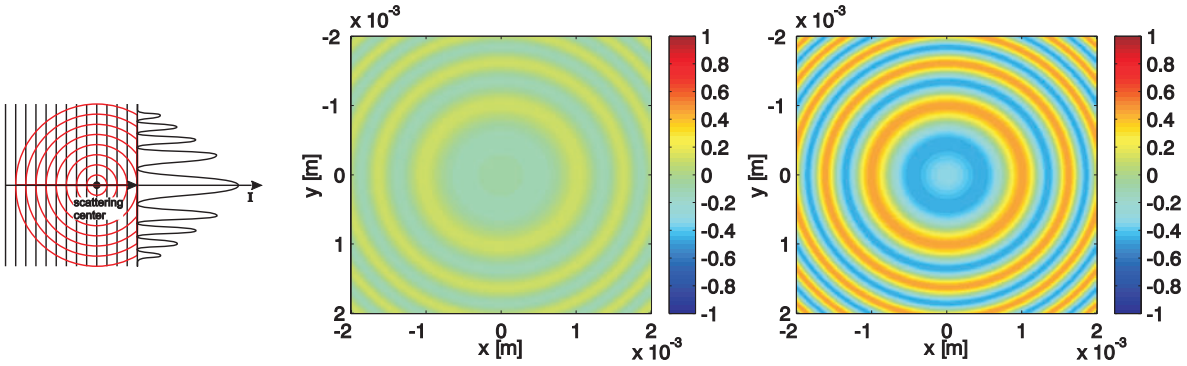

Figure 3.2: Left figure: a dust particle in the plain wave of the probe beam causes an interference pattern on the CCD chip. Right two figures: Remaining patterns on a 4 mm^2 area of the CCD chip when Eqn. (3.1) is applied to images where the particle has moved by 50 nm (left pattern) and 200 nm (right pattern) towards the CCD chip between the images, respectively. The calculation was performed for a distance of 30 cm between the scattering particle and the chip. The colour bars measure the relative amplitude of the pattern compared to full visibility, i.e. 180° phase shift between image and reference image.

our setup however, these mechanical sources of noise could not be eliminated completely. To overcome this drawback in a different way, we have implemented a method in our image evaluation software that has been developed by the group of Klaus Sengstock at Hamburg University [99] and presented on the annual meeting of the DPG (German Physical Society) 2005. Since this is not a standard method of image manipulation and has to my knowledge not been published in written form yet, I will discuss it in more detail.

The basic concept of this technique is to not use only one reference picture which contains a fringe pattern with an arbitrary phase with respect to the absorption image. Instead, the reference is constructed from an orthogonal set of reference images by projecting the absorption image onto their basis. In the ideal case, the basis contains a full set of orthogonal patterns, such that any pattern in the absorption image can be reproduced through the projection by linear combinations of the basis vectors and the fringes can be completely removed from the processed image.

To generate a suitable set of base vectors, first a number N of reference images in the form of matrices $\mathbf{R}_1..\mathbf{R}_N$ is chosen which have been taken within a not too long interval before or after the absorption image[4]. The reference basis is generated from these images using the Schmidt orthogonalisation method. The N vectors $\mathbf{B}_1..\mathbf{B}_N$ which span the new basis are calculated as follows:

[4] Pictures which have been taken a few minutes (and ideally not longer than half an hour) before or after the absorption image are best suited. If the delay is longer, the result is worse and a new set has to be generated.

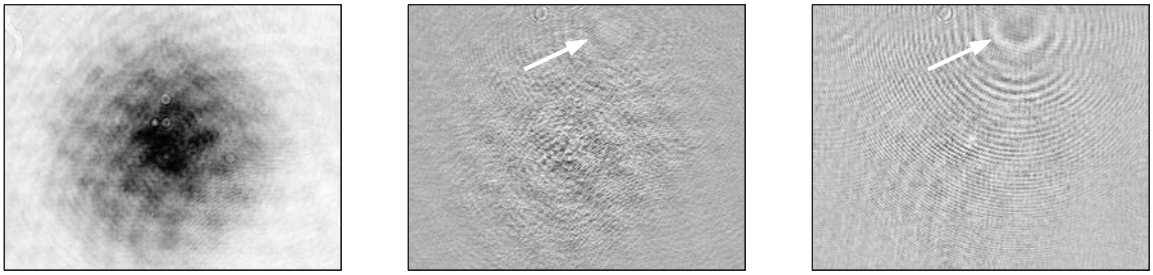

Figure 3.3: Three examples of orthogonal base vectors in a set of 30 reference images. The 1^{st}, 2^{nd} and 6^{th} elements of the set are shown (left to right). The phase shift between the fringes in the right two images is clearly visible (arrows).

- One of the reference pictures is chosen as the first base vector and normalised to unity length

$$\mathbf{B}_1 = \frac{\mathbf{R}_1}{\sqrt{\mathbf{R}_1 \bullet \mathbf{R}_1}}.$$

  where we define the scalar product of two pictures with n_x and n_y pixels in x and y direction, similar to the scalar product of vectors

$$\mathbf{U} \bullet \mathbf{V} = \sum_{x=1}^{n_x} \sum_{y=1}^{n_y} U[x,y]V[x,y]$$

- The further base vectors have to be constructed by taking the reference pictures one after another, eliminating all information from the image that can already be reproduced by the existing basis and normalising the remaining information $\mathbf{M}$.

$$\mathbf{M}_i = \mathbf{R}_i - \sum_{j=1}^{i-1} \mathbf{R}_i \bullet \mathbf{B_j}$$

$$\mathbf{B}_i = \frac{\mathbf{M}_i}{\sqrt{\mathbf{M}_i \bullet \mathbf{M}_i}}.$$

- The most effective result is obtained by taking a set of reference images which is larger than the desired number of base vectors and selecting the best suited images. Assume the basis already contains k vectors. The one image $\mathbf{R}$ which is worst represented in the already existing basis, i.e. the one which carries the most new information, is best suited to generate the next basis vector $\mathbf{B}_{k+1}$.
  A measure for the information content of a basis vector is its length before normalisation or the total count of the squares of all of its pixel values. Figure 3.5 displays the information content for a set of 40 vectors. Obviously, the larger the set already is, the less additional information comes with a new vector. One has to find a trade-off between quality and computation time to decide when the set

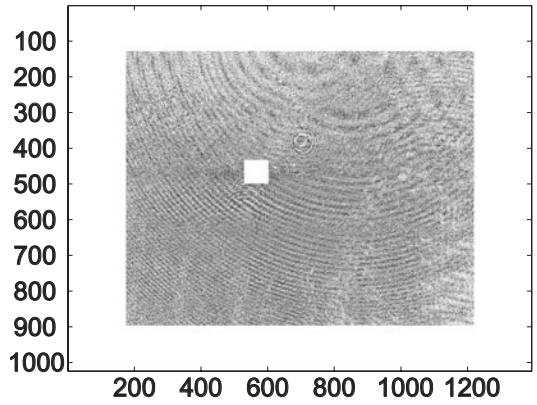

Figure 3.4: Part of the absorption image that is used for projection into the basis.

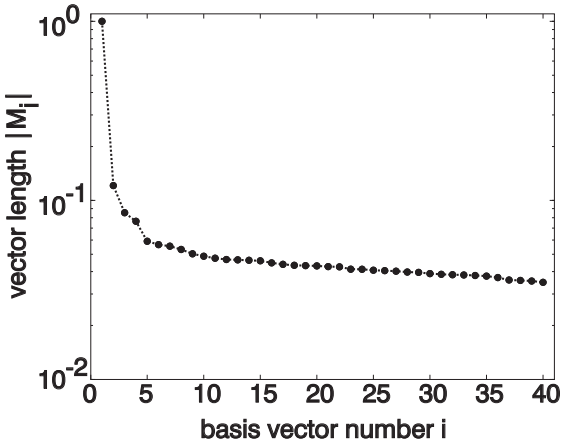

Figure 3.5: Information contend of an orthogonal set of 40 base vectors measured by the sum over the squares of all pixel values.

of basis vectors is large enough.
The computation time for the projection of the absorption images grows linearly with the size of the basis, whereas it grows quadratically for the generation of the basis itself because of the above-mentioned preselection. For every new basis vector, all remaining pictures have to be projected into the existing basis first to find the best suited image. It has turned out that efficient fringe reduction is achieved with 20 to 30 basis vectors, whereas larger sets do not significantly improve the images anymore.
The images shown in Figure 3.3 are typical basis vectors and display $\mathbf{B}_1$, $\mathbf{B}_2$ and $\mathbf{B}_6$ of an orthogonal set. In $\mathbf{B}_2$ and $\mathbf{B}_6$ the phase shift of one prominent pattern (marked with arrows) between the two images can be seen. $\mathbf{B}_1$ additionally contains the enveloping profile of the probe beam which is not contained in the other images because it is basically constant. If the basis set has reached the desired size, the generation process is stopped and the remaining reference images which with certainty carry less information than the last basis image are withdrawn.

To process an absorption image, the orthogonal basis is now used to generate a reference image. Before projecting the absorption image on every base image, the border of the images and the central area, which contains the cloud, are masked. The latter contains information that can not be displayed by the basis, whereas the outermost regions are almost dark and governed rather by stray light or background noise than by the probe beam, and therefore should not be taken into account, either. In practice this is done by multiplying the image in the following way with a matrix $\mathbf{M}$ which is filled with ones

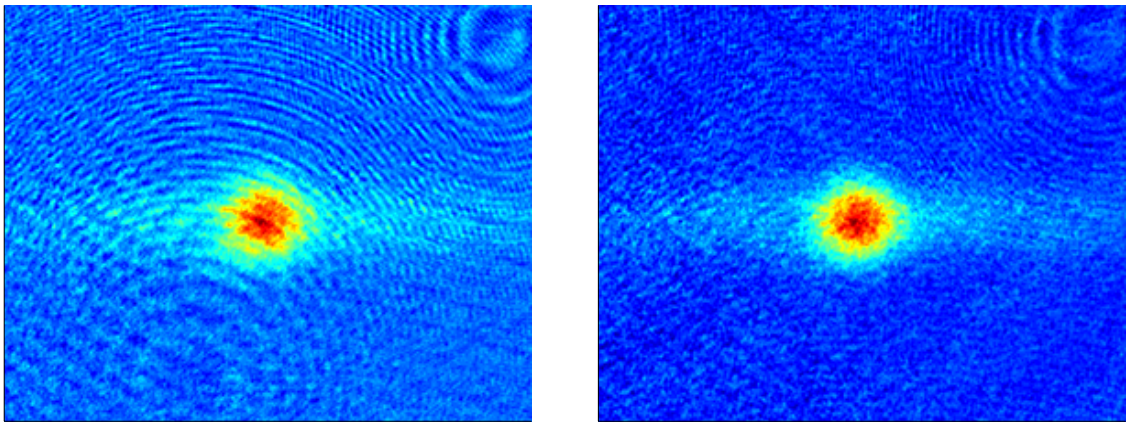

Figure 3.6: Comparison of a typical TOF image of a thermal cloud without (left image) and with (right image) projection into a basis of reference images. The basis that was used to process the right image contained 30 orthogonal vectors. Almost all fringes could be eliminated from the processed image and the improved quality is obvious.

except for the masked regions where all elements are zeros:

$$\widetilde{\mathbf{A}} = \mathbf{M} \odot \mathbf{A} = \begin{pmatrix} M_{1,1}A_{1,1} & M_{2,1}A_{2,1} & \dots \\ M_{1,2}A_{1,2} & M_{2,2}A_{2,2} & \dots \\ \dots & \dots & \dots. \end{pmatrix}$$

Here we have defined the element wise product of two images $\mathbf{A} \odot \mathbf{B}$. A typical absorption image, already multiplied with the mask $\mathbf{M}$, is shown in Fig. 3.4. White areas are covered by the mask $\mathbf{M}$.
The scalar product of the absorbtion images with the basis delivers a coefficient for every base vector:

$$c_j = \widetilde{\mathbf{A}} \bullet \mathbf{B}_j = (\mathbf{M} \odot \mathbf{A}) \bullet \mathbf{B}_j.$$

The reference image is then constructed by adding up the basis vectors after multiplying each with its coefficient c_j:

$$\widetilde{\mathbf{R}} = \sum_{j=1}^{N} c_j \mathbf{B}_j$$

This reference is finally used to gain the density profile of the cloud according to Eqn. (3.1). The result of a projection of a typical time of flight picture of 300000 thermal atoms onto a basis set of 30 images and the same image processed with only one reference are compared in Fig. 3.6.

3.3 Extracting data from images

All measurements with condensed and non-condensed clouds in this thesis rely on the correct determination of the density distribution of the atoms obtained from absorption images. Several aspects have to be considered, when evaluating these images. First, in general, all images produced in the above way measure the column density of the cloud, i.e. the integral of the density distribution along the probe beam direction. In our trap, this direction is always referred to as the x-axis. Only if one uses a tomographic technique that is capable of recording slice by slice [100] the distribution along the x-axis, would one directly gain knowledge of the 3D density distribution. With the usual absorption imaging technique in our experiment however, information about the full 3D distribution and in particular the distribution along the imaging axis can only be recovered by applying an adequate theoretical description of the distribution function and the trapping potential to fit the 2D image. Depending on the regime in which the cloud is prepared (far above, well below or close to T_c), the function used to fit the image must hence describe either the thermal density distribution, the distribution of the condensate fraction, or, in the intermediate regime, both fractions. In either case, their projection on the CCD chip plane has to be considered.
Because the extension of the trapped cloud is close to or even below the resolution of our imaging system, all images are taken after some time of flight. Such an image monitors not only the initial distribution of atoms in space, but, as the time of flight gets longer, it is more and more determined by the momentum distribution. Furthermore, in the Thomas-Fermi limit (Eqn. (1.4.3)), where the kinetic energy of the atoms is negligible compared to the external potential and interaction energy ($ng \gg \hbar\omega$), the largest energy in the system after the trap is switched off stems from interactions.
If the time of flight is very long compared to the inverse trapping frequency ($t \gg 1/\omega$), the initial spatial density distribution becomes negligible and the camera image describes the distribution of the thermal atoms in momentum space. This is of particular advantage for thermometry because in this case inaccuracies in the determination of the trap frequencies become negligible and the sources of errors are reduced to exact timing and determination of the widths of the cloud.

3.3.1 Determination of temperature and number of atoms

The total number of atoms is determined by fitting a distribution function to the density profile on the image and integrating this function over the whole image plane. The temperature of the cloud is determined from the width of the respective distribution. Depending on whether the cloud is purely thermal, partly condensed or a pure condensate, the proper distribution functions have to be used for the fits.

Thermal clouds far above T_c

The in-trap density distribution of a thermal cloud far from the critical temperature, where Bose enhancement is negligible, can be approximated by a Boltzmann distribution which has the shape of a Gaussian:

$$n_T(x,y,z) = \widehat{n}_T e^{-U(x,y,z)/k_BT} = \widehat{n}_T e^{-\frac{x^2}{2\sigma_x^2}-\frac{y^2}{2\sigma_y^2}-\frac{z^2}{2\sigma_z^2}}.$$

$\widehat{n}_T$ being the peak density of the thermal cloud, and $U(x,y,z) = \frac{1}{2}m(\omega_x x^2+\omega_y y^2+\omega_z z^2)$ the harmonic trapping potential. σ_x, σ_y and σ_z are the standard deviations

$$\sigma_i(0) = \sqrt{\frac{k_BT}{m\omega_i^2}}, \quad i = [x,y,z]$$

of the Gaussian in x, y and z direction, respectively. The *velocity distribution* $n_v(|\vec{v}|)$ is isotropic and given by a Boltzmann distribution with a standard deviation of $\sigma_v = \sqrt{k_BT/m}$. If interaction between the particles can be neglected, which is usually the case in thermal clouds, the velocity distribution is kept constant also after releasing the cloud from the trap. The density distribution of the cloud after time t of free flight is therefore given by the convolution $n(\vec{r},t) = \int n(\vec{r}-\vec{v}t, t=0)n_v(|\vec{v}|)d\vec{v}$. The resulting Gaussian has a standard deviation [101] of

$$\sigma_i(t) = \sqrt{\sigma_i(0)^2 + \frac{k_BT}{m}t^2} = \sqrt{\frac{k_BT}{m\omega_i^2} + \frac{k_BT}{m}t^2}, \qquad i = x,y,z$$

The column density distribution Eqn. (3.1) recorded on the camera chip is given by

$$\widetilde{n}_T(y,z) = \widehat{n}_T\sqrt{2\pi}\sigma_x e^{-\frac{(y-\widehat{y})^2}{2\sigma_y^2}-\frac{(z-\widehat{z})^2}{2\sigma_z^2}}$$

which is used to fit the image. Free parameters in these fits are the peak column density $\widehat{\widetilde{n}}_T = \sqrt{2\pi}\widehat{n}_T\sigma_x$, the position $(\widehat{y},\widehat{z})$ of the center of mass, and the standard deviations σ_y and σ_z. The number of atoms in the thermal cloud is

$$N_T = \int_{-\infty}^{+\infty} n_T(x,y,z)dV = (2\pi)^{3/2}\widehat{n}_T\sigma_x\sigma_y\sigma_z.$$

Solving equation (3.3.1), one obtains the temperature of the cloud:

$$T = \frac{m}{k_B}\frac{\sigma_i(t)^2}{\frac{1}{\omega_i^2}+t^2}$$

and the initial size

$$\sigma_i(0) = \sqrt{\frac{1}{1+\omega_i^2t^2}}\sigma_i(t)$$

which can be used in turn to calculate the initial peak density according to Eqn. (3.3.1)

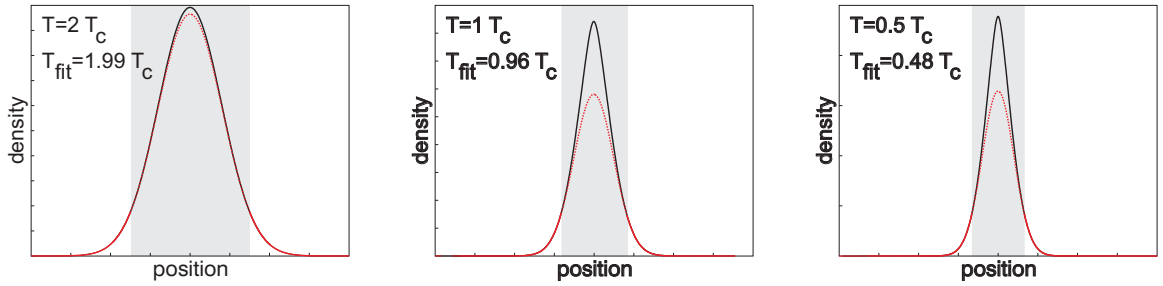

Figure 3.7: 2D projections of Bose distribution functions g_2 for 100000 atoms in a spherical potential with a trap frequency of 1 kHz at temperatures of $2T_c$, $1T_c$ and $0.5T_c$ from left to right. The distribution functions have been generated using numerical solutions of Eqn. (1.18) in Eqn. (3.3.1). Black solid lines are the g_2 functions, dotted red lines are Gaussian fits to obtain the temperatures. Grey shaded regions have been excluded from the data for the Gaussian fit. Real temperatures T and the results of the Gaussian fits T_{fit} are displayed in units of the critical temperature in every graph. As can be seen from these graphs, a Gaussian fit is not able to reproduce the distribution anymore if the system temperature is close to T_c. It is therefore not suited to determine the number of atoms with an ample accuracy whereas the fitted temperatures are in good agreement with the real values.

Systems close to T_c and partly condensed clouds

In clouds still above but close to the critical temperature, the difference between the Maxwell-Boltzmann and Bose-Einstein distribution starts to be important. Figure 3.7 displays numerically generated column density distributions of thermal atoms in the trap at $0.5\,T_c$, $1\,T_c$ and $2\,T_c$. It becomes clear that, at temperatures close to T_c, the enhanced occupation probability of lower lying states in the harmonic trapping potential has to be regarded when fitting the density distribution. To determine the temperature and number of atoms in the thermal cloud and the condensate phase, adequate fit functions have to be found. It has been shown by Bagnato et al. in [76] that in the ideal gas limit, at temperatures much higher than the level spacing $k_B T \gg \hbar\omega$, a semiclassical approach can be used to approximate the spatial distribution resulting in:

$$n(\vec{r}) = \frac{1}{\lambda_{dB}^3} \sum_{j=1}^{\infty} \frac{e^{\frac{j(\mu - U(\vec{r}))}{k_B T}}}{j^{3/2}} = \frac{1}{\lambda_{dB}^3} g_{3/2}\left(e^{\frac{(\mu - U(\vec{r}))}{k_B T}}\right).$$

Integration along the x-direction yields

$$n_T(y,z) = \widehat{n}_T \sqrt{\pi} x_0 g_2\left(e^{-\frac{y^2}{y_0^2} - \frac{z^2}{z_0^2}}\right).$$

Since the cloud usually contains a sufficiently large number of atoms (compare 1.4.3) in all experiments discussed here, the Thomas-Fermi distribution (1.4.3) is used to fit the

condensate fraction whose column density reads

$$\begin{aligned} n_c(y,z) &= max\left[\frac{\sqrt{2m\mu^3}}{3\pi\hbar^2 a\omega_x}\left(1-\frac{m\omega_y^2 y^2}{2\mu}-\frac{m\omega_z^2 z^2}{2\mu}\right),0\right] \\ &= max\left[\frac{4}{3}\widehat{n}_c R_x\left(1-\frac{y^2}{R_y^2}-\frac{z^2}{R_z^2}\right)^{3/2},0\right]. \end{aligned} \tag{3.1}$$

The free parameters in equations (3.3.1) and (3.1) are the peak column densities $\widehat{\widehat{n}}_T = \widehat{n}_T\sqrt{\pi}x_0$ and $\widehat{\widehat{n}}_c = \frac{4}{3}\widehat{n}_c x_{0,c}$, the $1/e$ widths y_0 and z_0 of the thermal cloud, and the Thomas-Fermi radii R_y and R_z of the condensate. The center of mass positions can be incorporated in the same manner as in equation (3.3.1).
Because of the superior accuracy compared to 1D fits, a full 2D fit of the functions (3.3.1), (3.1) or (3.3.1) is carried out to an area of the image which is approximately four times larger than the size of the cloud. To gain appropriate starting parameters for these 2D fits, we first fit 1-D Gaussians in two directions through the center of the cloud.
At temperatures far above T_c, Eqn. (3.3.1) is used to determine the temperature as well as the number of atoms.
Close to T_c and for partly condensed systems, the number of thermal atoms is determined from a fit of Eqn. (3.3.1) to the data. The g_2 function that is used in this equation assumes a chemical potential of $\mu = 0$ (i.e. a fugacity z of 1). Besides the fact that this is not true for partly condensed clouds, Eqn. (3.3.1) does neither include interaction of the thermal cloud with itself nor with the much denser condensate fraction in the center of the trap. Hence, using the width obtained from this fit to determine the temperature with Eqn. (3.3.1) would introduce a systematic error of up to 20% in the temperature [102]. In order to circumvent this error, we use first Eqn. (3.3.1) to measure the temperature, restricting the fit to the far outer wings of the thermal cloud. The high energetic atoms in this part of the trap spend most of their time in regions of low density where interaction is weak. In these high energy levels of the trapping potential, the chemical potential is much smaller than the kinetic energy. Hence Bose enhancement is low, and a Maxwell-Boltzmann distribution characterises the atomic distribution well [50]. The number of atoms obtained from the g_2 fit still contains a systematic error due to the above mentioned neglect of interaction.

Because the polylogarithm g_2 cannot be represented in a closed form, the sum in Eqn. (1.8) has to be carried out until the infinite sum is represented with sufficient accuracy. Figure 3.8 shows that when the summation index runs from one to more than ten, the distribution is well approximated. In our fitting routine, the summation is carried out up to $j = 20$. The resulting best fit is subsequently subtracted from the absorption image and we fit Eqn. (3.1) to the remaining part of the image to determine the size of the condensate.

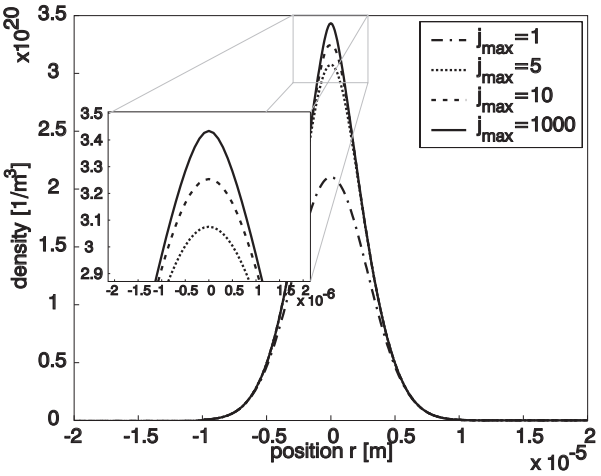

Figure 3.8: Bose distribution functions approximated by carrying out the summation (1.8) up to different limits of the summation index. We use $j_{max} = 20$ to evaluate our data.

Almost pure condensates far below T_c

Far below the BEC transition, the thermal fraction becomes very small and the extension of the cloud is comparable to the size of the condensate. The two fractions can not be clearly distinguished anymore, mainly because the optical density of the condensate becomes very large in contrast to the thermal fraction whose optical density becomes comparable to the noise on the image. In this regime, the fit on the thermal cloud does not yield reliable quantities anymore and is skipped in the fitting routine. A small error is introduced in the fit of the condensate fraction by this simplification, but since the thermal cloud has a much lower density, this error is always negligible. In this very low temperature regime, we speak of *almost pure condensates*.

3.4 Time of flight series

Taking a whole series of pictures of clouds (prepared in the same way and released from the same trapping potential but after different times of ballistic expansion), offers a much more accurate way of measuring temperatures than using Eqn. (3.3.1) and the cloud size obtained from only one image. Eqn. (3.3.1) indicates that if the time of flight is larger than the inverse trapping frequency $t_{tof} > 1/\omega$, the trap frequency and therefore the initial spatial distribution of the atoms become less and less important. For very long times, the $1/\omega$ term can be completely neglected and the cloud expands linearly. Hence,

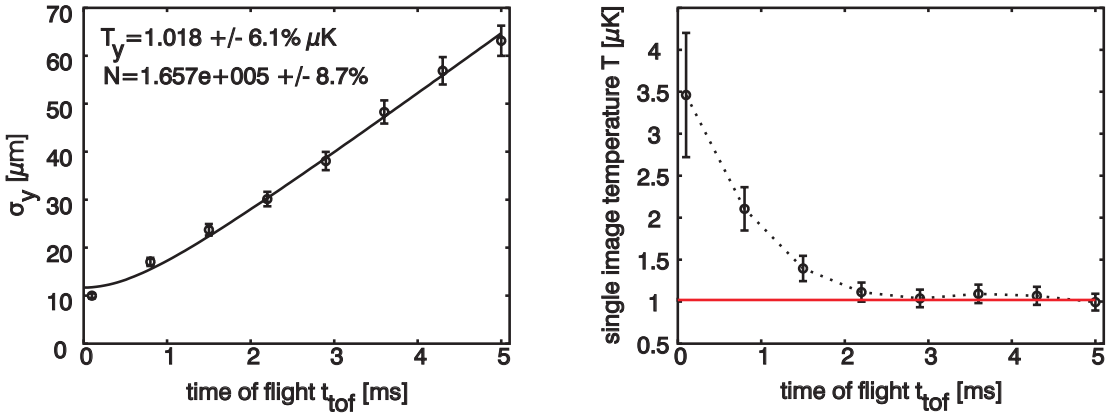

Figure 3.9: *Left*: TOF series of $1/\sqrt{e}$-widths σ_y of a thermal cloud of $\sim 1.7 \cdot 10^5$ atoms released from the crossed trap with 930 mW and 4.5 W laser power in the horizontal and vertical beam, respectively. Solid line: fit of Eqn. (3.3.1) to the data. The temperature obtained from this fit is 1.02 μK. *Right*: Temperatures obtained from Eqn. (3.3.1) for every single image of the same series as in the left figure. The solid line displays the 1.02 μK obtained from the fit on the left. For times of flight of more than 2.2 ms, the single-image temperatures are in very good agreement with the one from the series fit.

images of thermal clouds[5] taken after long expansion times reflect the initial momentum distribution, whereas the initial spatial distribution is unimportant. A fit of Eqn. (3.3.1) to an experimentally obtained series of data as shown in Fig. 3.9 therefore delivers a very precise measure of the temperature. In particular, the obtained temperature is independent of the type of model – Boltzmann or Bose statistics – that is used for the thermal distribution of atoms because both reveal the same linear expansion dynamics if interaction is neglected. In contrast to BECs, this is justified since the kinetic energy of thermal clouds is usually much larger than the interaction energy ($E_{kin} \gg E_{int}$).

[5] This is only true in the limit of weak interaction. If – like in an expanding condensate or very dense thermal clouds – interaction between atoms is not negligible, also the interaction energy influences the expansion. In a large condensate in the Thomas-Fermi limit, the expansion dynamics is even governed by the interatomic interaction whereas the momentum distribution can be neglected.

4 Chromium atoms in an optical dipole trap

Abstract

One of the crucial factors that made Bose-Einstein condensation of chromium possible is the step from a magnetic to a purely optical trapping potential. This technique allows one to trap atoms in the energetically lowest Zeeman state where dipolar relaxation is suppressed. The optical trap is loaded by superimposing the optical trap potential with the magnetic trap and cooling the trapped sample in this hybrid optical/magnetic trap to temperatures below the depth of the optical trap using radiofrequency (rf) evaporation. A large part of the sample is transferred to the pure optical trap by ramping down the magnetic trapping potential adiabatically subsequent to rf cooling. In this way, the atoms that were magnetically trapped before, slowly expand into the optical trapping potential.

Optical dipole traps make use of the conservative dipole force resulting from the dispersive interaction of the electric dipole moments of atoms that are induced by a far detuned light field with the field itself. The minima of the potentials arising from this interaction can be used to confine atoms in space. The absorptive part of the atom-light interaction in the form of scattering of photons from the light field represents a dissipative process which limits the lifetime of a trapped atomic sample in a dipole trap. It is also the part of the interaction that is used in optical cooling techniques like Zeeman slowers, magneto-optical traps (MOT) and Doppler-cooling which are described in [103].

Sections 4.1 to 4.3 discuss the general concept and physical basics of optical trapping. I concentrate on the aspects that are important for the experimental realisation of such a trap. For a quantum mechanical description of the interaction of atoms with light fields, I refer the reader to Appendix C of this thesis, where a summary of the standard textbook approach in the dressed atom picture can be found. A detailed discussion is found in e.g. [104, 105].

The experimental setup, the realisation of a dipole trap for chromium atoms and a discussion of the characteristic properties are presented in Sections 4.4 to 4.5. The experimental determination of the trapping parameters are presented in Section 4.6.

Section 4.7 treats the preparation of a pre-cooled sample of chromium atoms in the magnetic trap and the transfer to the optical trap. Finally, the transfer of the sample to the high field seeking state $m_J = -3$ is discussed in Section 4.8. This crucial step in the preparation scheme leads to a drastic increase of the lifetime of the trapped cloud and makes efficient evaporative cooling in the dipole trap possible at all.

4.1 The physics of optical trapping

A classical description of the dipole force has been discussed by Grimm, Weidemüller and Ovchinnikov in [106, 107] where they present a detailed review of theoretical and experimental aspects of optical traps. They also give some useful approximations which are derived using the Lorentz model for an atom in the laser field of an optical trap. In this model, the atom is considered as a classical oscillator where the electron is elastically bound to the nucleus with a characteristic eigenfrequency ω_0. An oscillating electric field with polarisation $\vec{\varepsilon}$, frequency ω_L and amplitude $E(\vec{r})$

$$\vec{E}(\vec{r},t) = \vec{\varepsilon}E(\vec{r})e^{i\omega t} + \vec{\varepsilon}E^*(\vec{r})e^{-i\omega t}$$

displaces the electron by a distance r which results in an induced dipole moment $\vec{p} = e\vec{r} = \alpha\vec{E}$ where $\alpha(\omega)$ is the complex polarisability. The interaction energy of the induced dipole moment with the laser field is determined by polarisability $\alpha(\omega)$ of the atom. Two parts contribute to the interaction of the induced electric dipole moment with the field:

- The in-phase component of the dipole oscillation i.e. the real part of the polarisability is responsible for the conservative *dipole potential*:

$$U_{dip} = -\frac{1}{2}\langle\vec{p}(\vec{r},t)\vec{E}(\vec{r},t)\rangle = -\frac{1}{2\epsilon_0 c}\Re(\alpha)I(\vec{r}). \tag{4.1}$$

  Here the brackets $\langle ...\rangle$ denote a time average over fast oscillations. $I(\vec{r}) = 2\epsilon_0 c|E(\vec{r})|^2$ is the intensity of the field. The frequency difference between the driving field and the resonance frequency of the electron results in a frequency dependent amplitude of the oscillation and a phase shift between driving field and oscillating dipole. The dispersive character of the interaction stems from this frequency dependence.

- The imaginary part of the polarisability is related to the out-of-phase part of the oscillation. It is responsible for absorption of power from the light field by the oscillator which the oscillator re-emits as dipole radiation. The absorbed power $P_{abs} = \langle\dot{\vec{p}}\vec{E}\rangle$ can be considered as repeated absorption – spontaneous emission processes of photons with energy $\hbar\omega$ at a *scattering rate*

$$\Gamma_{sc}(\vec{r}) = \frac{P_{abs}}{\hbar\omega} = \frac{1}{\hbar\epsilon_0 c}\Im(\alpha)I(\vec{r}). \tag{4.2}$$

4.1.1 The Lorentz model

To derive an expression for the polarisability, we make use of the Lorentz model, where an electron with mass m_e and charge $-e$ is elastically bound to the nucleus of an atom with a characteristic eigenfrequency ω_0 equal to the frequency of the optical transition. Energy loss due to the radiation emitted by the accelerated charge of the electron is taken into account by introducing a damping rate Γ. The solution of the equation of motion $\ddot{x} + \Gamma\dot{x} + \omega_0^2 = -eE(t)/m_e$ of the driven electron is then

$$x(t) = \frac{e}{m_e} \frac{1}{(-{\omega_0}^2 + i\Gamma\,\omega + \omega^2)} E(t) \tag{4.3}$$

and the polarisability resulting from this model is

$$\alpha(\omega) = \frac{e^2}{m_e} \frac{1}{\omega_0^2 - \omega^2 - i\omega\Gamma}. \tag{4.4}$$

The average total radiation power emitted by the oscillating charge is

$$\overline{P_{rad}} = \frac{e^2\omega^4 x_0^2}{12\pi\epsilon_0 c^3} \tag{4.5}$$

where x_0 is the amplitude of the oscillation and ϵ_0 is the dielectric constant. If the emitted power is not supplied to the oscillator from an external source, it has to be compensated for by a change of the energy $E_{osc} = E_{kin} + E_{pot} = \frac{1}{2} m_e \omega^2 x_0^2$ of the oscillator $P_{rad} = -\frac{d}{dt} E_{osc}$, i.e. the amplitude x_0 decays with time. The damping constant of the oscillation is therefore defined by the relative change of the oscillator energy

$$\Gamma(\omega) = -\frac{dE_{osc}/dt}{E_{osc}} = \frac{P_{rad}}{E_{osc}} = \frac{e^2\omega^2}{6\pi\epsilon_0 m_e c^3}. \tag{4.6}$$

Inserting this result in Eqn. (4.4), we get an expression for the polarisability:

$$\alpha(\omega) = 6\pi\epsilon_0 c^3 \frac{\Gamma_0/\omega_0^2}{\omega_0^2 - \omega^2 - i(\omega^3/\omega_0^2)\Gamma_0}, \qquad \Gamma_0 = \left(\frac{\omega_0}{\omega}\right)^2 \Gamma(\omega) \tag{4.7}$$

where Γ_0 is the damping rate on resonance and corresponds to the decay rate of the excited state.
In a semiclassical approach, where the atom is considered as a two-level quantum system but the light field is still classical, the classical damping in Eqn. (4.7) has to be replaced by the dipole matrix element

$$\Gamma_0 = \frac{\omega_0^2}{3\pi\epsilon_0\hbar c^3} \left| \langle\, e \,|\vec{p}\cdot\vec{\hat{e}}|\, g \,\rangle \right|^2, \tag{4.8}$$

where $|\, g \,\rangle$ is the ground state and $|\, e \,\rangle$ is the excited state of the atom. The classical approach of Eqn. (4.7) yields the same results as a full quantum-mechanical treatment

would if saturation effects of the transition can be neglected. Saturation, i.e. a significant occupation of the excited state, is only incorporated in a quantum mechanical calculation.
The regime, however, that is interesting for dipole traps, is the case of far detuned laser fields where the scattering rate of photons is much smaller than the spontaneous decay rate $\Gamma_{sc} << \Gamma$. This is equivalent to a negligible population of the excited state. In this situation, the expressions for the polarisability and dipole-potential derived from equations (4.7) and (4.1) are very good approximations. The decay rates Γ_0 and transition frequencies ω_0 of the transitions that have to be considered are best obtained from spectroscopic data and can for example be found in the NIST database [108].
The following expressions for the dipole potential and scattering rate, which have been used in the framework of this thesis to calculate the properties of the dipole trap, are obtained by substituting the above results (4.8) or (4.6) in (4.7):

$$U_{dip}(\vec{r}) = -\frac{3\pi c^2}{2\omega_0^3}\left(\frac{\Gamma}{\omega_0-\omega}+\frac{\Gamma}{\omega_0+\omega}\right) I(\vec{r})$$

$$\Gamma_{sc}(\vec{r}) = \frac{3\pi c^2}{2\hbar\omega_0^3}\left(\frac{\omega}{\omega_0}\right)^3\left(\frac{\Gamma}{\omega_0-\omega}+\frac{\Gamma}{\omega_0+\omega}\right)^2 I(\vec{r})$$

These equations give good approximations under most realistic conditions of dipole traps where the detuning is large and saturation effects can be neglected.
If the detuning $\delta \equiv \omega - \omega_0$ of the light from resonance is not too large ($|\delta| \ll \omega_0$), the counter rotating term $\frac{\Gamma}{\omega_0+\omega}$ in Eqn. (4.1.1) can be neglected and $\omega/\omega_0 \approx 1$. This is the so called rotating-wave approximation where expressions (4.1.1) and (4.1.1) simplify to

$$U_{dip}(\vec{r}) = \frac{3\pi c^2}{2\omega_0^3}\left(\frac{\Gamma}{\delta}\right) I(\vec{r}) \tag{4.9}$$

and

$$\Gamma_{sc}(\vec{r}) = \frac{3\pi c^2}{2\hbar\omega_0^3}\left(\frac{\Gamma}{\delta}\right)^2 I(\vec{r}). \tag{4.10}$$

Traps operating in this regime are often called *far off resonant traps (FORT)*. At light frequencies below the atomic transition ($\delta < 0$), the potential energy U_{dip} of an atom in the light-field is negative and the atom is attracted towards regions of higher intensity (*red detuned trap*). If the detuning is positive, the atoms are repelled from the light-field. The relation between scattering rate and dipole potential in FORT traps is very simple,

$$\Gamma_{sc} = \frac{\Gamma}{\hbar\delta} U_{dip}, \tag{4.11}$$

showing that in a trap with the same depth, the scattering rate can be reduced by increasing the detuning. Therefore, optical dipole traps are preferably operated rather at large intensities than small detunings. In practice, the available power at a desired

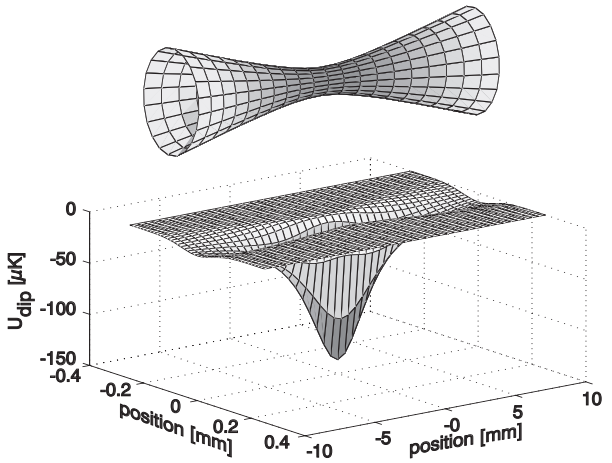

Figure 4.1: Shape of the beam and trapping potential for chromium atoms assuming a waist of 30 μm, a power of 9.5 W and a wavelength of 1060 nm. Trap depth measured in units of k_B.

wavelength and the costs of high power lasers as well as considerations like ease of use of the system and availability and costs of adequate optics force the experimentalist to compromise.

4.2 Trap geometry

The profile $I(\vec{r})$ of a Gaussian beam is given by

$$I(r,z) = I_0 \frac{1}{1+\left(\frac{z}{z_R}\right)^2} \exp\left(-\frac{2r^2}{w_0^2}\frac{1}{1+(z/z_R)^2}\right)$$

where r and z are the radial and longitudinal position with respect to the focus of the beam. The intensity drops within the distance w_0 (the minimum *beam waist* of the beam in the focus) from the optical axis from its maximum value I_0 in the focus to I_0/e^2 which leads to a Gaussian shape. The intensity dependence along the symmetry axis z is given by the *Rayleigh range* z_R which is fully defined by the waist and the wavelength λ_L of the laser:

$$z_R = \frac{\pi w_0^2}{\lambda_L}.$$

The beam waist at a position z along the direction of propagation is

$$w(z) = w_0\sqrt{1+\left(\frac{z}{z_R}\right)^2}.$$

According to Eqn. (4.1.1), the dipole potential U_{dip} is directly proportional to the light field intensity:

$$U_{dip}(r,z) = U_0 \frac{1}{1+\left(\frac{z}{z_R}\right)^2} \exp\left(-\frac{2r^2}{w_0^2}\frac{1}{1+(z/z_R)^2}\right),$$

where the *trap depth* U_0 can be calculated using I_0 in Eqn. (4.9). The high intensity region in the focus of the beam is an attractive center for an atom if the laser field is detuned to the red with respect to its transition. If the attractive potential is steeper in all directions than any inhomogeneity of other external fields like magnetic field gradients or - most prominent - the earth gravitational field, the potential is suited to trap at least one atom [1] if its kinetic energy is low enough.
Given a laser power P and a waist w_0, the maximum intensity is

$$I_0 = \frac{2P}{\pi w_0^2}.$$

Figure 4.1 shows the beam profile and corresponding potential calculated with the above formulae for one of the trapping beams of our experimental setup. If several laser beams are used to form the trapping potential, their contributions have to be summed according to the superposition principle to calculate the total trapping potential.

4.2.1 Harmonic approximation

In the case of atoms with a thermal energy $k_B T$ much smaller than the potential depth U_0, most of the atoms will always stay in the central region of the potential and the extension of the cloud is much smaller than the waist in radial direction and also much smaller than the Rayleigh range in axial direction. In this region, the optical potential in Eqn. (4.2) is best approximated by a three dimensional harmonic oscillator with an axial symmetry along the optical axis. According to equations (4.2), (4.2) and (4.9), the harmonic approximation of the trapping potential reads

$$U_{trap}(r,z) = -U_0\left(1 - 2\left(\frac{r}{w_0}\right)^2 - \left(\frac{z}{z_R}\right)^2\right).$$

With the harmonic oscillation frequencies

$$\omega_r = \sqrt{\frac{4U_0}{mw_0^2}}$$

[1] Repulsive interaction between atoms can prevent the trap from confining more than one atom [15].

in radial and

$$\omega_z = \sqrt{\frac{2U_0}{mz_R^2}}$$

axial direction, given by the beam waist, the wavelength and the laser power, this can be written

$$U_{trap}(r,z) = -U_0 + \frac{m}{2}(\omega_r^2 r^2 + \omega_z^2 z^2).$$

Typically, the radial trap frequencies of optical traps are relatively high compared to magnetic traps but the depth is much smaller. Another difference to magnetic traps is that trap depth and frequencies can not be varied independently[2]. When the laser power is ramped down, the depth as well as the maximum gradient of the potential drop linearly with the power. The trap frequencies, in contrast, drop proportional to the square root of the power. This leads to the fact that at very low trap depths, i.e. very low powers, the trap is not able to compensate for gravity anymore. This is the case when the potential gradient at the steepest point of the potential is smaller than gravity. The dependence of the potential on the position in radial direction is $U(r) = U_0 \exp(-2r^2/w_0^2)$, thus the force on an atom is

$$F(r) = -\frac{dU(r)}{dr} = 4\frac{r}{w_0^2}U_0 \exp\left(-\frac{2r^2}{w_0^2}\right).$$

The maximum of this force $F_{max} = F(r_{max})$ is at the position $r_{max} = w_0/2$ where $dF(r)/dr = 0$. Hence, if $F_{max} < mg$, the trap is to weak and can not hold the atoms anymore. This sets a limit for the minimum laser power that is needed to operate the trap. In our setup, the minimum power obtained from the above equation is

$$P_{min} = 107mW.$$

4.3 Heating by photon scattering

The *spontaneous force*

$$\vec{F}_{dip}(\vec{r}) = -\nabla U_{dip}(\vec{r}) = \frac{1}{2\epsilon_0 c}\Re(\alpha)\nabla I(\vec{r}). \tag{4.12}$$

on an atom in a light field is caused by the net momentum transfer during cycles of absorption and spontaneous emission where in each of these processes one photon momentum $\hbar\vec{k}$ is transferred to the atom. Although the momentum of an *absorbed* photon

[2] This is effectively the case in magnetic traps, since it is possible to limit the trap depth with a radio frequency shield but keep the trap frequencies constant [51].

from the laser field is always directed, the momentum transfer averaged over many *emission* processes cancels out and the net transfer is governed by the absorption of photons. Hence the spontaneous force is proportional to the photon scattering rate

$$\vec{F}_{sp}(\vec{r}) = \hbar\vec{k}\Gamma_{sc} = \hbar\vec{k}\Gamma\frac{s}{2(s+1)}.$$

The momentum transfer in each absorption and emission process also means deposition of energy in the trapped atomic cloud. Because this energy transfer represents a heating mechanism, the recoil energy an atom gets in form of kinetic energy in every such process, is commonly measured in units of k_B by the *recoil temperature* $T_{rec} = \frac{(\hbar k)^2}{2m} = E_{rec}/k_B$. The heating rate due to light scattering is given by the product of the energy transfer per scattered photon times twice the scattering rate to account for absorption and emission

$$\dot{E} = 2E_{rec}\Gamma_{sc} = 2k_B T_{rec}\Gamma_{sc}.$$

In the case of large detunings and weak saturation, the scattering rate can be approximated by Eqn. (4.1.1). In an optical trapping experiment, this rate should be as small as possible to keep the above heating rate small.
In equilibrium, every motional degree of freedom carries $1/2k_BT$, and the same amount is stored in potential energy if the trap is harmonic, leading to $E_{th} = E_{kin} + E_{pot} = 6\cdot 1/2k_BT$ for the thermal energy. Hence the rate at which the temperature of a trapped cloud in a harmonic potential changes, is given by

$$\dot{T} = \frac{2}{3}\frac{\dot{E}}{k_B} = \frac{2}{3}T_{rec}\Gamma_{sc}.$$

In this consideration, one neglects the directional dependence of absorption which always happens in the propagation direction of the trap light and leads to an increased heating in longitudinal direction. Because the collision rate, i.e. the rate at which energy redistribution among atoms happens, is much faster than the photon scattering rate, the assumption of an isotropic heating effect is nevertheless justified.

4.4 An optical trap for chromium atoms

In the previous sections, the simple case of only two levels contributing to the atom-light interaction has been discussed. Real atoms possess many electronic transitions between energy levels which can have a complex fine and hyperfine sub-structure. In such multilevel systems, the shift of a ground state $|\, g_j \,\rangle$ in the laser field depends on all dipole matrix elements between the ground state and the excited states $|\, e_i \,\rangle$:

$$\Delta E_j = \frac{|\langle\, e_i \,|\mu|\, g_j \,\rangle|^2}{\delta_{ij}}\frac{I}{2\pi\varepsilon_0 c}.$$

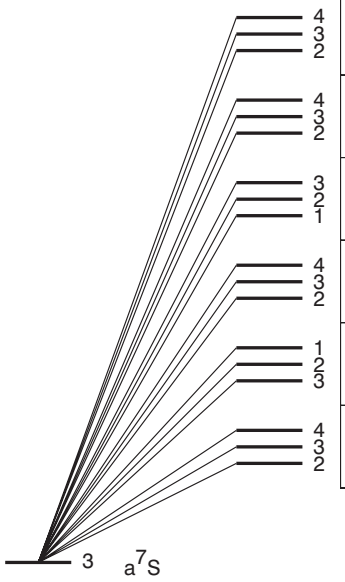

excited state	transition wavelength λ_j	line width Γ
w^7P	210nm	1.1×10^6 1/s
x^7P	236nm	5.5×10^6 1/s
y^5P	336nm	0.12×10^6 1/s
y^7P	360nm	150×10^6 1/s
z^5P	373nm	0.16×10^6 1/s
z^7P	427nm	31.5×10^6 1/s

Figure 4.2: Transitions contributing to the ground state $^7S_3$ trap potential of chromium atoms in the optical trap. Most important are the $a^7S \leftrightarrow y^7P$ transition at 359 nm and the cooling transition $a^7S \leftrightarrow z^7P$ at 427 nm. (numbers taken from [108])

The system may be treated like a two level atom only if the frequency of the light field is very close to one transition whereas it is far detuned with respect to all other possible transitions. In contrast, for the realisation of optical traps, usually far detuned lasers are used to prevent heating by keeping the photon scattering rate (Eqn. (4.1.1)) low. In the case of these large detunings, all states that couple to the ground state have to be considered. Figure 4.2 shows the properties of the transitions that have to be taken into account to calculate the trap parameters for ground state ^{52}Cr atoms. The data has been obtained from the NIST atomic spectra data base [108]. All transitions are at wavelengths below 427 nm. In the experiments presented in this thesis, a laser operating at a wavelength of 1064 nm was used to generate the optical trapping potential. In this very far detuned case, where the detuning of the trap laser from any transition is much larger than the fine structure splitting ($\delta \gg \Delta_{FS}$), can the fine, hyperfine, and the magnetic sub-structure be ignored [107]. The multilevel problem reduces to summing the contributions of the different electronic states that couple to the ground state without considering the substructure. Each of these transitions can be treated like a two level system with the same transition strength, independent of the laser polarisation. The electron spins [3] couple to the shifted states like in the unperturbed system and therefore all magnetic sub-states experience the same light shift. The resulting dipole potential

[3] For the hyperfine structure, the same arguments hold with regard to the nuclear spins.

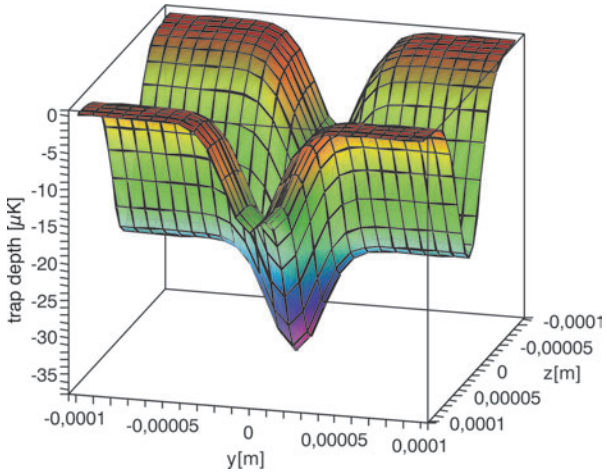

Figure 4.3: Potential of the crossed dipole trap in the y-z-plane where the z-beam is operated at 1 W and the y-beam at 4.5 W. Potential measured in units of k_B.

of the ground state and the total photon scattering rate are:

$$U_{dip} = \sum_j \frac{3\pi c^2 \Gamma_j}{2\omega_j^3} \left(\frac{1}{\omega_j - \omega} + \frac{1}{\omega_j + \omega} \right) I(\vec{r}, t)$$

and

$$\Gamma_{dip} = \sum_j \frac{3\pi c^2 \Gamma_j}{2\hbar\omega_j^3} \left(\frac{\omega}{\omega_j} \right)^3 \left(\frac{1}{\omega_j - \omega_i} + \frac{1}{\omega_j + \omega} \right) I(\vec{r}, t).$$

Where the average ω_j over the transition frequency of the fine structure levels is used as the transition frequency in these equations.
The transitions, that contribute significantly to the trap potential of chromium are the $a^7S \leftrightarrow y^7P$ transition at 359 nm and the cooling transition $a^7S \leftrightarrow z^7P$ at 427 nm. All other transitions are at least two orders of magnitude weaker and even farther detuned from resonance in the 1064 nm laser field. The resulting dipole potential and photon scattering rate are

$$U_{dip}(I) = -0.273 \cdot 10^{-36} J \frac{m^2}{W^2} \cdot I, \quad \Gamma_{sc}(I) = 0.533 \cdot 10^{-11} \frac{1}{s} \frac{m^2}{W^2} \cdot I$$

The heating rate due to photon scattering is

$$\dot{T}(I) = 1.79 \cdot 10^{-18} \frac{K}{s} \frac{m^2}{W^2} \cdot I.$$

4.5 Expected properties of the trap

The properties of the trapping beams were determined by shining them directly on the CCD chip of our camera. To measure the dependence of the waist on the axial

horizontal beam	
$f_{I,x}^{1W}$	513 Hz
$f_{I,y}^{1W}$	513 Hz
$f_{I,z}^{1W}$	4.15 Hz
depth U_0	-14.3 μK
scattering rate Γ_{sc}	$3.9{\cdot}10^{-3}$ 1/s
vertical beam	
$f_{II,x}^{1W}$	180 Hz
$f_{II,y}^{1W}$	0.86 Hz
$f_{II,z}^{1W}$	180 Hz
depth $-U_0$	-5.03 μK
scattering rate Γ_{sc}	$1.4{\cdot}10^{-3}$ 1/s
crossed trap at P_I=10 W, P_{II}=5 W	
f_x	1672 Hz
f_y	1622 Hz
f_z	402 Hz
heating rate $\dot{T}$	30.6 nK/s
scattering rate Γ_{sc}	$45{\cdot}10^{-3}$ 1/s

Table 4.1: Expected trap frequencies, heating rates, and photon scattering rates for our optical dipole trap. The frequencies in the horizontal and vertical beam are given for a laser power of 1 W in the corresponding beam. The crossed trap is specified at maximum power in both beams.

position, the camera was moved along the beams. By fitting Eqn. (4.2) to the measured dependence, we obtained waists of 29.0±0.58 μm in the horizontal and 50±0.36 μm in the vertical beam. Based on these values, the expected properties of the trap were calculated. Figure 4.3 shows the potential of the ODT in the y-z-plane in the crossed region. Both beams (beam I in horizontal direction and beam II in vertical direction) contribute to the total trap frequencies $f_i = \omega_i/2\pi$ in a direction $i = x, y, z$ with their frequency $f_{I,i}$ and $f_{II,i}$, respectively. The effective trap frequencies $f_{j,i}$ at given powers P_j (in W) are easily calculated if we define $f_{j,i}^{1W}$ as the trap frequency produced by beam $j = I, II$ on the $i-$axis at 1 W power in the respective beam:

$$f_{j,i} = f_{j,i}^{1W} P_j.$$

The trap frequencies in each direction in the field of multiple superimposed beams are given by

$$f_i = \sqrt{\sum_j f_{j,i}^2} \quad i = [x, y, z].$$

The expected trap frequencies as well as the photon scattering rates and heating rates for our setup are listed in table 4.1. The experimental determination of the trap parameters will be discussed in the next section.

4.6 Determination of the trapping parameters

Particularly for the crossed optical dipole trap, theoretical calculations do not deliver reliable values for the trap frequencies in all directions because the relative alignment of the two trap beams is decisive for the form of the trapping potential. As it turned out in our experiment, at least in one direction (the z-axis) in the crossed trap, the real value of the trap frequency always differs significantly from the calculated one. Thus an experimental determination of the trapping parameters is inevitable.

4.6.1 Axial frequency in the single beam trap

A number of techniques have been used by several groups to determine trap frequencies by either directly observing oscillations of the atomic cloud in the trap [109] or by observing atom loss when the trap is being shaken in space [110] or modulated [106] in strength on resonance.

The most intuitive method is to observe directly the oscillation of a cloud in a series of absorption images. After displacing the cloud in a controlled way from the center of the trapping potential, it is allowed to live and slosh in the trap for a variable time

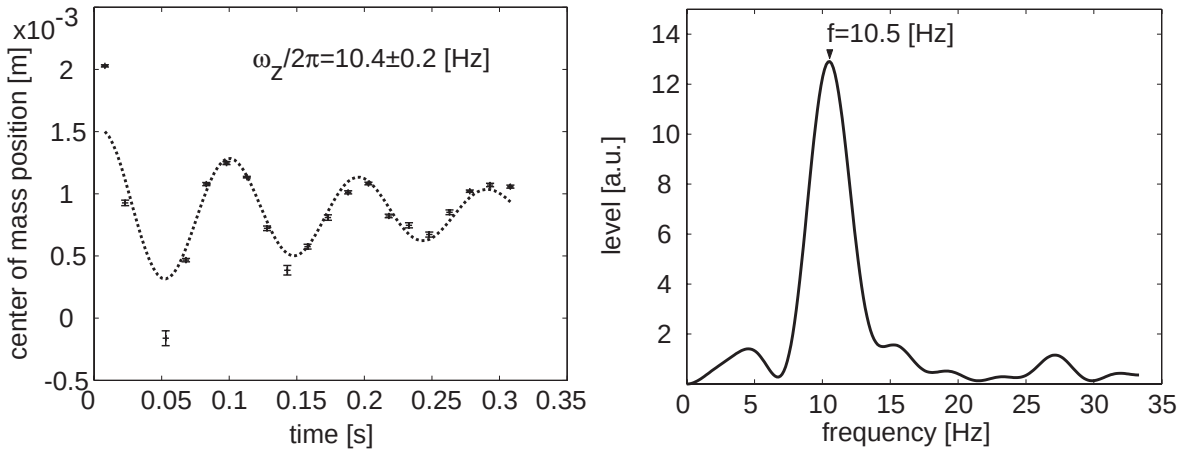

Figure 4.4: Frequency measurement in the single beam trap along the symmetry axis (z direction). Left: Experimental data with error bars. The dashed line displays the best fit of a damped sine oscillation to the data. Right: Frequency spectrum obtained by a Fourier analysis of the same data. Both methods of analysing the data yield the same result of ∼10.5 Hz.

before an image is taken. By determining the position of the center of mass depending on the storage time, it is possible to resolve its trajectory if the time shift between two subsequent images is smaller than half of an oscillation period $\Delta t < \tau/2 = 1/(2f)$ (Nyquist theorem [111]). The time resolution in our experiment is on the order of 100 μs and would in principle allow measurement up to 5 kHz. Since the size of the cloud in the trap is on the order of the size of a camera pixel, the position would have to be determined from time of flight images. On the other hand, the cloud expands and loses optical density during time of flight such that in practice the images become worse and this method is not suited for the measurement of the high radial trapping frequencies in our experiment.

In the elongated axial direction of the horizontal single beam trap however, we expect a trapping frequency of 10 to 15 Hz and the method is well suited to determine this frequency. The initial kick on the cloud can be applied easily by switching off the magnetic trapping potential rapidly after rf evaporation instead of transforming the trap adiabatically from the magnetic to the optical trap (see Section 4.7). The left graph of Fig. 4.4 shows typical experimental data measured in a trap with a laser power of 9.2 W with this method. As a simple model for the oscillation, we assume a sinusoidal dependence with an exponential damping like

$$z(t) = ze^{-\gamma t}\sin(2\pi f t + \phi_0) + \bar{z}$$

and use it as a fit function for the experimental data. Free parameters of the fit are the initial amplitude A_0, initial phase ϕ_0, damping rate γ, an offset $\bar{z}$ and the frequency f. A best fit of this function to the data (displayed by the dashed curve in the left graph of Fig. 4.4) yields a trap frequency of 10.4 Hz with a remarkably small error of ±0.2 Hz.

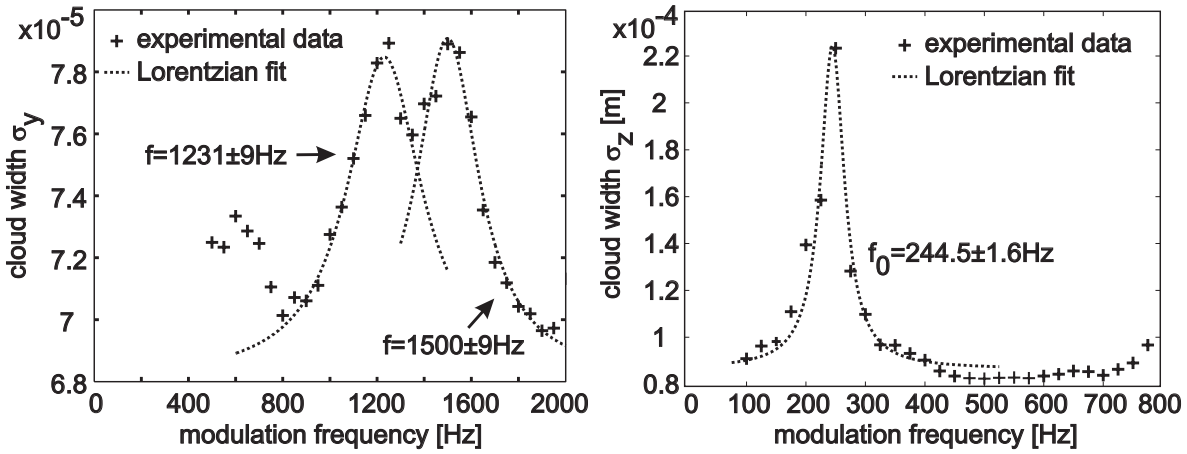

Figure 4.5: Frequency measurement in the crossed trap. Width of the cloud after 4 ms expansion plotted versus modulation frequency. Left graph: width in y-direction when the horizontal beam is modulated. Right graph: width in z-direction when the vertical beam is modulated.

The frequency spectrum obtained by a Fourier analysis of the same experimental data is shown in the right graph of Fig. 4.4. The measured 10.4 Hz is 16 % lower than the expected 12.6 Hz, most likely due to an imperfect beam.

4.6.2 Trap frequencies in the crossed dipole trap

The frequencies that are expected in the crossed dipole trap are on the order of 1 kHz. To determine these frequencies experimentally, we use a parametric heating technique with a trapped thermal cloud by modulating the trap frequencies ω_{trap} at a modulation frequency ω_{mod}. In such a trap, the motion of an atom in one direction is described by the following equation:

$$\ddot{x}(t) + \omega_{trap}^2(1 + \varepsilon_0 \sin(\omega_{mod} t))x(t) = 0$$

where ε_0 is the modulation index. This equation can be transformed into a *Mathieu differential equation* which is well known from classical studies of parametric resonances [112] in mechanical systems. It has been shown that it has periodic solutions $x(t) = x_0(t)\cos(\omega_{trap} t)$ whose energy increases exponentially with a rate constant $\varepsilon_0\omega_{mod}$ when $\omega_{mod} = 2\omega_{trap}$ [113]. The width of the resonance is also given by $\varepsilon_0\omega_{mod}$. Subharmonic resonances with a smaller growth rate of the oscillation energy occur when the modulation frequency is $\omega_{mod} = 2\omega_{trap}/n$, where $n > 1$ is an integer number. Thus, if the modulation frequency in the experiment is close to a resonance in one direction $\omega_m = 2\omega_{trap}$ or subharmonics $\omega_m = 2\omega_{trap}/n$, energy is transferred to the atoms and the atomic cloud heats up. This heating effect is most effective at twice the trap frequency

	calculated	measured	relative deviation
f_x	799 Hz	750 Hz	6%
f_y	714 Hz	616 Hz	14%
f_z	358 Hz	122 Hz	66%

Table 4.2: Comparison of measured vs. calculated trap frequencies in a trap with laser powers of 1.91 W in the horizontal and 3.95 W in the vertical beam.

which is reflected in a decrease of the number of atoms and a drastic increase of the width of the expanded cloud.
Each beam of a crossed dipole trap contributes mainly to the trap frequencies in the directions orthogonal to the corresponding beam. Its contribution in the longitudinal direction is rather small and this frequency is mainly determined by the other beam. Therefore, it is only possible to excite the transversal directions efficiently.
For the measurements, we prepare a cold thermal cloud by stopping the evaporation ramp just above T_c and subsequently change the trap parameters adiabatically (within $\sim$100 ms) to form the trapping potential that has to be calibrated. A remote programmable function generator (Stanford Research Systems DS345) in burst mode modulates the intensity of one of the trapping beams by a few percent ($\leq 3\%$ in the horizontal and $\leq 4\%$ in the vertical beam) by varying the rf-power of one of the AOMs that control the laser intensities sinusoidally for $\sim$500 ms. Subsequently, the cloud is released and we take an image of the cloud after 4 ms time of flight. In a series of experiments, the intensity is varied at different frequencies. The resonance frequency is obtained by fitting a Lorentzian to the measured widths of the cloud. Since the atoms thermalise within the 500 ms of modulation, the heating reflects in the widths of the cloud in both visible axes. To measure ω_x and ω_y, we modulate the horizontal beam whereas ω_z is measured by modulating the vertical beam.
The measurements presented in Fig. 4.5 were carried out in a trap with laser powers of 1.91 W in the horizontal and 3.95 W in the vertical beam. These powers corresponded to 80 % and 20 % of the maximum power of the trap, respectively and have both been measured while modulating the power. The resonance at the highest frequency of 1500$\pm$9 Hz in the left figure corresponds to twice the trapping frequency f_x =750 Hz in x-direction, where both the horizontal and the vertical beam contribute with their strong radial confinement. The resonance peak at 1231$\pm$9 Hz belongs to the y-axis which is almost solely determined by the radial frequency of the horizontal beam and yields a frequency of f_y =616 Hz.

Comparison with theoretical values

Table 4.2 contains a comparison of the measured trap frequencies with the calculated values according to Chapter 4.5. The measured frequency in x-direction, which is dominated by the horizontal beam, matches the calculation with a relative difference of only 6 %. In contrast, the frequencies in y- and z-directions in which the vertical beam contributes more, differ significantly from the calculations. The frequency on the z-axis shows a deviation of as much as 66 %. Possible reasons are a deviation of the beam profile from a perfect Gaussian and imperfect alignment of the two trapping beams since the frequencies depend strongly on the overlap of the two beams. If the crossing point of the vertical and the horizontal beam is displaced from their foci, the depth of the potential dimple and the trap frequencies are reduced.

4.6.3 Radial frequencies in the single beam trap

The same method as in the previous section has been used to measure the radial frequency in the single beam trap. In a trap with 8.9 W in the horizontal beam, the measured frequency was 1416±10 Hz. The theoretically expected value for this power is 1532 Hz. Thus the relative deviation of the measured value from the theoretical prediction is 7.5 %. This deviation is a bit smaller than the deviation on the long axis of the trap measured in Section 4.6.2. At 6.4 W the same measurement yielded a radial frequency of 1294±4 Hz compared to a theoretical value of 1299 Hz.

4.7 Loading the optical trap

4.7.1 Preparation of a cold cloud in the magnetic trap

The high magnetic moment in the ground state as well as in the metastable states of chromium (see Section A) allows for a continuous loading scheme (CLIP-trap) [69, 67] of magneto-optically cooled atoms directly into a magnetic Ioffe-Pritchard (cloverleaf) trap. The loading procedure is illustrated in Figure 4.6. After being slowed down by a Zeeman slower, the atoms are laser cooled and trapped in a 2−dimensional magneto-optical trap (MOT) in radial direction of the Ioffe-Pritchard trap. The curved field along the trap axis does not allow a usual MOT operation. Therefore the atoms are only cooled in this direction using a $\sigma^+ - \sigma^+$ optical molasses. For both the MOT and the molasses, the $^7P_4 \leftrightarrow {}^7S_3$ is used. Due to the branching ratio of $\Gamma_{P\to S}/\Gamma_{P\to D}$ =250000:1 between transitions from the excited $^7P_4$ to the $^7S_3$ ground state or the long lived $^5D_4$ and $^5D_3$ states, respectively, an atom undergoes on average 250000 cycles on the

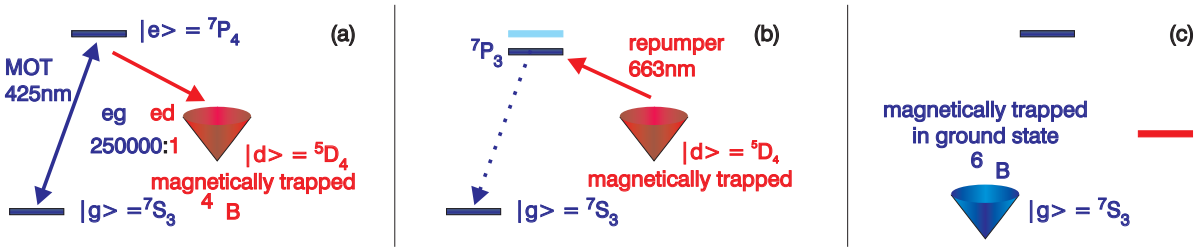

Figure 4.6: The continuous loading scheme consists of three stages: (a) Loading: accumulation of $1.3 \cdot 10^8$ magnetically trapped cold atoms in the metastable D-state due to a branching ratio of 250000 : 1 between transitions to the ground state and the metastable state. (b) Repumping: The MOT light is switched off and the atoms are pumped to the ground state via the $^5D_4 \rightarrow {}^7P_3$ transition. (c) Ground state trap: all lasers off, atoms are trapped in the ground state.

cooling transition before it eventually decays to one of the metastable states. These states have a magnetic moment of $6\mu_B$ and $4\mu_B$, respectively. Without the repumping laser, the metastable states are decoupled from the cooling cycle and atoms which end up in a low-field seeking sub-state[4] of these states stay trapped in the shallow magnetic potential (radial gradient[5] B' =9.5 G/cm, axial curvature B'' =7.5 G/cm^2) used during the loading stage. With this technique it is possible to accumulate about $1.3 \cdot 10^8$ magnetically trapped atoms at roughly the Doppler temperature [114] of 124 μK and a phase-space density (PSD) of a few times 10^{-9} within a loading time of 10 s. The number of magnetically trapped atoms in the metastable states is limited due to light induced collisions [68]. After the steady state number of atoms in the magnetic trap is reached, the cooling lasers are switched off and the atoms in the $^5D_4$ state are pumped back to the ground state within 20 ms using laser light resonant with the $^5D_4 \leftrightarrow {}^7P_3$ transition at 663.2 nm (see Section 2.3). The magnetic trap is subsequently being fully compressed by ramping up the currents through the trap coils to 300 A. In doing so the cloud is heated up again to ∼1 mK and Doppler cooling of the optically dense cloud [71] is performed within the trap at an offset field of 14 G using the cooling beam propagating in z-direction. This Doppler cooling step increases the phase-space density by two orders of magnitude to $\sim 10^{-7}$ without losing atoms. Subsequently, the currents through the coils are lowered to form a trap with an aspect ratio as close as possible to the later shape of the optical dipole trap to provide for efficient transfer between the traps.

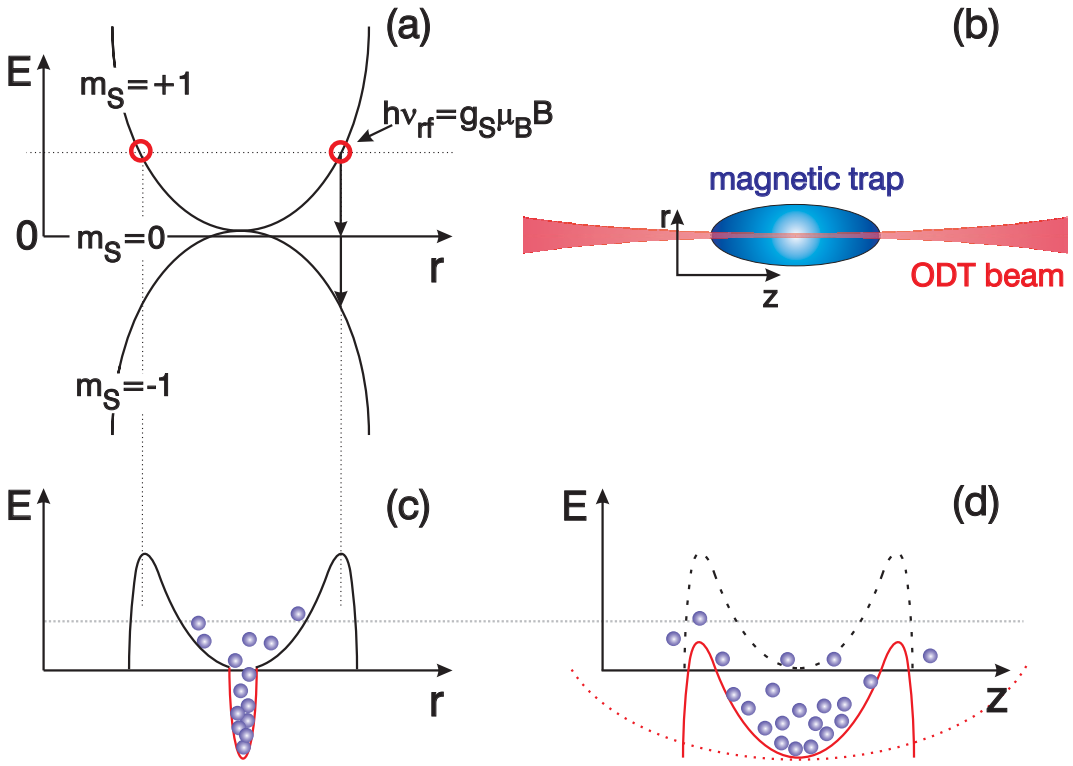

Figure 4.7: rf cooling in the hybrid trap. (a): Schematic drawing of the pure magnetic trap potential for an atom with total spin $S = 1$. At the positions marked with red circles, the frequency of the rf-field matches the resonance condition and drives transitions from trapped ($m_S = +1$) to untrapped ($m_S = 0, -1$) states when an atom gets into this region. (b): Alignment of the optical trapping beam in the magnetic trap. (c) and (d): Hybrid magnetic/optical trap potential, when both traps are operated at the same time. (c): Potential in radial direction. The confinement of the optical trap (red line) is much stronger than the magnetic trap. The black curve is the pure magnetic trap potential. Its outer regions are tied down by the presence of the rf-field. (d): Solid red line: hybrid potential in z-direction. The dashed black and dotted red curves are the pure magnetic and optical potentials, respectively. The horizontal grey dotted line marks the energy of the two upper atoms in figure (c) and (d). Although this energy is in a range that can be trapped by the magnetic potential in the radial direction (c), it is larger than the cut off energy in the axial direction (d). Thus an atom having this energy would be expelled from the trap in axial direction.

Radio-frequency evaporation

In this trap, we perform radio frequency (rf) evaporation [22, 23]. The principle of rf-evaporation is to remove high energetic atoms selectively from the trap by transferring them to untrapped Zeeman states. This is achieved by applying a radio frequency field. Let m_S be the magnetic quantum number of the total spin S of an atom and g_S be the associated Landé factor. Due to the inhomogeneity of the magnetic field, the rf-field is resonant with transitions between neighbouring m_S levels on a surface around the center of the trap, provided that the rf frequency is larger than the resonance frequency $\omega = g_S \mu_B B_0/\hbar$ in the center of the trap. If an atom has a sufficiently large energy to reach this surface, the rf-field drives a Landau-Zener-transition to low-field seeking Zeeman states and the atom is expelled from the trap. The trap depth is determined by the difference between the offset field in the center of the trap and the magnetic field B_{res} at which the resonance condition is fulfilled. A schematic illustration is found in Figure 4.7 (a). The rf-sweep is composed of 3 linear rf-ramps from 45 MHz down to 1.25 MHz. After this step, the cloud contains $4.5 \cdot 10^6$ to $5 \cdot 10^6$ atoms at a phase-space density of 10^{-5} and a temperature of 22 μK. The overall gain in phase-space density during the magnetic trapping phase is thus about four orders of magnitude whereas the number of atoms is reduced by 1.5 orders of magnitude.

4.7.2 Transfer into the optical trap

Beginning from the first step of the rf-ramp, the magnetic trap is superimposed by a single beam ODT in horizontal direction with the same symmetry axis as the magnetic trap. This trap is formed by beam I in Fig. 2.4 and Fig. 2.1 b) with a maximum power of 9.8 W. Figure 4.7 shows a schematic drawing of the hybrid potential formed by the superposition of the two traps. The energy cutoff in this trap is still given by the resonance position of the rf field. In contrast to the radial direction, where the optical trap is much steeper than the magnetic trap, the axial confinement is still dominated by the magnetic potential. Thus atoms need a larger energy to reach the region where the rf-field is resonant in radial than in axial direction as becomes clear from Fig. 4.7. If the temperature of the atoms is comparable or smaller than the depth of the optical trap, evaporation can only happen in z-direction and the cooling efficiency becomes weak.

The combination of the optical and magnetic potential produces a dimple in the

[4] Low-field seeking states or "low field seekers" are Zeeman states that have lower Zeeman energy $E_Z = g_F m_F \mu_B B$ in lower magnetic fields, i.e. $g_F m_F > 0$.

[5] In addition, the trap produces a magnetic offset field $B_0 \neq 0$ in the center of the trap that leads to a harmonic potential in radial direction, in a certain range around the trap center, too [51].

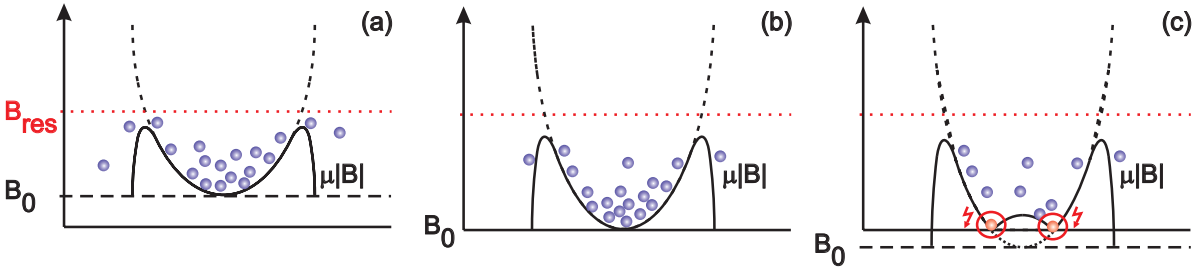

Figure 4.8: Occurrence of loss when the offset field is overcompensated. The black curve shows the magnetic trapping potential $\mu|B|$ formed by the inhomogeneous magnetic field (dashed line) along the symmetry axis of the magnetic trap. B_{res} (marked by a horizontal red dotted line) is the magnetic field strength where the rf-field is resonant with the Larmor frequency of the atoms. The dashed horizontal line marks the magnetic offset field (negative sign of B_0 stands for $\vec{B}_0$ pointing in opposite direction.) (a) Positive offset in the center of the trap. Not ideal regarding dipolar relaxation. (b) Very low but no-zero offset field. Lowest dipolar relaxation and highest compression in radial direction. (c) Overcompensation of the magnetic field. Majorana loss occurs in the marked regions.

trap potential and leads to an increased density in the center which promotes density dependent loss mechanisms like dipolar relaxation. To achieve the lowest possible dipolar relaxation rate, the magnetic offset in the center of the trap has to be as low as possible. Besides that, lowering the offset leads to a radial compression of the magnetic trap which improves the mode matching of the magnetic and optical traps. The offset field is adjusted close to 0 G by applying some extra current in the bias coils. The calibration of this offset field is performed by looking at loss from the purely magnetic trap due to Majorana spin-flips [102] in regions of very small magnetic field. In such regions, the Larmor frequency of the precessing magnetic moments is so low that they are not able anymore to follow the changing magnetic field adiabatically as they move through the trap. Hence, if such regions are produced by compensating the offset field as depicted in Figure 4.8 close to zero, Majorana loss leads to a decrease of the number of trapped atoms. This zero field adjustment has an accuracy of ∼35 mG corresponding to the scale on which the number of atoms changes from maximum number of atoms to no atoms when changing the current in the bias coils as depicted in Fig. 4.9. Perfect alignment of the ODT with best possible overlap between the magnetic and the optical trap is essential for an efficient transfer into the ODT. In particular, the first beam must be aligned in perfectly horizontal direction because of its rather poor confinement in axial direction resulting in a longitudinal trap frequency of only ∼ 13 Hz. In radial direction, the trap has a frequency of ∼ 1450 Hz. Best alignment is achieved by taking absorption images of the dipole trap within the magnetic trap as depicted in Fig. 4.10 to overlap the two trapping potentials.
The final frequency of the rf-sequence is chosen such that the highest number of atoms is

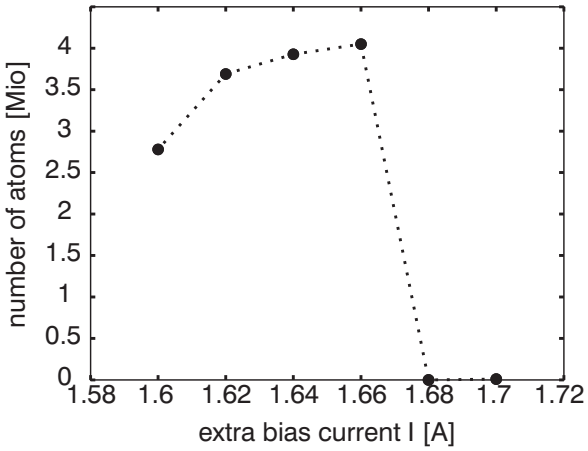

Figure 4.9: Calibration of zero magnetic field. Number of remaining atoms after rf cooling plotted vs. extra offset current in the bias coils. The extra offset field produced in by the coils is ∼1.6 G/A. The cloud vanishes at a current of 1.68 A which overcompensates the magnetic offset field whereas at 1.66 A the maximum number of atoms remain. At lower currents, the number of atoms decreases because the offset and therefore the minimum of the magnetic trapping potential comes closer to the rf frequency knife.

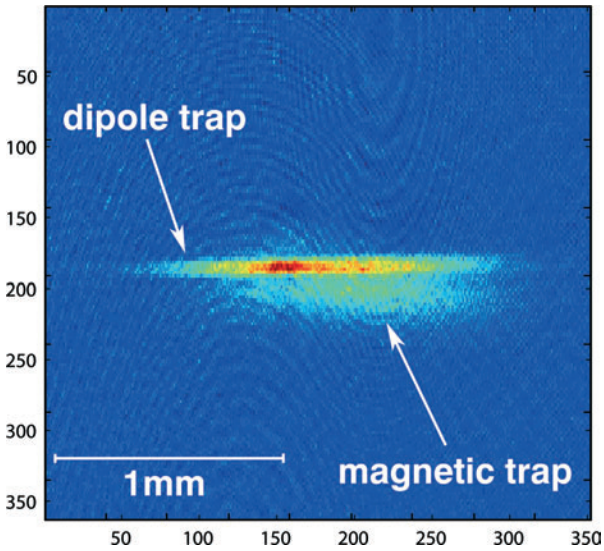

Figure 4.10: Image of the hybrid magnetic/optical trap. The beam of the optical trap was intentionally misaligned for this image to show both traps.

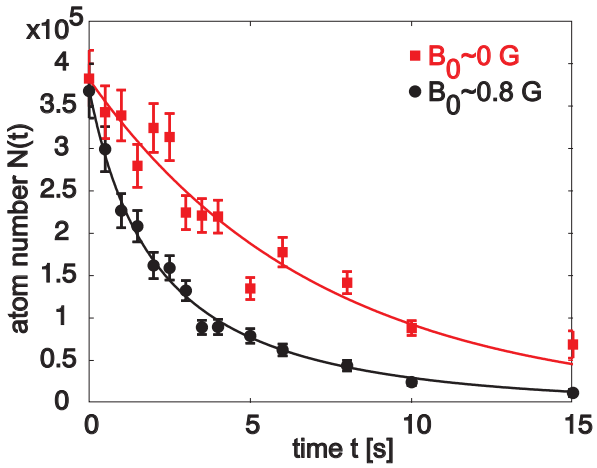

Figure 4.11: Dipolar relaxation of ^{52}Cr atoms measured in an optical dipole trap. Two lifetime measurements were performed at different homogeneous magnetic fields ($B_0 \approx 0.8\,\mathrm{G}$ and $B_0 \approx 0\,\mathrm{G}$). The life time of the trapped sample clearly depends on the magnetic field.

transferred adiabatically to the single beam optical trap by ramping down the magnetic trapping potential within 100 ms. With these optimisations, the transfer efficiency from the magnetic to the optical trap is 40% and we start with up to $2 \cdot 10^6$ atoms in the ODT. The phase-space density at this stage is $5 \cdot 10^{-5}$, a factor of five higher than the phase-space density that is found in the pure magnetic trap after the final rf-ramp without an optical trap present. The phase space densities in the dipole trap and the magnetic trap have both been determined from time of flight series of absorption images.

4.8 Transfer to the lowest Zeeman state

Even at very low magnetic offset field, dipolar relaxation leads to a redistribution of the atoms among the Zeeman sub states and to heating. A heating rate of $3\,\mu\mathrm{K/s}$ at an offset field of 0.7 G, and a relaxation rate constant on the order of $\beta_{dr} = 1 \cdot 10^{-12} 1/\mathrm{cm}^3$ at 0.15 G have been measured in an optical dipole trap [86]. Figure 4.11 shows the field dependence of dipolar relaxation in the results of two lifetime measurements in the optical trap at magnetic offset fields of 0.8 G and ∼0 G, respectively.
The only way to suppress this relaxation process completely is to bring all atoms to the energetically lowest Zeeman state in a magnetic offset field $B_0 \gg k_B T/\mu$. In this state, atoms can not gain energy anymore by flipping their spins. This means that relaxation to higher states is energetically forbidden if the atoms do not have enough kinetic energy

to bring up the difference in Zeeman energy that is needed to occupy such a level[6].
Previous attempts to circumvent dipolar relaxation by a radio frequency-induced Landau-Zener transition to the lower Zeeman-states have not been successful [86] because such a technique can only invert the already existing spin distribution but not purify it. Since the optical trap is loaded from a magnetic trap where not only the extreme but all low field seeking Zeeman states are present, the atoms in the optical trap are also in a spin mixture.
It is possible however to use optical means to polarise the atoms in the lowest Zeeman state. We make use of the fact that if the trapped atoms are exposed to pure σ^- light resonant with the $^7\mathrm{S}_3 \leftrightarrow {}^7\mathrm{P}_3$ transition [7] at a wavelength of 427.6 nm , the energetically lowest $m_J = -3$ state is a dark state and not influenced by the light field. The σ^- light drives $\Delta m_J = -1$ transitions from $|\, g, m_J \,\rangle$ to $|\, e, m_J - 1 \,\rangle$ from where the decay happens to $|\, g, m_J - 1 \,\rangle$, $|\, g, m_J \,\rangle$ or $|\, g, m_J + 1 \,\rangle$ with a probability given by the corresponding Clebsch-Gordan coefficients as depicted in Figure 4.12. If an atom ends up in state $|\, g, -3 \,\rangle$, there is no $\Delta m_J = -1$ transition and the atom stays in this state – unaffected by the light field. The suppression of light scattering in this state is additionally supported by a magnetic field which breaks the degeneracy of the magnetic substructure and leads to a shift between $\Delta m_J = +1$, $\Delta m_J = -1$, and $\Delta m_J = 0$ transitions. A magnetic field of 11.5 G along the axis of the pumping beam requires a detuning of 32 MHz to the red with respect to the resonance at zero magnetic field. Because the Landé factors in $^7S_3$ and $^7P_4$ are almost equal, the shift between different transitions with the same Δm_J is negligible at the magnetic fields that are used. In contrast, the relative detunings for $\Delta m_J = 0$ and $\Delta m_J = +1$ transitions induced by this field are 2.3Γ and 6.2Γ if the laser is tuned on resonance with the $\Delta m_J = -1$ transition. This helps prevent transitions other than the desired $\Delta m_J = -1$ which are not fully suppressed if the polarisation of the beam is not purely circular. The average number of photons needed to bring an atom from $m_J = +3$ to $m_J = -3$ has been calculated using a recursive algorithm which can be found in Appendix D of this thesis. Assuming perfectly σ^- polarised light, the average number of scattered photons is $n_{phot} = 6.2$. To keep heating due to these scattered photons low, the pumping beam is retro-reflected after passing through the cloud and passes it again. Assuming that the atoms scatter photons with equal probability from either of these two beams, heating is only due to momentum diffusion and thus proportional to the square root of the number of scattered photons.

[6] This effect has recently been suggested to be used for a novel cooling scheme [115] where the external magnetic field is low enough for the atoms to undergo spin flips by converting energy from external degrees of freedom into internal Zeeman energy. In this scheme, the atoms are always optically pumped back to the lowest lying substate subsequent to such a flip. If the energy loss through the Zeeman-flips is larger than the afterward heating by the photon-scattering from the pumping beam, this constitutes a lossless cooling mechanism that is currently being investigated experimentally by our group.

[7] Compare the level scheme in Chapter A. For the setup of the laser system refer to Section 2.5.

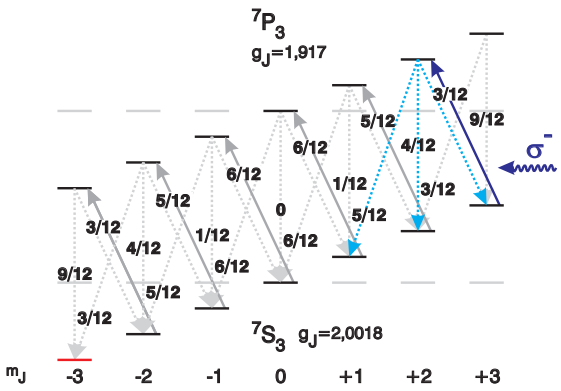

Figure 4.12: Magnetic substructure of the $^7\mathrm{S}_3 \leftrightarrow {}^7\mathrm{P}_3$ transition. The σ^- polarised light drives the atoms which are initially mainly in the energetically highest state $m_J = +3$ to the lowest state $m_J = -3$. The numbers close to the transitions are the squares of the Clebsch-Gordan coefficients.

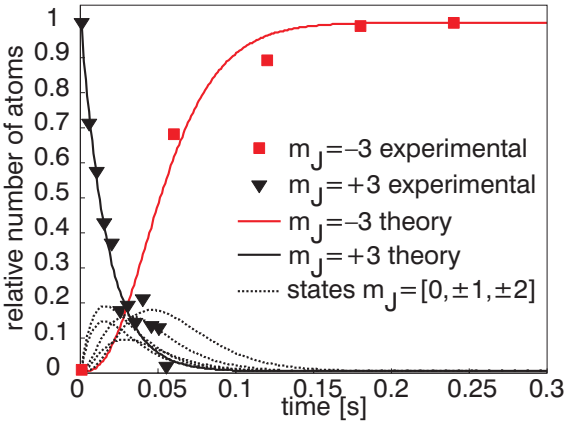

Figure 4.13: Time dependent occupation numbers of the Zeeman sub-states of $^7S_3$ during optical pumping. Theoretical data calculated using Eqn. (4.13).

The energy transferred to the cloud during optical pumping is thus

$$\Delta E = \sqrt{n_{phot}}\frac{\hbar^2 k_{phot}^2}{2m} = 2.15\mu K \cdot k_B$$

per atom which is low compared to the temperature of $>50\,\mu$K at that time.
To tune the laser on resonance with the $^7\mathrm{S}_3 \leftrightarrow {}^7\mathrm{P}_3$ transition, we expose the MOT to the light. On resonance, the $^7\mathrm{P}_3$ state becomes occupied from where atoms can – in addition to transitions back to the ground state and metastable D-states – also decay to the $^5S_2$ state. This state is not reachable from $^7\mathrm{P}_4$ and is decoupled from the lasers. Such transitions constitute a loss mechanism in the MOT which is only present when atoms are pumped to $^7\mathrm{P}_3$. Hence, a decrease in the fluorescence of the MOT due to a reduction of the number of trapped atoms indicates the pumping laser being on resonance. The atoms are pumped to $m_J = -3$ by shining in 0.5 mW of σ^--polarised light for 1 ms in the optical dipole trap immediately after the magnetic trap is switched off. The intensity of the beam is on the order of $1\,\mathrm{mW/cm^2}$ and the light propagates in radial (y-)direction. The rather small intensity and correspondingly long pumping time are chosen such that power fluctuations at frequencies far above the bandwidth of the doubling-cavity and diode laser stabilisation are averaged out.
The pumping process is described by the rate equations of the occupation numbers N_j

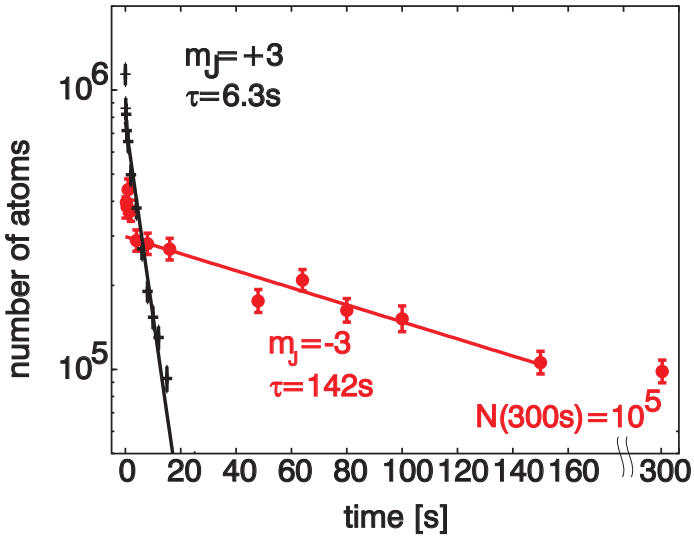

Figure 4.14: Comparison of trap lifetimes in the single beam ODT before (crosses) and after (circles) pumping the atoms to the lowest Zeeman substate. Solid lines are fits of an exponential decay $N(t) = N_0 \exp(-\gamma t)$ to the data where γ is the decay rate.

of the levels $m_J = 0, \pm 1, \pm 2, \pm 3$ of the $^7S_3$ ground state in presence of the light field:

$$\frac{d}{dt}N_j(t) = -\sum_{\Delta m_J=-1}^{1}\left(C_{j,j+\Delta m_J}\Gamma_{sc}^{\Delta m_J}N_j(t)\right) + \tag{4.13}$$
$$+\sum_{\Delta m_J=-1}^{1}\left(\sum_{l=\Delta m_J-1}^{\Delta m_J+1}\left(C_{j+l,j+\Delta m_J}C_{j,j+\Delta m_J}\Gamma_{sc}^{\Delta m_J}N_{j+l}(t)\right)\right)$$

$$\Gamma_{sc}^{\Delta m_J} = \begin{cases} \Gamma_{sc}(I,\delta) & : \quad \Delta m_J = P \\ 0 & : \quad \Delta m_J \neq P \end{cases},$$

where C_{m_J,m'_J} are the squares of the Clebsch-Gordan coefficients for transitions from m_J to m'_J, $\Delta m_J = m'_J - m_J = 0, \pm 1$, and $\Gamma_{sc}^{\Delta m_J}$ is the scattering rate on the Δm_J transition. The polarisation of the pumping beam is characterised by the parameter P which is $P = 0$ for π-light, $P = 1$ for σ^+-light, and $P = -1$ for σ^--light[8]. This set of rate equations has been solved numerically to obtain the time dependent occupation numbers of the states $m_J = +3$ and $m_J = -3$.

The solutions are plotted together with the experimental data in Fig. 4.13 where the saturation parameter in the calculation has been adjusted such that the numerical data match best with the experiment. The time dependent populations of $m_J = +3$ and $m_J = -3$ during the pumping process have been recorded by taking images of the cloud trapped in the horizontal ODT beam after variable time of exposure to the pumping

[8] Perfect polarisation of the pumping beam is assumed.

light. To be able to resolve the time dependence, the power in the beam was reduced to only a few μW such that 300 ms were needed to transfer the atoms to $m_J = -3$. The same sequence was repeated twice, where in one run blue detuned $\sigma+$-light and in the other red detuned $\sigma-$-light was used to image the $m_J = +3$ and $m_J = -3$ atoms, respectively. Because the number of trapped atoms decays very rapidly due to plain evaporation after the optical trap is loaded (this is discussed in Section 5.2.1), the number of atoms found in $m_J = -3$ after 300 ms never reaches the starting value of $m_J = +3$[9]. The atom numbers in the graph have therefore been corrected by the decay rate to be comparable to be able to compare the experimental time dependence with the theoretical calculation. With higher pumping light intensity and therefore much faster pumping that is commonly used in the experiment, the efficiency of the transfer is close to 100% which is reflected in a dramatic increase of the lifetime of the trapped cloud from $\sim$6 s in $m_J = +3$ to $>$140 s in $m_J = -3$ as shown in Fig. 4.14. This long lifetime is a very important precondition for efficient evaporative cooling in the optical dipole trap.
To prevent later thermal redistribution of the spins, the magnetic offset field of 11.5 G used for pumping is kept on during all further preparation steps.

[9] It is not possible to delay the pumping stage until plain evaporation is over because dipolar relaxation leads to strong loss and limits the trapping period to a time shorter than that.

5 Evaporative cooling in the dipole trap

Abstract

Most experiments with ultracold atoms make use of optical cooling techniques. They have been used very successfully in almost all[1] BEC experiments. However, all these techniques have fundamental limits (see eg. [103]) and the phase space densities which can be reached are usually orders of magnitude away from the critical value. The temperatures which can be reached by the optical cooling techniques that are used in the experiments I discuss in this thesis to prepare a cloud of chromium atoms in the magnetic trap are given by the Doppler limit of $T_D = \hbar\Gamma/2k_B = 120\,\mu K$*. The phase-space density (PSD) at this stage is on the order of* 10^{-7}*, yet seven orders of magnitude away from degeneracy. To overcome this gap, we use evaporative cooling first in the magnetic and then in the optical dipole trap. Radio frequency (rf) induced evaporative cooling of chromium atoms in a magnetic trap has been demonstrated in earlier works [86] and will not be further discussed here. In the experimental part, I will concentrate on evaporative cooling of chromium in an optical dipole trap. However, the general theoretical description of evaporative cooling that will be presented in the next section applies to rf evaporation as well.*

The principle of evaporative cooling is the withdrawal of atoms from a sample which carry more than the average energy. Thus the average energy per atom in the remaining sample is lower than before. This is well known in everyday life as it is for example the principle that cools a cup of coffee when the most energetic water molecules – the steam – are blown away. Evaporative cooling has been discussed already 20 years ago in 1986 in the context of ultracold gases and Bose-Einstein condensation by Hess [20] and was demonstrated with magnetically trapped hydrogen in 1988 [21]. In 1994, rf induced evaporative cooling was demonstrated with sodium and rubidium atoms by the groups of Cornell and Ketterle [22, 23] who managed to generate the first BECs in dilute gases one year later using exactly this technique. In our experiment, the evaporative cooling technique permits us to cool the sample in the dipole trap from an initial temperature of $50\,\mu$K to temperatures around 100 nK. The gain in phase-space density is about 4 orders of magnitude, while one order of magnitude in the number of atoms is lost during

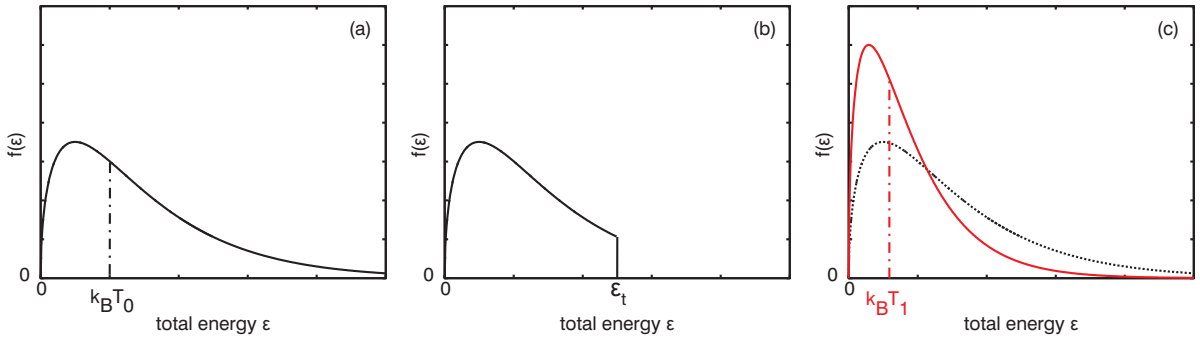

Figure 5.1: Left: Maxwell-Boltzmann distribution corresponding to a temperature T_0; Center: truncated Maxwell-Boltzmann distribution. Atoms with total energies $E_{tot} > \epsilon_t$ are removed from the trap; Right: distribution after the system has relaxed again (red solid line) compared to the initial distribution (dotted black line). The temperature of the system is lower than before ($T_1 < T_0$) if the cutoff energy was higher than the average energy of the atoms $\epsilon_t > \eta k_B T_0$.

evaporation.

5.1 Theoretical description

In the classical regime, far away from the BEC transition, the equilibrium distribution of atoms in phase space is given by the Maxwell-Boltzmann (MB) distribution[2]

$$f(\vec{r},\vec{p}) = \left(\frac{\omega}{2\pi k_B T}\right)^3 \exp\left(-\frac{U(\vec{r}) + \vec{p}^2/2m}{k_B T}\right), \tag{5.1}$$

whose integral is normalised to 1. It is closely related to the density distribution of atoms in space. The spatial distribution in an infinitely deep trap is given by the product of the total number of atoms with the integral of Eqn. (5.1) over the whole momentum space:

$$n(\vec{r}) = N \int f(\vec{r},\vec{p}) d^3p = N \left(\frac{m\omega^2}{2\pi k_B T}\right)^{3/2} \exp\left(-\frac{U(\vec{r})}{k_B T}\right).$$

As a side effect we have found the peak density in the center of the cloud by identifying it with all the prefactors of the integral: $n_0 = N\left(\frac{m\omega^2}{2\pi k_B T}\right)^{3/2}$.
If the system is ergodic, i.e. the whole phase space can be reached, the energy distribution is a function $f(\varepsilon)$ of the single particle energy ε and can be derived from

[2] In comparison to the Bose distribution, which is strictly speaking the correct distribution function of Bosonic atoms, the MB distribution does not show an enhanced population of low energy states. In the classical regime however, the difference between the two is small and the distribution is well approximated by the MB distribution. Compare also Section 3.3.1.

Eqn. (5.1):

$$f(\varepsilon) = \sqrt{\frac{4\varepsilon}{\pi(k_B T)^3}} e^{-\frac{\varepsilon}{k_B T}} \tag{5.2}$$

where $\varepsilon(\vec{r},\vec{p}) = \frac{\vec{p}^2}{2m} + U(\vec{r})$ is the total single particle energy.
The energy distribution function $f(\varepsilon)$ is shown by the solid line in Fig. 5.1 (a). Obviously, in thermal equilibrium there is always a finite probability of finding an atom at energies much higher than the mean energy $3k_BT$.
The idea of evaporative cooling is now to cut away the high energy tail of the MB distribution by taking away atoms with energies higher than ε_t as displayed in Fig. 5.1 (b). Without energy exchange among the atoms, this truncated energy distribution would just stay like it is for all times and one would not find an atom with $\varepsilon > \varepsilon_t$ anymore, nor would a real temperature be defined in this non-equilibrium system. Efficient cooling becomes possible if elastic collisions among the atoms happen which rethermalise the gas. With atoms which have all the same mass, about 3 elastic collisions per atom are necessary to bring the system from an initially non-thermal distribution back to thermal equilibrium [116, 117, 70]. If the gas is left alone without a restriction of the atomic energies after throwing away the high energy atoms, it will reproduce the tail of the MB distribution but with a final temperature that is lower than before like depicted in Figure 5.1 (c).
Now one could remove the high energy tail again in a second step and so on, cooling the sample further and further. On the other hand, the ratio between the cutoff energy ε_t and the thermal energy k_BT becomes larger and larger with every such imaginary evaporation step if ε_t stays constant. Thus the probability that atoms acquire energies larger than that becomes lower and lower and the cooling slows down.

5.1.1 Forced evaporation

To cool the sample further, evaporation is forced by lowering the cutoff energy continuously (*forced evaporation*). Finding out the rate at which ε_t has to be lowered to achieve the most effective cooling is crucial for all BEC experiments. The following theoretical description of evaporative cooling follows the argumentation of Luiten et al. [118] and O'Hara et al. [119]. Since the rate at which high energy states are populated depends on elastic scattering, the change of ε_t on the timescale of the inverse scattering rate should be small, to keep the rate at which atoms are thrown away small. In this case, Luiten et al. [118] have shown that the gas stays in a quasi-equilibrium where the energy distribution is described by a truncated MB distribution function which can be written

by multiplying the MB function with the Heaviside step function $\Theta(\varepsilon_t - \varepsilon)$:

$$f_t(\varepsilon) = f(\varepsilon)\Theta(\varepsilon_t - \varepsilon) = n_0\lambda_{dB}^3 e^{-\frac{\varepsilon}{k_B T}}\Theta(\varepsilon_t - \varepsilon).$$

This distribution is still characterised by a "temperature" T which is at any time related to the cutoff energy ε_t via the cutoff parameter η:

$$\varepsilon_t = \eta k_B T.$$

In the strict sense, this T is only a temperature in the limit $\eta \to \infty$ which is the usual equilibrium situation in an infinitely deep trap.
The rate at which atoms in high energy states are produced determines the rate $\dot{N}_{evap}$ at which atoms are lost by evaporation. This rate is proportional to the elastic scattering rate

$$\gamma_{el} = n_0\sigma_{el}\overline{v}_t,$$

where $\overline{v}_t$ is the average thermal velocity of the atoms and σ_{el} is the elastic scattering cross section. Including a collision energy dependence up to second order in the atom momentum k, the elastic scattering cross section is given by[3]

$$\sigma_{el} = \frac{8\pi a^2}{1 + k^2 a^2},$$

where a is the s-wave scattering length. $\dot{N}_{evap}$ also depends on the cutoff parameter η. The larger the trap depth is compared to the average thermal energy, the less the probability that an atom gains enough energy to escape the trap. This is taken into account by a Boltzmann-factor $e^{-\eta}$. Hence the evaporative loss rate reads

$$\frac{\dot{N}_{evap}}{N} = -n_0\sigma_{el}\overline{v}_t e^{-\eta}.$$

The total energy of a trapped gas in the classical limit is given by the partition function [118] $E = (3/2 + \chi)Nk_BT$. The parameter $\chi = (T/U_{eff})\partial U_{eff}/\partial T$ determines the fraction of potential energy in the total energy $E_{pot} = \chi k_B T$. In trap potentials which can be described by power laws of the form $U(\vec{r}) = c_x|x|^{1/\chi_x} + c_y|y|^{1/\chi_y} + c_z|z|^{1/\chi_z}$, χ is given by [76, 118]

$$\chi = \sum_i \chi_i.$$

Thus $\chi = 3/2$ in harmonic potentials where $\chi_x = \chi_y = \chi_z = 1/2$. In such power law potentials, the density of states $D(E)$ is proportional to E^χ. The rate at which the total energy changes in a constant harmonic potential is therefore $\dot{E} = 3k_B(\dot{N_{evap}}T + N\dot{T})$. O'Hara et al. find that for any harmonic potential, the average energy that is taken

[3] For an introduction to ultracold collision see e.g. [81].

away by an evaporated atom is $(\eta-5)/(\eta-4)\eta k_B T$ which is $\eta k_B T$ for large η. Hence the energy loss rate is also proportional to this average energy and the evaporative loss rate $\dot{E} = (\eta-5)/(\eta-4)\eta k_B T \dot{N}_{evap}$. Equating the above two expressions for $\dot{E}$ finally yields an equation for the change of the temperature:

$$\dot{T}/T = (\eta/3 - 1)\,\dot{N}/N.$$

The evaporation is more efficient (stronger decrease of the temperature with the same atom loss rate) the larger the cutoff parameter η is. On the other hand Eqn. (5.1.1) shows that a larger η slows down the evaporation. A trapped cloud of atoms is always subject to loss due to background gas collisions or inelastic collisions among the atoms. Therefore a slower evaporation leads to an increased loss due to such processes.

5.1.2 Evaporative cooling in dipole traps

As has been shown in Chapter 4, optical trapping potentials possess a finite depth. If the total energy $E_{kin} + E_{pot}$ of an atom exceeds this depth, it will escape the trap by climbing up the trapping potential unless it loses the excess energy in a collision process before it can leave the trap. Thus evaporation is always present in optical dipole traps. The evaporation rate however is suppressed by $\exp(-U_0/k_B T)$ and stagnates in a trap with constant depth as the sample cools down. When the cutoff parameter reaches values $\eta > 10$, evaporation becomes very slow. Evaporative cooling in a dipole trap can be forced by reducing the intensity of the trapping laser adiabatically and thus lowering the trap depth. Unlike in magnetic potentials, where the trap depth can be varied independently from the trap parameters by applying an rf-knife, the trap parameters of a dipole trap are connected to the trap depth by equations (4.2.1) and (4.2.1). Hence the density and elastic collision rate scale with the trap depth, too. O'Hara et al. [119] have found scaling laws which can be used to calculate the evolution of the thermodynamic properties for a given constant cutoff parameter η as well as the time dependence of the trap depth that is needed to keep η constant. According to their theory, the time dependence of the trap depth has to follow the equation

$$\frac{U_0(t)}{U_i} = \left(1 + \frac{t}{\tau}\right)^{-2(\eta'-3)/\eta'}$$

where the time constant τ of the evaporation is given by

$$\frac{1}{\tau} = \frac{2}{3}\eta'(\eta-4)e^{-\eta}\gamma_i$$

and $\eta' = \eta + (\eta-5)/(\eta-4)$. U_i, $\gamma_i = 4\pi N_i m \sigma_{el}(\omega_{ho}/(2\pi))^3/(k_B T_i)$, N_i, and T_i are the initial trap depth, collision rate, number of atoms, and temperature, respectively. To

take background loss into account, they rescale time with the background loss rate Γ_{bg}:

$$t \rightarrow \frac{1 - e^{-\Gamma_{bg} t}}{\Gamma_{bg}}.$$

Atom loss now consists of two parts: the evaporative loss and loss by background gas collisions:

$$\dot{N} = \dot{N}_{evap} - \Gamma_{bg} N.$$

The evolution of the phase-space density is given by

$$\rho(t) = N(t) \left(\frac{\hbar \omega_{ho}(t)}{k_B T(t)} \right)^3$$

These results have been successfully used to produce Bose-Einstein condensates in running beam traps [120]. Eqn. (5.1.2) shows that successful cooling in a single beam dipole trap strongly depends on the initial collision rate which determines the time constant τ throughout the evaporation. It has turned out that this initial collision rate is too low in our chromium experiment. Attempts to cool the cloud in the single beam trap using this method only lead to a small increase of the PSD (see Section 5.2.2).

5.2 Evaporative cooling of chromium

5.2.1 Plain evaporation

During the first seconds in the ODT, a very fast decay of the number of atoms is observed which becomes slower after about half of the atoms are lost (see fig. 5.2). Along with this decrease of the number comes a very large increase in the phase-space density which was determined from time of flight pictures taken during the lifetime of the trap. As two-body loss processes are suppressed in the lowest Zeeman state and there is also no hint for three-body loss in the regime of relatively low density at this stage of optical trapping, the observed loss can be attributed to essentially pure plain evaporation. Figure 5.3 shows the evolution of the phase-space density during the first 120 s in the ODT plotted vs. the number of remaining atoms and vs. time. The straight line in the main graph has a slope of 3.6 orders of magnitude gain in phase-space density per lost order of magnitude in the number of atoms and is a linear fit to the data. This illustrates the very high efficiency of the plain evaporation stage. After 5 s it gets less efficient which is identifiable by the data points in fig. 5.3 snapping off from the straight line. During plain evaporation the temperature of the trapped cloud drops from an initial value of 60 μK to 14 μK at the end. After about 10 s in the dipole trap, the change of the temperature is so small that it can not be measured anymore. Even

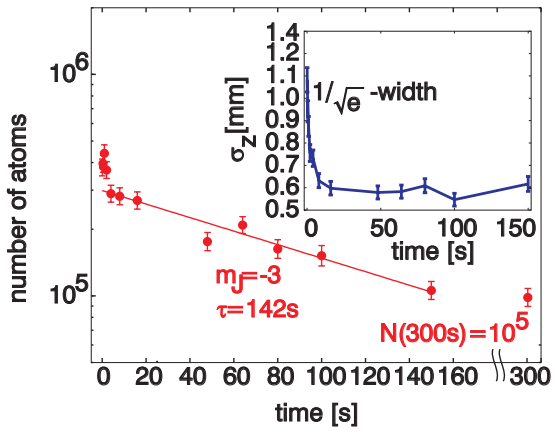

Figure 5.2: Lifetime measurement in the single beam ODT after pumping the atoms to the lowest Zeeman substate. The inset shows the change of the axial size of the expanded cloud in time of flight images depending on the time it lived in trap.

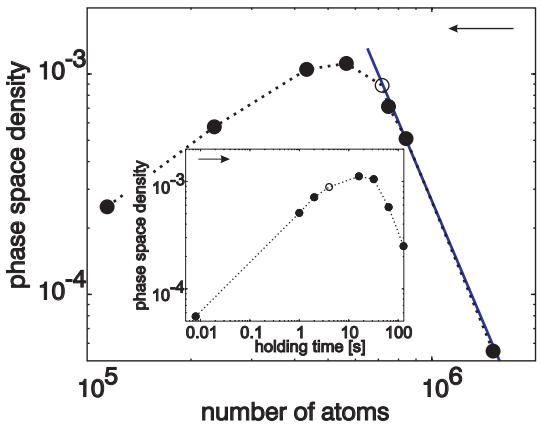

Figure 5.3: Double logarithmic plots of the phase-space density vs. number of remaining atoms and vs. holding time in the single beam trap (inset). Arrows mark the chronology in the plots. An open circle marks in both plots the optimum point in time to start forced evaporation.

after 300 s in the trap, when still more than 100000 atoms are trapped, we find the same temperature within error bars. It corresponds to a cutoff parameter of η =9.6 .

5.2.2 Forced evaporative cooling in the single beam trap

The approach of Section 5.1.2 has been used to estimate the possibility of successful cooling of chromium atoms in the single beam configuration by calculating the evolution of the phase-space density, number of atoms, and trap depth under the starting conditions that are possible in the chromium experiment. Best values that could be achieved are 10^6 atoms at 15 μK after plain evaporation in a trap with a depth of 148 μK and a mean frequency of $\omega_{ho} = 2\pi(1650\,\text{Hz}\cdot 1650\,\text{Hz}\cdot 14.5\,\text{Hz})^{1/3}$ using 12.8 W of laser power in the horizontal trapping beam. The background loss rate obtained from a fit of an exponential decay on the data of Fig. 4.14 is γ =1/150 1/s. Figure 5.4 shows the evolution of the phase-space density and number of atoms under these assumptions as well as the evaporation ramp of the trap depth which would keep the cutoff parameter at the value of $\eta \approx 10$ found at the end of the plain evaporation stage. These figures indicate that with the starting conditions that could be achieved, it is not possible to reach degeneracy. A factor of two higher number of atoms at the beginning would produce a large enough elastic scattering rate to reach Bose-Einstein condensation in principle (dash-dotted line in Figure 5.4(d)) after more than 50 s. However, the final trap depth

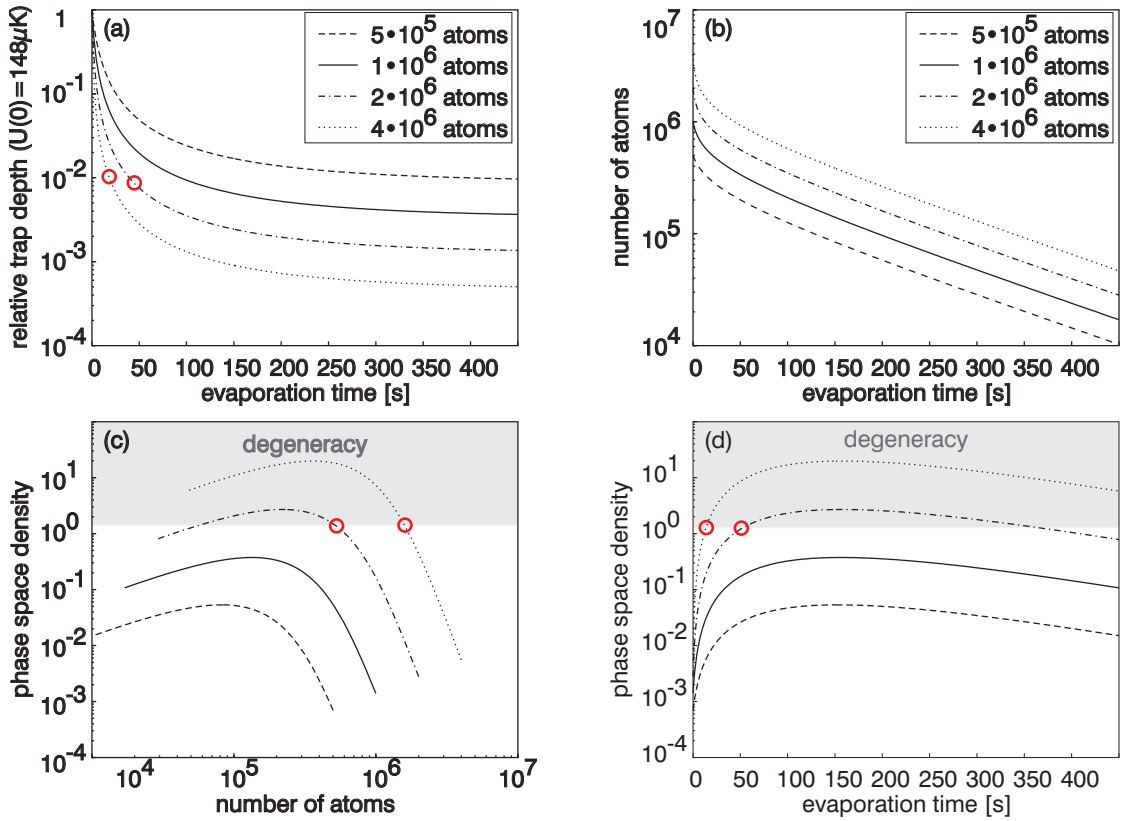

Figure 5.4: Evaporation ramp in the single beam dipole trap calculated for the different atom numbers in the beginning. (a) Time dependence of the trap depth starting with a depth of 148 μK. (b) Evolution of the number of atoms. (c) Phase-space density as a function of the remaining number of atoms. The grey shaded area shows the border to quantum degeneracy. (d) Evolution of the phase-space density. Red circles in plots (a), (c), and (d) mark the points, where degeneracy could be reached when starting with 2 and 4 million atoms, neglecting the influence of gravity.

would have to be very low (below 1% of the initial trap depth). In such a shallow optical trap, evaporation happens mainly in vertical direction due to the influence of gravity. Since in such a "one-dimensional" (1-D) evaporation process, the kinetic energy in only one direction instead of the total kinetic energy of an atom decides whether the atom stays trapped or can leave the trap, evaporation in this 1-D case is known to be less efficient than 3-D evaporation [121, 122, 118]. The above model does not consider this lower efficiency at the end of the evaporation ramp. It is thus questionable whether BEC could be realised experimentally under these conditions. Starting with 4 million atoms, which would be an approvement by a factor of 4 in the number of atoms compared to the current status of our experiment, the above model leads to degeneracy already after ~10 s and successful condensation is more likely in this case. The smaller efficiency of 1-D evaporation could be compensated by slowing down the evaporation ramp at the

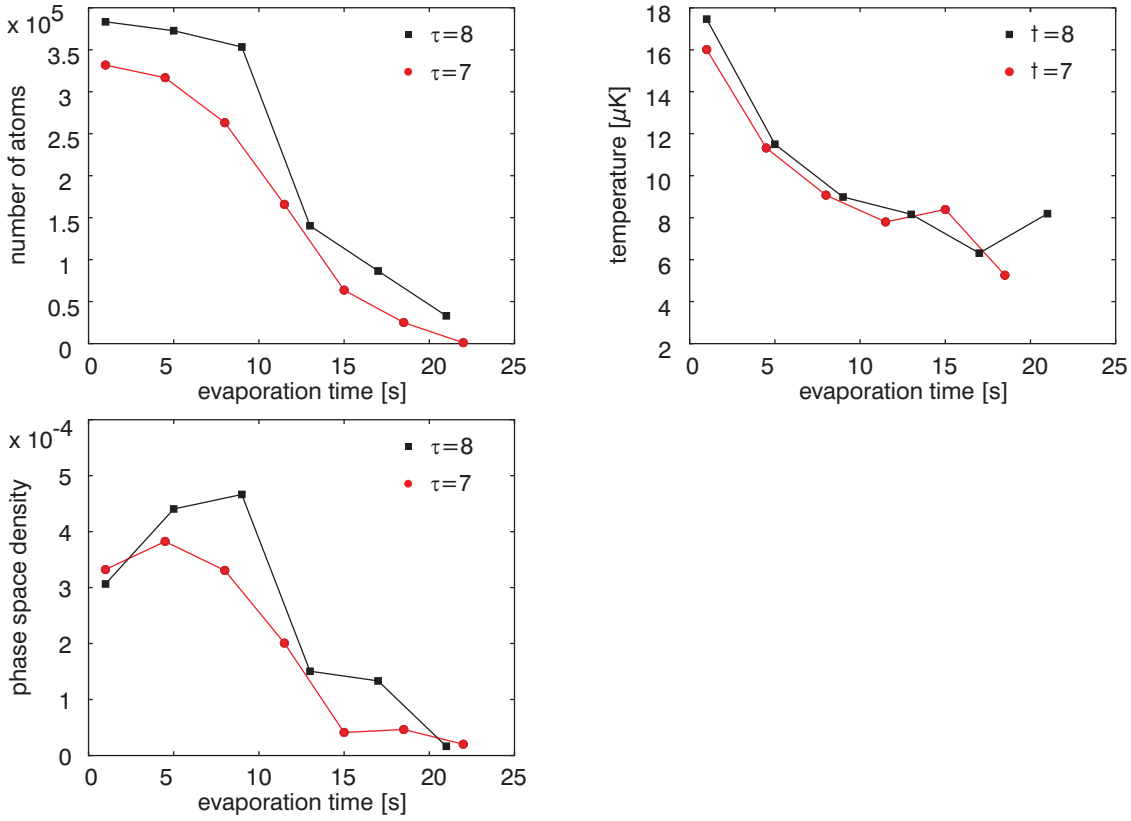

Figure 5.5: Results of evaporative cooling performed in the single beam trap with two different time constants τ. The figures show the evolution of the number of atoms, temperature, and phase-space density depending on the time over which the trap depth was reduced according to Eqn. (5.1.2).

end. In this case, BEC in the single beam ODT could be possible if we assume that all other parameters would not change to the worse when the number of atoms is improved e.g. by the use of a stronger laser for the generation of deeper traps.

Early attempts to perform evaporative cooling only in the horizontal beam have confirmed these findings. Starting with about 400000 atoms in a trap with 12.5 W and an initial elastic collision rate of 60 1/s, the laser power was ramped down subsequent to the plain evaporation stage following the time dependence given by Eqn. (5.1.2). Figure 5.2.2 shows the best result (black squares) obtained with this method. The black curve was obtained with the theoretically expected $\tau = 8\,\mathrm{s}$ corresponding to the above collision rate and $\eta = 10$. The second set of data (red curve) resulted from a slightly faster ramp with $\tau = 7\,\mathrm{s}$. Slower ramps lead to even worse results. The figures show that with $\tau = 8\,\mathrm{s}$, after a small initial gain of phase-space density of roughly a factor of 1.6, evaporative cooling does not work anymore and the phase-space density drops again. The maximum phase-space density that could be reached was $\rho = 5 \cdot 10^{-4}$.

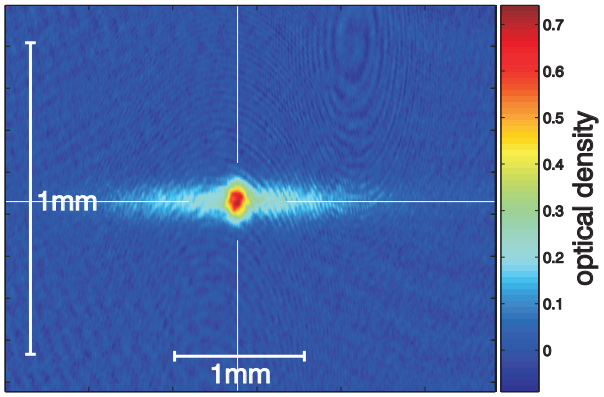

Figure 5.6: False colour image of atoms 1.2 ms after release from the trap where the vertical beam has been ramped up during plain evaporation. The increased density of the atoms in the crossed region is indicated by the central pixels appearing in red which corresponds to a large optical density (see the colour bar on the right side). The white bars in the figure indicate the length scales of the two directions. Note that the image has been stretched in the vertical direction to show more detail. The in-trap aspect ratio in the horizontal beam is in reality $\sim 1/140$.

5.2.3 Cooling in the crossed configuration

The results of the previous section showed that the collision rates in the optical trap formed by only one beam are not high enough to support evaporative cooling under the starting conditions we have or that could be expected. To increase the density and the collision rate, we increase the power of the vertical trapping beam (Fig. 2.1 b) during the plain evaporation stage linearly from 0 W to ∼4.5 W. This creates a dimple in the center of the trapping potential. Such an adiabatic deformation can be viewed as changing the power law (compare Section 5.1.1) of the trapping potential and thus leads to an increased density and phase-space density as suggested and experimentally demonstrated by Pinkse et al. [123]. The principle has since then been used successfully for the reversible generation of Bose-Einstein condensates in a hybrid magnetic/optical trap [124] and for Bose-Einstein condensation in optical traps [7]. The increase of the phase-space density $\rho = \lambda_{dB}^3 n_0$ by an adiabatic deformation (constant entropy $\Delta S = 0$) can be understood if we use the relation $A = -k_B T ln Q$ between the Helmholtz energy A and the partition function $Q = (V/\lambda_{dB})^N/N!$. With the entropy being given by $S = -\frac{\partial A}{\partial T}$, we can calculate the entropy per particle

$$\frac{S}{N} = -\frac{1}{N}\frac{\partial A}{\partial T} = \frac{k_B}{N}\left(lnQ + T\frac{\partial lnQ}{\partial T}\right).$$

In the case of power law potentials, the volume $V_i = \int e^{-U(\vec{r})/k_B T_i} d^3r$ that gives the right peak density $\widehat{n} = N/V$ at a temperature T_i, scales as $V_i \propto T_i^{\chi}$ with χ from Eqn. (5.1.1).

The entropy per particle is then given by

$$\frac{S}{N} = k_B \left(\frac{5}{2} + \chi - ln(\widehat{n}\lambda_{dB}^3) \right),$$

where $\rho_i = \widehat{n}\lambda_{dB}^3$ is the initial phase-space density. If we change the shape of the trapping potential $\chi_i \rightarrow \chi_f$ adiabatically ($\Delta S = S_f - S_i = 0$), the phase-space density becomes $\chi_f = \chi_f e^{\chi_f - \chi_i}$. The adiabatic transformation from the single beam to the crossed beam configuration can be understood as such a change of the potential shape. Stamper-Kurn explains this effect by a two-box model [102]. Consider N atoms with a phase-space density ρ_0 in a homogeneous box with volume $V_0 = V_1 + V_2$. If we now lower the potential in the small volume V_2 to a depth U_2 while keeping the entropy and number of particles constant, the phase-space density in the small volume V_2 is given by

$$\rho_f = \rho_i \exp\left(\frac{U/k_B T_f}{1 + (V_2/V_1) e^{U/k_B T_f}} \right).$$

If the volume of the well V_2 is much smaller than the overall volume $V_2/V_1 \ll 1$ (as in the case of the dimple trap), the increase in phase-space density is given by the Boltzmann factor $e^{U/k_B T_f}$. If the number of atoms in the dimple region is sufficiently small, the rest of the atoms act as a heat bath and the final temperature T_f does not differ much from the initial temperature T_i but the density in V_2 is larger than that in V_1 by a factor of $e^{U/k_B T_f}$. For a crossed dipole trap with chromium atoms, an increase of the phase-space density by a factor of 50 has been already shown [86]. Figure 5.6 shows an image of atoms released from a trap at this stage. About 20 % of the $7.5 \cdot 10^5$ atoms are trapped in the crossed region at a peak density and phase-space density which is one order of magnitude larger than the peak density of the atoms in the wings.
The increased density in the center also leads to a higher collision rate (see Eqn. (5.1.1)) and allows forced evaporation ro proceed in the crossed configuration by gradually reducing the laser intensity in the horizontal trapping beam. To keep the density and collision rate in the dimple at a high level, the intensity of the vertical beam is held at 100 % throughout the further evaporation steps.
The theoretical description of evaporative cooling in this configuration is however not as straightforward as in the single beam trap (Section 5.1). One has to take into account the atoms that are trapped in the crossed region as well as those located in the wings of the horizontal trap. This leads to much more complicated dynamics in the trap. Although evaporative cooling in a crossed configuration was demonstrated already in 1995 by Adams et al. [125] and has been used in several experiments to cool an atomic sample down to degeneracy [126, 7, 10] since then, an adequate theoretical description of evaporative cooling in such a trap is still missing. The main feature of these traps is the persistent loading of atoms from the wings into the crossed region [127, 128] by elastic collisions. This effect clearly shows up in our experiment (Section 5.2.4). In this

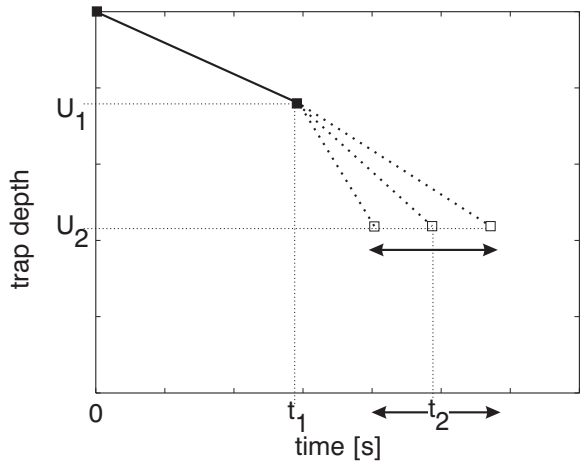

Figure 5.7: Optimisation of the evaporation ramp. The duration $t_2 - t_1$ of the ramp during which the trap depth is reduced from U_1 to U_2 is varied. In every experiment, the phase space density and number of remaining atoms is measured.

situation, one can not expect that the exponential form of the evaporation ramp that is found to be the optimum for a single beam setup (see previous section) is still suited to obtain highest phase-space densities and smallest possible atom loss. The "road" to degeneracy has to be found experimentally. This experimental method will be described in the next section. The efficiency of the evaporation is however not determined by an optimised ramp alone. The trap geometry, particularly the waist of the dimple beam also plays a crucial role. Although our setup led to success and allowed us to reach degeneracy with a substantial number of atoms, there might still be room for improvements of the trap geometry with regard to the number of atoms that can be obtained in the condensate. Since changing the trap parameters in the experiment involves substantial modifications of the experimental setup and requires a lot of experimental effort to find a suitable evaporation ramp before the situations can be compared, I have developed a fast numerical simulation method of evaporative cooling in arbitrary trap geometries that will be discussed in Chapter 6.

Optimisation of the cooling procedure

Evaporation in the crossed trap is carried out by decreasing the intensity of the horizontal beam. The intensity of the vertical beam is kept constant throughout the whole evaporation procedure. The aim of optimising the evaporation ramp is to reach highest possible phase space densities at the end of the ramp and to keep atom loss as small as possible. The evaporation ramp is divided into several consecutive segments. In every segment, the trap depth is decreased linearly from a starting value U_i to an endpoint U_{i+1}. Optimisation of the ramp is achieved by varying the duration of every segment

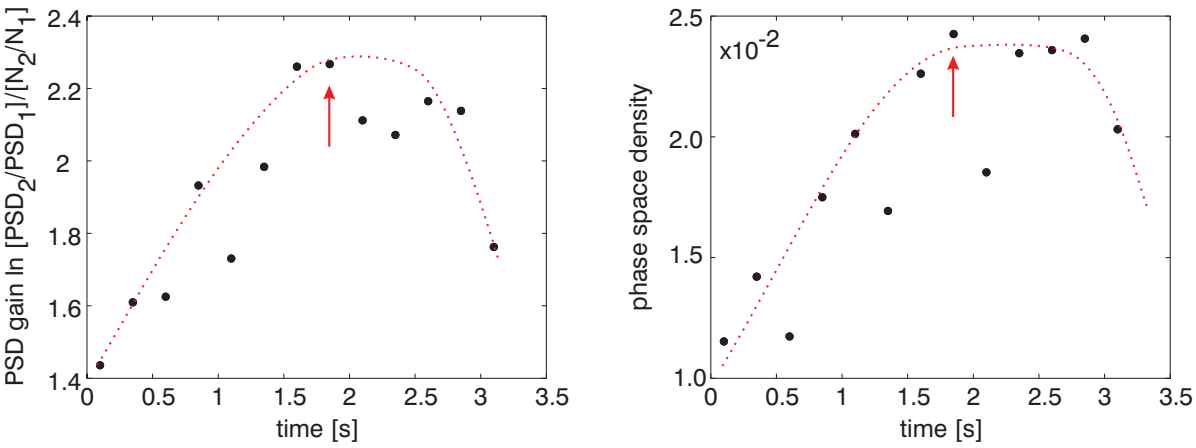

Figure 5.8: Optimisation of the second evaporation ramp from 50% to 70%. Left graph: phase-space density gain per atom loss $\ln \frac{\rho_{i+1}/\rho_i}{N_{i+1}/N_i}$. Right graph: phase-space density at the end of the ramp. Red dashed lines are guides to the eye. The red arrows mark the duration that was finally chosen.

as depicted in Fig. 5.7, where the measure for the efficiency of a ramp is the gain G_i of orders of magnitude in PSD per order of atom loss:

$$G_i = \frac{\log\left[\rho_{i+1}/\rho_i\right]}{\log\left[N_{i+1}/N_i\right]}$$

and the maximum phase-space density that can be reached at the end of the ramp. Figure 5.8 shows an example of such an optimisation experiment for the second ramp step from 70% to 50% of the initial trap depth. In the left graph, the efficiency G_2 is plotted vs. the duration of the ramp. The right graph displays the phase-space density at the end of the ramp. In this example, the highest phase-space density and efficiency was obtained with a duration of 1800 ms.

5.2.4 Discussion of the optimised evaporation ramp

With the final optimised evaporation ramp, degeneracy was reached with 100.000 atoms at a temperature of 450nK . Six evaporation steps were needed to increase the phase-space density to values larger than one. The final roadmap to reach quantum degeneracy is the ramp of the horizontal beam depicted in Figure 5.9: within 5 s to 70%, 1.8 s to 50%, 1.1 s to 30%, 1.2 s to 20%, and 1.6 s to 10% which is just above condensation. In a final ramp, we finally pass the critical PSD of ∼1.2 and Bose-Einstein condensation occurs. This last ramp takes 250 ms and we additionally hold the trap at constant power for another 250 ms to let the system equilibrate before the atoms are released from the trap to take an absorption image.

Fig. 5.10 illustrates the evolution of the phase-space density during the whole prepa-

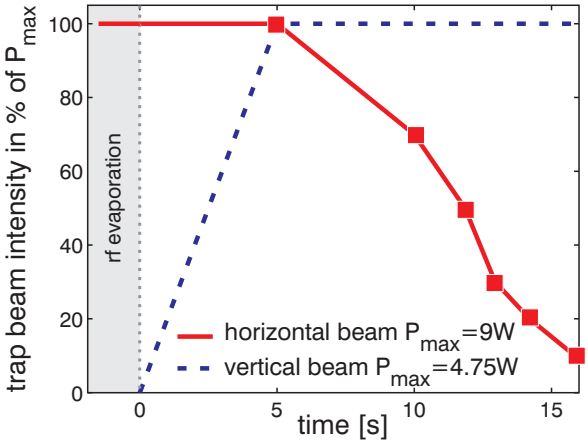

Figure 5.9: Optimised evaporation ramp of trap beam intensity. After switching off the magnetic trap, transferring the atoms to the lowest Zeeman state, the intensity of the vertical beam is ramped up to 100% during 5 s of plain evaporation in the horizontal beam. Subsequently the intensity of the horizontal beam is lowered in 5 steps to 10% of its maximum. About $1.7 \cdot 10^5$ atoms are left after this ramp and the temperature is 1.0 μK. One final ramp is needed to bring the sample from there to degeneracy.

ration cycle plotted vs. the number of atoms. Step (I) represents the magnetic trap after repumping the atoms to the ground state where we find $1.3 \cdot 10^8$ atoms at a PSD of $\sim 10^{-9}$. After Doppler cooling (step (II)), the same number of atoms is found but the PSD increases by two orders of magnitude to 10^{-7}. During rf-cooling, 2.5 orders of magnitude in the number of atoms are lost and we end up at step (III) with $\sim 5 \cdot 10^6$ atoms and a PSD of 10^{-5}. The transfer to the optical trap (step (IV)) increases the phase-space density by a factor of 5 after the magnetic trap has been ramped down while we lose about 60 % of the atoms. Right after step (IV), the atoms are transferred to the lowest Zeeman state and plain evaporation increases the PSD to 10^{-3} at step (V). Between step(IV) and (V), we ramp up the second beam of the crossed trap. The number of atoms at this point is $> 7.5 \cdot 10^5$.
From there on, evaporation is forced by ramping down the horizontal beam in 6 steps. The phase-space density and number of atoms after each of these evaporation steps are represented by (VI) to (XI). From step (VI) on, open circles represent the number of atoms trapped in the crossed region of the trap. Particularly during the first evaporation steps, a larger number of atoms are still trapped in the outer regions ("wings") of the first beam shown in the inset of Figure 5.10. During the evaporation process, atoms are permanently loaded from the wings into the crossed region, causing the number of atoms in this region to stay almost constant during steps (VI) to (IX). After stage (IX), finally all remaining atoms are in the crossed trap and the wings of the horizontal beam are empty. From there on we lose less than half of the atoms in steps (X) and (XI) until quantum degeneracy is reached at a remaining $\sim 6\%$ of the initial power corresponding

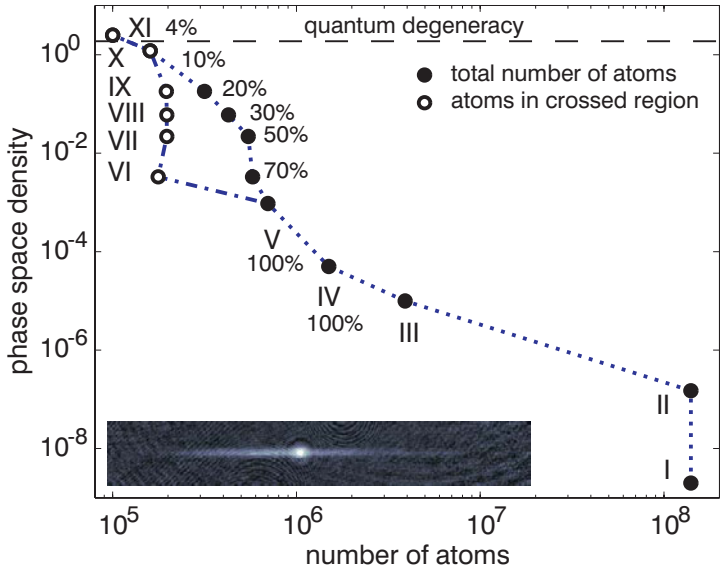

Figure 5.10: Evolution of phase-space density vs. number of atoms during the whole preparation process. After CLIP-loading (I). Doppler-cooling (II). RF-cooling (III). Transfer to the ODT (IV). Plain evaporation (V). Forced evaporation (VI) to (XI). From step (VI) on, filled circles represent the total number of atoms. Open circles represent only the atoms trapped in the steep potential in the crossed region. For steps (IV) to (XI), the power in the horizontal trapping beam in percent of the maximum power is also displayed. The inset shows a typical image of a cloud at 70% power in the horizontal beam. A large number of atoms are still located in the wings of the horizontal beam. Note that beginning from step (VI), the phase-space density always refers to the measured peak value in the *crossed region*.

to ∼600 mW.

The overall gain in phase-space density during the optical trapping period, starting at a PSD of $5 \cdot 10^{-5}$ with $1.5 \cdot 10^{6}$ atoms and ending at a PSD on the order of 1 with 10^{5} atoms, is more than 4 orders of magnitude, whereas we lose only 1.2 orders in the number of atoms. Thus the overall quotient of orders of PSD gain vs. orders of atom loss is > 3.6 – almost twice as large as in the magnetic trap. This suggests the use of higher laser power for the optical trap to form a deeper potential and therefore be able to reduce the time of rf-evaporation in the magnetic trap and transfer the atoms into the ODT already at an earlier stage.

6 Molecular dynamics simulation of the evaporation process

Abstract

To optimise the evaporation strategy and the trap geometry used for evaporative cooling, a theoretical model is needed to estimate the PSD gain and atom number loss during evaporation. The non-trivial trap potential and the complicated interplay between the atoms trapped in the crossed region and those roaming around in the wings of the single beams at very different densities and trap frequencies complicate such an analysis. A mathematical description of evaporation in a crossed dipole trap in a way similar to what was discussed in Chapter 5 has not been formulated yet. In this situation, where a theoretical model for the evolution of the thermodynamic quantities of the whole system is missing, the analytical approach has to be replaced by a microscopic description of the particle motion. A molecular dynamics simulation usually uses such a microscopic treatment of the motion and interaction of a relatively small number of particles. Except for the generation of starting conditions (and in the present case loss due to background collisions which is implemented as a random removal of particles), these simulations are completely deterministic by keeping track of all particle trajectories and using well defined laws to calculate their motion and interaction. The basic structure of a molecular dynamics simulation therefore consists of a linear approximation of the particle motion by calculating the momentary velocity, letting the system evolve on the single particle trajectories with constant velocity for a short time step, testing for collisions and computing the results, re-calculating the particle velocities, and so on.

The intention of simulating evaporative cooling in the crossed optical trap is obvious: the experimental effort to implement a new trap geometry in the real apparatus, and to test and compare the performance of the different setups is immense. However, it is of great interest to know the right strategy that should be chosen when the setup has to be changed. In our situation, the 20 W trapping laser was to be replaced by a device with 100 W output at the same wavelength. The concrete question is, where to

invest the extra power. Having four times more power in this beam, one could either increase the waist by a factor of two, producing a dimple with the same depth but twice the volume, or keep the volume constant and increase the depth by a factor of four. The argument of increasing the density by an adiabatic deformation, as discussed in Section 5.2.3, would suggest to make the dimple deeper to have the largest initial gain in phase-space density. In addition, the gain in spatial density would lead to high collision rates rates in the crossed region. However, not only is the density and phase space density of interest but so are the number of atoms that can be cooled to high phase space density. Additionally, it is clear that the density in the crossed region will become larger, the deeper the dimple is. Although there is at the moment no evidence for a large three-body loss constant, such loss could arise suddenly due to its n^3 dependence if the densities become larger than in the situations that have been studied up to now. It would therefore be a valuable result to have an estimation of the maximum densities that are expected in a certain setup.
Furthermore, it was also the question whether it would be possible at all to simulate a comparably large system of millions of atoms with such a small number of particles in the simulation that motivated me to write a molecular dynamics simulation.

6.1 Basic idea

Molecular dynamics (MD) simulations have one major drawback, namely the immense increase of computation time with increasing number of simulated particles. To test the system for collisions and to calculate the collision processes, one has to compare all particle coordinates with each other. That means the computation time grows quadratic with the number of particles[1]. For realistic system sizes, like in the case of our evaporation problem, the number of simulated particles would have to be on the order of millions, leading to extremely long computation times[2]. To circumvent this restriction, other groups have used Bird's method [129] which simulates atom motion by tracing the classical trajectories like in the MD method but uses a Monte-Carlo acceptance-rejection method for the collision by randomly selecting a pair of atoms which are close in space [3] and comparing a random number with the calculated probability that they will collide. The method has for instance been applied to the simulation of evaporative cooling of cesium [130, 131, 132] and the generation of a sodium BEC [133].

The approach that I use is a strict molecular dynamics simulation where a Monte-

[1] The time needed for collisionless simulations however only grows linearly with the number of particles.

[2] Using the program that will be discussed in this chapter and trying to simulate 2 million atoms, one simulation step which corresponds to 1 μs real time would take more than 12 hours.

[3] The whole space is divided into cells and only atoms living in the same cell can possibly collide.

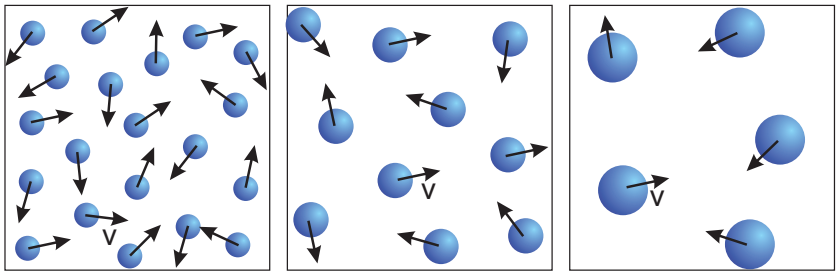

Figure 6.1: Three equivalent systems at equal temperature and mean velocity v. The particles all have the same mass. Left: 20 hard spheres with radius r_0; middle: 10 hard spheres with radius $\sqrt{2}r_0$; right: 5 hard spheres with radius $2r_0$.

Carlo step is only used to generate new particles in the system. The atoms are treated as classical hard spheres whose collision dynamics follows straight-forward classical rules of energy and momentum conservation. To keep the computation time on an acceptable level, the number of atoms that can be stimulated is restricted to a few hundred or thousand. On first sight, this seems to prevent one from simulating evaporative cooling of as many as one million or more atoms in a straight forward way. On the other hand, the discussion in Chapter 5 suggests that the only determinant factor for evaporative cooling is the elastic collision rate:

$$\gamma_{el} = n_0 \sigma_{el} \overline{v}_t.$$

If we intend to use a number N_s particles in the simulation instead of N_r particles in the real system, this means that the collision rate is reduced by N_s/N_r and the simulation will not be able to reproduce the real dynamics if all other parameters that describe the system (length and time units, cutoff energy, system volume, temperature, and trap frequencies), are identical to the real system. On the other hand, Eqn. (6.1) shows that it is possible to conform the elastic scattering rate in the simulation to the one in the real system by scaling the elastic scattering cross section. A multiplication of σ_{el} with N_r/N_s in the simulation increases the scattering rate to the value in the real one. In this case, the considerations made in Chapter 5 lead to the conclusion that the efficiency of evaporative cooling should be the same in both the simulated and the real system.
The classical cross section of colliding hard spheres is given by

$$\sigma_{el}^{cl} = 4\pi R^2,$$

where R is the radius of the sphere. The quantum mechanical scattering cross section in the s-wave regime is

$$\sigma_{el}^{qm} = \frac{8\pi a^2}{1 + k^2 a^2}$$

If we demand that within a certain time, a classical particle in the simulation undergoes the same number of collisions as a quantum mechanical atom in the real system, the

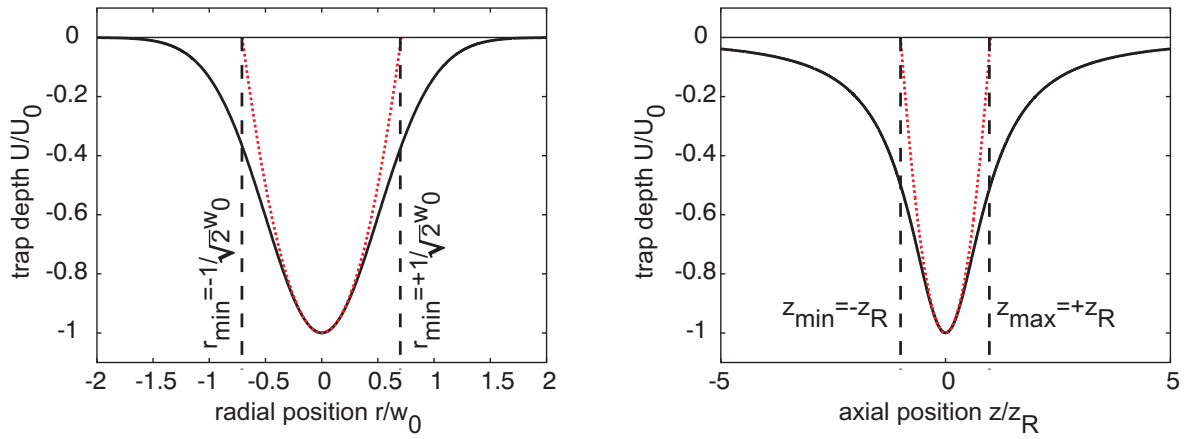

Figure 6.2: Harmonic approximation of the trapping potential in one beam. Black solid line: real potential; red dotted line: harmonic approximation. The horizontal line in both plots marks the zero energy level.

radius of the simulated particles has to be

$$R = \sqrt{2\frac{N_r}{N_s}\frac{a^2}{1+\frac{m^2a^2}{\hbar^2}v_r^2}},$$

where v_r is the relative velocity of the colliding atoms. This can be viewed as a simulation of macro-atoms, each of which represents $\alpha = N_r/N_s$ real atoms. This is illustrated in Figure 6.1 for three different numbers of atoms. The collision rate in all three systems would be the same. The macro-atom method has also been used in the previously mentioned Bird's-type simulations [130, 131, 132, 133].

In the following, I will describe the general functionality of the MD simulation without going too much into detail concerning programming and the concrete implementation. For a nice overview over MD methods and general physical simulation, see for example [134, 135].

The external potential in which the particles shall move is formed by two dipole trap beams plus gravity. Some simplifications were made to allow for easy handling of the external potential. Firstly, since we are not interested in rapid evaporation and systems far from equilibrium but rather in optimum evaporation where the ratio between trap depth and temperature is always large, the atoms will mainly be found in regions of the trap where the potential can be approximated by a harmonic oscillator as depicted in Figure 6.2. Second if we use this harmonic approximation, the acceleration at a position $\vec{r}$ is $a_i = P_1\omega_{1,i}^2 r_i + P_2\omega_{2,i}^2 r_i \quad (\ i = x, y, z\ )$ where P_1 and P_2 are the powers in W of the two trap lasers, respectively, and $\omega_{1,i}$ and $\omega_{2,i}$ are the trap frequencies at 1 W. In y-direction, gravity accelerates the atoms additionally. Finally, the energy cutoff is easily implemented with the harmonic approximation, since the approximated potential crosses zero energy at $z = \pm z_r$ in axial direction and $r = \pm 1/\sqrt{2}w_0$ in radial direction.

Thus, if $|z| > z_r$ of the horizontal beam, or $y > 1/\sqrt{2}w_0$ of the horizontal beam, or $x > 1/\sqrt{2}w_0$ of the vertical beam, the particle will be removed from the system. Usually, if one would discard a particle from the simulation without replacing it, the system would soon be empty. To keep the number of particles in the simulation constant, a new particle is generated every time when one is removed from the system. Since this changes the number of real atoms represented by one macro-atom in the simulation, the hard-sphere radius has to be adapted according to Eqn. (6.1) to keep the elastic scattering rate constant. The question that remains is which phase space coordinates such a new particle should get. Wu et al. [130] have used a duplication method where they wait until half of the atoms have been discarded from the system and then generate the same number of atoms by mirroring the existing particles. Every new particle is a "clone" of another particle in the system. They only differ by the sign of their phase space coordinates. In the simulation discussed here, a different approach was chosen. Since the number of simulated particles is only 200 to 400 (Wu et al. were using several thousand), copying one particle's coordinates and simply inverting them would possibly produce too strong correlations between the particles and could significantly influence the collision probability[4]. Therefore, the new phase space coordinates of the new particle that is born immediately after evaporating one particle are generated by a Monte-Carlo method. The idea was to assume that the system is close to equilibrium, and thus the coordinates can be generated with random numbers such that the probability of generating a particle with a certain set of coordinates $\vec{p}$ and $\vec{r}$ follows the Maxwell-Boltzmann distribution $f(E(\vec{r},\vec{p})) = \exp(-E(\vec{r},\vec{p})/k_BT)$ for the total energy that corresponds to these coordinates. It has to be mentioned that the largest deficiency of the whole method is directly related to this way of generating the particles. First, generating particles with the above method implies the assumption that the temperature T exists at all and second it is assumed that the properties of the whole system do not change with the creation of such a particle. The temperature of the system is determined by calculating the total energy of all particles and assuming that, according to the equipartition theorem,

$$T(\{\vec{p}_i,\vec{r}_i\}) = \frac{1}{3Nk_B}\left(\sum_{i=1}^{N}\frac{\vec{p}_i{}^2}{2m} + \sum_{i=1}^{N}U(\vec{r}_i)\right).$$

This restricts the method to systems close to equilibrium, where the above assumptions are fulfilled. The distribution of energies in the system was compared with the expected distribution in thermal equilibrium at different times during the evaporation. Figure 6.3 shows an example of such a comparison for the kinetic energy. The agreement is even

[4] Imagine for instance a particle with an orbital trajectory. If this particle would be "cloned" by just inverting the momentum $\vec{p}_{clone} = -\vec{p}_{original}$ and spatial coordinates $\vec{r}_{clone} = -\vec{r}_{original}$, they would simply circle on the same orbit with a 180 ° phase shift and not meet again before one of them is thrown out of its orbit by a collision with another particle.

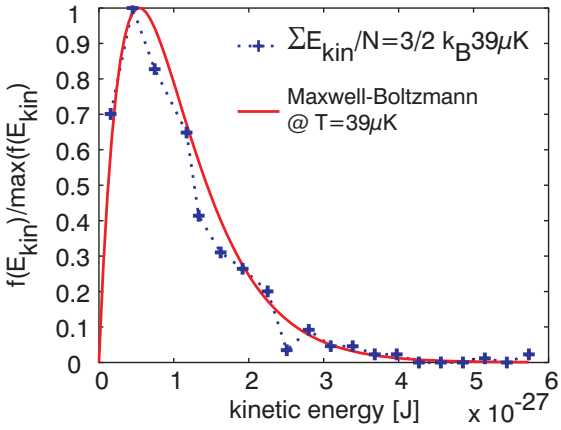

Figure 6.3: Blue dotted line and crosses: Example of a histogram of the kinetic energies found at an intermediate stage of the evaporation. The mean kinetic energy corresponded to $3/2k_B{\cdot}39\,\mu$K. Red solid line: Maxwell-Boltzmann distribution for a temperature of $39\,\mu$K. Both the histogram and the expected curve are measured relative to the maximum value of the distribution.

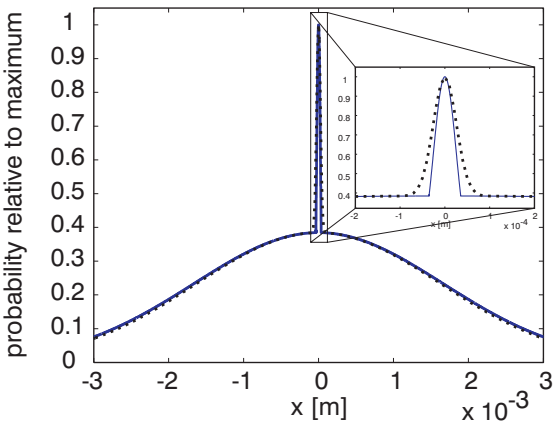

Figure 6.4: Comparison of the real spatial distribution in equilibrium (blue solid line) with the distribution generated by many random placements (black dotted line).

better when the potential energy is also considered. This leads to a better statistics since twice the number of degrees of freedom are considered in this way. In all cases where such a comparison was made, the assumed equilibrium distribution and the histogram closely agreed.

The problem is now to generate random coordinates which reproduce the Maxwell-Boltzmann distribution at temperature T. Random number generators always produce equally distributed numbers. One method to generate random numbers with a Gaussian normal distribution is the Box-Muller transformation method [136]. The distribution that we have to generate is even more complicated due to the dimple in the potential. The solution of this problem was to first decide whether an atom should be placed in the dimple region or in the wings. This is accomplished by comparing an equally distributed random number to the relative probability

$$p_{dimple} = \frac{1}{1+\xi} \text{ with } \xi = \frac{e^{-\frac{\widehat{U}_1}{k_B T}}}{-e^{-\frac{\widehat{U}_1+\widehat{U}_2}{k_B T}} - e^{-\frac{\widehat{U}_1}{k_B T}}};$$

of finding an atom in the dimple. Here $\widehat{U}_2$ is the trap depth of the dimple and $\widehat{U}_1$ is the depth of the single beam trap. If the random number is larger than p_{dimple}, the atom will be placed in the wings, otherwise in the dimple. Once we have decided in which potential the atom will be placed, the generation of adequate coordinates is simple. One

has to calculate the variance of the thermal Gaussian in the respective potential and generate normal distributed random numbers with the same variance. In Figure 6.4, the real thermal distribution is compared with the distribution resulting from many such random placements. Only a small difference is visible at the border between the dimple and the wings.
The algorithm used to integrate Newton's equations of motion is the "Leap frog algorithm" [137]. After an initial configuration is generated, the system propagates as follows

- The system time is increased by one time-step Δt that is adapted to the largest speed in the system, such that within one time step, two particles can not penetrate each other by more than 1% of their radius. The maximum time step is $1\,\mu$s.
- If one of the coordinates of a particle is larger than the previously discussed limits, it is evaporated, N_r/N_s is adapted, the total energy (i.e. the quasi temperature) is calculated, and a new particle is generated randomly. If the newly generated atom would overlap with another one in the system, the procedure is repeated until the atom sits at a position where it is not in direct contact with another atom.
- Background loss is incorporated by removing atoms randomly from the trap with a probability that fits with the experimentally observed lifetime of the trapped sample.
- The speeds of all particles are updated to $\vec{v}_i(t) = \vec{v}_i(t - \Delta t) + \vec{a}_i(t - \Delta t)\Delta t$.
- The particle positions are updated to $\vec{r}_i(t) = \vec{r}_i(t - \Delta t) + \vec{v}_i(t)\Delta t$.
- The system is checked for collisions by calculating the distances $\delta\vec{r}_{i,j} = \vec{r}_i - \vec{r}_j$ for all pairs i, j of atoms. If $|\delta\vec{r}_{i,j}| < N_r/N_s a$, where a is the scattering length in the unitarity limit, the relative velocity $\delta\vec{v}_{i,j} = \vec{v}_i - \vec{v}_j$ is calculated and the inter-particle distance is compared to the velocity dependent scattering length from Eqn. (6.1). If the distance is smaller than this number, the new velocities are calculated using simple hard-sphere collision mechanics with total momentum and energy conservation. Furthermore, the atoms are moved radially outwards such that they just touch and do not penetrate each other anymore. Otherwise a collision of the same two particles would be detected in the next simulation step again.
- If the external potentials are time dependent, they are now set to the new values according to the given time-dependence.
- The acceleration $\vec{a}_i(t)$ are calculated depending on the position of a particle.
- After a certain number of simulation steps, the total energy, total kinetic energy,

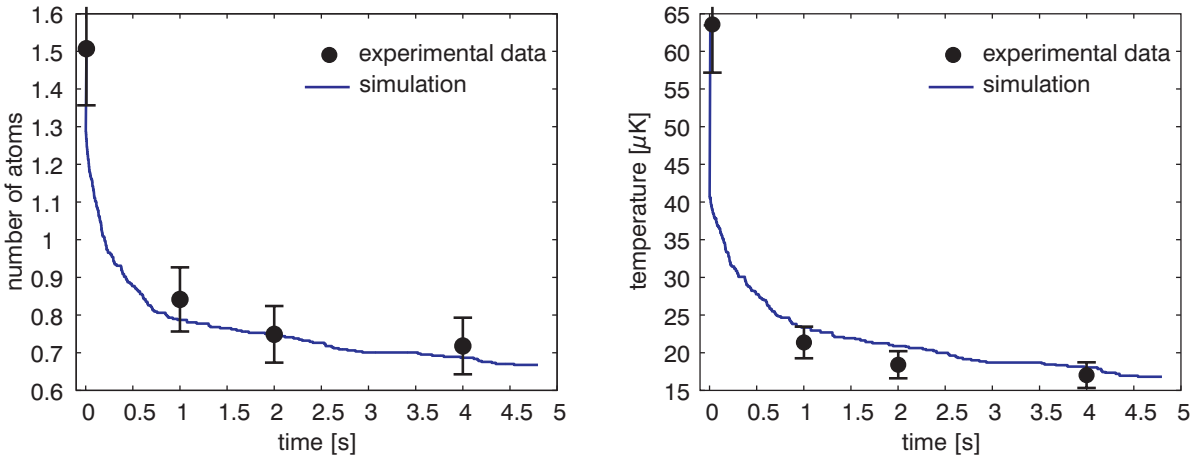

Figure 6.5: Comparison of experimental results (black circles) and simulation (blue line) of the plain evaporation stage in the single beam trap. The simulation was performed using 250 particles. Error bars on the experimental data are estimated ±10% deviations of the temperature and the number of atoms (compare Section 7.2).

total potential energy, the numbers of atoms in the dimple and the whole trap, the trap parameters and the system time, and optionally all phase space coordinates of the atoms are written to file.

- The whole procedure is repeated.

The data output is analysed by external Matlab programs, either by generating $2D$ histograms of the particle coordinates and using gaussian fits to determine the temperature, density distribution and phase space density or by extracting these numbers from the temperature, number of atoms and the trap parameters which are exactly known. To get rid of fluctuations due to the small number of simulated particles, these numbers are averaged over some tens of milliseconds by a moving average over the data output. A simulation of the full evaporation ramp takes about 4 hours on a standard PC[5].

6.2 Comparison with experimental data

To prove that it is possible to simulate the evolution of a sample of $1.5 \cdot 10^6$ atoms using only a few hundred particles in the simulation, an initial configuration was created that corresponds to the situation found in the single beam trap directly after pumping the atoms to $m_J = -3$ (compare Chapter 5.2.1). The evolution of the trapped cloud was simulated for 5 s at constant power in the horizontal beam and without the vertical beam. Figure 6.5 shows a comparison of the simulation results with the experimentally

[5] Intel Pentium IV, 3GHz, 2GB RAM, Linux

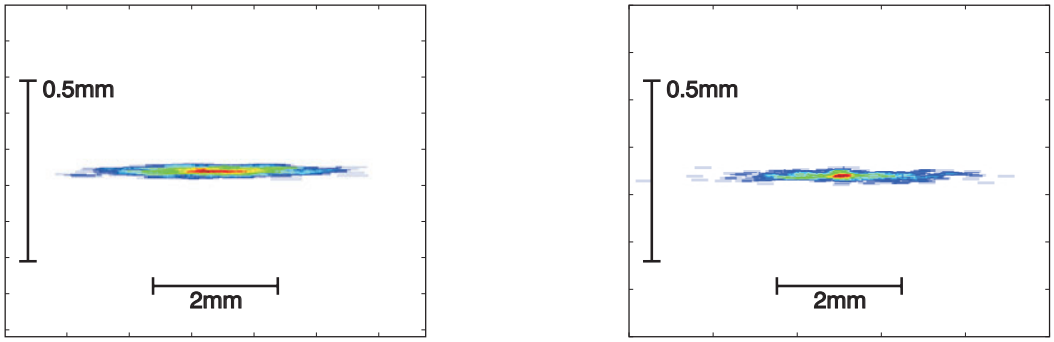

Figure 6.6: Snapshots of the density distribution in the simulation. Left figure: Initial distribution in the single beam trap. Right figure: Distribution with about 60% power in the horizontal beam. The black bars give the real length scale in the figure.

measured time dependence of the number of atoms and the temperature.

The next step is to simulate the whole plain and forced evaporation with exactly the time dependent potentials as in the experimental procedure (see Fig. 5.9). Two snapshots of the spatial distribution of the particles at the beginning of the plain evaporation and at one intermediate time are represented in Figure 6.6 in the form of 2-dimensional histograms of the y- and z- spatial coordinates.

The result of a simulation using only 200 particles is compared to the experimental findings in Fig. 6.7. The experimental data is the same as in Fig. 5.10 and error bars correspond to a 20 % uncertainty in the number of atoms. As for plain evaporation, the simulation agrees very well with the experimental data. The number of atoms at the end of the ramp deviates only by 15% and the phase space density found at the end of the simulation is 50% smaller than in the experiment. This is a small difference, having in mind that we simulate the evolution of the phase space density over four orders of magnitude. Moreover, the starting conditions in the experimental runs, where the evaporative cooling in the crossed trap was studied, were probably better with regard to the initial number of atoms[6]. The larger difference between the experimental data and the simulation in the earlier data points between 70% and 30% power in the horizontal beam is probably caused by the different methods of counting the number of atoms in the simulation and the experiment. The number of atoms in the dimple is not easy to measure experimentally if the number of atoms in the wings of the horizontal beam is still larger. In such a situation, the distribution of the atoms in the dimple sits on top of a large background produced by the atoms in the wings along the z-axis whereas in the y-direction the offset is essentially 0. Our standard 2-D fit of time of flight images does not deliver reliable numbers in this case. On the other hand, in the simulation the number of atoms can simply be determined by deciding whether an atom has to be

[6] These measurements were performed a few months after the plain evaporation had been studied and the whole experimental setup was already more optimised.

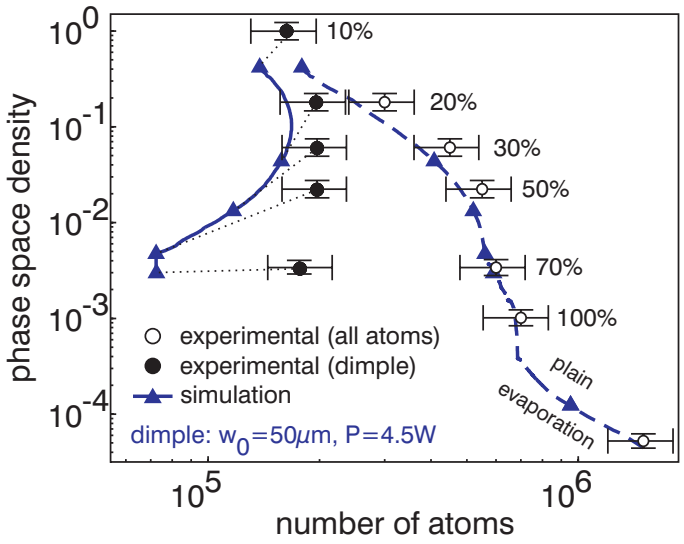

Figure 6.7: Comparison of a simulation of the full evaporation ramp using 200 particles with experimental data. Dashed/solid line: PSD vs. total number of atoms in simulation and vs. number of atoms in the crossed region only, respectively. Full/open circles: corresponding experimental results. Numbers: remaining power in the horizontal beam. Triangles: phase space density after the evaporation steps in the simulation. Dotted lines link them with the corresponding experimental data.

counted or not on the basis of its spatial coordinate.

6.3 Simulation with different parameters

6.3.1 Comparison of phase space densities

Since the simulation agrees well with the experimental data, it is expected to give realistic results also for other traps. The concrete task is finding a strategy for the implementation of the 100 W laser. In a first set of simulation runs, the performance of the evaporation ramp was simulated with a waist of 86 μm because this waist has already been used in an earlier setup. The required extra telescope in the beam path of the vertical beam is already prepared and could be easily reactivated by inserting lenses in posts which are already mounted at the correct positions. Three simulations were carried out with two different maximum powers in the vertical beam and the time dependent potential of the experimental ramp. First with 4.5 W laser power in the vertical beam like in the previous run and second with 13.3 W which produces a dimple with the same depth as with 4.5 W and 50 μm waist. In a third run I finally simulated evaporation with 13.3 W and 50 μm where the extra power was used to increase the

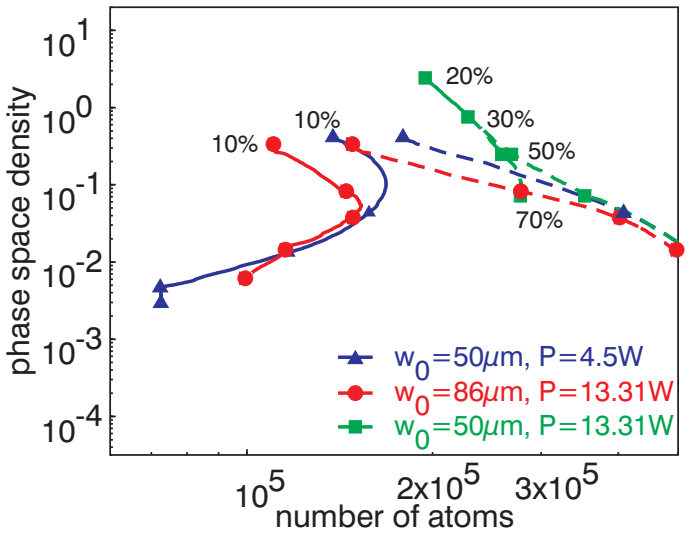

Figure 6.8: Comparison of the efficiencies of three different combinations of laser powers and waists of the vertical (dimple) beam.

depth and frequencies but not the volume. The results of these simulations are shown in Figure 6.8. This shows clearly that evaporation in the 86 μm configuration works less efficient (less atoms in the end at a smaller final phase space density) than in our experimental setup whereas evaporation in the deeper trap with 13 W laser power and a waist of 50 μm leads to a higher final phase space density. Moreover this phase space density is reached with a larger number of remaining atoms.

As already mentioned, the trap depth scales linearly with the power and inversely quadratic with the waist whereas the frequencies scale with the square-root of the power and inversely with the waist. The trap frequencies produced by the vertical beam in the second simulation are therefore smaller than in the experiment although the depth is the same. Hence finding a less efficient evaporation in the 86 μm setup with the same ramp could also be due to the wrong evaporation ramp because it is optimised for the larger collision rate in the 50 μm waist trap. To check this the ramp was also simulated with a different time dependence. Strictly speaking, the ramp would have to be optimised for this geometry first to be able to make a full quantitative comparison of the evaporation performances, which could in principle be done with the simulation. However, we are mainly interested in a qualitative trend and it is therefore sufficient to estimate the change of the collision rate to adapt the slope of the evaporation ramps. The main contribution to the trapping frequencies in the x- and y-direction stems from the horizontal beam. The only frequency that is mainly affected by the vertical beam is the frequency on the z-axis. At the same trap depth, the frequency in the 86 μm configuration is a factor $50/86 \approx 1/1.7$ smaller than with 50 μm, i.e. the volume of the trap is smaller by the same factor, too. Assuming that the density changes approximately

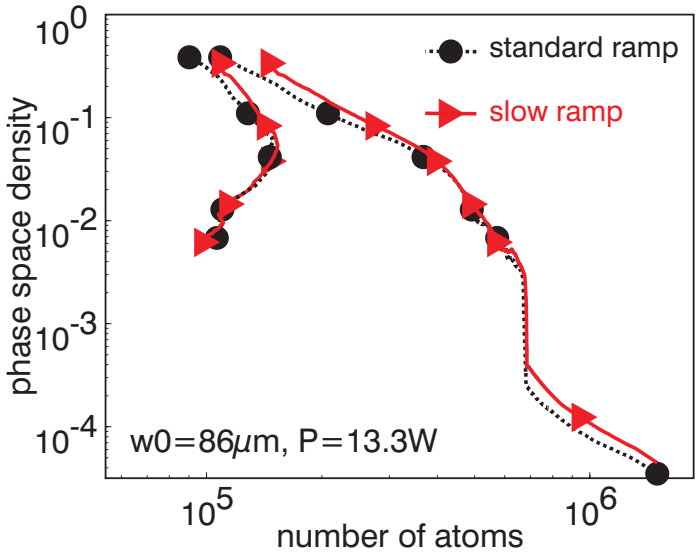

Figure 6.9: Comparison of the efficiencies of two different speeds of the evaporation ramp in a dimple with 86 μm waist and 13.3 W power. One ramp uses the "standard" time dependence that was optimised experimentally for a dimple with 50 μm waist and 4.5 W laser power. The other evaporation ramp at half speed to compensate for the smaller collision rate. Obviously, the slower ramp thus not significantly improve the effectiveness of evaporative cooling.

proportional to the trap volume, the times for all ramps in that run were doubled. Since the background collision limited lifetime is relatively long compared to the ramps, the optimum should be close to that. If a general trend in the dependence on the ramp speed would be observed, the simulation could be repeated with yet another time dependence. Figure 6.9 shows a comparison of the simulation with 50 μm and 4.5 W and 86 μm and 13.3 W with the slower ramp. Remarkably, the two ramps produce nearly the same final results, as well as a similar evolution during the ramp. The use of three times more power did not improve the evaporation efficiency in both cases compared to our experimental setup. One can therefore clearly argue that the best way of investing extra laser power is to increase the trap depth instead of the volume.

6.3.2 Comparison of spatial densities

However, one problem in interpreting this result is that no loss mechanisms other than background gas collisions are incorporated in the simulation, mainly because there is no experimental hint that would suggest the use of a certain value for the three-body loss rate. This could give rise to deviations between the simulation and the real system if the densities that occur during the ramp would be much higher than the density ranges that have been explored experimentally because three-body loss increases very fast with growing density. A comparison of the maximum densities in the different simulations

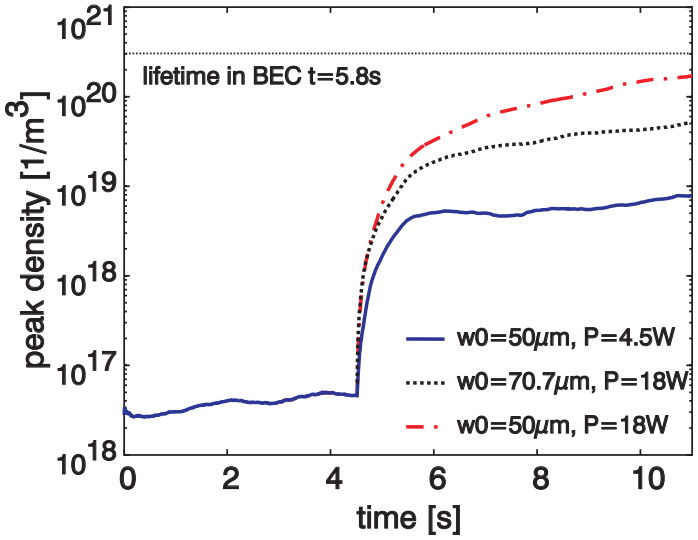

Figure 6.10: Evolution of the spatial density in three different combinations of waist and laser power in the dimple beam. The horizontal dotted line marks the maximum density that has been observed in a chromium BEC. The measured lifetime of the condensate at that density was 5.8 s.

gives an estimation of whether density dependent loss will play a roll in the case of a deeper dimple. The evolution of the spatial density for evaporative cooling in three different traps is displayed in Figure 6.10. The first one is the usual 50 μm,4.5 W trap. The second is a trap twice as deep but with a $\sqrt{2}$ larger waist of 70.7 μm at 18 W. The third one with a waist of 50 μm and a laser power of 18 W produces the largest number of atoms and phase space density at the end and was another factor of 1.4 deeper than the 50 μm, 13.3 W trap considered before. This ramp resulted in 210000 atoms in the dimple when a phase space density of 1 was reached after 7 s of forced evaporation. Figure 6.10 shows that even in this trap, the maximum density stays below 10^{20} 1/m^3 most of the time, i.e. a factor of 2.5 smaller than the maximum density observed in a chromium condensate where a lifetime of 5.8 s was found (discussed later in Chapter 7). Although this lifetime was probably not limited by three-body loss, let us assume such a limit in a conservative approximation. Since these losses would depend on n^3, the three-body loss rate would be more than 10 times smaller than that. Even taking into account the sixfold suppression of three body recombination in a BEC [138, 139] compared to thermal clouds, one can expect a three-body limited lifetime of around 10 s also in the deep trap. This is not expected to be a limiting factor for an efficient evaporation. Moreover, we have not taken into account so far that the evaporation in this steep trap can be much faster due to a higher collision rate. The collision rate increases proportional to the density in the dimple which is almost two orders of magnitude larger in the deep dimple than in the standard configuration, theoretically allowing the evaporation to happen 100

times faster. Hence the lifetime relative to the time needed for evaporative cooling is even increased in the deep trap. Another possibility to circumvent potential three-body loss is to make use of the deep dimple in the beginning of the evaporation ramp to load as many atoms as possible into the crossed region and lowering the depth of the dimple gradually during evaporation to keep the density on a constant, acceptable level.

6.4 Conclusions

The molecular dynamics simulation that has been presented in this chapter has proven to give results that agree very well with experimental studies of evaporative cooling in the crossed dipole trap. It provides a fast possibility to try evaporation under different conditions. The simulation has been used to find a strategy on how to take advantage of the enhanced laser power that is now available in our lab. It was found that the best strategy is to invest the power to generate a deeper dimple instead of increasing its volume. The simulation also showed that one can expect a four times larger number of atoms in the condensate when the dimple is made a factor of four deeper. The maximum density that occurs in this configuration is lower than densities that have been observed experimentally and which showed no evidence of density dependent loss.
Some improvements of the program could however increase its consistence when very dense clouds are simulated. Loss processes other than loss due to background collisions are not implemented in the simulation yet. Therefore the results of simulations at much higher densities than those found in the experiments that have been performed so far would be questionable. Once the three body loss constant is known, such losses could be implemented in the simulation by introducing a local, density dependent loss. This would require a routine which is able to determine the density distribution at any time within the simulation program. Such a routine is not implemented up to now. Furthermore, to be able to also simulate situations which are further away from thermal equilibrium, like a continuously loaded trap or rapid cooling, it would be necessary to change the method that is used to generate particles in the system. One solution might be the cloning method used by Wu and Ma [130, 131]. But due to the small number of atoms in the simulation, one should first analyse the consequences on the probability of collisions among the atoms before employing the method.
Additionally valuable insight into the transfer from the magnetic to the optical trap could be gained by simulating this situation with different depths and frequencies of the optical potential. This would require dipolar relaxation to be implemented in the program.

7 Bose-Einstein condensation of chromium atoms

Abstract

This chapter documents the first experimental realisation of a Bose-Einstein condensate of chromium atoms. By comparing the shape of the momentum distribution and the expansion dynamics qualitatively with the predictions for a degenerate Bose gas (see Chapter 1), it is proven that the gas has indeed undergone the phase transition. Cuts through the density distribution and corresponding fits to the data under different conditions show that the system is well described by the functions used to determine the thermodynamic quantities under all these conditions. A quantitative analysis of the dependence of the condensate fraction on the reduced temperature is presented. It is compared to theoretical predictions (compare Section 1.4.3) and used to calibrate the atom number determination in the experiment. The basic results presented in this chapter have been published in [1] and [47].

7.1 Reaching degeneracy

When the trap depth is lowered in one final evaporation ramp to a value below 6% of the maximum, Bose-Einstein condensation of chromium atoms is observed at a temperature of 450 nK by the appearance of a narrow peak (compare Section 1.4.1) in the center of the density distribution gained from time of flight images taken 4 ms after the sudden switch-off of the two trapping lasers. Shortly before the peak appears, the closeness to degeneracy announces itself by a deviation of the momentum distribution from the ideal gas limit. As has been discussed in Section 3.3.1, the proper distribution function to describe a Bose gas is the Bose-Einstein integral. Only at temperatures far above T_c, this distribution is well approximated by the Maxwell-Boltzmann distribution, such that a Gaussian is suited to fit the density profile in an absorption image in this case. Close to T_c, the Gaussian and Bose fits on the wings of the density distribution start to differ. This effect is illustrated in Figure 7.1. The first column shows 3-dimensional

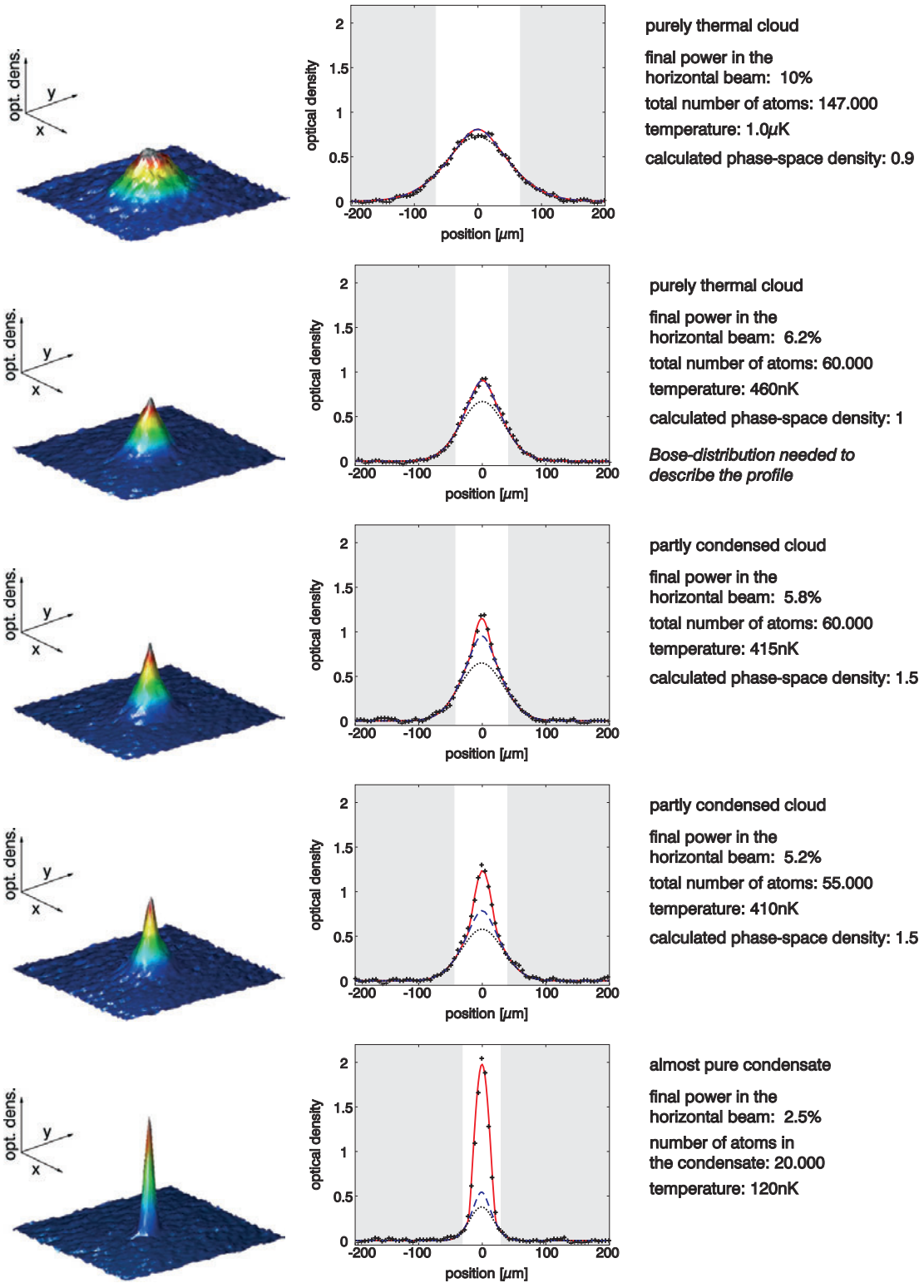

Figure 7.1: Density profiles of clouds obtained from absorption images that have been taken after 4 ms of free expansion. Dotted black lines: results of a Gaussian fit to the wings of the thermal cloud; dashed blue lines: fits of the g_2-function to the wings in the grey shaded area; solid red lines: fits of a g_2 plus Thomas-Fermi distribution to the complete profile.

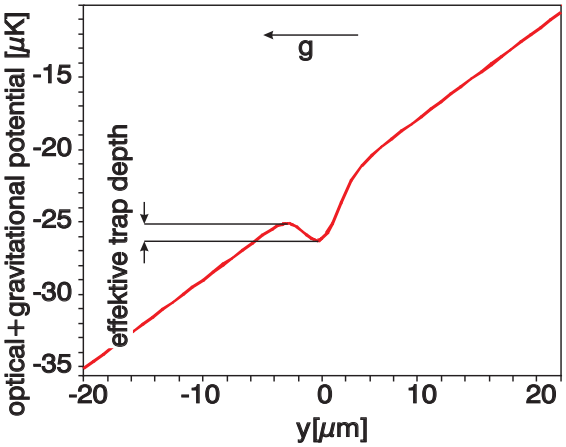

Figure 7.2: Trap potential in the vertical y direction at the final 2.5 % of the maximum power in the horizontal beam. Gravity g adds an additional gradient in y direction to the trap potential which lowers the effective depth of the trap.

representations of the density distributions obtained from images taken after different final powers of the last evaporation ramp. In these 3-D diagrams, dense regions are represented by large values on the vertical axis. The x- and y- directions correspond to the position on CCD chip. Cuts through the density profiles obtained from cuts through the center of mass of the distribution along one axis are displayed in the second column together with the Gaussian-, Bose-, and Thomas-Fermi-fits to the distributions. The third column contains some important data obtained from these fits. The profile in the first row is well represented by a Gaussian (Eqn. (3.3.1)), whereas the one in the second row is clearly non-Gaussian although it is still not in the degenerate regime. In this case, Eqn. (3.3.1), represented by the red line, has to be used to describe the distribution properly. In the center, where the distribution is affected most by the Bose enhancement, the Gaussian fit represented by the black line deviates significantly from the measured density profile. Beginning from the third row, corresponding to 5.8 % of the maximum trap depth, the density profile shows a Bose-Einstein condensate in the center. When the trap depth is reduced further, this central peak grows on cost of a diminishing number of atoms in the surrounding thermal cloud. The last row shows the profile of a nearly pure Bose-Einstein condensate at a very low final power of 2.5% of the maximum corresponding to 230 mW. Gravity adds a potential gradient in vertical direction and 'tilts' the trapping potential as depicted in Fig. 7.2. Therefore the trap depth in this situation is less than 2 μK. The temperature of the remaining thermal atoms has been measured 120 nK which is the lowest temperature ever observed in a sample of chromium atoms.

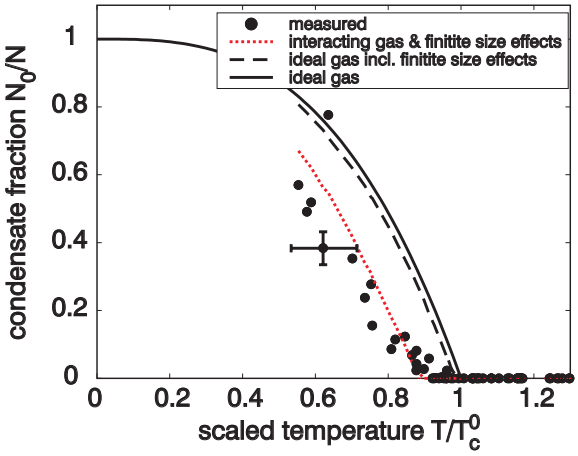

Figure 7.3: Condensate fraction (N_0/N) dependence on scaled temperature (T/T_c^0). Black circles represent the measured data. The red dotted line represents the predicted fraction, approximated by $\frac{N}{N_0} = 1 - \left(\frac{T}{T_c}\right)^3$ where $T_c = T_c^0 + \delta T_c^{int} + \delta T_c^{fs}$. $\delta T_c^{fs} = -0.73 \frac{\overline{\omega}}{\omega_{ho}} N^{-1/3} T_c^0$ is a shift in the critical temperature due to the finite number of atoms and $\delta T_c^{int} = -1.33 \frac{a}{a_{ho}} N^{1/6} T_c^0$ takes into account the contact interaction (Eqn. (1.4.3)). Here $a = 103\ a_0$ is the chromium scattering length [19] at 10 G (Compare Appendix B), a_{ho} is the harmonic oscillator length, T is the temperature of the thermal cloud, ω_{ho} is the geometric and $\overline{\omega}$ the arithmetic mean of the trap frequencies. The dashed line is for an ideal gas but takes into account the finite number of atoms. The solid line shows the dependence for the ideal gas. The error-bars are representative for all data points. They are due to a uncertainty in the number of atom determination which affects both the calculated critical temperature and partly the condensate fraction and in the determination of the temperature. For the condensate fraction, the uncertainty of the total number of atoms (such as a detuning of the probe laser) does not contribute but only the error in the weighting between the two fractions.

7.2 Analysing the BEC transition

To analyse the dependence of the condensate fraction on the system temperature, the trap depth was lowered in subsequent experiments from 10 % to 2.1 % in a series of consecutive experiments. Absorption images were taken after a relaxation time of 250 ms in the final trap and a time of flight of 4 ms. The temperature was determined from the width of a 2-dimensional gaussian to the outer wings of the thermal cloud (see Section 3.3.1) and the number of atoms in the thermal and the condensed part was determined from 2-dimensional fits of Eqns. (3.1) and (3.3.1) to the density profiles. In an optical dipole trap, the trap parameters vary together with the depth of the trap and lead to a dependence of T_c on the final trap depth. To eliminate this dependence, the measured temperature was re-scaled to the corresponding prediction for the transition temperature T_c^0 of an ideal gas which was calculated from the measured number of

atoms and the trap parameters using Eqn. (1.16). This re-scaled temperature, the trap parameters, and the total number of atoms from the fits were used to calculate the expected condensate fraction under consideration of the finite size of the system (Eqn. (1.4.2)) and contact interaction among the atoms (Eqn. (1.4.3)) for every data point. A comparison of the T/T_c dependence of the measured condensate fraction with this prediction showed a systematic $\sim$5 % shift of the measured dependence to higher temperatures. The trapping parameters have been determined with remarkable precision (see Chapter 4.6), the calibration of the imaging system was cross-checked to exclude errors in the measurement of sizes, and timing errors are also expected to be orders of magnitude below the 4 ms of time of flight. Therefore the determination of the number of atoms was supposed to be the most likely source for this systematic deviation. Right at the critical temperature, equation (1.4.3) can be used to calculate the total number of atoms by setting N_0 to zero and inserting the measured temperature in the equation

$$N_{tot} = N_T = \frac{T^3 \zeta(3) {k_B}^3}{{\omega_{ho}}^3 \hbar^3}. \tag{7.1}$$

To calibrate the number determination with this method, an image was chosen, where no condensate was visible yet but which was just above T_c. It turned out that a correction factor of 1.16 had to be applied to correct the number of atoms obtained from the image such that it fulfills Eqn. (7.1). If the imaging light is assumed to be detuned from resonance by 0.20Γ =1 MHz, the measured number of atoms is increased by the 16 % according to Eqn. (3.1). The assumption of a deviation of the laser detuning from $\delta_L = 0$ on this order is reasonable since the width of the error signal for the 426 nm light stabilisation is about 40 MHz (corresponding to 8 times the linewidth). A 0.20Γ detuning therefore corresponds to a shift of the lock point by only 1/40 of the signal amplitude. Additionally, the spectroscopy signal is subject to a long term drift with respect to the resonance in the chamber due to changes of the magnetic fields at the position of the chamber and the position of the spectroscopy cell. With this calibration of the atom number determination, the measured dependence of the condensate fraction on the scaled temperature agrees with the prediction for an interacting Bose-gas given by Eqn. (1.4.3) within errors as depicted in Figure 7.3. However, the experimental data seems to lie systematically slightly below the theoretical prediction. Since this kind of measurement is obviously very sensitive to a correct determination of the number of atoms, this deviation could still be due to an error in the atom number. An interpretation is therefore not possible.

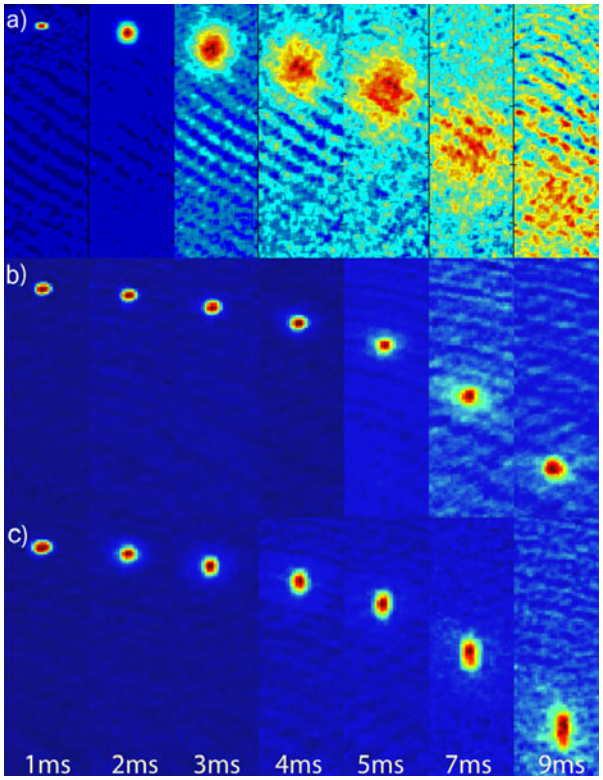

Figure 7.4: Three series of absorption images of expanding clouds taken after 1..9 ms time of flight. a) Thermal cloud just above T_c b) Condensate released from an *almost* spherical trap. c) Clearly anisotropic expansion after release from a trap with an aspect ratio of 1 : 4.8

7.3 Expansion of the condensate

A further clear signature of Bose-Einstein condensation is the anisotropy of the expansion in time of flight [1] when the sample is released from an anisotropic trapping potential as has been discussed in Section 1.5. To study this effect, we prepared condensates in traps with different anisotropy. Figure 7.4 shows typical series of time of flight images taken after 1 ms to 9 ms of free expansion. The upper row a) shows images of a thermal cloud just above condensation and b) shows a condensate which was released from a trap with a power of 240 mW in the horizontal beam. The trap frequencies on the visible axes are f_z=144 Hz and f_y=222 Hz, resulting in a relatively small anisotropy of f_y/f_z =1.5 , reflected in an almost isotropic expansion of the condensate. For the set of images in the second row, the condensate was prepared in the same trap, but before releasing the

[1] An anisotropy in the expansion of thermal clouds has also been predicted by Kagan et al. [140] and observed experimentally by Shvarchuck et al. [141] in a thermal gas of ^{87}Rb. However, this only happens in the hydrodynamic regime, where the mean free path is much smaller than the extension of the cloud and the collision rate is much higher than the trap frequencies which is not the case in the experiments presented here.

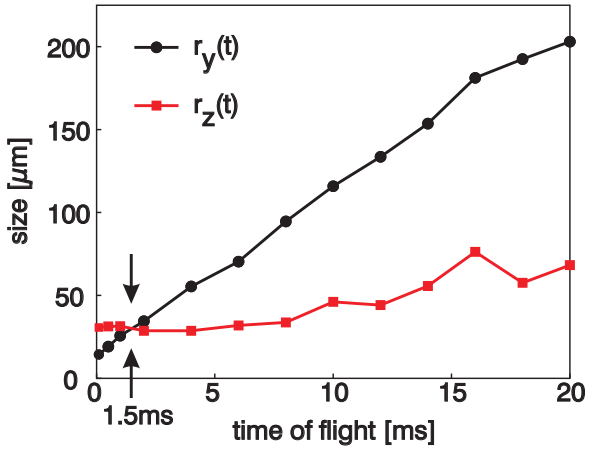

Figure 7.5: Dependence of the condensate size on the expansion time. The recorded quantities r_y and r_z are the radial extensions of the BEC in vertical and horizontal direction, respectively. Initially, the condensate is elongated in horizontal direction ($r_z > r_y$). After 1.5 ms time of flight, the aspect ratio is one. For larger times, the aspect ratio is inverted.

atoms, the laser power was adiabatically increased to 2.3 W within 250 ms. The frequencies are f_z=144 Hz and f_y=689 Hz corresponding to an aspect ratio of f_y/f_z =4.8 . As expected, the condensate expands faster on the vertical y-axis in which it was confined more before the trap was switched off. This leads to the typical change of the aspect ratio.

Figure 7.5 shows the widths in the two visible directions plotted versus the expansion time. At $t \approx$1.5 ms, the radii r_y and r_z are equal (the aspect ratio of the condensate is 1) and for longer expansion times, the condensate is elongated in vertical direction.

7.4 Lifetime of the condensate

The lifetime of the Bose-Einstein condensate in the trap is of special interest, since only if this state is stable for a sufficient time, can one hope to have enough time for experiments.[2] Changes of the trap parameters, of the external magnetic fields, and transfer of the condensate into an optical lattice in future experiments, have to be performed adiabatically to prevent unwanted excitations or even destruction of the condensate. The relevant timescale is the trap frequency which is on the order of 100 Hz in the trap where the evaporation ends. Thus, manipulations like the ones mentioned above take

[2] Studying the density dependence of the condensate lifetime is also of scientific interest, since the 2-body and 3-body loss coefficients K_2 and K_3 that one gains from analysing the decay are closely related to the correlations between the particles [139]. Such an analysis was however not the intend of the measurement presented here.

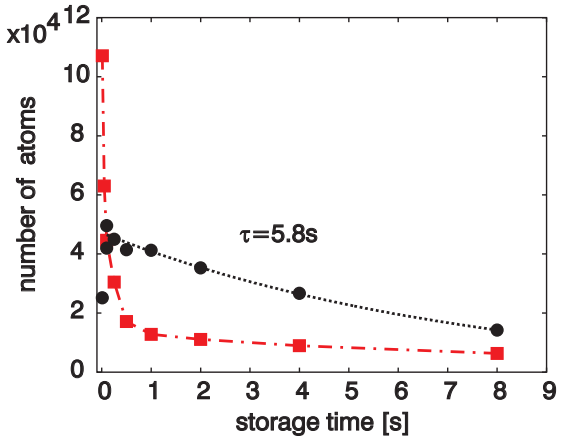

Figure 7.6: Number of atoms in the condensed phase (black circles) and the thermal cloud (red squares) vs. time in a 3.3 μK deep trap at 3 %=0.28 W laser power. The dotted line is a fit of an exponential decay to the data beginning at 100 ms and yields τ =5.8 s.

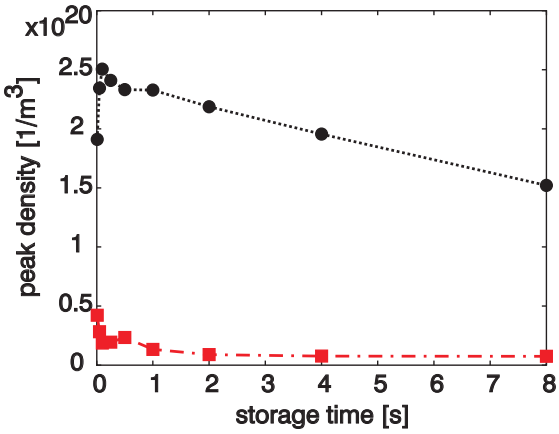

Figure 7.7: Density of the condensate (black circles) and thermal cloud (red squares) in the same trap.

several milliseconds. For the detection of the dipolar interaction between the atoms (see Chapter 8), the trap had to be compressed to generate an anisotropic potential and the magnetic field had to be rotated by 90 ° during the lifetime. In this trap, the spatial peak density of the condensate reaches values of $\widehat{n}_c \approx 5 \times 10^{20}\,1/\mathrm{m}^3$. A three-body loss constant larger than the $K_3^c = 5.8 \cdot 10^{-42}\mathrm{m}^6/\mathrm{s}$ measured in condensates of Rb^{87} in $|\,F=1, m_F=1\,\rangle$ [139] and $K_3^c = 1.8 \cdot 10^{-41}\mathrm{m}^6/\mathrm{s}$ in $|\,F=2, m_F=2\,\rangle$ [139, 142] would limit the condensate lifetime in this regime to much less then a second and possibly limit the experimental possibilities. Additionally, heating rates in the stored sample can be different at different trap parameters due to noise induced parametric heating [143] and limit the lifetime at certain parameters. Therefore, we have measured the condensate lifetime under two conditions to have a rough estimate of these limits.

The first measurement was carried out under the conditions found after the final evaporation ramp. Figures 7.6 and 7.7 show the dependence of the condensate and thermal atom number and density on the storage time in the trap, directly after the end of the evaporation ramp. The 250 ms holding time after the ramp, that is usually given to the cloud to equilibrate, is also contained in the data. Within the first 100 ms, the condensate fraction is still growing and reaches its maximum at t =100 ms. This growth of the condensate and the initial decay of the thermal atom number can be better viewed in Figure 7.8 where the number of atoms in the BEC as well as the number of thermal atoms and the total number are plotted vs. a logarithmic timescale. Up to the time 500 ms after the end of the evaporation ramp, the thermal atom number drops rapidly while the condensate is growing. This is a hint that the system has not equilibrated

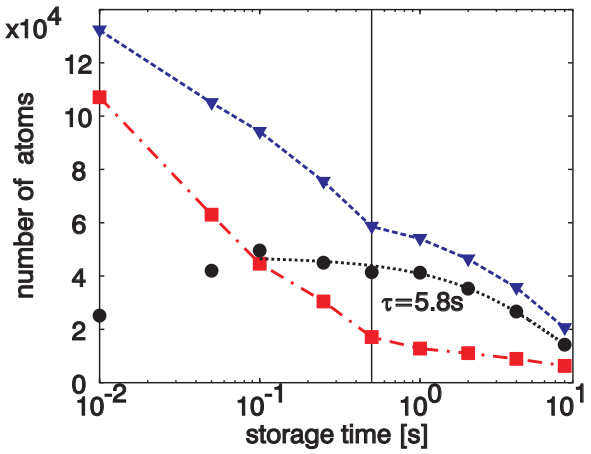

Figure 7.8: Number of atoms in the condensate (black circles), in the thermal cloud (red squares) and the total atom number (blue triangles) plotted vs. logarithmic time. Lines connecting the thermal and total number data are guides to the eye. The solid line is the fit result for one-body loss.

yet and evaporation is still going on. Such a supposition is encouraged by the fact that within the same time, the temperature of the cloud drops from 400 nK to 170 nK. Assuming only one-body loss which is justified by the decay of the condensate number of atoms showing an apparently pure exponential behaviour, the lifetime of the condensate has been determined. Fitting an exponential decay according to $dN/dt = -\gamma N(t)$ to the data, beginning at 100 ms where the condensate atom number is maximum, yields a lifetime of τ =5.8 s or $\gamma = 1/\tau$=0.17 $\cdot$1/s in the shallow trap which is a convenient time scale for experiments to be performed with the condensate.
The reason why the lifetime of the condensate is substantially smaller than that of the thermal cloud remains unclear. Since the decay of the condensate atom number is – like the decay of the thermal cloud – obviously governed by one-body loss, one would expect the same lifetime for both the thermal and the condensed fraction. For the second measurement at higher densities, we prepared a BEC in a trap with 3 % power in the horizontal beam. After the end of the evaporation ramp, the system was given an equilibration time of 250 ms. Subsequently we increased the intensity of the horizontal beam adiabatically[3] to 25 % within 25 ms. The condensate was held in this compressed trap for variable times before it was released and an image was taken after an expansion time of 5 ms.
The measured number of atoms in the condensate and the thermal cloud are shown in Fig. 7.9. The corresponding peak densities are plotted in Fig. 7.10. As can be seen from these figures, the lifetime of the condensate in this trap is much shorter than

[3] The timescale for this change of the trap frequencies was given by the lowest trap frequency in the initial potential of 128 Hz in z direction.

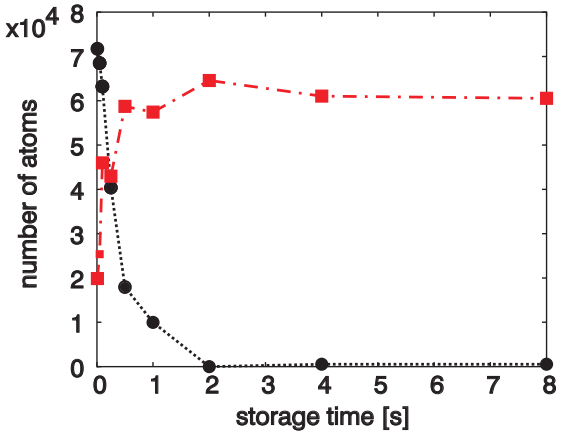

Figure 7.9: Decay of the number of atoms in the condensate (black circles) and the thermal cloud (red squares) in the steep trap at 25 % power in the horizontal beam corresponding to 2.3 W.

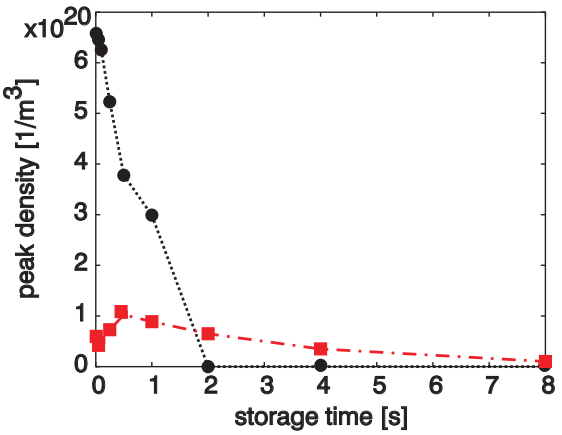

Figure 7.10: Time dependence of the peak density of the condensate (black circles) and the thermal cloud (red squares) in the steep trap.

in the weak one. The condensate number decays to zero within 2 s. The density in the condensate is initially $6.5 \cdot 10^{20} 1/\mathrm{m}^3$, almost a factor of three higher than in the weak trap. Due to this fact, one could suspect three-body loss as the reason for the rapid decay since these recombination losses depend on the probability of three atoms colliding and therefore are proportional to the third power of the density. A threefold increase of the local density increases the three-body loss rate by a factor of 27. But since in our measurements, the decay of the condensate happens in favour of a growing number of atoms in the thermal cloud, the faster decay of the BEC is attributed rather to a heating effect than to three-body loss. This assumption is strengthened when viewing the time dependence of the temperature of the cloud.

Figure 7.11 shows the temperature determined from the width of the expanded thermal cloud. Starting at 500 nK, the cloud heats up at a rate of ∼350 nK/s and approaches the critical temperature from below which is reached after 2 s, consistent with the finding that after 2 s, the condensate has vanished completely. Such a plot however has to be viewed with care: the observation that there is no condensate and that the temperature is above T_c are equipollent. As discussed in Chapter 1, the condensate fraction and critical temperature of the system are both fully determined by the trap parameters, the interaction strength and the *total* number of atoms in the system. The condensed and non condensed fraction are in a balance. If the number of atoms in the system is reduced by a loss mechanism, the system temperature and the critical temperature approach each other, too – with one difference: in the latter case, the critical temperature lowers. This is not the case in the measurement being discussed. Here the critical temperature stays almost constant because the total number of atoms

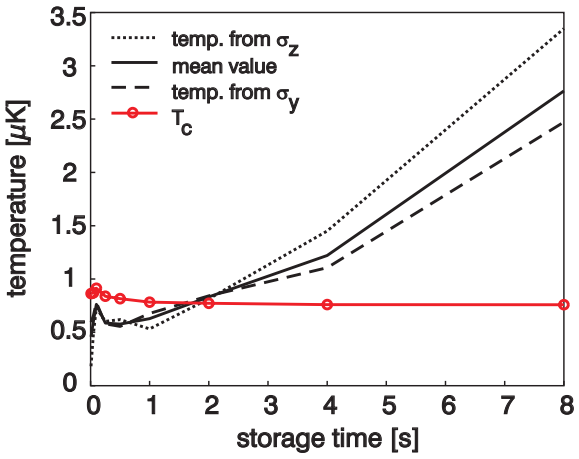

Figure 7.11: Temperature of the trapped cloud vs. storage time in the steep trap. Dotted line: temperature determined from the width of the thermal cloud in y-direction; dashed line: temperature determined form the width in z-direction; solid line: mean value; red dots: calculated transition temperature for the atom number at each point in 7.9.

is stable and the temperature of the atoms in fact rises. As an additional argument against three-body recombination being the main reason for the fast loss, the decay does not level off when the density of $2{\cdot}10^{20}\,1/\mathrm{m}^3$ is reached where a lifetime of 5.8 s was found in the weak trap.
The source of the heating remains yet unclear. Most likely, the motion of the trapped atoms is resonantly excited by fluctuations of the laser pointing or intensity at frequencies close to subharmonics of the trap frequencies. A similar heating rate of 150 nK/s has also been found in a trap operated at 4.2 % directly after the evaporation but was not present in the 3 % trap which shows almost the same peak density. An excitation during the ramp up of the laser power can be excluded since the heating rate seems to stay constant throughout the measurement period.

7.5 Conclusion

In this chapter I have presented the first experimental realisation of a Bose-Einstein condensate of chromium atoms – the first realisation of a Bose-Einstein condensate of atoms which carry a large magnetic dipole moment.
The first almost pure condensates that we were able to produce already contained 20000 to 30000 atoms which is an excellent basis for further experiments. Meanwhile, we are able to produce condensates containing up to 100.000 atoms. The observation of the typical features of Bose-Einstein condensates – the appearance of a sharp and dense

peak in the momentum distribution and the typical anisotropy in the expansion – are clear proof that the atoms have undergone the Bose-Einstein phase transition. I have also shown that the condensate is very stable. The measured lifetime of 5.8 s in the shallow trap is a very comfortable basis for upcoming experiments, giving us enough time for all kinds of manipulation and the possibility to work under stable conditions. The somewhat shorter lifetime that is observed in a eight times deeper trap is probably limited by technical noise.

As a conclusion, there is no hint for strong three body loss in the density regime that has been studied so far. At least such processes are weak enough loss mechanisms to be covered by other sources of atom loss. In the 25 % trap, a relatively strong heating rate has been made up, that could so far not be explained. Closer analysis of the laser intensity and positioning noise spectrum as well as a detailed examination of the dependence of the heating rate on the trap parameters could help find the reason for the heating. Despite this reduced lifetime, it is sufficiently long to carry out experiments with this trap and the decay is not too rapid to prevent the generation of stable starting conditions in a series of experiments.

The successful generation of a chromium Bose-Einstein condensate, together with its sufficiently long lifetime, opens the door to new types of experiments which aim on the anisotropic and long-range character of the magnetic dipole-dipole interaction among the chromium atoms. So far it is the only system where one can expect to observe such effects.

The manifestation of this kind of interaction in the chromium BEC will be presented in the next chapter.

8 Magnetic dipole-dipole interaction in a Bose-Einstein condensate

8.1 Theoretical description

Abstract

In this chapter, I will discuss the first experimental observation of dipole-dipole interaction in a degenerate quantum gas. The chapter starts with a summary of the theoretical description of dipole-dipole interaction in a BEC in Sections 8.1.1 and 8.1.2. The expansion of a dipolar BEC will be discussed in Section 8.1.3. A theoretical introduction is followed by a presentation of the first experimental observation of magnetic dipole-dipole interaction in a gas.
The magnetic dipole-dipole interaction between the ^{52}Cr atoms is identified by monitoring the expansion of the condensate from an anisotropic trap potential. With a significant change of the aspect ratio, depending on the orientation of the atomic magnetic dipoles with respect to the orientation of the trap, we observe a clear evidence of dipole-dipole interaction in the BEC. The results of the measurements are compared to exact solutions of the superfluid hydrodynamic equations in Section 8.2. The analysis of the expansion dynamics will be used in Section 8.3 to determine the relative strength of the dipole-dipole interaction and the s-wave scattering length of chromium, both with a high degree of accuracy and in excellent agreement with theoretical predictions and previous measurements. Parts of the results presented in this chapter have been published in [2], [144], and [145].

8.1.1 Interaction potential

Consider two atoms (Fig. 8.1) with a magnetic moment $\vec{\mu}_m = \mu_m \vec{e}_\mu$ oriented along the direction of an external magnetic field $\vec{B}$ ($\vec{\mu}_m \| \vec{B}$). Here $\vec{e}_\mu$ is a unit vector defining the orientation of the magnetic moment. The interaction energy of the two dipoles separated

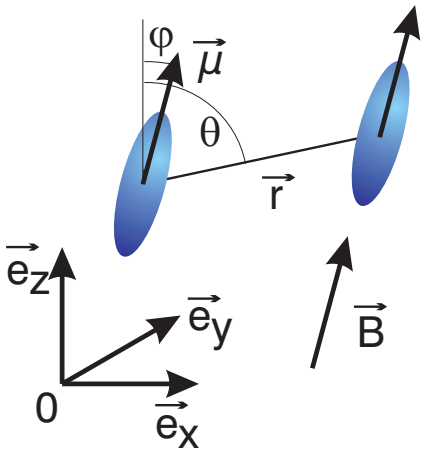

Figure 8.1: Two dipoles $\vec{\mu}$ aligned in an external field $\vec{B}$.

by the vector $\vec{r}$ is given by

$$U_{dd}(\vec{r}) = \frac{\mu_0 \mu_m^2}{4\pi r^3}\left(1 - \frac{3(\vec{e}_\mu \vec{r})^2}{r^2}\right)$$

The strength of the dipole-dipole interaction is given by the pre-factor of Eqn. (8.1.1). This strength can be compared to the coupling constant g of the s-wave interaction (1.4.3) and measured by the dimensionless dipole-dipole strength parameter

$$\varepsilon_{dd} = \frac{\mu_0 \mu_m^2 m}{12\pi\hbar^2 a}.$$

Per definition, homogeneous condensate is unstable [1] against collapse if $\varepsilon_{dd} > 1$ in a static magnetic field [26]. With the scattering length $a = 103\ a_0$ of ^{52}Cr [19] and its magnetic moment of $\mu = 6\,\mu_B$ in the ground state [2], the dipole-dipole strength parameter of chromium is $\varepsilon_{dd} = 0.148$. This is much larger than for any other element that has been cooled to quantum degeneracy so far. The alkalis which form the largest family of Bose-Einstein condensates have a magnetic moment which is six times smaller than that of chromium, thus the magnetic dipole-dipole interaction among them is a factor of 36 smaller than in a chromium BEC. The corresponding strength parameters are $\varepsilon_{dd} = 0.0064$ for ^{87}Rb and $\varepsilon_{dd} = 0.0035$ for ^{23}Na.
As has been shown in [40], in general, the dipole-dipole interaction U_{dd} can be tuned by using a time dependent field to align the dipoles

$$B(t) = B\left(\cos\varphi \vec{e_z} + \sin\varphi\left(\cos(\Omega t)\vec{e_x} + \sin(\Omega t)\vec{e_y}\right)\right),$$

[1] If the effective interaction is attractive, the condensate collapses [14].
[2] The value of 103 a_0 corresponds to the theoretical prediction for the scattering length at magnetic fields around 10 G at which the experiments are carried out. Compare Appendix B.

where $\vec{e_x}$, $\vec{e_y}$ and $\vec{e_z}$ are unit vectors defining the x-, y- and z- axis, respectively. The rotation frequency Ω of the magnetic field around the z-axis has to be chosen such that the magnetic moments can adiabatically follow the rotation but fast enough for the atomic motion on the time scale of one rotation to be negligible. In this case, the atoms will feel a time averaged dipole-dipole interaction. This is provided if $\omega_{Larmor} \gg \Omega \gg \omega_{trap}$ and puts a constraint on the minimum field to be used since the Larmor frequency of the atomic precession is $\omega_{Larmor} = \mu_m B/\hbar$. However, in a trap with frequencies in the $\omega_{trap}/2\pi \approx 1\,\mathrm{kHz}$ range, this lower boundary is at very small fields of $10^{-4}\,\mathrm{G}$ corresponding to the magnetic moment of chromium of $6\mu_B$ and does not restrict the experimental possibilities. The effective long-range interaction between atoms oriented in such a field and separated by the vector $\vec{r}$ is then given by

$$U_{dd}(\vec{r},\varphi) = -\frac{\mu_0\mu_m^2}{4\pi}\left(\frac{3\cos^2\varphi - 1}{2}\right)\left(\frac{3\cos^2\Theta - 1}{r^3}\right),$$

where φ is the angle between the magnetic field direction and the z-axis and Θ is the angle between the separation vector r and the z-axis.
Using this method to tune the dipole-dipole interaction strength and additionally utilising a Feshbach resonance [19] (see also Appendix B) to tune the s-wave scattering length a close to zero will permit one to explore different regimes of dominating short-range or long-range interaction and attractive or repulsive dipole-dipole interaction.

8.1.2 Trapped dipolar condensates

In contrast to the s-wave interaction which can be understood as a local, contact-like interaction (Eqn. (1.4.3)), the dipole-dipole interaction is long-range and anisotropic. In a condensate with density distribution $n(\vec{r})$, it gives rise to the mean field potential [26, 31]

$$\Phi_{dd} = \int U_{dd}(\vec{r}-\vec{r}\,')n(\vec{r}\,')d^3r\,' = \int U_{dd}(\vec{r}-\vec{r}\,')|\phi(\vec{r}\,')|^2 d^3r\,'.$$

The integral in equation (8.1.2) reflects the non local character of the interaction. Taking this interaction into account in addition to the contact interaction, the Gross-Pitaevskii equation (1.22) gets the form

$$i\hbar\frac{\partial}{\partial t}\phi(\vec{r},t) = \left(-\frac{\hbar^2}{2m}\nabla^2 + U_{ext}(\vec{r}) + g|\phi(\vec{r},t)|^2 + \int U_{dd}(\vec{r}-\vec{r}\,')|\phi(\vec{r}\,')|^2 d^3r\,'\right)\phi(\vec{r},t).$$

O'Dell et al. have shown in [31], that even under the influence of the dipole-dipole mean field potential $\Phi_{dd}(\vec{r})$, the wave function has the shape of an inverted parabola in the Thomas-Fermi limit (compare Section 1.4.3). Like in the case of pure contact

interaction, a wave function of the form

$$|\phi(\vec{r})|^2 = n_c(\vec{r}) = n_{c,0}\left(1 - \frac{x^2}{R_x^2} - \frac{y^2}{R_y^2} - \frac{z^2}{R_z^2}\right)$$

is a self consistent solution of the superfluid hydrodynamic equations [79] derived from the Gross-Pitaevskii equation (8.1.2), also in presence of dipole-dipole interaction [31, 146]. R_x, R_y, and R_z are the Thomas-Fermi radii similar to the discussion in Section 1.4.3. The anisotropy of the dipole-dipole interaction manifests itself in a modification of the aspect ratio of the trapped condensate. In the case of an axially symmetric trap, one derives the following equations for the aspect ratio $\kappa = R_\perp/R_z$ [40, 146]:

$$\lambda^2 = \kappa^2 \frac{1 - \varepsilon_{dd}(f(\kappa) + \kappa\frac{\partial f}{\partial \kappa}(\kappa))([3\cos^2\varphi - 1]/2)}{1 - \varepsilon_{dd}(f(\kappa) - \frac{1}{2}\kappa\frac{\partial f}{\partial \kappa}(\kappa))([3\cos^2\varphi - 1]/2)}$$

where $\lambda = \frac{\omega_z}{\omega_\perp}$ and $f(\kappa) = \frac{1+2\kappa^2}{1-\kappa^2} - \frac{3\kappa^2 \tanh^{-1}\sqrt{1-\kappa^2}}{(1-\kappa^2)^{3/2}}$. Setting the dipole-dipole interaction to zero ($\varepsilon_{dd} = 0$), i.e. notionally 'switching off' the dipole-dipole interaction, Eqn. (8.1.2) reveals the well known TF relation (1.4.3) for the aspect ratio. Given a trap anisotropy λ, one can find a solution for the condensate anisotropy κ by solving Eqn. (8.1.2) numerically. To understand the anisotropy of the condensate, we look for the dipole potential (8.1.2) that is generated by the aligned dipoles of the BEC. Let us, for simplicity, assume a spherically symmetric trap ($\omega_x = \omega_y = \omega_z \equiv \omega_0$). Eberlein et al. have solved the problem of the integral (8.1.2) for dipolar condensates in axial symmetric trap potentials using a Green's functional approach [146]. The solutions, however, are not illustrative. The anisotropy, which is introduced by the dipole-dipole interaction, becomes even more obvious in the case of an isotropic distribution. Qualitatively, an anisotropic trap and distribution does not change the following considerations.

As already discussed, the density distribution of the Bose-Einstein condensate has the shape of an inverted paraboloid as depicted in Fig. 8.2. Inside the condensate ($r < R_{TF}$), the dipole-dipole mean-field potential at a position $\vec{r}$ with distance r from the center of mass is given by [31, 40, 146]

$$\Phi_{dd}^{inside}(\vec{r}) = \frac{\varepsilon_{dd} m\omega_0^2}{5}\left[1 - 3\left(\frac{\vec{e}_{mu}\cdot\vec{r}}{|r|}\right)^2\right] r^2 \quad r \leq R_{TF}.$$

This equation shows that the potential is harmonic in r but has an angular dependence. Note that the term in square brackets varies depending on the angle between the orientation of the dipoles $\vec{e}_\mu$ and the position vector $\vec{r}$ between -2 if the position and the polarisation are parallel and $+4$ if they are anti-parallel. The potential therefore has the form of a saddle with a negative curvature along the direction of magnetisation and a positive curvature in transverse direction. Outside the condensate, the potential looks

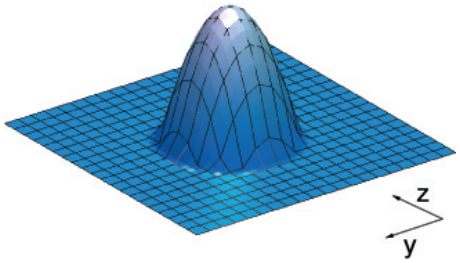

Figure 8.2: Inverted parabolic profile of a BEC in the Thomas-Fermi limit without dipole-dipole interaction. The distribution corresponds to a spherically symmetric trap potential.

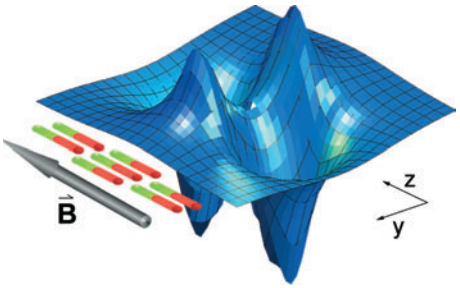

Figure 8.3: Saddle shaped dipole potential generated by dipolar atoms of a BEC in a spherical trap. The atomic dipoles which are illustrated as small magnets in the figure are aligned by an external magnetic field B. Note the orientation of the saddle potential relative to the magnetic field direction.

like the field generated by N dipoles sitting in the center of the distribution and is given by

$$\Phi_{dd}^{outside}(\vec{r}) = \frac{\varepsilon_{dd} m\omega_0^2}{5}\left[1 - 3\left(\frac{\vec{e_{mu}}\cdot\vec{r}}{|r|}\right)^2\right]\frac{R_{TF}^5}{|r|^3} \quad r > R_{TF}.$$

The total potential $\Phi_{dd}(\vec{r}) = \Phi_{dd}^{inside} + \Phi_{dd}^{outside}(\vec{r})$ in the $y-z-$plane is depicted in Fig 8.3. where z is the direction in which the dipoles are aligned.
The presence of such an anisotropic potential, in addition to the isotropic trap, has the consequence that the total energy

$$E_{tot} = E_{trap} + E_{contact} + E_{dd}$$

can be minimised if the atoms redistribute from regions where Φ_{dd} is positive to regions where it is negative. The redistribution leads to a decreasing contribution of the dipole-dipole energy E_{dd} and a repulsive contact interaction among the atoms prevents the BEC from collapsing. Even if the redistribution happens on the cost of an increased potential energy and contact-interaction energy, it will be favoured as long as the total energy is diminished in doing so. Hence the redistribution leads to an elongation along the direction of magnetisation and a contraction perpendicular to it.

8.1.3 Expansion dynamics of a dipolar condensate

Now let us consider the case of a sudden switch-off of the external potential. First of all, this will change the terms that contribute to the energy in the Gross-Pitaevskii equation (8.1.2). After the switch off, the only contributions stem from the contact

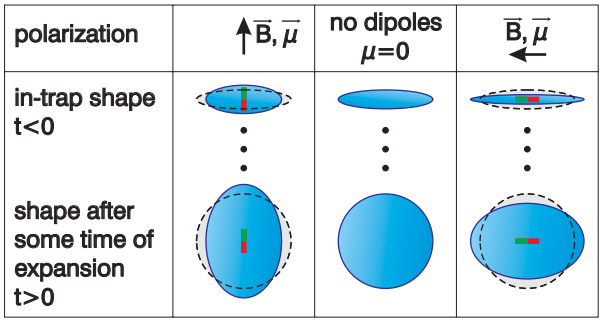

Figure 8.4: Figure to illustrate the change of the condensate shape under the influence of magnetisation in-trap (top row) and during time of flight (bottom row). Left column: magnetisation in transversal direction; center column: non-dipolar atoms; right column: longitudinal polarisation. Dashed ellipses represent the non-dipolar condensate.

interaction and the dipole-dipole interaction. Since this interaction energy will be converted into kinetic energy due to the lack of a confining potential, the kinetic energy term has to be considered, too. Due to its direct proportionality to the local density, the contact interaction part of the mean field potential reveals the same parabola shape as depicted in Fig. 8.2. The dipole potential $\Phi_{dd}(\vec{r})$ still has its (harmonic) saddle shape (see Figure 8.3). Caused by the negative curvature of this energy term in the direction of magnetisation, the gradient of the total mean field energy ($U_{mf} = g|\phi(\vec{r})|^2 + \Phi_{dd}(\vec{r})$) in this direction will be larger than without dipole-dipole interaction. Therefore the atoms will obey a larger acceleration along the direction of magnetisation than without dipole-dipole interaction. In the directions perpendicular to the magnetisation, the curvature of the dipole potential is positive, heaving an attractive character. Thus the repulsive contact interaction is weakened by the dipole-dipole interaction in transversal direction and the acceleration that atoms feel perpendicular to the magnetisation will be smaller. The general trend of deforming the condensate with an elongation along the magnetisation and a contraction in the transversal directions is kept also during the expansion of the condensate as can be seen from the schematic drawing of Figure 8.4.
At this point, it has to be stressed, that the argument of minimisation of the total energy leads to a behaviour of the expanding condensate that is somewhat counterintuitive. Having in mind the simple picture of holding two parallel bar magnets in hands and observing that they repel in the direction perpendicular to the bars, one could expect, that the atoms expand faster in the transversal direction. But on the contrary, the opposite is the case. Since the atoms can move almost freely (i.e only on the cost of higher potential energy and restricted by the repulsive contact interaction) in 3 dimensions, the total energy is minimised by redistributing atoms from the transversal to the longitudinal direction as long as the gain in potential energy and contact interaction energy is small compared to the loss of dipole-dipole interaction energy. This happens also during time of flight since the shape of the condensate and therefore also the shape of the dipole-dipole potential

stays qualitatively constant even during expansion.
For a quantitative analysis, the expansion has to be treated numerically but with a much simpler equation (Eqn. (8.1.3) below) than a 3-dimensional nonlinear Schrödinger equation (8.1.2) [28, 29, 85, 64]. In the Thomas-Fermi limit (Section 1.4.3), solutions for the density distribution $\sqrt{n(\vec{r},t)} = \phi(\vec{r},t)e^{i\varphi(\vec{r},t)}$ and velocity field $\vec{v}$ that is related to the phase $\varphi(\vec{r},t)$ by $\vec{v}(\vec{r},t) = (\hbar/m)\vec{\nabla}\varphi(\vec{r},t)$ have the form

$$n(\vec{r},t) = |\Phi(\vec{r},t)|^2 = \frac{15N}{8\pi R_x R_y R_z}\left(1 - \frac{x^2}{R_x^2} - \frac{y^2}{R_y^2} - \frac{z^2}{R_z^2}\right) \tag{8.1}$$

$$\vec{v}(\vec{r},t) = \frac{1}{2}\vec{\nabla}\left(\alpha_x x^2 + \alpha_y y^2 + \alpha_z z^2\right). \tag{8.2}$$

According to the hydrodynamic theory of Bose-Einstein condensates [147, 148, 79], the density and the superfluid velocity fulfill the continuity equation and the Euler equation

$$\frac{\partial n}{\partial t} = -\vec{\nabla}(nv) \tag{8.3}$$

$$\frac{\partial \vec{v}}{\partial t} = -\vec{\nabla}\left(\frac{v^2}{2} + U_{ext} + \frac{\hbar^2\nabla^2\sqrt{n}}{2m^2\sqrt{n}} + \frac{U_{mf}(\vec{r})}{m}\right), \tag{8.4}$$

respectively, where the external potential U_{ext} has to be set to 0 to study the expansion, and where U_{mf} is the mean-field potential including s-wave and dipole-dipole interactions. The density and velocity are time dependent through the radii $R_i(t)$ and the coefficients $\alpha_i(t)$. Because $\alpha_i = \frac{v_i}{r_i}$, the $\alpha_i(t)$ are given by

$$\alpha_i(t) = \frac{\partial}{\partial t}(\log(R_i(t)).$$

The radii follow the equations of motion

$$m\frac{d^2R_i}{dt^2} = -7\frac{\partial}{\partial R_i}\frac{H_{tot}(R_x,R_y,R_z)}{N},$$

H_{tot}/N being the total energy per particle. $H_{tot} = H_{kin} + H_{ext} + H_{mf}$ consists of the classical kinetic energy (neglecting ground state motion)

$$H_{kin} = \frac{1}{14}Nm(\dot{R_x}^2 + \dot{R_y}^2 + \dot{R_z}^2),$$

the energy in the external trapping potential

$$H_{ext} = \frac{1}{14}Nm(\omega_x^2R_x^2 + \omega_y^2R_y^2 + \omega_z^2R_z^2),$$

and the mean-field energy which consists of the s-wave scattering and dipole-dipole interaction energies

$$H_{mf} = H_{cont} + H_{dd} = \frac{15}{7}\left(\frac{N^2\hbar^2a}{m}\right)\frac{1}{R_xR_yR_z}(1 - f(R_x,R_y,R_z)\varepsilon_{dd}).$$

Where $f(R_x, R_y, R_z)$ is a function that depends on the trap anisotropy and the orientation of the atomic dipoles [64].
If we define the aspect ratios $\kappa_{yx} = R_y/R_x$ and $\kappa_{zx} = R_y/R_x$ and consider the case of polarisation along x, function $f(\kappa_{yx}, \kappa_{zx})$ is given by

$$f(\kappa_{yx}, \kappa_{zx}) = 1 + 3\kappa_{yx}\kappa_{zx}\frac{\mathrm{E}(\varphi \setminus \alpha) - \mathrm{F}(\varphi \setminus \alpha)}{(1-\kappa_{zx}^2)\sqrt{1-\kappa_{yx}^2}},$$

with

$$\sin\varphi = \sqrt{1-\kappa_{yx}^2},$$

and

$$\sin^2\alpha = \frac{1-\kappa_{zx}^2}{1-\kappa_{yx}^2},$$

and where $\mathrm{F}(\varphi \setminus \alpha)$ and $\mathrm{E}(\varphi \setminus \alpha)$ are incomplete elliptic integrals of first and second kind,respectively [149]. The equations of motion (8.1.3) can now be solved numerically, using Eqns. (8.1.3), (8.1.3), and (8.1.3) to calculate the derivatives of H_{tot}.

8.2 Observation of dipole-dipole interaction in a degenerate quantum gas

To measure the effect of the magnetic dipole-dipole interaction on the expansion dynamics of the condensate, we prepare an almost pure BEC as described in Chapters 5 and 7 by decreasing the power in the horizontal trapping beam to 280 mW. A schematic illustration of the subsequent experimental cycle is depicted in Figure 8.5. After 250 ms equilibration, the intensity of the horizontal beam is increased adiabatically to 2.3 W to form an anisotropic trap (trap parameters f_x =942 Hz, f_y =712 Hz, and f_z =128 Hz; compare Section 7.4). The homogeneous offset field of ∼11.5 G along the y-axis that is used for optical pumping (Section 4.8) is always kept on until the trap has been ramped up. After this change of the trap parameters, we either keep the field aligned along y (situation b) in Fig. 8.5) or we rotate the field adiabatically from the y- to the z-direction (situation a) in Fig. 8.5). This is done by increasing the field in z-direction linearly within 40 ms to ∼11.5 G while reducing the field in y-direction during the same time to 0 G. After the field has reached the steady state, we keep the atoms for another 7 ms in the trap to give them enough time to redistribute. The total storage time in both cases of longitudinal ($\|\vec{e}_z$) or transversal ($\|\vec{e}_y$) magnetisation is equal. Subsequently, the atoms are released by a sudden switch-off of the trapping beams. The polarisation field is kept constant for 1 ms after release from the trap and then rotated suddenly to the

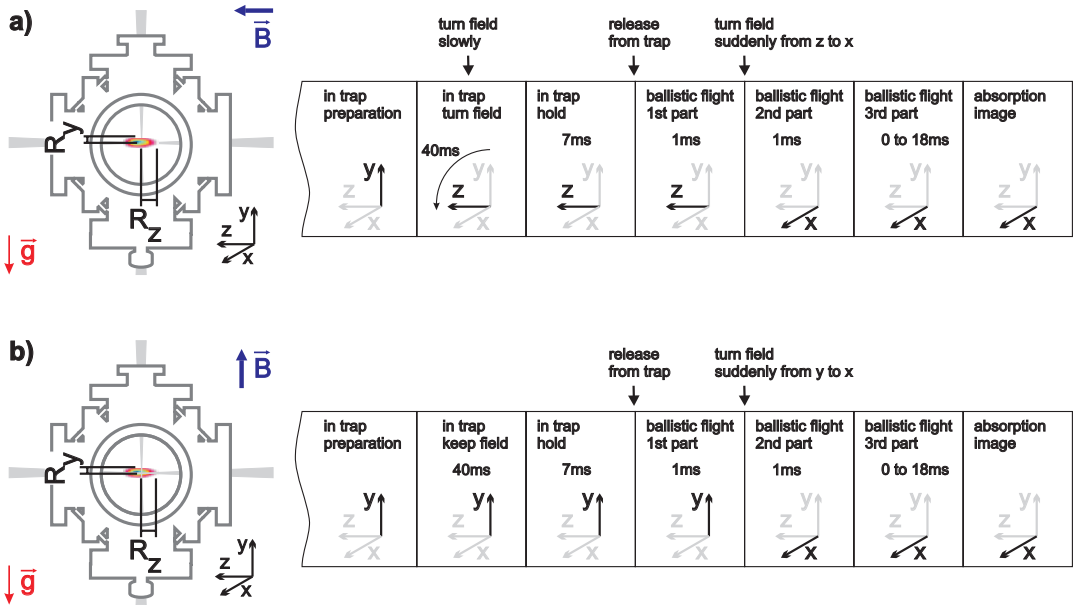

Figure 8.5: Experimental cycle for measuring the dipole-dipole interaction. Left figures: alignment of the field relative to the chamber just before releasing them. Gravity $\vec{g}$ marks y as the vertical axis. Right figures: schematic cycle. The magnetic field during preparation is in either case along the y-axis. To measure with z-polarisation (a), the field has to be turned slowly (within 40 ms) within the trap before releasing the atoms. After 1 ms of expansion, the field is switched suddenly to x-direction. For y-polarisation (b), the field is kept in y-direction until 1 ms after release.

transversal x-axis in either case by switching on the field in the x-direction and switching off the z- or y-fields. This 1 ms of free expansion is long enough for the mean-field energy to drop to such a small part of its initial value that changing the alignment of the dipoles after this time does not influence the expansion anymore. In other words, after this time the gas is already so dilute that any kind of interaction among the atoms can be neglected compared to the kinetic energy. After an additional time of flight of up to 18 ms plus 1 ms for the detection field to settle (total time of flight 2 ms to 20 ms), an absorption image of the cloud is taken.

The images were evaluated using the fringe reduction method described in Appendix 3.2 and two dimensional fits to the density profiles. Figure 8.6 shows 1D cuts through the density profile of an expanded, almost pure condensate. The most convenient quantity to analyse the expansion is the aspect ratio $\kappa = R_y/R_z$ since it is insensitive to fluctuations of the number of atoms (Section 1.5). The only quantities that have to be known exactly are the trap parameters and the ratio ε_{dd} between magnetic dipole-dipole interaction and contact interaction (Eqn. (8.1.1)). The trap frequencies of $\omega_x/2\pi$ =(942±6) Hz, $\omega_y/2\pi$ =(712±4) Hz, and $\omega_z/2\pi$ =(128±7) Hz have been determined using the method described in Chapter 4.6.

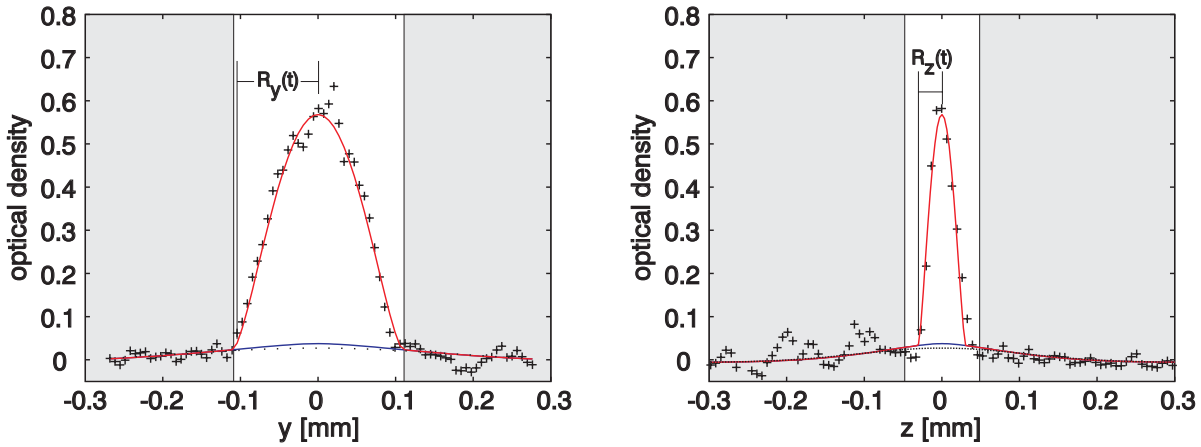

Figure 8.6: Density profiles in y- and z-direction of an almost pure condensate of 84000 atoms after 90 ms of expansion. Grey shaded areas have been excluded from the fit of the thermal cloud.

Figure 8.7 shows the aspect ratio of the BEC for different times of ballistic expansion. The set of data marked with red squares represent the experiments performed with the polarisation in vertical (y-) direction and black circles represent the results with horizontal (z-) polarisation. The upper graph shows the result of sequential experiments where the total time of flight was varied between 2 ms and 14 ms. Since one shot, (i.e. catching atoms in the CLIP trap, Doppler cooling, compressing, rf-cooling, transfer to the ODT, pumping, plain evaporation in the ODT, forced evaporation, modification of the trap and the fields, taking an image, resetting the system), takes about 1 minute and 20 seconds, the data of the time of flight series presented in Figure 8.7 corresponds to a total measuring time of more than 4 hours [3]. To reduce the influence of systematic drifts during that time, the time of flight of subsequent pictures was chosen randomly. For the same reason, we also changed between y- and z-polarisation every 10 shots. An 11-point linear moving average (corresponding to averaging over 2.2 ms in the figure) has been applied to both sets of data in the left graph to average out fluctuations in the condensate widths. A moving average of that length is reasonable since the expected behaviour does not show features on shorter time scales that could be concealed by averaging. As proof, Figure 8.8 shows the same moving average applied to the theoretical values. Even a 20-point average would produce deviations much less than the error bars of the measurements. To be able to display all measured data, the range of the moving average was increased from 1 to 11 within the first six data points. The data point corresponding to 2 ms time of flight is thus not averaged, the one at 2.2 ms is averaged

[3] Such kind of measurements under conditions as stable as possible (concerning stability of the laser system and thus a reproducible number of atoms in every measurement as well as a minimum of vibrations transmitted to the apparatus by the building) were only possible late at night. Hence the above data represent measurements that were taken between 1.00 to 7.30 in the morning.

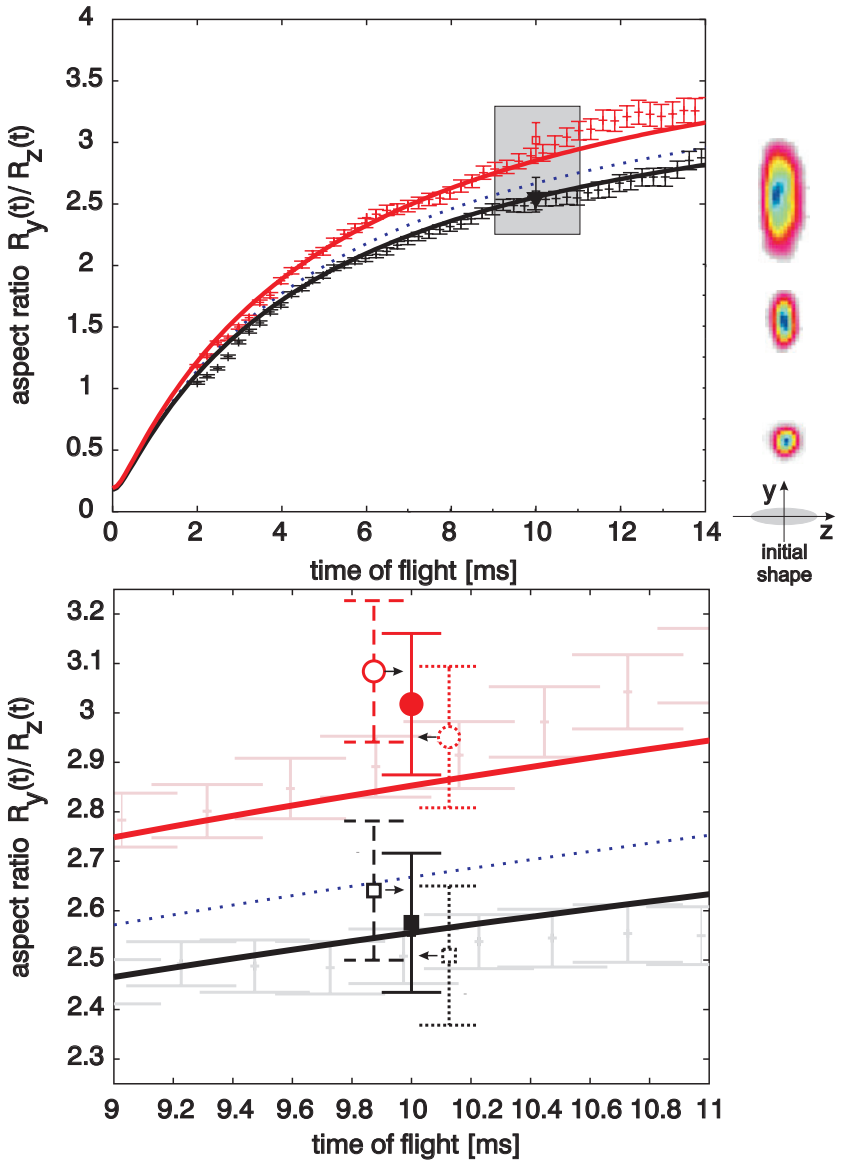

Figure 8.7: Aspect ratio of the expanding dipolar condensate. Data points in the left figure are averaged with an 11-point moving average. Error bars in the upper graph represent errors from the fits to the density distribution. Upper, red data: Field aligned in vertical y-direction. Lower, black data: Field in horizontal z-direction. The solid lines represent the corresponding theoretical predictions. The blue dotted line is the behaviour that one would expect for pure contact interaction without the presence of dipole-dipole interaction among the atoms. The pictures on the right illustrate the evolution of the condensate shape as seen by the camera. The lower figure shows a detail of the upper figure (grey shaded area). We have performed a series of measurements under the same conditions at ten milliseconds time of flight. The two corresponding data points represent the mean values of 42 measurements with y-polarisation (red circle) and 32 with z-polarisation (black square). The solid error bars are derived from the statistics of the measured value and represent one standard deviation in both directions. They do not include the systematic error on the single measurements. These errors affect both the measurements with z- and y-polarisation in the same way and do not change the significance of the measured difference in the expansion dynamics with different polarisation. The shift of the measured aspect ratios due to such systematic errors is indicated by the dashed/dotted representation of the error-bars (displaced laterally for clarity) in the lower figure.

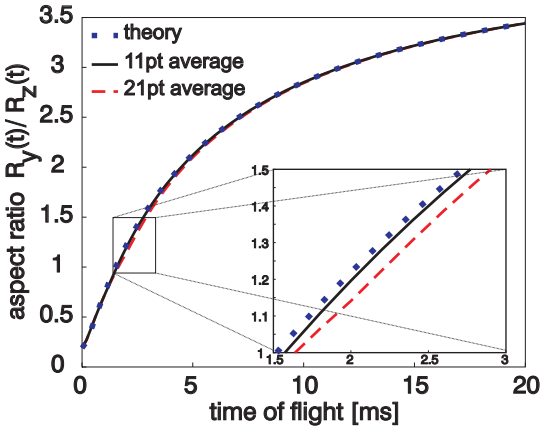

Figure 8.8: Comparison of the plain theory data with 11-point and 21-point moving averages over the data. Theoretical values are sampled with the same 0.2 ms resolution as the experimental data. No significant deviation is introduced by an 11-point moving average. The inset displays an enlarged detail of the area where the maximum deviation occurs with the 21-point moving average.

over 3 points, the one at 2.4 ms over 5, and so on.

The measured data are compared to the results of theoretical calculations carried out as discussed in Section 8.1.3. The theory does not contain any adjustable parameters. Instead it only relies on known or measured quantities, namely the number of atoms, the trap frequencies, the magnetic moment, and the s-wave scattering length that characterises the contact interaction [19]. The blue dotted line represents the expectation for a gas interacting solely via s-wave scattering. Compared to this non-dipolar behaviour, the expansion of the condensate shows a dependence on the polarisation of the atoms that is in agreement with theory: With transversal polarisation (field along the y-axis), the condensate is elongated in the transversal direction and the aspect ratio is increased; if the polarisation is in longitudinal direction (field along the z-axis), the condensate is contracted in vertical direction and the aspect ratio is decreased. The quantitative agreement is remarkable.

The error bars in the upper graph of Figure 8.7 include only errors that stem from the fit of the condensate size. Systematic errors, e.g. uncertainty of the magnification, are not contained. These systematic errors can be found in the lower graph of Figure 8.7 where the mean value of the results of 42 and 32 measurements with y- and z-polarisation are

represented by a red circle and a black square, respectively[4]. All measurements were performed after the same time of flight of 10 ms.
The solid error bars in the lower graph are the statistical errors of all measurements and represent ±1 standard deviation with respect to the mean value. Systematic errors that stem from a systematic 2 % uncertainty in the size of the cloud affect all measurements in the same way, i.e. they shift the measured aspect ratios of both longitudinal and transversal polarisation by the same amount but do not change the relative difference between the expansion data for the two polarisations. The shift of the measured aspect ratios due to systematic errors is indicated by the dashed/dotted representation of the error-bars (displaced laterally for clarity) in the lower figure. Taking the systematic error into account, also the upper data point for y-polarisation (which deviates a little from the theoretical expectation), agrees with theory within error bars.
A t-test analysis [150] of the two sets of data at 10 ms yields a 99% confidence interval of 0.35 to 0.53 for the difference $\kappa_\perp - \kappa_\parallel$ between the aspect ratios in the two cases of transversal and longitudinal polarisation. Although the theoretical prediction of $\kappa_\perp - \kappa_\parallel = 0.31$ does not lie within this interval, the large confidence level confirms that the two mean values of the measurements are clearly separated and strongly correlated with the polarisation of the sample. In the series of measurements at different times of flight however (upper graph), the agreement between theoretical prediction and measurement seems to be much better. Since these measurements were performed first and also closer to the measurement of the trap frequencies, the deviation between the experimental and theoretical values at 10 ms TOF is most likely due to a temporal drift in the laser power or the adjustment of the trap.

8.3 Measurement of the dipole-dipole strength parameter and the scattering length

In this section, I will present and discuss a method of measuring the relative strength of the dipole-dipole interaction with high accuracy. Since the contribution of the dipole-dipole interaction is exactly known, the relative strength of the dipole-dipole interaction can be used to calculate the s-wave scattering length. The special feature of this method

[4] In all, 50 measurements have been performed at 10 ms with both polarisations. Some of the measurements had to be withdrawn due to an obvious instability of the system which on the one hand lead to a number of shots where the number of atoms was substantially smaller than the average $4.0 \pm 0.6 \cdot 10^4$ of the remaining measurements. On the other hand, in the measurements with z-polarisation, some of the condensates did not fall down vertically but moved significantly to one or the other side during their flight, which we considered a signature that the condensate was kicked (probably by mechanical noise on the optical table) prior to or during a switching of the trap. These images were also withdrawn.

is that the result is independent of the number of atoms and provides results with a high degree of accuracy. For comparison I will first also present a more direct measurement of the scattering length which has a small statistical error but relies on the number of atoms in the condensate which is always associated with large systematic error (see e.g. [9]).
The starting point for the determination of the dipole-dipole strength parameter ε_{dd} is to analyse the asymptotic behaviour of the condensate radii $R_i(t)$ for long times of flight. In this asymptotic limit, which is governed by a collisionless and potential free (except for gravity) ballistic flight, the radii of the cloud can be parameterised as

$$R_i(t) = R_i^* + v_i^* t.$$

These radii, as well as the asymptotic velocities $v_i^* = \dot{R}_i(t)$ of the expansion scale with the square-root of the total energy Eqn. (1.4.3). Hence, they are proportional to $(Na)^{1/5}$:

$$v_i^* \propto (Na)^{1/5}$$

and

$$R_i(t) = R_i^* + v_i^* t \propto (Na)^{1/5}, \quad i = [x, y, z].$$

Note that the initial values $R_i(0) = R_i^*$ are not the Thomas-Fermi radii R_i but are actually smaller than these because the initial acceleration due to the conversion of mean-field energy to kinetic energy is neglected if the parametrisation (8.3) is used. To proof the proportionality, we consider the equations of motion (8.1.3) in the steady state at $t = 0$, where the accelerations $\ddot{R}_i(0)$ have to vanish. The radii at $t = 0$ are given by the solution

$$\widehat{R}_i \equiv R_i(0) \tag{8.5}$$

of the Thomas-Fermi equation including dipole-dipole interaction

$$\ddot{R}_i(0) = -\frac{2}{m}\frac{\partial}{\partial R_i}\left(\frac{m\omega_i^2}{14}R_i(t)^2 + \frac{15}{7}\frac{N\hbar^2 a}{m}\frac{1}{R_x R_y R_z}(1 - \varepsilon_{dd} f(\{R_i\}))\right) = 0.$$

Up to a small correction caused by the dipole-dipole interaction, this solution is similar to the solution obtained for pure contact interaction $R_i(0) \approx R_i = \sqrt{\frac{2\mu}{m\omega_i^2}}$ (see Section 1.4.3). Now we define dimensionless radii $\tilde{R}(t)$ that are re-scaled to the Thomas-Fermi radii in the form

$$\tilde{R}_i(t) = \frac{R_i(t)}{R_i},$$

with $\tilde{R}_i(0) = 1$. With these re-scaled radii, Eqn. (8.3) gets the form

$$\ddot{\tilde{R}}_i(0) = -\frac{2}{m}\frac{\partial}{\partial \tilde{R}_i}\left(\frac{m\omega_i^2}{14}\tilde{R}_i^2 + \frac{15}{7}\left(\frac{N\hbar^2 a}{m}\right)\frac{1}{\widehat{R}_i^2\prod_j \widehat{R}_j}\frac{1}{\prod_k \tilde{R}_k}\left(1 - \varepsilon_{dd} f\left(\{\widehat{R}_i\}\right)\right)\right) = 0$$

polarisation	$v_y^* = C_y \cdot (30000 \cdot 103\ a_0)^{1/5}$	$C_y\ [m^{4/5}]$
no dipoles	$8.528 \cdot 10^{-3} m/s$	0.0488
y-polarisation	$9.085 \cdot 10^{-3} m/s$	0.0519
z-polarisation	$8.283 \cdot 10^{-3} m/s$	0.0474

Table 8.1: Asymptotic velocity in y-direction and corresponding proportionality constant C_y for the case of vanishing dipole-dipole interaction $\varepsilon_{dd} = 0$, polarisation along the y-axis, and along the z-axis. The scattering length of 103 a_0 corresponds to a dipole-dipole strength parameter of $\varepsilon_{dd} = 0.148$.

Since this condition must hold for any number of atoms N and any trap geometry defined by the set of trap parameters $\{\omega_x, \omega_y, \omega_z\}$, all radii fulfill the condition

$$R_i(0) = \widehat{R}_i \propto (aN)^{1/5},$$

which was what we wanted to prove.

8.3.1 Direct determination of the scattering length

One can now use Eqn. (8.3) to calculate the scattering length from a measurement of the asymptotic velocity, having in mind that the constant of proportionality C_y that connects v_i^* to (Na):

$$v_i^* = C_y (Na)^{1/5}$$

only depends on the known or measured quantities that determine the chemical potential, i.e. $\omega_x, \omega_y, \omega_z, m$ and a small contribution of ε_{dd}. Using the hydrodynamic theory of an expanding dipolar condensate, the asymptotic velocity for a certain number of atoms and scattering length can be calculated numerically. Because the scaling is known from Eqn. (8.3.1), this immediately delivers the constant C_y. Table 8.1 shows the expected asymptotic velocities in y-direction and the corresponding values for C_y, calculated numerically for pure contact interaction ($\varepsilon_{dd} = 0$), y-polarisation and z-polarisation. The velocities are calculated for the measured trap parameters, 30000 atoms, and a scattering length of $a = 103\ a_0$

To determine the asymptotic velocity, we use the condensate radii $R(t)$ measured in a time-of-flight series. Since the number of camera pixels that are covered by the condensate is much larger in the direction of fast expansion, one can expect the most accurate results from the radius $R_y(t)$ in y-direction. We first consider the case of polarisation along the y-axis. The left Figure 8.9 shows the dependence of the condensate radius y-axis with polarisation along y on the time of flight for 67 different expansion times. Since the number of atoms is fluctuating during such a series of experiments, a linear fit

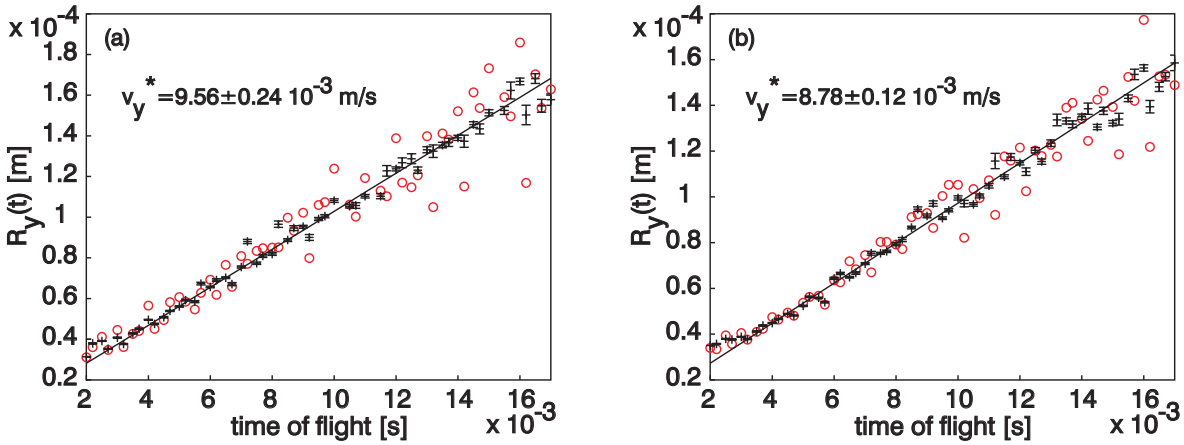

Figure 8.9: Measured dependence of the condensate radius $R_y(t)$ on the time of flight. Left figure: dipoles aligned along the y-axis, average number of atoms: 29100; Right figure: dipoles aligned along the z-axis, average number of atoms: 31000. Open circles: measured radii; crosses: measured radii rescaled using Eqn. (8.3.1); solid black line: linear fit to the re-scaled radii.

directly to the measured data would contain these fluctuations as a statistical error. To get rid of this dependence, we make use of the scaling behavior (Eqn. (8.3)). By dividing all measured radii R_y by the number of atoms in the condensate and multiplying them with the mean value of the fifth root of all measured atom numbers $< N^{1/5} >$, we get a series of time dependent radii which are now independent of the atom number

$$\overline{R}_y = \frac{R_y}{N^{1/5}} < N^{1/5} > .$$

The average number of atoms in this measurement was $< N >= 29100$. Red circles in Fig. 8.9 represent the measured $R_y(t)$, black crosses with error bars mark the re-scaled $\overline{R}(t)$ which show much less fluctuations. A linear fit to the re-scaled data for times larger than 3 ms to focus only on the asymptotic behavior yields $v_y^*(\vec{B}\|\vec{e}_y) = (9.56 \pm 0.24)$m/s and $R_y^* = (10.1 \pm 1.0)\mu$m for $y-$polarisation. For $z-$polarisation, we get $v_y^*(\vec{B}\|\vec{e}_z) = (8.78 \pm 0.12)$m/s and $R_y^* = (10.3 \pm 0.9)\mu$m. By using the above re-scaling, the errors $\Delta v_y^* = \pm 0.24$m/s and $\Delta v_y^* = \pm 0.12$m/s in the fitted slope v_y^* for y- and z-polarisation, respectively, do not contain fluctuations of the atom-number anymore.
If we invert equation (8.3.1) and insert this number and the constant C_y for z-polarisation from table 8.1, we get a value for the scattering length:

$$a = \frac{1}{< N >} \left(\frac{v_y^*(\vec{B}\|\vec{e}_z)}{C_y} \right)^5 = 133\ a_0.$$

The error on this measurement consists of two contributions: first, the fitted asymptotic velocity comes with an error Δv^* due to the noise on the data that is not correlated

with the number of atoms. Since v^* appears in the fifth power in a, Δv^* appears with a factor of 5 in Δa. Second, the mean value of the number of atoms has an uncertainty, mainly due to an uncertainty in the detuning of the probe beam (compare Section 7.2). Since a detuning from resonance can only lead to an underestimation of the number of atoms, the error in the scattering length a caused by this uncertainty is only towards smaller values of a. We estimate a maximum detuning of $\Delta\delta_{probe} = \pm 0.25\Gamma$ which leads to an estimated error in the number of atoms of $\Delta N/N = -0.25\%$. The relative error in a is then

$$\frac{\Delta a}{a} = \frac{\Delta < N >}{< N >} + 5\frac{\Delta v_y^*}{v_y^*} = -0.25 \pm 0.073.$$

Hence, the scattering length of ^{52}Cr determined with this method is

$$a = \left(133\,^{+9}_{-42}\right) a_0.$$

For y-polarization, we get a consistent value of $\left(138\,^{+10}_{-45}\right) a_0$. Due to the relatively large systematic error in the number of atoms, determining the scattering length this way yields only quite inaccurate values, typical for condensate expansion experiments.

8.3.2 Determination of the dipole-dipole strength parameter

If the expansion data that was obtained for polarisation along the z-axis (Fig. 8.9) is additionally taken into account, one can extract the dipole-dipole strength parameter ε_{dd} by analysing the ratio of the two asymptotic velocities. In particular, this ratio depends only on the asymmetry introduced by the dipole-dipole interaction since the contribution of the s-wave scattering to the total energy is independent of the polarisation. We use the two rescaled asymptotic velocities

$$\widetilde{v}_y^* = \frac{v_y^*}{< N^{1/5} >}$$

$\widetilde{v}_y^*(\vec{B}\|\vec{e}_y)$ and $\widetilde{v}_y^*(\vec{B}\|\vec{e}_z)$ for polarisation along $\vec{e}_y$ and $\vec{e}_z$, respectively to determine ε_{dd} by analysing their ratio. To first order in ε_{dd} (in the expected range of ε_{dd}, higher orders are negligible), the ratio has the form

$$\frac{\widetilde{v}_y^*\,(\vec{B}\|\vec{e}_y)}{\widetilde{v}_y^*\,(\vec{B}\|\vec{e}_z)} = 1 + D\varepsilon_{dd},$$

where $D = 0.6523$ is a real constant that can be obtained from a numerical solution of $v_y^*(\vec{B}\|\vec{e}_y)/v_y^*(\vec{B}\|\vec{e}_z)$ for the given trap parameters. It is now possible to calculate ε_{dd} for the measured ratio $v_y^*(\vec{B}\|\vec{e}_y)/v_y^*(\vec{B}\|\vec{e}_z)$ by inverting relation (8.3.2). This relation has

been tested numerically and is a very good approximation for a wide range of scattering lengths. It delivers the correct value for ε_{dd} with less than 5% error if the scattering length is larger than 37 a_0. For $a > 60\ a_0$ (i.e. $\varepsilon_{dd} < 0.25$), the error is smaller than 1% and for $a > 85\ a_0$, it is smaller than 0.2%, i.e. in the expected range of $\varepsilon_d d$, higher order terms are negligible. If we use the measured asymptotic velocities, we obtain

$$\varepsilon_{dd} = \left(\frac{\widetilde{v}_y^*\ (\vec{B} \| \vec{e}_y)}{\widetilde{v}_y^*\ (\vec{B} \| \vec{e}_z)} - 1 \right) / D.$$

Including the error

$$\Delta\varepsilon_{dd} = \sqrt{\left(\frac{\partial \varepsilon_{dd}}{\partial v_y^*(\vec{B} \| \vec{e}_y)} \right)^2 (\Delta v_y^*(\vec{B} \| \vec{e}_y))^2 + \left(\frac{\partial \varepsilon_{dd}}{\partial v_y^*(\vec{B} \| \vec{e}_z)} \right)^2 (\Delta v_y^*(\vec{B} \| \vec{e}_z))^2}$$

from the velocity fits, this yields a measured value of

$$\varepsilon_{dd} = 0.159 \pm 0.034.$$

This is in very good agreement with the strength parameter of $\varepsilon_{dd} = 0.148$ that is expected for a scattering length of $a = 103\ a_0$.

8.3.3 s-wave scattering length of ^{52}Cr

Since the dipole-dipole interaction strength is exactly known (Eqn. (8.1.1)), this result can be used to calculate the scattering length:

$$a = \frac{\mu_0 \mu_m^2 m}{12\pi\hbar^2 \varepsilon_{dd}} = (5.08 \pm 1.06) \cdot 10^{-9}\ \mathrm{m} = (96 \pm 20)\ a_0.$$

This result is in excellent agreement with the value of $(103 \pm 13)\ a_0$ that has been obtained by comparing the measured positions of Feshbach resonances in chromium collisions with multichannel calculations [19], see also Appendix B. Furthermore, the relative error of ±20% makes it a comparably precise method. Many different techniques have been used to determine the s-wave scattering lengths of ultra-cold atoms but most of them come along with large error bars, often because the number of atoms enters the measurement. Examples are the ^{23}Na scattering length in $|\, F = 1, m_F = -1 \,\rangle$ of $a_{\mathrm{Na}} = (92 \pm 25)\ a_0$ (i.e. 27% error) determined from thermalization measurements [22], and $a_{\mathrm{Na}} = (65 \pm 30)\ a_0$ (i.e. 46% error) from the measurement of the mean field energy of a BEC [51]. The scattering length of metastable $a_{He^*} = (16 \pm 8)\,\mathrm{nm}$ was determined from the mean field energy by analysing the size of the BEC [151]. The

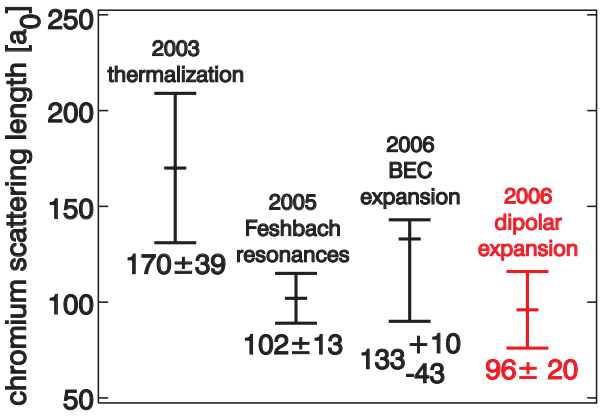

Figure 8.10: Comparison of the values of the s-wave scattering length of chromium determined using three different approaches. The earliest measurement from cross-dimensional thermalisation experiments depended strongly on the number of atom determination, whereas the value obtained from the theoretical description of the measured positions of Feshbach resonances and the measurement presented here, are independent of the number of atoms.

error of 50% stems from an uncertainty of the number of atoms in the condensate. Our first determination of the chromium scattering length [70] was based on cross-dimensional thermalisation measurements [152] and resulted in $a_{Cr} = (170 \pm 39)\ a_0$. The error was mostly due to an uncertainty in the density and atom-number determination. Some other scattering lengths have been determined with much better accuracy, from photoassociation spectroscopy e.g. ^7Li in $|\, F = 2, m_F = 2 \,\rangle$: $a_{[7]Li} = (27.3 \pm 0.8)\ a_0$, i.e. 3% error, and very recently $a = (7.512 \pm 0.005)$nm for metastable He* with per mille accuracy [153, 154, 155]. However, such methods require detailed knowledge of the molecular potentials. Figure 8.10 shows a comparison of the measured values of the s-wave scattering length of chromium.

8.4 Conclusion

In conclusion, the above experiments constitute the direct observation of magnetic dipole-dipole interaction in a quantum gas. This is the first mechanical manifestation of dipole-dipole interaction in a gas. When a homogeneous magnetic field is applied to magnetise the chromium BEC, the atoms redistribute to minimise the total energy. The alignment of the dipolar chromium atoms along the direction of magnetisation is similar to what is known as magnetostriction [156] from magnetic solids or ferrofluids – an effect that has been identified first by James Joule in 1842. The experimental results show that the magnetic dipole-dipole interaction among the atoms in a chromium BEC is strong enough to influence the properties of the condensate. The good agreement of the measured dynamics with a parameter-free theory proves that the theory

of dipolar superfluids is well suited to describe the expansion dynamics of a dipolar Bose-Einstein condensate. Furthermore, the relative strength parameter was measured $\varepsilon_{dd} = 0.159 \pm 0.034$ and was used to calculate the s-wave scattering length of ^{52}Cr $a = (5.08 \pm 1.06 \cdot 10^{-9})m= (96 \pm 20)\ a_0$ in excellent agreement with the results of theoretical analysis of measured Feshbach resonances ($a = (103 \pm 13)\ a_0$).

9 Summary and outlook

The achievement of Bose-Einstein condensation of chromium atoms in a dilute gas and the proof of magnetic dipole-dipole interaction among the atoms in the condensate were the central subjects of this thesis.
The observation of the transition from a classical gas to a quantum degenerate state in a chromium vapour not only constitutes the first generation of such a state with chromium atoms but also the first observation of a dipolar BEC. Among all existing BECs, a chromium BEC is the only one in which atoms interact significantly via magnetic dipole-dipole forces.
Starting with a descriptive discussion of the relation between indistinguishability and statistical properties of particles, I presented an overview of basic condensate physics. The theoretical concepts that are important to understand and interpret the experimental findings were discussed. These considerations started with the case of a free ideal gas and were extended to real systems of finite size, interacting particles and confinement in external potentials. Under these conditions, the critical temperature and the fraction of condensed atoms are subject to a shift with respect to an ideal gas.
A brief overview of the experimental setup has been given. Besides the large parts of the setup that already existed and were discussed in detail in other works, a frequency-doubled diode-laser system that is used for optical pumping between Zeeman states, and a crossed optical dipole trap based on a 20 W, 1064 nm fibre laser were assembled within the framework of this thesis.
All experimental data presented in this thesis rely on only one method of measuring, namely absorption imaging of atomic clouds. The methods of taking, processing and evaluating such images were discussed.

The considerations that are necessary for optical trapping of chromium in a far-off-resonant light field have been presented as well as the characterisation of the crossed optical dipole trap. The trap consists of two beams with different waists of 30 μm and 50 μm in the horizontal and vertical beam, respectively. At an optical power of 10 W in in the horizontal beam, the trap has a depth of 143 μK. I discussed the methods that we use to measure the trap frequencies and compared them to the expected numbers. Although two of the three trap frequencies agree well with the calculated ones, one fre-

quency deviates significantly. The reason for this discrepancy could not be explained definitely.
Huge dipolar relaxation rates prevent chromium from reaching degeneracy in a magnetic trap and necessitate a transfer into an optical trap which can also trap the lowest lying Zeeman state. Loading of the optical trap is achieved by overlapping the optical potential with an rf cooled sample of chromium atoms in the magnetic trap. At this stage $4.5 \cdot 10^6$ atoms at a phase space density of 10^{-5} are located in the magnetic trap. The transfer efficiency to the optical trap after reducing the magnetic trapping potential to zero is 40%. To polarise the sample, we utilise the ${}^7S_3 \leftrightarrow {}^7P_3$ transition of chromium at a wavelength of 427.2 nm. When we apply 0.5 mW of σ^--polarised light immediately after the transfer to the optical trap for 1 ms, we achieve a transfer efficiency from $m_J = +3$ to $m_J = -3$ of nearly 100%. The lifetime of the trapped cloud is increased dramatically from 6.3 s in the $m_J = +3$ state to 142 s if the atoms polarised in $m_J = -3$ and is only limited by background gas collisions. A long lifetime is the most important prerequisite for successful evaporative cooling.
I continued with a presentation of the results of evaporative cooling in the optical dipole trap. The starting conditions are $1.5 \cdot 10^6$ atoms at 60 μK and a phase space density of $5 \cdot 10^{-5}$. After turning off the magnetic trap, we observe a rapid decay of the number of atoms to about 50% of its starting value which could be attributed to plain evaporative cooling. After this initial decay, the phase space density has increased to 10^{-3}. Attempts to cool the cloud in only one beam did not succeed due to an insufficient elastic scattering rate. Evaporative cooling became possible by applying a second trapping beam to increase the density in the central region of the trap. I presented the technique used to optimise the evaporation technique and the evaporation ramp that is finally used to reach BEC. We achieve a total efficiency of evaporative cooling in the ODT of 3.6 orders of magnitude gain in phase space density per lost order of magnitude in the number of atoms.
Bose-Einstein condensation of chromium is achieved at a remaining power of 6 % of the initial power in the horizontal beam. Ramping the optical potential further down, we are able to produce almost pure condensates of 10^5 atoms. We identify the occurrence of BEC by the typical appearance of a bimodal momentum distribution and an anisotropic expansion when releasing the cloud from an asymmetric trap. I analysed the dependence of the condensate fraction on the rescaled temperature and measured the lifetime of the trapped condensate. In the weak trapping potential at the end of the evaporation ramp, the condensate lives for 5.8 s. Found when the trap is compressed adiabatically afterwards, we attributed a shorter lifetime to a heating mechanism whose origin remains unclear. We find no hint for strong three body loss.
The presence of dipole-dipole interaction between the atoms in a chromium BEC has been confirmed by analysing the expansion of the condensate in a homogeneous magnetic field. Depending on the Polarisation of the atoms, the condensate expands anisotropi-

cally after release from the trap. I summarised the superfluid hydrodynamic theory for dipolar condensates followed by the discussion of the experimental results. The measured dependence of the condensate aspect ratio on the time of free flight with different polarisation – along and perpendicular to the weak axis of the trap – was compared to numerical results of the hydrodynamic equations. The experimental findings reproduce the theoretical predictions very well and constitute the first observation of a mechanical effect of MDDI in a gas. I have discussed a method to measure the relative strength of the MDDI compared to the contact interaction. The value of $\varepsilon_{dd} = 0.159 \pm 0.034$ that we measure with this method is in excellent agreement with the predicted value $\varepsilon_{dd} = 0.148$ that is obtained assuming a s-wave scattering length of $a = 103\ a_0$ resulting from Feshbach resonance measurements. I have used the experimental value of ε_{dd} for a determination of the s-wave scattering length of chromium. The result of $a = (96 \pm 20)\ a_0$ agrees with the above results. Since this way of measuring a is independent of measurements of the number of atoms and density, there are some advantages in this technique compared to many other techniques. Furthermore, it does not require knowledge of any details of the molecular potentials.

Outlook

The above experiments constitute proof of the dipolar character of a Bose-Einstein condensate of chromium atoms. The possibility to generate BECs in series of experiments under stable conditions and to store them for sufficiently long time make the chromium BEC the most promising system for further studies of dipolar effects in quantum gases (see the introduction). Although heteronuclear molecular BECs are expected to have much larger (electric) dipole moments, such condensates are not available at the moment. It is also questionable whether these condensates would live for reasonably long time to perform experiments, once they are available. Long lifetimes and large dipole moments are only expected for heteronuclear fermion-fermion molecules [157, 158, 159] that are generated in a low vibrational state which is not easy to achieve (for a review on ultracold molecules see [160]).
Since it is in fact favourable for most of the expected phenomena to have an even larger relative strength of the MDDI, gaining control over the s-wave scattering length is certainly one of the most important future goals. We have already found 14 Feshbach resonances in ultracold chromium collisions (see Appendix B) but up to now we were limited by the stability of the currents used to generate the magnetic fields. With a precision control of the currents that is currently being set up in our lab, it should become possible to gain exact control over the magnetic field and to study the characteristic dependence of the s-wave scattering length on the applied field. The method of measuring

the scattering length that was discussed in Chapter 8 might in this respect become a useful tool to determine the magnetic field dependence of the scattering length close to a Feshbach resonance. Once this dependence is known, one of the Feshbach resonances can be utilised [161, 162, 9, 163, 14, 164, 165, 166] to tune the s-wave interaction strength close to zero and thereby increase the relative strength of the dipole-dipole interaction.

Recent publications have shown that the MDDI is tuneable. If an external magnetic field that aligns the atoms is rotated on a cone with a frequency that is fast compared to the atomic motion, the atoms feel a time averaged MDDI potential whose strength can be tuned by changing the apex angle of the cone. In this way, the MDDI can not only be varied in strength but also its sign can be changed [40]. The electronic circuitry to drive precisely rotating fields at 10 kHz rotation frequency has been assembled but not yet tested with a condensate. Measurements similar to the ones that were used to proof the dipolar interaction in this thesis could be used to demonstrate the tunability of the MDDI in the BEC.

The results of the molecular dynamics simulation of evaporative cooling that I have presented in this thesis show that there is a large potential of reaching quantum degeneracy with a much larger number of atoms under the same starting conditions in the ODT. The old 20 W fibre laser is currently being replaced by a new one with a maximum power output of 100 W. According to the simulation results, a fourfold increase of the number of atoms can be expected when 15 W extra laser power is used to create a deeper dimple. This will result in an even better signal to noise ratio for all measurements and will enhance the experimental possibilities.

The occurrence of new quantum phases, the “supersolid” and “checkerboard” phase [36], is predicted if the dipolar BEC is stored in a two-dimensional lattice. Also pancake shaped trapping geometries promise exciting effects like the existence of a roton-maxon in the excitation spectrum [32]. Modifications of the experimental setup that will allow the generation of steep standing-wave traps are on the way.□

A Chromium

Abstract

All experiments presented in this thesis were performed with the bosonic chromium isotope ^{52}Cr. In this section, I summarise the most important properties that are relevant for the experiments that have been discussed in this thesis. For a detailed discussion of the scattering properties and the aspects of magneto-optical and magnetic trapping of chromium and (also of the fermionic isotope and bosonic ^{50}Cr), refer to [88, 68, 86].

element	mass [au]	natural abundance	nuclear spin I	statistic s
chromium	50	4.35%	0	bosonic
chromium	52	83.79%	0	bosonic
chromium	53	9.5%	3/2	fermionic
chromium	54	2.36%	0	bosonic

Table A.1: Chromium isotopes, their natural abundance, spin and statistics.

^{52}Cr is the isotope with the largest natural abundance of 83.79% (see table A.1). The nuclear charge of chromium is 24 and the bosonic isotopes ^{52}Cr, ^{50}Cr, and ^{54}Cr have no nuclear spin. Only the fermionic ^{53}Cr isotope has a nuclear spin of $I = 3/2$. In its pure

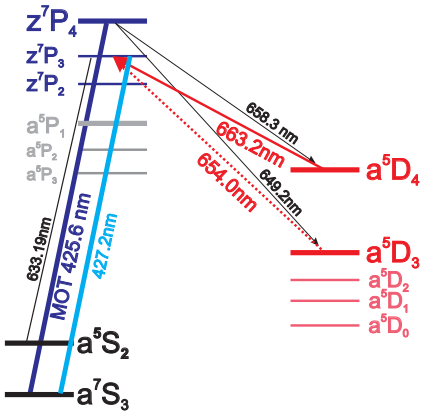

Figure A.1: Part of the level scheme of ^{52}Cr that is relevant for laser cooling.

nuclear charge	24
mass	$8.7{\cdot}10^{-26}$ kg
nuclear spin	0
ground state	$^7S_3$
electron configuration in $^7S_3$	$1s^2 2s^2 2p^6 3s^2 3p^6 3d^5 4s$
Landé factor g_J in ground state	2
MOT transition	$^7S_3 \leftrightarrow {}^7P_4$
Landé factor g_J in excited state	1.75
wavelength MOT transition λ	425.5 nm
recoil temperature T_{rec}	1.02 μK
recoil velocity v_{rec}	1.8 cm/s
line width $\Gamma/2\pi$	5.02 MHz
excited state lifetime	32 ns
saturation intensity I_s	8.52 mW/cm^2
Doppler temperature T_D	124 μK
transition used for optical pumping	$^7S_3 \leftrightarrow {}^7P_3$
wavelength λ	427.2 nm

Table A.2: Important general and spectroscopic properties of bosonic ^{52}Cr .

natural form, chromium at room temperature is a very hard crystalline metal. Its melting point is 1850 °C and its boiling point is at 2690 °C. To create gaseous chromium atoms, the experimental setup makes use of the fact that chromium sublimates under vacuum conditions. The vapour pressure of chromium at 1500 °C is $6{\times}10^{-7}$ mbar. Therefore we generate a beam of chromium atoms by the use of a high temperature effusion cell (normal operation is at 1600 °C) in the ultra-high vacuum chamber. Operating an oven at such a high temperature under vacuum conditions, is eased by the getter property of chromium. Similar to titanium, which is a well known getter material and often used in ultra-high vacuum technologies, gas atoms that hit a chromium surface get stuck. The chromium gas evaporated out of the effusion cell continuously coats the inner walls of the vacuum chamber and in that way constantly renews the getter surface, providing good vacuum even during operation of the effusion cell.

The spectroscopic properties of chromium are important for laser cooling and trapping (Chapter 4). The part of the level scheme that is relevant for optical cooling is depicted in Figure A.1. The figure shows all relevant levels of the septet and quintet system and the transitions that are relevant for laser cooling: cooling transition at 425.6 nm, repumping transitions 654.0 nm and 663.2 nm (usually only the latter one is used in the experiments), and the decay channels from the excited state of the cooling transition to

the metastable ^{5}D states (corresponding transition wavelengths 658.3 nm and 649.2 nm). The magneto-optical trap is operated on the strong transition between the $^7S_3$ ground state and the excited $^7P_4$ state with a transition wavelength of 425.6 nm in the blue. The important properties of this transition are summarised in table A.2. Atoms in the ^{7}P state can undergo (spin-forbidden) transitions to the ^{5}D states which is used to load the magnetic trap continuously with ^{5}D atoms. Atoms that undergo transitions on the $^7P_4 \leftrightarrow ^5D_4$ intercombination line accumulate in the $^5D_4$ state during operation of the magneto-optical trap and are later on pumped back to the ground state via the $^5D_4 \leftrightarrow ^7P_3$ transition at 663.2 nm [69, 88](see also Section 4.7).
The $^7S_3 \leftrightarrow ^7P_3$ is used to pump the atoms optically from the low-field seeking $m_J = +3$ to the high-field seeking $m_J = -3$ state after transferring them from the magnetic to the optical trap (Section 4.8).

B Feshbach resonances in chromium collisions – an overview

Abstract

We have observed 14 *Feshbach resonances in collisions of chromium atoms (for ultra-cold collision theory see e.g. [80, 81, 82, 89]). The experimental resonance positions are in very good agreement with theory taking into account only dipole-dipole coupling and allowing us to extract the scattering lengths* $a_6 = (112 \pm 14)\ a_0$, $a_4 = (58 \pm 6)\ a_0$ *and* $a_2 = (-7 \pm 20)\ a_0$ *of the molecular potentials involved in the resonances. The zero-field scattering length of* $a = 102\ a_0$ *that results from the comparison of theory and experiment is a very important quantity since it determines the interaction energy among the atoms (see Chapter 1). The experimental accessability of Feshbach resonances in chromium is a very promising step towards tuning* a *and exploring regimes of degenerate quantum gases where the magnetic dipole-dipole interaction is the dominating interaction effect. The results and theoretical background of our Feshbach resonance measurements will be discussed in detail by Jörg Werner [89] and have been published in [19] and partly in [167].*

A Feshbach resonance occurs when the kinetic energy of a colliding pair of atoms (open channel) is equal to the energy of a (quasi-) bound state of an interatomic potential (closed channel) to which a coupling exists from the incoming channel. In this case, the probability of occupying the bound state temporally during the collision is resonantly enhanced. Depending on the energy difference of the bound state and the energy of the incoming channel, the radial part of the asymptotic wave function of the scattering particles is shifted in radial direction relative to the wave function of non-interacting atoms. Far away from any kind of scattering resonance, the shift, i.e. the scattering length, is determined by the molecular potential of the two atoms in the incoming channel. If the bound state in the other channel has an energy just above/below the collision energy, the shift of the scattering length is negative/positive. Exactly on resonance, the scattering length and the elastic scattering cross section diverge. Generally, the scattering channels in ultra-cold atomic Feshbach resonances are molecular potentials stemming from different configurations of the atomic spins which in most cases also have different

magnetic moments. It is therefore possible to generate such a resonance situation artificially by applying an external magnetic field of a certain strength. In this field, the energy shift of the dissociation limit in the incoming channel and bound states in other molecular potentials will be different due to the different magnetic moments and with an appropriate magnetic field the incoming channel and the bound level can be brought into resonance.
To localise and characterise a Feshbach resonance, one can analyse the elastic scattering properties, e.g. by measurement of the mean-field energy of a Bose-Einstein condensate depending on the external magnetic field [164] or by cross-dimensional re-thermalisation measurements [166, 152]. Since not only the elastic scattering rate but also the three-body loss rate increases [168], monitoring the occurrence of strong loss in the vicinity of a Feshbach resonance is also a very powerful technique. This has some experimental advantages compared to techniques which detect the elastic properties because it does neither require the atoms to be in the condensed phase nor a time-consuming tracing in time of the re-thermalisation . We have found 14 Feshbach resonances in ultra-cold chromium collisions by analysing atom loss from the crossed optical trap. For the measurements, we prepared 120000 atoms at 6 μK in the crossed trap with $\sim$5 W power in both beams. Subsequently, we rapidly switched on a magnetic field in z- direction and performed short sweeps of 30 G between 0 G and 600 G and a duration of 5 s. Once an enhanced loss was located, the resolution in that region was increased by decreasing the width of the sweep. We used either a pair of coils in Helmholtz configuration (B <20 G) or the pinch coils of the cloverleaf trap (20 G< B <600 G) to generate the magnetic field. The first set of coils produces no significant inhomogeneity of the magnetic field on the scale of the extension of the cloud. With the pinch coils, the magnetic field varies by 50 mG over the cloud at the highest applied magnetic fields. This inhomogeneity contributes to the errors of the measured widths. To finally resolve the structure of the resonance, a different technique was chosen because the high currents of up to 450 A used to generate the magnetic field lead to a substantial change of the temperature of the coils. After setting such high currents, the system has to equilibrate first to prevent a broadening of the measured resonance by thermal drifts. For this purpose, the field was switched on rapidly but with a value just above the resonance. We held this value for 2 s to let the magnetic field and temperature settle, followed by a quick ramp to the final value which was kept for a variable time between 0.1 s and 10 s, depending on the strength of the resonance. Finally, the atoms where released and an image was taken to determine the number of remaining atoms. Figure B.1 shows all resonances that have been detected in the range from 0 G to 600 G.

The channels involved in the resonances can be identified having in mind the selection rules for the angular momenta ℓ of the nuclei, their projections M_ℓ on the quantisation axis, and the total spin S with dipole-dipole coupling between colliding atoms. In

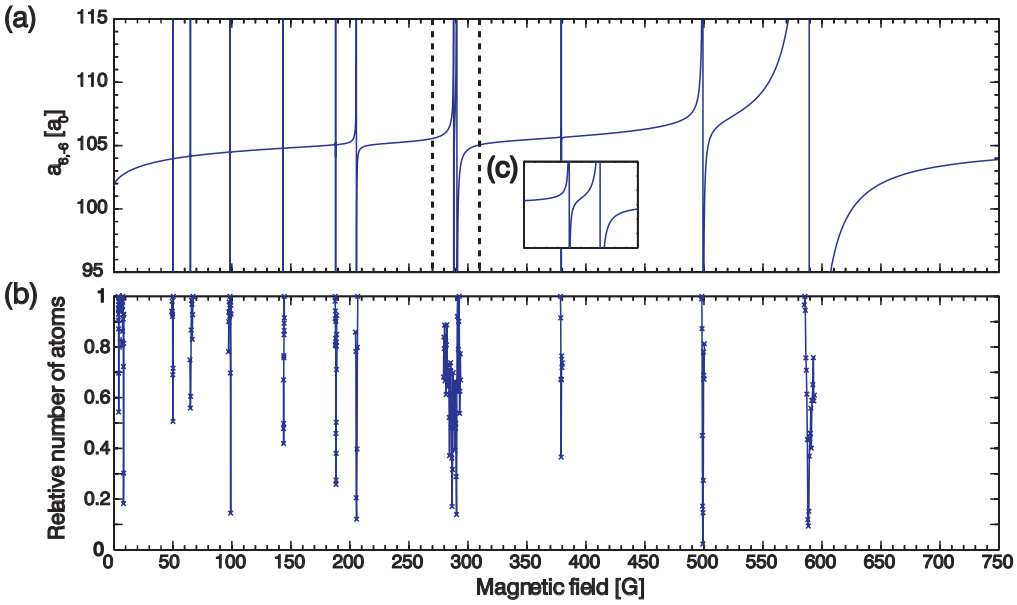

Figure B.1: Comparison of the positions of all measured resonances with theoretical calculations. Upper graph: Theoretical dependence of the s-wave scattering length a on the magnetic field. Lower graph: remaining number of atoms found after holding the cloud in the crossed dipole trap at different magnetic field. The number of atoms is normalised to the maximum number found away from the resonances.

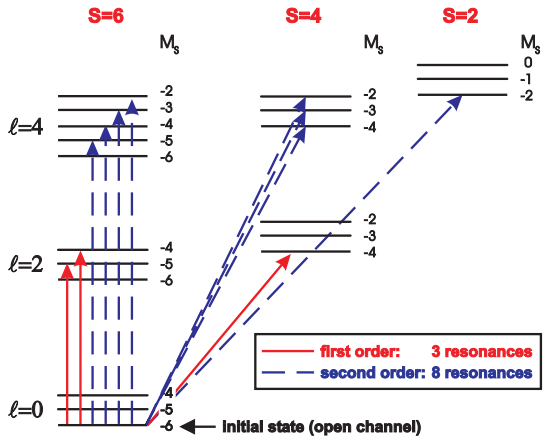

Figure B.2: Illustrated selection rules for first order and second order transitions from the $\ell = 0, M_\ell = 0, S = 6, M_S = -6$ entrance channel.

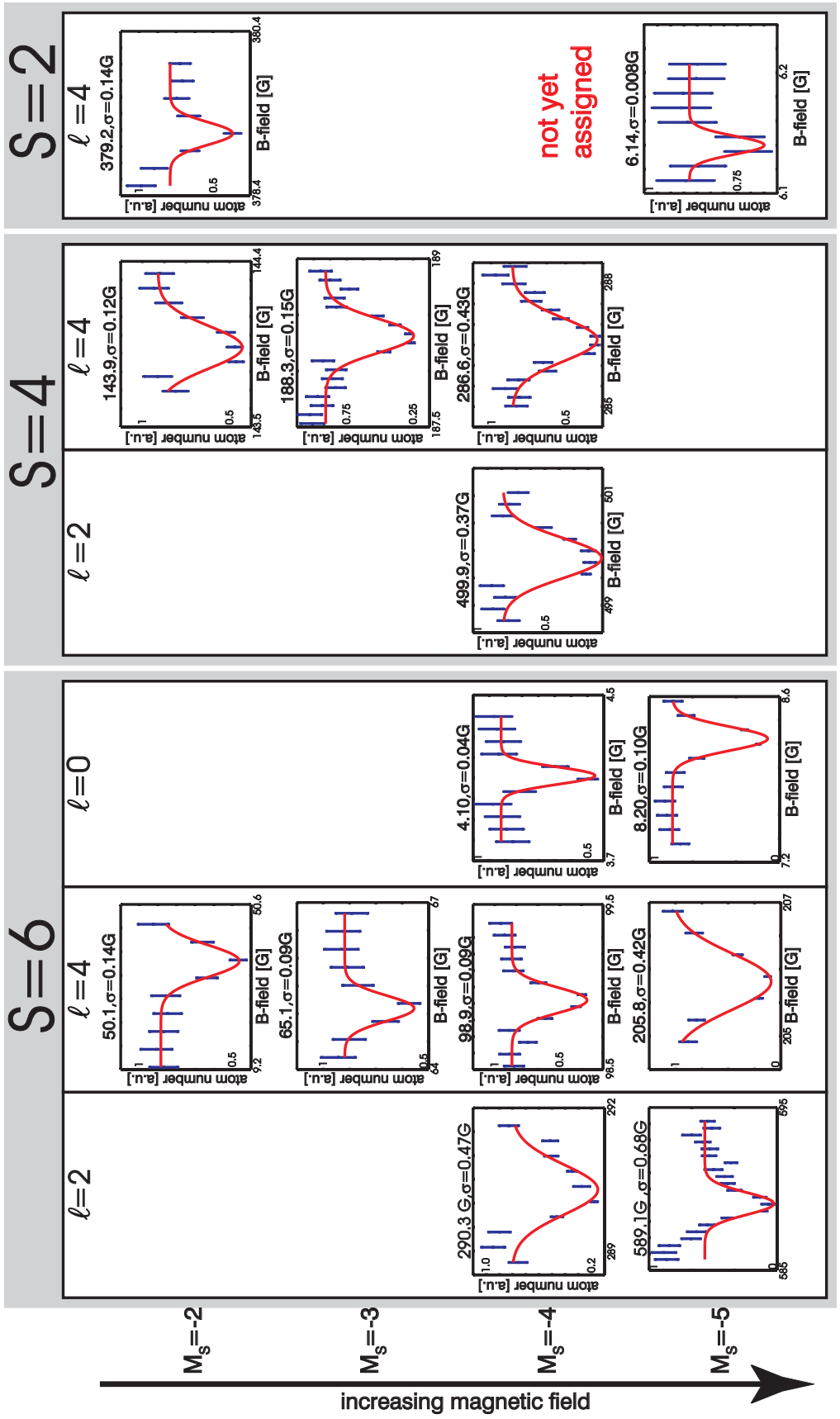

Figure B.3: Recorded atom loss at the 14 resonances. S: total spin; M_S: projection of the spin on the direction of the magnetic field B; ℓ: angular momentum of the nuclei; numbers above the graphs measure the field on resonance and the measured width σ of the resonance.

addition to momentum conservation $\Delta M_S = -\Delta M_\ell$, the following selection rules hold for first order coupling:

$$\Delta S = \pm 0, \pm 2; \quad \Delta \ell = 0, \pm 2; \quad \Delta M_\ell = 0, \pm 1 \pm 2$$

and for second order:

$$\Delta S = \pm 0, \pm 2, \pm 4; \quad \Delta \ell = 0, \pm 2, \pm 4; \quad \Delta M_\ell = 0, \pm 1, \pm 2, \pm 3, \pm 4.$$

Additionally transitions from $\ell = 0$ to $\ell = 0$ are forbidden and only channels which have different spin projections $\Delta M_S \neq 0$ can be shifted relative to each other by a magnetic field. Entering the collision in an s-wave channel ($\ell = 0$, $M_\ell = 0$), first order rules allow three resonances, and eight more are allowed in second order. This explains the eleven strongest resonances. Two of the weaker resonances that have been additionally found at low fields can be explained by collisions entering on the d-wave. The resonance at 6.14 G can not be explained up to now. Comparison of the experimentally determined positions of the resonances with multi-channel scattering calculations results in values for the scattering lengths $a_6 = (112 \pm 14)\ a_0$, $a_4 = (58 \pm 6)\ a_0$ and $a_2 = (-7 \pm 20)\ a_0$ and the C_6 and C_8 values that parameterise the molecular potential [19]. Figure B.3 shows all measured resonances in their highest resolution and their positions together with the theoretically predicted widths.

The Feshbach resonance at 589 G has a theoretical width of 1.7 G and is related to a three-body loss coefficient $L_3 \approx 3 \cdot 10^{-36} \mathrm{m}^6/\mathrm{s}$ which is smaller than the ones observed in ^{85}Rb [169] and Cs [170] but larger than for ^{23}Na [162] and ^{87}Rb [171]. The zero-field s-wave scattering length of chromium can be extracted from the intersection of the theoretical curve in Figure B.1 with the vertical axis at $B = 0$. It carries the same relative error as a_6 and we therefore specify $a = (102 \pm 13)\ a_0$ and $a = (103 \pm 13)\ a_0$ at zero field and at 10 G offset field, respectively.

We expect that one of the resonances can be used to tune the contact interaction to increase the relative strength ε_{dd} of the dipole-dipole interaction (compare Section 8) by performing experiments at a magnetic field close to the zero-crossing of a. The requirements on the stability of the magnetic field for such an experiment depends on the slope of the field dependence of a close to $a = 0$. It is expected that a resonance with a large width ΔB relative to the absolute field B is best suited. The resonance with the largest theoretical $\Delta B/B$ is the one measured at B =589 G with a theoretical width of 1.7 G. Performing an experiment with stable scattering length on such a resonance requires a control and stability of the current through the coils on the 10^{-5} level at currents around 400 A. Already the measurement of currents with an accuracy on that level is challenging. An experimental realisation of such a precision control by the means of a feed-back loop which uses the signal of a high-precision current transducer[1] is currently being implemented in the setup.

[1] Danfysik ULTRASTAB 866

C Atoms in light fields

In the presence of a light field, the coupling of the atomic dipole moment $\vec{p}$ to the electric component $\vec{E}$ of the light field disturbs the stationary Eigenfunctions $\Phi_i(\vec{r})$ with eigenenergies $E_n = \hbar\omega_n$ of the free Hamiltonian H_0. Since the $\Phi_i(\vec{r})$ form a complete set of basis vectors, the new Eigenfunctions $\Psi(\vec{r}, t)$ of the disturbed Hamiltonian $H(t) = H_0 + H'(t)$ can be displayed as linear combinations of the $\Phi_i(\vec{r})$:

$$\Psi(\vec{r}, t) = \sum_i c_i(t)\Phi_i(\vec{r})$$

The evolution of the amplitudes $c_i(t)$ is described by the time dependent Schr¨odinger equation:

$$i\hbar\frac{d}{dt}c_i(t) = \sum_k c_k(t)H'_{ik}(t)e^{i\omega_{ik}t},$$

where $H_{ik} \equiv \langle \Phi_i | H'(t) | \Phi_k \rangle$ and $\omega_{ik} = \omega_i - \omega_k$ is the energy difference between two states$i$ and k. If we consider an atom with ground state $|\, g \,\rangle$ in a monochromatic light field with a frequency ω_L close to resonance[1] with a transition to an excited state $|\, e \,\rangle$, the problem can be reduced to two-level system with state vector

$$|\, \Psi \,\rangle = c_g |\, g \,\rangle + c_e |\, e \,\rangle.$$

By displacing an electron with charge $-e$ by a distance $\vec{r}$, the oscillating electric field of a plane wave which propagates in z-direction with wave vector k_L, frequency ω_L, amplitude $E(\vec{r})$ and unit polarisation vector $\vec{\epsilon}(\vec{r}, t)$ induces an electric dipole moment

$$\widetilde{p}(\omega) = \alpha(\omega)E$$

which oscillates at the frequency of the driving field and whose amplitude $\widetilde{p}$ is related to the field amplitude E by the frequency dependent polarisability $\alpha(\omega)$. The interaction energy $H'(t)$ is determined by the coupling of this induced dipole moment to the

[1] For the two level system approximation to hold, the detuning $\delta = \omega_L - \omega_0$ between the light and the considered transition has to be small compared to the energy difference between the considered excited state $|\, e \,\rangle$ and any other excited state $|\, e' \,\rangle$ of the atom $\delta \ll (E'_e - E_e)$.

oscillating field: $H'(t) = -eE_0\vec{\epsilon}(\vec{r},t)\cos(k_L z - \omega_l t)\cdot\vec{r}$ and can be written in the basis of $|\,g\,\rangle$ and $|\,e\,\rangle$:

$$H'_{eg} = \hbar\Omega\cos(k\cdot z - \omega_L t),$$

where we have introduced the *Rabi-frequency*

$$\Omega = \frac{-eE_0}{\hbar}|\langle\, e\,|\vec{r}\vec{\epsilon}|\,g\,\rangle|.$$

To solve the remaining two Eqns. (C), two approximations have to be made. The first one – the so called rotating-wave approximation – is to neglected terms of order$1/\omega_L$ compared to terms of order $1/\delta$ where δ is the detuning of the laser frequency ω_L with respect to the atomic resonance frequency $\delta \equiv \omega_L - \omega_0$. Secondly, the spatial variation of the field amplitude $\epsilon(\vec{r},t)$ is neglected – the so called *dipole approximation*, which is reasonable because the wavelength λ of the laser field is much larger than the extension of the wave functions $\Phi_n(\vec{r})$. Under these estimations, Eqns. (C) decouple and $c_g(t)$ and $c_e(t)$ can be calculated. The probabilities of finding the atom in either state $|\,g\,\rangle$ or $|\,e\,\rangle$ are then the time dependent squares of the amplitudes $|c_g(t)|^2$ and $|c_e(t)|^2$, respectively. They oscillate at the effective Rabi-frequency $\Omega' = \sqrt{\Omega^2+\delta^2}$.
So far, we have only considered stimulated absorbtion and emission. In a semi-classical treatment, spontaneous emission can be accounted for by introducing a spontaneous exponential decay of the excited to the ground state at a certain rate Γ which is the inverse lifetime of the excited state $\tau = 1/\Gamma$. The optical Bloch equations describe the time evolution $i\hbar\frac{d\rho}{dt} = [H,\rho]$ of the density matrix

$$\rho = \begin{pmatrix} \rho_{ee} & \rho_{eg} \\ \rho_{ge} & \rho_{gg} \end{pmatrix} = \begin{pmatrix} c_e c_e^* & c_e c_g^* \\ c_g c_e^* & c_g c_g^* \end{pmatrix}. \tag{C.1}$$

under consideration of spontaneous emission. The solution for the probability of finding an atom in the excited state is

$$\rho_{ee} = \frac{1}{2}\frac{s}{1+s} = \frac{s_0/2}{1+s_0+(2\delta/\Gamma)^2}, \tag{C.2}$$

where

$$s = \frac{s_0}{1+(2\delta_{eff}/\Gamma)^2}, \tag{C.3}$$

$$s_0 = I/I_s, \tag{C.4}$$

$$I_s = \frac{\pi hc\Gamma}{3\lambda^3}, \tag{C.5}$$

$$\Omega = \Gamma\sqrt{s_0/2}. \tag{C.6}$$

The resonant saturation parameter s_0 normalises the intensity I of the resonant light field on the saturation intensity I_s of the two level system. $\delta_{eff} = \delta + \delta_D + \delta_Z ...$ is the

effective detuning in the rest frame of the atom and takes into account all shifts like Doppler- $\delta_D = \vec{k}\vec{v}$ and Zeeman-shift $\delta_Z = \Delta\mu B/\hbar$ in addition to the detuning of the laser. Here $\vec{v}$ is the velocity of the atom, $\vec{k}$ is the wave vector of the light field, B is the magnetic field and $\Delta\mu$ the difference between the magnetic moment in ground and excited state. If an atom is excited by a light field with the saturation intensity $I = I_s$ at resonance, i.e. vanishing effective detuning $\delta_{eff} = 0$, the population of the excited state is 1/4. A further increase of the intensity lets the excited state population approach its saturation value of 1/2 asymptotically.

The spontaneous force

In the stationary case where the excitation rate is equal to the rate Γ at which the excited state decays to the ground state, the total scattering rate in our two-level problem is given by the product of excited state population and decay rate:

$$\Gamma_{sc} = \Gamma\rho_{ee} = \frac{s_0\Gamma/2}{1 + s0 + (2\delta_{eff}/\Gamma)^2}$$

In every absorption process, the photon momentum $\hbar\mathbf{k}$ is transferred to the atom. The re-emission process is isotropic, such that the net momentum transfer by emission averaged over many absorption–re-emission cycles is zero whereas the momentum transferred during absorbtion processes is always directed along the direction of the laser. Thus the dissipative net force on the atom due to absorption, the so called *spontaneous force* or *radiation pressure* is given by

$$\vec{F}_{sp}(\vec{r}) = \hbar\vec{k}\Gamma_{sc}(\vec{r}). \tag{C.7}$$

The dipole force

The additional *conservative* force exerted on an atom by a spatially varying light field is best understood in the dressed atom picture that was used by Dalibard and Cohen-Tannoudji to explain the origin of this *dipole force* [172]. In the presence of the light field, the eigenvalues E_e and E_g of the undisturbed Hamiltonian H_0 are no longer eigenvalues of the full Hamiltonian $H(t) = H_0 + H'(t)$. Instead, one has to consider the coupled atom+laser system whose eigenstates are the so called *dressed states*. The eigenvalues differ from the free eigenenergies by a value which is proportional to the square of the local Rabi-frequency (*ac Stark shift or light shift*) and the new eigenstates are superpositions of the "bare" states $|\,g\,\rangle$ and $|\,e\,\rangle$. The shift is space dependent if the atom is placed in a spatially inhomogeneous light field. Thus the dipole force results from the gradient of this potential energy.

Light shifts and the dressed atom picture

In the dressed-atom picture, the Hamiltonian at a position $\vec{r}$ consists of three parts: the internal energy of the atom, the energy in the light mode and the atom-light coupling:

$$H(\vec{r}) = H_a + H_l + H_{al}.$$

Without the coupling between atom and laser mode, the eigenstates of Hamiltonian are given by manifolds $\varepsilon(N)$ consisting of two states $|\, g, N+1 \,\rangle$ and $|\, e, N \,\rangle$. The meaning of $|\, g, N+1 \,\rangle$ and $|\, e, N \,\rangle$ is here: atom in state $|\, g \,\rangle$ or $|\, e \,\rangle$ and $N+1$ or N photons in the laser mode, respectively. These states are separated by the energy $\hbar\delta$ which is small when we assume the detuning to be much smaller than the transition frequency $\delta = \omega_L - \omega_0 \ll \omega_0$. The manifolds $\varepsilon(N)$ in turn are separated by the energy $\hbar\omega_L$. Only the two states of each manifold are now coupled by the stimulated absorbtion of one photon from the field ($N+1 \rightarrow N$) and the transition $|\, g \,\rangle \rightarrow |\, e \,\rangle$ or the inverse process. The interaction energies are given by

$$\langle\, e, N \,|H_{al}|\, g, N+1 \,\rangle = \langle\, g, N+1 \,|H_{al}|\, e, N \,\rangle = -\sqrt{N+1}\vec{p}\vec{E}(\vec{r}) = \frac{1}{2}\hbar\Omega(\vec{r}).$$

The new eigenenergies of the manifold $\varepsilon(N)$ are

$$E_{1N}(\vec{r}) = (N+1)\hbar\omega_L - \frac{\hbar\delta}{2} + \frac{\hbar\Omega_{eff}(\vec{r})}{2},$$

$$E_{2N}(\vec{r}) = (N+1)\hbar\omega_L - \frac{\hbar\delta}{2} - \frac{\hbar\Omega_{eff}(\vec{r})}{2},$$

where

$$\Omega_{eff}(\vec{r}) = \sqrt{\Omega(\vec{r})^2 + \delta_{eff}(\vec{r})^2}$$

is the *effective Rabi-frequency*. The left diagram in Fig. C represents the eigenstates of the dressed Hamiltonian which are bunched in manifolds $\varepsilon(N)$. In the right diagram, the variation of the energy levels in radial direction within a Gaussian beam is illustrated. The corresponding eigenvectors are mixtures of the base vectors$|\, g, N+1 \,\rangle$ and $|\, e, N \,\rangle$:

$$|\, 1, N \,\rangle = +\cos\Theta|\, e, N \,\rangle + \sin\Theta|\, g, N+1 \,\rangle$$

$$|\, 2, N \,\rangle = -\sin\Theta|\, e, N \,\rangle + \cos\Theta|\, g, N+1 \,\rangle,$$

where Θ is the so called *Stückelberg angle* with, $\cos 2\Theta(\vec{r}) = -\frac{\delta}{\Omega_{eff}(\vec{r})}$,$\sin 2\Theta(\vec{r}) = \frac{\Omega(\vec{r})}{\Omega_{eff}(\vec{r})}$, $\tan 2\Theta = -\frac{\Omega}{\delta}$ and $\Omega = \Gamma\sqrt{I/2I_s}$.

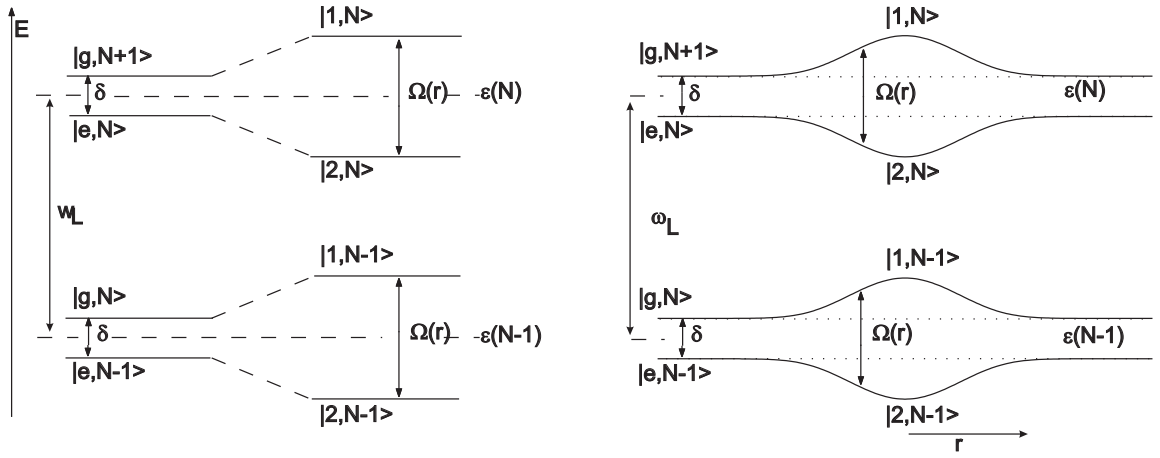

Figure C.1: Energy diagram in the dressed atom picture. Left: Eigenstates of the combined system of atom and laser-mode at a fixed position with and without coupling. The states form manifolds $\varepsilon(N)$ which are well separated by the laser frequency$\omega_L \gg \delta$. The coupling splits the two levels of a manifold by the Rabi frequency Ω. Without the coupling, the splitting is given by the detuning δ. Right: Dressed states in the field of a gaussian laser mode depending on the location r in the field. The splitting depends on the local Rabi frequency $\Omega(\vec{r})$. Outside the laser beam, the eigenstates approach the uncoupled states.

Mean dipole force

The spatial variation of the eigenenergies of the dressed states in an inhomogeneous light field leads to a force given by the gradient of the light shift

$$\vec{F}_{dip}(\vec{r}) = -\nabla U_{dip}(\vec{r})$$

Its sign is determined by the sign of δ and the state the atom is in. In a red detuned[2] laser field, the energy shift for the population Π_1 of state $|\,1, N\,\rangle$ is positive, i.e. an atom experiences a repulsive force from regions of high intensity, whereas for the population Π_2 of state $|\,2, N\,\rangle$ or blue detuning, the sign is inverted and the force points towards high intensities. Since the disturbed states $|\,1\,\rangle$ and $|\,2\,\rangle$ are both mixtures of the undisturbed states $|\,g\,\rangle$ and $|\,e\,\rangle$, spontaneous transitions are allowed between all states of a manifold $\varepsilon(N)$ and the manifold $\varepsilon(N+1)$ which results in the so called *Mollow triplet* [173] of fluorescence lines with frequencies $\omega_L \pm [\Omega_{eff}, 0]$. Consequently, the atom is found in a mixture of $|\,1\,\rangle$ and $|\,2\,\rangle$ and the probabilities Π_1 and Π_2 of finding an atom in these states are needed to calculate the exact resulting force:

$$\vec{F}_{dip}(\vec{r}) = -\Pi_1 \vec{\nabla} E_1(\vec{r}) - \Pi_2 \vec{\nabla} E_2(\vec{r})$$

[2] Red (blue) detuned in this context means that the laser frequency is lower (higher) than the resonance frequency of the atoms $\delta < 0$ ($\delta > 0$).

Formulating the equations of motion of the populations and setting the time derivative to zero, one gets the stationary populations

$$\Pi_1 = \frac{\sin^4\Theta}{\sin^4\Theta + \cos^4\Theta}, \Pi_2 = \frac{\cos^4\Theta}{\sin^4\Theta + \cos^4\Theta}.$$

The resulting total Potential is

$$U_{dip} = \frac{\hbar\delta}{2}\ln(1 + \frac{\Omega^2}{2\delta^2}).$$

when the logarithm is expanded to first order of $\frac{\Omega^2}{2\delta^2}$, this result is identical to the one of Eqn. (4.1.1). From Eqns. (C) and (C) one gets

$$\vec{F}_{dip} = -\frac{\hbar\delta}{4}\frac{\vec{\nabla} I/I_s}{1 + I/I_s + (2\delta/\Gamma)^2}.$$

This is the expression for an atom at rest where the population is always in equilibrium with the field. If the atom moves in the inhomogeneous field, the populations can not instantaneously follow the local intensity and start to deviate from the stationary distribution which results in an additional dissipative contribution to the dipole force. This non adiabatic effects have been discussed in [172] and shall only be mentioned at this point.
If a weak laser field is switched on adiabatically, the state that emerges from the uncoupled state $|\, g, N \,\rangle$ is the state $|\, 2, N \,\rangle$. Therefore, in a red detuned field, atoms which are initially in the ground state are attracted by regions of high intensity (high field seeking state). Neglecting the energy of the field $N\hbar\omega_L$ and the splitting $\hbar\delta$ which are identical for two levels of a manifold, the energies of the dressed states are

$$E_1(\vec{r}) = +\frac{1}{2}\hbar\Omega(\vec{r}), \qquad E_2(\vec{r}) = -\frac{1}{2}\hbar\Omega(\vec{r}) = -E_1(\vec{r}).$$

This leads to the well known energy diagram in the dressed atom picture depicted in C.

D A short recursive algorithm in Matlab to calculate the average number of scattered photons in an optical pumping process

The following Matlab program was used to calculate the average number of photons that are needed in the optical pumping process to bring an atom from $m_J = +3$ to $m_J = -3$ (see Section 4.8). The calculation weights every possible path from $m_J = +3$ to $m_J = -3$ with its statistical weight by recursively going along the path and multiplying the squares of the corresponding Clebsch-Gordan coefficients of all transitions from states $|\,^7P_3, m_J\,\rangle$ to $|\,^7S_3, m'_J\,\rangle$ that occur on the way with each other. Such a transition implies that a photon has been scattered before to bring the atom to state $|\,^7P_3, m_J\,\rangle$ and hence the product of the result of this multiplication with the number $n_{states,i}$ of visited $|\,^7P_3, m_J\,\rangle$ states yields the probability of scattering $n_{states,i}$ on path i. Without an exit condition, in principle arbitrarily long paths would be allowed and the calculation would never stop. Thus, if a path passes more than 25 states, the path is withdrawn because such paths are very unlikely. The average number of scattered photons is then given by the sum over all these paths. $n_{phot} = \sum_i n_{states,i}$.

```
function n=photcount
global CG;
CG=defCG;                          % table with Clebsch-Gordan coefficients
[n]=gs(3+6,0);                     % all paths start in m_J=+3
                                   % (+6 is to avoid negative indices)

%                                 ground state                                  %
%%%%%%%%%%%%%%%%%%%%%%%%%%%%%%%%%%%%%%%%%%%%%%%%%%%%%%%%%%%%%%%%%%%%%%%%%%%%%%%
function [n]=gs(j,n)               % function for the ground states
global CG;
persistent reccount;               % make table of recursion level persitent in gs
if isempty(reccount)               % if first call on path then generate an empty
    reccount=zeros(length(CG),1);  % array to map the number of recursive calls
                                   % (visits of state j)
end;
reccount(j)=reccount(j)+1;
if sum(reccount)>25,               % assume that paths where more than 25 states
    n=0;                           % are visited are very unlikely. Thus,
                                   % if number of recursive calls >25
```

```
                                % withdraw this path by setting photon count to 0
else
    if j<-3+6|j>3+6,            % only states mJ=-3..mJ=+3 exist
      n=0;                      % paths which end in mJ>+3 or mJ<-3 are invalid
    else
        if j==-3+6,             % this is the trivial case:
            n=n;                % if mJ=-3 the path is finished, return number of
                                % return number photons
        else
            n=n+1;              % photon count increased by one
            n=es(j-1,n);        % purely sigma- light ->
                                % transition happen only to excited state mJ'=mJ-1
        end;
    end;
    reccount(j)=0;
end;

%                               excited state                                   %
%%%%%%%%%%%%%%%%%%%%%%%%%%%%%%%%%%%%%%%%%%%%%%%%%%%%%%%%%%%%%%%%%%%%%%%%%%%%%%%
function [nout]=es(j,nin)
    global CG;
                                % from every excited state, there are
                                % three possible paths: decay to mJ'=[mJ+1, mJ, mJ-1].

    [n1]=gs(j-1,nin);           % number photons needed on that path
    p1=CG(j-1,j);               % probability (C.-G.^2 coefficient) of that path
    n1=n1;

    [n2]=gs(j,nin);
    p2=CG(j,j);
    n2=n2;
    j+1;

    [n3]=gs(j+1,nin);
    p3=CG(j+1,j);
    n3=n3;
    nout=n1*p1+n2*p2+n3*p3;     % return number of photons multiplied with their
                                % statistical weight

%  define squares of the Clebsch-Gordan coefficients for 7S3 -> 7P3 transition   %
%%%%%%%%%%%%%%%%%%%%%%%%%%%%%%%%%%%%%%%%%%%%%%%%%%%%%%%%%%%%%%%%%%%%%%%%%%%%%%%
function CG=defCG
CG(-5+6,-4+6)=0;CG(-4+6,-5+6)=0;CG(-4+6,-4+6)=0;CG(-4+6,-3+6)=0;
CG(-3+6,-4+6)=0;CG(-3+6,-3+6)=9/12;CG(-3+6,-2+6)=3/12;CG(-2+6,-3+6)=3/12;
CG(-2+6,-2+6)=4/12; CG(-2+6,-1+6)=5/12; CG(-1+6,-2+6)=5/12;
CG(-1+6,-1+6)=1/12; CG(-1+6,0+6)=6/12; CG(0+6,-1+6)=6/12;
CG(0+6,0+6)=0; CG(0+6,1+6)=6/12; CG(1+6,0+6)=6/12; CG(1+6,1+6)=1/12;
CG(1+6,2+6)=5/12; CG(2+6,1+6)=5/12; CG(2+6,2+6)=4/12;
```

```
CG(2+6,3+6)=3/12; CG(3+6,2+6)=3/12; CG(3+6,3+6)=9/12; CG(3+6,4+6)=0;
CG(4+6,3+6)=0; CG(4+6,4+6)=0; CG(4+6,5+6)=0; CG(5+6,4+6)=0;
```

E List of publications

Reviewed papers

A. Griesmaier, J. Stuhler, T. Koch, M. Fattori, T. Pfau, and S. Giovanazzi
"Comparing contact and dipolar interactions in a Bose-Einstein condensate"
Physical Review Letters **97**, 250402 (2006)

M. Fattori, T. Koch, S. Goetz, A. Griesmaier, S. Hensler, J. Stuhler, and T. Pfau,
"Demagnetization cooling of a gas"
Nature Physics **2**, 765 (2006)

J. Stuhler, A. Griesmaier, J. Werner, T. Koch, M. Fattori, and T. Pfau
"Ultracold chromium atoms: From Feshbach resonances to a dipolar Bose-Einstein condensate"
Journal of Modern Optics, Manuscript ID: 179869, (2006)

S. Giovanazzi, P. Pedri, L. Santos,
A. Griesmaier, M. Fattori, T. Koch, J. Stuhler, and T. Pfau
"Expansion dynamics of a dipolar Bose-Einstein condensate"
Physical Review A **74**, 013621 (2006)

A. Griesmaier, J. Stuhler and T. Pfau
"Production of a chromium Bose-Einstein condensate"
Applied Physics B **82**, 211-216 (2006) *invited paper*

J. Stuhler, A. Griesmaier, T. Koch, M. Fattori, T. Pfau,
S. Giovanazzi, P. Pedri, and L. Santos
"Observation of Dipole-Dipole Interaction in a Degenerate Quantum Gas"
Physical Review Letters **95**, 150406 (2005)

A. Griesmaier, J. Werner, S. Hensler, J. Stuhler and T. Pfau
"Bose-Einstein Condensation of Chromium"
Physical Review Letters **94**, 160401 (2005)

J. Werner, A. Griesmaier, S. Hensler, J. Stuhler, T. Pfau,
A. Simoni and E. Tiesinga
"Observation of Feshbach Resonances in an Ultracold Gas of [52]Cr"
Physical Review Letters **94**, 183201 (2005)

S. Hensler, A. Griesmaier, J. Werner, A. Görlitz, T. Pfau
"A two species trap for chromium and rubidium atoms"
Journal of Modern Optics **51**, 1807-1816 (2004)

S.Hensler, J. Werner, A. Griesmaier, P. O. Schmidt, A. Görlitz, T. Pfau,
K. Rzazewski and S. Giovanazzi
"Dipolar relaxation in an ultra-cold gas of magnetically trapped chromium atoms"
Applied Physics B **77**, 765-772 (2003)

P. O. Schmidt, S. Hensler, J. Werner, A. Griesmaier, A. Görlitz, T. Pfau, and A. Simoni
"Determination of the s-Wave Scattering Length of Chromium"
Physical Review Letters **91**, 193201 (2003)

Conference Proceedings

A. Griesmaier, J. Stuhler and T. Pfau
"Observation of Bose-Einstein condensation in a gas of chromium atoms"
in *Laser Spectroscopy XVII - Proceedings of the XVII International Conference*,
World Scientific, Singapore (2006)

A. Griesmaier, J. Stuhler and T. Pfau
"Observation of Feshbach resonances and Bose-Einstein condensation in a gas of chromium atoms"
in *Proceedings of SPIE* Vol. 6256 "ICONO 2005",
Bellingham WA, USA (2006)

Bibliography

[1] A. Griesmaier, J. Werner, S. Hensler, J. Stuhler, and T. Pfau: "Bose-Einstein Condensation of Chromium". *Physical Review Letters* **94** ,160401 (2005). v, 1, 103

[2] J. Stuhler, A. Griesmaier, T. Koch, M. Fattori, T. Pfau, S. Giovanazzi, P. Pedri, and L. Santos: "Observation of Dipole-Dipole Interaction in a Degenerate Quantum Gas". *Physical Review Letters* **95** ,150406 (2005). v, 115

[3] M. H. Anderson, J. R. Ensher, M. R. Matthews, C. E. Wieman, and E. A. Cornell: "Observation of Bose-Einstein Condensation in a Dilute Atomic Vapor". *Science* **269** ,198 (1995). v, 1

[4] K. B. Davis, M.-O. Mewes, M. R. Andrews, N. J. van Druten, D. S. Durfee, D. M. Kurn, and W. Ketterle: "Bose-Einstein Condensation in a Gas of Sodium Atoms". *Physical Review Letters* **75** ,3969 (1995). v, 1

[5] C. C. Bradley, C. A. Sackett, J. J. Tollett, and R. G. Hulet: "Evidence of Bose-Einstein Condensation in an Atomic Gas with Attractive Interactions". *Physical Review Letters* **75** ,1687 (1995). v, 1

[6] G. Modugno, G. Ferrari, G. Roati, R. J. Brecha, A. Simoni, and M. Inguscio: "Bose-Einstein Condensation of Potassium Atoms by Sympathetic Cooling". *Science* **294** ,1320 (2001). v, 1

[7] T. Weber, J. Herbig, M. Mark, H.-C. Nägerl, and R. Grimm: "Bose-Einstein Condensation of Cesium". *Science* **299** ,232–235 (2003). v, 1, 82, 83

[8] D. G. Fried, T. C. Killian, L. Willmann, D. Landhuis, S. C. Moss, D. Kleppner, and T. J. Greytak: "Bose-Einstein Condensation of Atomic Hydrogen". *Physical Review Letters* **81** ,3811 (1998). v, 1

[9] A. Robert, O. Sirjean, A. Browaeys, J. Poupard, S. Nowak, D. Boiron, and C. W. A. Aspect: "A Bose-Einstein of Metastable Atoms". *Science* **292** ,461–464 (2001). v, 1, 128, 138

[10] Y. Takasu, K. Maki, K. Komori, T. Takano, K. Honda, M. Kumakura, T. Yabuzaki, and Y. Takahashi: "Spin-Singlet Bose-Einstein Condensation of Two-Electron Atoms". *Physical Review Letters* **91** ,040404 (2003). v, 1, 83

[11] K. W. Madison, F. Chevy, W. Wohlleben, and J. Dalibard: "Vortex Formation in a Stirred Bose-Einstein Condensate". *Physical Review Letters* **84** ,806–809 (2000). vi, 2

[12] M. R. Matthews, B. P. Anderson, P. C. Haljan, D. S. Hall, C. E. Wieman, and E. A. Cornell: "Vortices in a Bose-Einstein Condensate". *Physical Review Letters* **83** ,2498–2501 (1999). vi, 2

[13] J. R. Abo-Shaeer, C. Raman, J. M. Vogels, and W. Ketterle: "Observation of Vortex Lattices in Bose-Einstein Condensates". *Science* **292** ,476–479 (2001). vi, 2

[14] E. A. Donley, N. R. Claussen, S. L. Cornish, J. L. Roberts, E. A. Cornell, and C. E. Wieman: "Dynamics of collapsing and exploding Bose-Einstein condensates". *Nature* **412** ,295 (2001). vi, 2, 116, 138

[15] M. Greiner, O. Mandel, T. Esslinger, T. Hänsch, and I. Bloch: "Quantum Phase Transition from a Superfluid to a Mott Insulator in a Gas of Ultracold Atoms". *Nature* **415** ,39 (2002). vi, 2, 52

[16] T. Stoferle, H. Moritz, C. Schori, M. Kohl, and T. Esslinger: "Transition from a Strongly Interacting 1D Superfluid to a Mott Insulator". *Physical Review Letters* **92** ,130403 (2004). vi, 2

[17] B. Paredes, A. Widera, V. Murg, O. Mandel, S. Fölling, I. Cirac, G. V. Shlyapnikov, T. W. Hänsch, and I. Bloch: "Tonks-Girardeau gas of ultracold atoms in an optical lattice". *Nature* **429** ,277 (2004). vi, 2

[18] I. Bloch: "Ultracold quantum gases in optical lattices". *Nature Physics* **1** ,1745–2473 (2005). vi, 3

[19] J. Werner, A. Griesmaier, S. Hensler, A. Simoni, E. Tiesinga, J. Stuhler, and T. Pfau: "Observation of Feshbach resonances in an ultracold gas of ^{52}Cr". *Physical Review Letters* **94** ,183201 (2005). vi, 4, 106, 116, 117, 126, 132, 143, 147

[20] H. F. Hess: "Evaporative cooling of magnetically trapped and compressed spin-polarized hydrogen". *Physical Review B* **34** ,3476–3479 (1986). vii, 73

[21] N. Masuhara, J. M. Doyle, J. C. Sandberg, D. Kleppner, T. J. Greytak, H. F. Hess, and G. P. Kochanski: "Evaporative cooling of spin-polarized atomic hydrogen". *Physical Review Letters* **61** ,935–938 (1988). vii, 73

[22] K. B. Davis, M.-O. Mewes, M. A. Joffe, M. R. Andrews, and W. Ketterle: "Evaporative cooling of sodium atoms". *Physical Review Letters* **74** ,5202–5205 (1995). vii, 65, 73, 132

[23] W. Petrich, M. H. Anderson, J. R. Ensher, and E. A. Cornell: "Evaporative cooling of rubidium atoms in a magnetic trap. ". In C. Wieman and D. Wineland, editors, *Atomic Physics 14*New York (1994).AIP. vii, 65, 73

[24] W. Ketterle and D. E. Prichard: "Trapping and Focusing Ground State Atoms with Static Fields". *Appl. Phys. B* **54** ,403 (1992). vii

[25] S. Hensler, J. Werner, A. Griesmaier, P. O. Schmidt, A. Görlitz, T. Pfau, and K. R. S. Giovanazzi: "Dipolar Relaxation in an ultra-cold gas of magnetically trapped chromium atoms". *Appl. Phys. B* **77** ,765–772 (2003). vii, 4

[26] K. Goral, K. Rzazewski, and T. Pfau: "Bose-Einstein condensation with magnetic dipole-dipole forces". *Physical Review A* **61** ,051601 (2000). viii, 3, 116, 117

[27] L. Santos, G. V. Shlyapnikov, P. Zoller, and M. Lewenstein: "Bose-Einstein Condensation in Trapped Dipolar Gases". *Physical Review Letters* **85** ,1791–1794 (2000). viii, 3

[28] S. Yi and L. You: "Trapped atomic condensates with anisotropic interactions". *Physical Review A* **61** ,041604 (2000). viii, 3, 121

[29] S. Yi and L. You: "Trapped condensates of atoms with dipole interactions". *Physical Review A* **63** ,053607 (2001). viii, 3, 121

[30] K. Goral and L. Santos: "Ground state and elementary excitations, of single and binary Bose-Einstein condensates of trapped dipolar gases". *Physical Review A* **66** ,023613 (2002). viii, 3

[31] D. H. J. O'Dell, S. Giovanazzi, and C. Eberlein: "Exact Hydrodynamics of a Trapped Dipolar Bose-Einstein Condensate". *Physical Review Letters* **92** ,250401 (2004). viii, 3, 117, 118

[32] L. Santos, G. V. Shlyapnikov, and M. Lewenstein: "Roton-Maxon Spectrum and Stability of Trapped Dipolar Bose-Einstein Condensates". *Physical Review Letters* **90** ,250403 (2003). viii, 3, 138

[33] L. Santos and T. Pfau: "Spin-3 Chromium Bose-Einstein Condensates". *Physical Review Letters* **96** ,190404 (2006). viii, 3

[34] R. B. Diener and T.-L. Ho: "[sup 52]Cr Spinor Condensate: A Biaxial or Uniaxial Spin Nematic". *Physical Review Letters* **96** ,190405 (2006). viii, 3

[35] Y. Kawaguchi, H. Saito, and M. Ueda: "Einstein–de Haas Effect in Dipolar Bose-Einstein Condensates". *Physical Review Letters* **96** ,080405 (2006). viii, 3

[36] K. Góral, L. Santos, and M. Lewenstein: "Quantum Phases of Dipolar Bosons in Optical Lattices". *Physical Review Letters* **88** ,170406 (2002). viii, 3, 138

[37] N. R. Cooper, E. H. Rezayi, and S. H. Simon: "Vortex Lattices in Rotating Atomic Bose Gases with Dipolar Interactions". *Physical Review Letters* **95** ,200402 (2005). viii, 3

[38] E. H. Rezayi, N. Read, and N. R. Cooper: "Incompressible Liquid State of Rapidly Rotating Bosons at Filling Factor 3/2". *Physical Review Letters* **95** ,160404 (2005). viii, 3

[39] J. Zhang and H. Zhai: "Vortex Lattices in Planar Bose-Einstein Condensates with Dipolar Interactions". *Physical Review Letters* **95** ,200403 (2005). viii, 3

[40] S. Giovanazzi, A. Görlitz, and T. Pfau: "Tuning the Dipolar Interaction in Quantum Gases". *Physical Review Letters* **89** ,130401 (2002). viii, 3, 116, 118, 138

[41] E. W. Streed, A. P. Chikkatur, T. L. Gustavson, M. Boyd, Y. Torii, D. Schneble, G. K. Campbell, D. E. Pritchard, and W. Ketterle: "Large atom number Bose-Einstein condensate machines". *Review of Scientific Instruments* **77** ,023106 (2006). 1, 15

[42] A. G. Truscott, K. E. Strecker, W. I. McAlexander, G. B. Partridge, and R. G. Hulet: "Observation of Fermi Pressure in a Gas of Trapped Atoms". *Science* **291** ,2570–2572 (2001). 1

[43] H. C. W. Beijerinck, E. J. D. Vredenbregt, R. J. W. Stas, M. R. Doery, and J. G. C. Tempelaars: "Prospects for Bose-Einstein condensation of metastable neon atoms". *Physical Review A* **61** ,023607 (2000). 1

[44] V. Vuletic, A. J. Kerman, C. Chin, and S. Chu: "Observation of Low-Field Feshbach Resonances in Collisions of Cesium Atoms". *Physical Review Letters* **82** ,1406–1409 (1999). 1

[45] C. Chin, V. Vuletic, A. J. Kerman, and S. Chu: "High Resolution Feshbach Spectroscopy of Cesium". *Physical Review Letters* **85** ,2717–2720 (2000). 1

[46] P. J. Leo, C. J. Williams, and P. S. Julienne: "Collision Properties of Ultracold [sup 133]Cs Atoms". *Physical Review Letters* **85** ,2721–2724 (2000). 1

[47] A. Griesmaier, J. Stuhler, and T. Pfau: "Production of a chromium Bose-Einstein condensate". *Appl. Phys. B* **82** ,211–216 (2006). 1, 4, 103

[48] M. Weidemüller and C. Zimmermann: "Interactions in Ultracold Gases" . Wiley-VCH Verlag GmbH, Berlin (2003). and references therein. 2

[49] J. R. Anglin and W. Ketterle: "Bose-Einstein condensation of atomic gases". *Nature* **416** ,211–218 (2002). and references therein. 2

[50] J. R. Ensher, D. S. Jin, M. R. Matthews, C. E. Wieman, and E. A. Cornell: "Bose-Einstein Condensation in a Dilute Gas: Measurement of Energy and Ground-State Occupation". *Physical Review Letters* **77** ,4984–4987 (1996). 2, 44

[51] M.-O. Mewes, M. R. Andrews, N. J. van Druten, D. M. Kurn, D. S. Durfee, and W. Ketterle: "Bose-Einstein Condensation in a Tightly Confining dc Magnetic Trap". *Physical Review Letters* **77** ,416 (1996). 2, 27, 53, 65, 132

[52] M.-O. Mewes, M. R. Andrews, N. J. van Druten, D. M. Kurn, D. S. Durfee, C. G. Townsend, and W. Ketterle: "Collective Excitations of a Bose-Einstein Condensate in a Magnetic Trap". *Physical Review Letters* **77** ,988–991 (1996). 2

[53] D. M. Stamper-Kurn, H.-J. Miesner, S. Inouye, M. R. Andrews, and W. Ketterle: "Collisionless and Hydrodynamic Excitations of a Bose-Einstein Condensate". *Physical Review Letters* **81** ,500–503 (1998). 2

[54] D. M. Stamper-Kurn, A. P. Chikkatur, A. Gorlitz, S. Inouye, S. Gupta, D. E. Pritchard, and W. Ketterle: "Excitation of Phonons in a Bose-Einstein Condensate by Light Scattering". *Physical Review Letters* **83** ,2876–2879 (1999). 2

[55] S. Jochim, M. Bartenstein, A. Altmeyer, G. Hendl, S. Riedl, C. Chin, J. Hecker Denschlag, and R. Grimm: "Bose-Einstein Condensation of Molecules". *Science* **302** ,2101–2103 (2003). 2

[56] C. A. Regal, M. Greiner, and D. S. Jin: "Observation of Resonance Condensation of Fermionic Atom Pairs". *Physical Review Letters* **92** ,040403 (2004). 2

[57] M. W. Zwierlein, C. A. Stan, C. H. Schunck, S. M. F. Raupach, S. Gupta, Z. Hadzibabic, and W. Ketterle: "Observation of Bose-Einstein Condensation of Molecules". *Physical Review Letters* **91** ,250401 (2003). 2

[58] C. Chin, M. Bartenstein, A. Altmeyer, S. Riedl, S. Jochim, J. H. Denschlag, and R. Grimm: "Observation of the Pairing Gap in a Strongly Interacting Fermi Gas". *Science* **305** ,1128–1130 (2004). 2

[59] T. Bourdel, L. Khaykovich, J. Cubizolles, J. Zhang, F. Chevy, M. Teichmann, L. Tarruell, S. J. J. M. F. Kokkelmans, and C. Salomon: "Experimental Study of the BEC-BCS Crossover Region in Lithium 6". *Physical Review Letters* **93** ,050401 (2004). 2

[60] M. W. Zwierlein, C. A. Stan, C. H. Schunck, S. M. F. Raupach, A. J. Kerman, and W. Ketterle: "Condensation of Pairs of Fermionic Atoms near a Feshbach Resonance". *Physical Review Letters* **92** ,120403 (2004). 2

[61] M. Bartenstein, A. Altmeyer, S. Riedl, S. Jochim, C. Chin, J. H. Denschlag, and R. Grimm: "Crossover from a Molecular Bose-Einstein Condensate to a Degenerate Fermi Gas". *Physical Review Letters* **92** ,120401 (2004). 2

[62] C. A. Regal, M. Greiner, and D. S. Jin: "Observation of Resonance Condensation of Fermionic Atom Pairs". *Physical Review Letters* **92** ,040403 (2004). 2

[63] J. Kinast, S. L. Hemmer, M. E. Gehm, A. Turlapov, and J. E. Thomas: "Evidence for Superfluidity in a Resonantly Interacting Fermi Gas". *Physical Review Letters* **92** ,150402 (2004). 2

[64] S. Giovanazzi, A. Görlitz, and T. Pfau: "Ballistic expansion of a dipolar condensate". *J. Opt. B: Quantum Semiclass. Opt.* **5** ,S208–S211 (2003). 3, 121, 122

[65] P. Pedri and L. Santos: "Two-dimensional bright solitons in dipolar Bose-Einstein condensates. ". arXiv: cond-mat/0503019 (2005). 3

[66] A. S. Bell, J. Stuhler, S. Locher, S. Hensler, J. Mlynek, and T. Pfau: "A magneto–optical trap for chromium with population repumping via intercombination lines". *Europhys. Lett.* **45** ,156–161 (1999). 4

[67] J. Stuhler, P. O. Schmidt, S. Hensler, J. Werner, J. Mlynek, and T. Pfau: "Continuous loading of a magnetic trap". *Physical Review A* **64** ,031405(R) (2001). 4, 62

[68] J. Stuhler: "Kontinuierliches Laden einer Magnetfalle mit lasergekühlten Chromatomen. " PhD thesis. Universität Konstanz, Lehrstuhl J. Mlynek, Ufo-Verlag, Allensbach (2002). 4, 25, 27, 63, 139

[69] P. O. Schmidt, S. Hensler, J. Werner, T. Binhammer, A. Görlitz, and T. Pfau: "Continuous loading of cold atoms into a Ioffe-Pritchard magnetic trap". *J. Opt. B: Quantum Semiclass. Opt.* **5** ,S170–S177 (2003). 4, 62, 141

[70] P. O. Schmidt, S. Hensler, J. Werner, A. Griesmaier, A. Görlitz, and T. Pfau: "Determination of the s-wave Scattering Length of Chromium". *Physical Review Letters* **91** ,193201 (2003). 4, 75, 133

[71] P. O. Schmidt, S. Hensler, J. Werner, T. Binhammer, A. Görlitz, and T. Pfau: "Doppler cooling of an optically dense cloud of trapped atoms". *J. Opt. Soc. Am. B* **20** ,960–967 (2003). 4, 63

[72] J. D. Weinstein, R. deCarvalho, C. I. Hancox, and J. M. Doyle: "Evaporative cooling of atomic chromium". *Phys. Rev. A* **65** ,021604 (2002). 4

[73] J. D. Weinstein, R. Decarvalho, J. Kim, D. Patterson, B. Friedrich, and J. M. Doyle: "Magnetic trapping of atomic chromium". *Physical Review A* **57** ,3173 (1998). 4

[74] L. D. Landau and E. Lifshitz: "Course of theoretical physics: Statistical Physics Part 1" , Vol. 5 . Butterworth-Heinemann, Oxford, United Kingdom, 3. edition (1980). 7

[75] J. E. Robinson: "Note on the Bose-Einstein Integral Functions". *Physical Review* **83** ,678–679 (1951). 11

[76] V. Bagnato, D. E. Pritchard, and D. Kleppner: "Bose-Einstein condensation in an external potential". *Physical Review A (General Physics)* **35** ,4354–4358 (1987). 14, 43, 76

[77] A. S. Tychkov, T. Jeltes, J. M. McNamara, P. J. J. Tol, N. Herschbach, W. Hogervorst, and W. Vassen: "A Large Atom Number Metastable Helium Bose-Einstein Condensate. ". arXiv: cond-mat/0510006 (2005). 15

[78] W. Ketterle and N. J. van Druten: "Bose-Einstein condensation of a finite number of particles trapped in one or three dimensions". *Physical Review A* **54** ,656–660 (1996). 16

[79] F. Dalfovo, S. Giorgini, L. P. Pitaevskii, and S. Stringari: "Theory of Bose-Einstein condensation in trapped gases". *Reviews of Modern Physics* **71** ,463–512 (1999). 16, 21, 118, 121

[80] P. S. Julienne: "Ultra-cold Collisions of Atoms and Molecules. ". In E. R. Pike and P. Sabatier, editors, *Scattering*, Vol. 2 of *Direct and Inverse Scattering in Pure and Applied Science*Chap. 2.6.3, pages 1043–1067.Academic PressNew York (2001). 17, 143

[81] J. Weiner, V. S. Bagnato, S. Zilio, and P. S. Julienne: "Experiments and theory in cold and ultracold collisions". *Rev. Mod. Phys.* **71** ,1–85 (1999). 17, 76, 143

[82] J. Weiner: "Cold and Ultracold Collisions in Quantum Microscopic and Mesoscopic Systems" . Cambridge University Press, The Edinburgh Building, Cambridge CB2 2RU, UK (2003). 17, 143

[83] V. V. Goldman, I. F. Silvera, and A. J. Leggett: "Atomic hydrogen in an inhomogeneous magnetic field: Density profile and Bose-Einstein condensation". *Physical Review B* **24** ,2870–2873 (1981). 20

[84] S. Giorgini, L. P. Pitaevskii, and S. Stringari: "Condensate fraction and critical temperature of a trapped interacting Bose gas". *Physical Review A* **54** ,R4633–R4636 (1996). 21

[85] Y. Castin and R. Dum: "Bose-Einstein condensates in time dependent traps". *Physical Review Letters* **77** ,5315 (1996). 22, 121

[86] S. Hensler: "Wechselwirkungen in ultrakalten dipolaren Gasen. " PhD thesis. 5. Physikalisches Institut, Universität Stuttgart, Pfaffenwaldring 57, 70550 Stuttgart (2003). 25, 68, 69, 73, 83, 139

[87] A. Griesmaier: "Aufbau einer kombinierten magneto-optischen Falle für Chrom und Rubidium. " Diplomarbeit. 5. Physikalisches Institut, Universität Stuttgart, (2002). 25, 27

[88] P. O. Schmidt: "Scattering properties of ultra-cold chromium atoms. " PhD thesis. Universität Stuttgart, 5. Physikalisches Institut, 70550 Stuttgart (2003). 25, 27, 139, 141

[89] J. Werner: "Observation of Feshbach resonances in an ultracold gas of 52Cr. " PhD thesis. 5. Physikalisches Institut, Universität Stuttgart, 70550 Stuttgart (2006). Verlag Dr. Hut, München, ISBN 3-89963-384-9 (2006). 25, 27, 31, 143

[90] J. Werner: "Kontinuierliches Laden einer Magnetfalle mit lasergekühlten Chromatomen. " Diplomarbeit. Universität Konstanz, (2000). 25, 27

[91] L. Ricci, M. Weidemüller, T. Esslinger, A. Hemmerich, C. Zimmermann, V. Vuletic, W. König, and T. W. Hänsch: "A compact grating-stabilized diode laser system for atomic physics". *Opt. Comm.* **117** ,541–549 (1995). 27

[92] S. Hensler: "Eine magneto-optische Falle mit Chromatomen. " diploma thesis. Universität Konstanz, Lehrstuhl J. Mlynek, (1999). 27

[93] R. W. P. Drever, J. L. Hall, F. V. Kowalski, J. Hough, G. M. Ford, A. J. Munley, and H. Ward: "Laser phase and frequency stabilization using an optical resonator". *Appl. Phys. B* **31** ,97 (1983). 28

[94] J. P. Bouyer: "Spectral stabilization of an InGaAsP Semiconductor laser by injection-locking.". *Annales de Physique* **18** ,89 (1993). 29

[95] E. S. Polzik and H. J. Kimble: "Frequency doubling with $KNbO_3$ in an external cavity". *Opt. Lett.* **16** ,1400 (1991). 29

[96] G. J. Mizell, W. R. Fay, J. Harrison, and G. J. Dixon: "Performance of $KNbO_3$ in the generation of blue laser light using Ti:Al_2O_3. ". In *Proc. SPIE*, Vol. 1104 page 61 (1989). 29

[97] B. Steinheil: "Aufbau eines frequenzverdoppelten Dodenlaser-Systems zur Untersuchung ultrakalter Chromatome. " Diploma thesis. 5. Physikalisches Institut, Universität Stuttgart, Pfaffenwaldring 57, 70550 Stuttgart (2003). 29

[98] A. Marte: "Feshbach-Resonanzen bei Stößen ultrakalter Rubidiumatome. " PhD thesis. Technische Universität, München (2003). 36

[99] M. Brinkmann and J. Kronjäger. Institut für Laser-Physik, Universität Hamburg, presented at the DPG spring meeting, Berlin, March 2005 and private communication (2005). 37

[100] M. R. Andrews, C. G. Townsend, H.-J. Miesner, D. S. Durfee, D. M. Kurn, and W. Ketterle: "Observation of interference between two Bose condensates". *Science* **275** ,637 (1997). 41

[101] S. Kunze, S. Dürr, K. Dieckmann, M. Elbs, U. Ernst, A. Hardell, S. Wolf, and G. Rempe: "Standing wave diffraction with a beam of slow atoms". *J. of Mod. Opt.* **44** ,1863–1881 (1997). 42

[102] D. M. Stamper-Kurn: "Peeking and poking at a new quantum fluid: Studies of gaseous Bose-Einstein condensates in magnetic and optical traps. " PhD thesis. Massachusetts Institute of Technology, (2000). 44, 66, 83

[103] H. Metcalf and P. van der Straten: "Laser Cooling and Trapping" . Springer, New York (1999). 47, 73

[104] C. Cohen-Tannoudji and S. Reynaud: "Dressed-atom descriptiom of resonance fluorescence and absorption spectra of a multi-level atom in an intense laser beam". *J. Phys. B: At. Mol. Opt. Phys.* **10** ,345 (1977). 47

[105] C. Cohen-Tannoudji, J. Dupont-Roc, and G. Grynberg: "Atom-photon interactions" . John Wiley & Sons, , 1. edition (1992). 47

[106] R. Grimm, M. Weidemüller, and Y. B. Ovchinnikov: "Optical dipole traps for neutral atoms". *Advances in Atomic, Molecular, and Optical Physics* **42** ,95–170 (2000). 48, 58

[107] I. Manek, U. Moslener, Y. Ovchinnikov, P. Rosenbusch, A. Sidorov, G. Wasik, M. Zielonkowski, and R. Grimm: "Novel dipole-force atom traps. ". In G. Drake, editor, *Proceedings of the International Conference on Atomic Physics (ICAP-16)* (1998). 48, 55

[108] NIST. Atomic Spectra Databases (2003). 50, 55

[109] K. Dieckmann: "Bose-Einstein Condensation with High Atom Number in a Deep

Magnetic Trap. " PhD Thesis. FOM-Instituut voor Atoom- en Molecuulfysica (AMOLF), The Netherlands, (2001). 58

[110] S. R. Granade: "All-Optical Production of a Degenerate Gas of 6Li: Characterization of Degeneracy. " PhD thesis. Department of Physics Duke University, (2002). 58

[111] H. Nyquist: "Certain topics in telegraph transmission theory". *Trans. AIEE* **47** ,617– 644 (1928). 59

[112] A. B. Pippard: "The physics of vibrations" . Cambridge University Press, Cambridge, United Kingdom (1978). chapter 11. 60

[113] L. D. Landau and E. Lifshitz: "Course of theoretical physics: Mechanics" , Vol. 1 . Butterworth-Heinemann, Oxford, United Kingdom, 3. edition (1976). 60

[114] S. Chu, L. Hollberg, J. E. Bjorkholm, A. Cable, and A. Ashkin: "Three-Dimensional Viscous Confinement and Cooling of Atoms by Resonance Radiation Pressure". *Physical Review Letters* **55** ,48 (1985). 63

[115] S. Hensler, A. Greiner, J. Stuhler, and T. Pfau: "Depolarisation cooling of an atomic cloud". *Europhys. Lett.* **71** ,918 (2005). 69

[116] G. Delannoy, S. G. Murdoch, V. Boyer, V. Josse, P. Bouyer, and A. Aspect: "Understanding the production of dual Bose-Einstein condensation with sympathetic cooling". *Physical Review A* **63** ,051602 (2001). 75

[117] M. Mudrich, S. Kraft, K. Singer, R. Grimm, A. Mosk, and M. Weidemuller: "Sympathetic Cooling with Two Atomic Species in an Optical Trap". *Physical Review Letters* **88** ,253001 (2002). 75

[118] O. J. Luiten, M. W. Reynolds, and J. T. M. Walraven: "Kinetic theory of the evaporative cooling of a trapped gas". *Physical Review A* **53** ,381–389 (1996). 75, 76, 80

[119] K. M. O'Hara, M. E. Gehm, S. R. Granade, and J. E. Thomas: "Scaling laws for evaporative cooling in time-dependent optical traps". *Physical Review A* **64** ,051403 (2001). 75, 77

[120] G. Cennini, G. Ritt, C. Geckeler, and M. Weitz: "All-Optical Realization of an Atom Laser". *Physical Review Letters* **91** (2003). 78

[121] P. W. H. Pinkse, A. Mosk, M. Weidemuller, M. W. Reynolds, T. W. Hijmans, and J. T. M. Walraven: "One-dimensional evaporative cooling of magnetically trapped atomic hydrogen". *Physical Review A* **57** ,4747–4760 (1998). 80

[122] E. L. Surkov, J. T. M. Walraven, and G. V. Shlyapnikov: "Collisionless motion and evaporative cooling of atoms in magnetic traps". *Physical Review A* **53** ,3403–3408 (1996). 80

[123] P. W. H. Pinkse, A. Mosk, M. Weidemuller, M. W. Reynolds, T. W. Hijmans, and J. T. M. Walraven: "Adiabatically Changing the Phase-Space Density of a Trapped Bose Gas". *Physical Review Letters* **78** ,990–993 (1997). 82

[124] D. M. Stamper-Kurn, H.-J. Miesner, A. P. Chikkatur, S. Inouye, J. Stenger, and W. Ketterle: "Reversible Formation of a Bode-Einstein condensate". *Physical Review Letters* **81** ,2194 (1998). 82

[125] C. S. Adams, H. J. Lee, N. Davidson, M. Kasevich, and S. Chu: "Evaporative cooling in a crossed dipole trap". *Physical Review Letters* **74** ,3577–3580 (1995). 83

[126] M. D. Barrett, J. A. Sauer, and M. S. Chapman: "All-Optical Formation of an Atomic Bose-Einstein Condensate". *Physical Review Letters* **87** ,010404 (2001). 83

[127] M. Hammes, D. Rychtarik, H.-C. Nagerl, and R. Grimm: "Cold-atom gas at very high densities in an optical surface microtrap". *Physical Review A* **66** ,051401 (2002). 83

[128] L. Viverit, S. Giorgini, L. P. Pitaevskii, and S. Stringari: "Adiabatic compression of a trapped Fermi gas". *Physical Review A* **63** ,033603 (2001). 83

[129] G. A. Bird: "Molecular Gas Dynamics and the direct simulation of gas flow." . Clarendon Press, Oxford, UK (1994). 90

[130] H. Wu and C. Foot: "Direct simulation of evaporative cooling". *J. Phys. B: At. Mol. Opt. Phys.* **29** ,L321 (1996). 90, 92, 93, 102

[131] Z.-Y. Ma, A. M. Thomas, C. J. Foot, and S. L. Cornish: "The evaporative cooling of a gas of caesium atoms in the hydrodynamic regime". *J. Phys. B: At. Mol. Opt. Phys.* **36** ,3533 (2003). 90, 92, 102

[132] A. M. Thomas: "Ultra-cold Collisions and Evaporative Cooling of Caesium in a Magnetic Trap. " PhD thesis. University of Oxford:2004, (2004). 90, 92

[133] E. Cerboneschi, C. Menchini, and E. Arimondo: "Monte Carlo simulations of Bose-Einstein condensation of trapped atoms". *Physical Review A* **62** ,013606 (2000). 90, 92

[134] F. Ercolessi: "A molecular dynamics primer; Spring College in Computational

Physics, ICTP, Trieste 1997" . International School for Advanced Studies (SISSA-ISAS), Trieste, Italy (1997). 92

[135] J. M. Haile: "Molecular dynamics simulation : elementary methods" . Wiley-Interscience, New York, NY, USA, xvii. edition (1997). 92

[136] G. Box and M. Muller: "A note on the generation of random normal deviates". *Annals Math. Stat* **29** ,610–611 (1958). 94

[137] R. P. Feynman, R. B. Leighton, and M. Sands: "The Feynman Lectures on Physics. " , Vol. 1 Chap. 9 "Newton's Laws of Dynamics". Addison-Wesley (1963). 95

[138] Y. Kagan, B. V. Svistunov, and G. V. Shlyapnikov: "Effect of Bose condensation on inelastic processes in gases". *JETP Letters* **42** ,209–212 (1985). 101

[139] E. A. Burt, R. W. Ghrist, C. J. Myatt, M. J. Holland, E. A. Cornell, and C. E. Wieman: "Coherence, Correlations, and Collisions: What One Learns about Bose-Einstein Condensates from Their Decay". *Physical Review Letters* **79** ,337–340 (1997). 101, 109, 110

[140] Y. Kagan, E. L. Surkov, and G. V. Shlyapnikov: "Evolution of a Bose gas in anisotropic time-dependent traps". *Physical Review A* **55** ,R18–R21 (1997). 108

[141] I. Shvarchuck, C. Buggle, D. S. Petrov, M. Kemmann, W. von Klitzing, G. V. Shlyapnikov, and J. T. M. Walraven: "Hydrodynamic behavior in expanding thermal clouds of [sup 87]Rb". *Physical Review A* **68** ,063603 (2003). 108

[142] J. Schuster, A. Marte, S. Amtage, B. Sang, G. Rempe, and H. C. W. Beijerinck: "Avalanches in a Bose-Einstein Condensate". *Physical Review Letters* **87** ,170404 (2001). 110

[143] T. A. Savard, K. M. O'Hara, and J. E. Thomas: "Laser-noise-induced heating in far-off resonance optical traps". *Physical Review A* **56** ,R1095–R1098 (1997). 110

[144] A. Griesmaier, J. Stuhler, T. Koch, M. Fattori, T. Pfau, and S. Giovanazzi: "Comparing contact and dipolar interactions in a Bose-Einstein condensate". *Physical Review Letters* (2006). in press. 115

[145] S. Giovanazzi, P. Pedri, L. Santos, A. Griesmaier, M. Fattori, T. Koch, J. Stuhler, and T. Pfau: "Expansion dynamics of a dipolar Bose-Einstein condensate". *Physical Review A* **74** ,013621 (2006). 115

[146] C. Eberlein, S. Giovanazzi, and D. H. J. O'Dell: "Exact solution of the Thomas-Fermi equation for a trapped Bose-Einstein condensate with dipole-dipole interactions". *Physical Review A* **71** ,033618 (2005). 118

[147] S. Stringari: "Collective Excitations of a Trapped Bose-Condensed Gas". *Physical Review Letters* **77** ,2360–2363 (1996). 121

[148] W.-C. Wu and A. Griffin: "Quantized hydrodynamic model and the,dynamic structure factor for a trapped Bose gas". *Physical Review A* **54** ,4204–4212 (1996). 121

[149] M. Abramowitz and I. A. Stegun: "Handbook of Mathematical Functions. " Chap. 20. Dover PublicationsNew York, 5.. edition (1968). 122

[150] I. Bronshtein, K. Semendyayev, G. Musiol, H. Muehlig, and H. Mhlig: "Handbook of Mathematics" . Springer, New York, 4. edition (2004). 127

[151] F. P. D. Santos, J. Leonard, J. Wang, C. J. Barrelet, F. Perales, E. Rasel, C. S. Unnikrishnan, M. Leduc, and C. Cohen-Tannoudji: "Bose-Einstein Condensation of Metastable Helium". *Physical Review Letters* **86** ,3459–3462 (2001). 132

[152] C. R. Monroe, E. A. Cornell, C. A. Sackett, C. J. Myatt, and C. E. Wieman: "Measurement of Cs-Cs elastic scattering at T=30 mu K". *Physical Review Letters* **70** ,414–417 (1993). 133, 144

[153] E. R. I. Abraham, W. I.McAlexander, C. A. Sackett, and R. G. Hulet: "Spectroscopic determination of the s-wave scattering length of lithium". *Physical Review Letters* **74** ,1315–1318 (1995). 133

[154] S. Moal, M. Portier, J. Kim, J. Dugue, U. D. Rapol, M. Leduc, and C. Cohen-Tannoudji: "Accurate Determination of the Scattering Length of Metastable Helium Atoms Using Dark Resonances between Atoms and Exotic Molecules". *Physical Review Letters* **96** ,023203 (2006). 133

[155] J. Weiner, V. S. Bagnato, S. Zilio, and P. S. Julienne: "Experiments and theory in cold and ultracold collisions". *Rev. Mod. Phys.* **71** ,1–85 (1999). and references therein. 133

[156] C. Kittel: "Introduction to Solid State Physics" . J.Wiley and Sons Inc., New York, USA, fifth edition. edition (1997). 133

[157] D. S. Petrov, C. Salomon, and G. V. Shlyapnikov: "Weakly Bound Dimers of Fermionic Atoms". *Physical Review Letters* **93** ,090404 (2004). 137

[158] D. S. Petrov, C. Salomon, and G. V. Shlyapnikov: "Diatomic molecules in ultracold Fermi gases—novel composite bosons". *Journal of Physics B: Atomic, Molecular and Optical Physics* **38** ,S645–S660 (2005). 137

[159] S. J. J. M. F. Kokkelmans, G. V. Shlyapnikov, and C. Salomon: "Degenerate

atom-molecule mixture in a cold Fermi gas". *Physical Review A* **69** ,031602 (2004). 137

[160] J. Doyle, B. Friedrich, R. V. Krems, and F. Masnou-Seeuws: "Editorial: Quo vadis, cold molecules?". *The European Physical Journal D* **31** ,149 (2004). 137

[161] S. Inouye, M. R. Andrews, J. Stenger, H.-J. Miesner, D. M. Stamper-Kurn, and W. Ketterle: "Observation of Feshbach resonances in a Bose-Einstein condensate". *Nature* **392** (1998). 138

[162] J. Stenger, S. Inouye, M. R. Andrews, H.-J. Miesner, D. M. Stamper-Kurn, and W. Ketterle: "Strongly Enhanced Inelastic Collisions in a Bose-Einstein Condensate near Feshbach Resonances". *Physical Review Letters* **82** ,2422–2425 (1999). 138, 147

[163] J. L. Roberts, N. R. Claussen, J. James P. Burke, C. H. Greene, E. A. Cornell, and C. E. Wieman: "Resonant Magnetic Field Control of Elastic Scattering in Cold Rb". *Physical Review Letters* **81** ,5109–5112 (1998). 138

[164] T. Volz, S. Durr, S. Ernst, A. Marte, and G. Rempe: "Characterization of elastic scattering near a Feshbach resonance in [sup 87]Rb". *Physical Review A* **68** ,010702 (2003). 138, 144

[165] S. L. Cornish, N. R. Claussen, J. L. Roberts, E. A. Cornell, and C. E. Wieman: "Stable [sup 85]Rb Bose-Einstein Condensates with Widely Tunable Interactions". *Physical Review Letters* **85** ,1795–1798 (2000). 138

[166] T. Loftus, C. A. Regal, C. Ticknor, J. L. Bohn, and D. S. Jin: "Resonant Control of Elastic Collisions in an Optically Trapped Fermi Gas of Atoms". *Physical Review Letters* **88** ,173201 (2002). 138, 144

[167] J. Stuhler, A. Griesmaier, J. Werner, T. Koch, M. Fattori, and T. Pfau: "Ultracold chromium atoms: From Feshbach resonances to a dipolar Bose-Einstein condensate.". *Journal of Modern Optics* (2006). in press. 143

[168] J. Stenger, S. Inouye, A. Chikkatur, D. Stamper-Kurn, D. Pritchard, and W. Ketterle: "Bragg Spectroscopy of a Bose–Einstein Condensate". *Physical Review Letters* **82** ,4569 (1999). 144

[169] J. L. Roberts, N. R. Claussen, S. L. Cornish, and C. E. Wieman: "Magnetic Field Dependence of Ultracold Inelastic Collisions near a Feshbach Resonance". *Physical Review Letters* **85** ,728–731 (2000). 147

[170] T. Weber, J. Herbig, M. Mark, H.-C. Nagerl, and R. Grimm: "Three-Body Recombination at Large Scattering Lengths in an Ultracold Atomic Gas". *Physical Review Letters* **91** ,123201 (2003). 147

[171] A. Marte, T. Volz, J. Schuster, S. Dürr, G. Rempe, E. G. M. van Kempen, and B. J. Verhaar: "Feshbach Resonances in Rubidium 87: Precision Measurement and Analysis". *Physical Review Letters* **89** ,283202 (2002). 147

[172] J. Dalibard and C. Cohen-Tannoudji: "Dressed-atom approach to atomic motion in laser light: the dipole force revisited". *J. Opt. Soc. Am. B* **2** ,1707–1720 (1985). 151, 154

[173] B. R. Mollow: "Power Spectrum of Light scattered by Two-Level Systems". *Physical Review* **188** ,1969–1975 (1969). 153